ICARUS

INTERNATIONAL JOURNAL OF SOLAR SYSTEM STUDIES

PUBLISHED IN AFFILIATION WITH THE
DIVISION FOR PLANETARY SCIENCES
AMERICAN ASTRONOMICAL SOCIETY

UNIVERSITY OF HAWAII
JUL -6 198
LIBRARIES

EDITOR: Joseph A. Burns

Space Sciences Building
Cornell University
Ithaca, New York 14853

This Number Completes Volume 79

Volume 79, Number 2, June 1989

ACADEMIC PRESS, INC.
Harcourt Brace Jovanovich, Publishers
San Diego New York Boston
London Sydney Tokyo Toronto

PERIODICAL
QB
1
I3
U.H. LIBRARY

ISSN 0019-1035

ICARUS: International Journal of Solar System Studies

EDITOR
Joseph A. Burns
Space Sciences Building, Cornell University
Ithaca, New York 14853

Telephone: 607-255-4875 Telex: 937478
Bitnet: BURNS @ CRNLASTR

EDITORIAL BOARD

M. J. S. Belton (1987–1989)
Kitt Peak National Observatory
950 Cherry Avenue
Tucson, Arizona 85726

William K. Hartmann (1988–1990)
Planetary Science Institute
2030 East Speedway, Suite 201
Tucson, Arizona 85719

Bruce M. Jakosky (1989–1991)
Geological Sciences and LASP
University of Colorado
Boulder, Colorado 80309-0392

Gerald Schubert (1987–1989)
Earth and Space Sciences
University of California
Los Angeles, California 90024

William B. McKinnon (1988–1990)
Earth and Planetary Sciences
Washington University
Saint Louis, Missouri 63130

Morris Podolak (1989–1991)
Geophysics and Planetary Sciences
Tel Aviv University
Ramat-Aviv 69978, Israel

ASSOCIATE EDITORS

E. Anders
University of Chicago
A. G. W. Cameron
Harvard University
Michael H. Carr
U.S. Geological Survey
Menlo Park, California
Clark Chapman
Planetary Science Institute
Tucson, Arizona
Dale P. Cruikshank
NASA–Ames Research Center
A. H. Delsemme
University of Toledo
A. Dollfus
Observatoire de Paris
Therese Encrenaz
Observatoire de Paris
Peter J. Gierasch
Cornell University
Peter Goldreich
California Institute of Technology
G. S. Golitsyn
Institute of Atmospheric Physics, Moscow
Richard M. Goody
Harvard University

Ronald Greeley
Arizona State University
Richard J. Greenberg
University of Arizona
W. B. Hubbard
University of Arizona
D. M. Hunten
University of Arizona
Andrew Ingersoll
California Institute of Technology
William M. Irvine
University of Massachusetts
William M. Kaula
University of California
Los Angeles
John S. Lewis
University of Arizona
M. Ya. Marov
Institute of Applied Mathematics, Moscow
Harold Masursky
U.S. Geological Survey
Flagstaff, Arizona
Robert L. Millis
Lowell Observatory

V. I. Moroz
Space Research Institute
U.S.S.R. Academy of Sciences, Moscow
David Morrison
NASA–Ames Research Center
Tobias Owen
State University of New York
Stony Brook
Gordon H. Pettengill
Massachusetts Institute of Technology
James B. Pollack
NASA–Ames Research Center
A. E. Ringwood
Australian National University
V. S. Safronov
Institute of Physics of the Earth, Moscow
Carl Sagan
Cornell University
Darrell F. Strobel
Johns Hopkins University
L. Trafton
University of Texas, Austin
Joseph Veverka
Cornell University
A. T. Young
San Diego State University

SENIOR MANUSCRIPT EDITOR: *Cheryl L. Hall*

ICARUS: International Journal of Solar System Studies

"In ancient days two aviators procured to themselves wings. Daedalus flew safely through the middle air and was duly honoured on his landing. Icarus soared upwards to the sun till the wax melted which bound his wings and his flight ended in fiasco. . . . The classical authorities tell us, of course, that he was only 'doing a stunt'; but I prefer to think of him as the man who brought to light a serious constructional defect in the flying-machines of his day.

"So, too, in science. Cautious Daedalus will apply his theories where he feels confident they will safely go; but by his excess of caution their hidden weaknesses remain undiscovered. Icarus will strain his theories to the breaking-point till the weak joints gape. For the mere adventure? Perhaps partly, that is human nature. But if he is destined not yet to reach the sun and solve finally the riddle of its construction, we may at least hope to learn from his journey some hints to build a better machine."

From *Stars and Atoms*, by Sir Arthur Eddington
(Oxford University Press, 1927, p. 41)

ICARUS
(ISSN 0019-1035)

Published monthly by Academic Press, Inc., 1 East First Street, Duluth, MN 55802

1989: Volumes 77–82. Price: $648.00 U.S.A. and Canada; $742.00 all other countries
All prices include postage and handling.

Special subscription rates are available to members and affiliate members of the Division for Planetary Sciences of the American Astronomical Society. Information may be obtained by writing to the Journal Subscription Department at Academic Press. All correspondence and subscription orders should be sent to the office of the Publishers at 1 East First Street, Duluth, MN 55802. Send notices of change of address to the office of the Publishers at least 6 to 8 weeks in advance. Please include both old and new addresses. POSTMASTER: Send changes of address to *Icarus*, 1 East First Street, Duluth, MN 55802.

Second-class postage paid at Duluth, MN, and at additional mailing offices.

Copyright © 1989 by Academic Press, Inc.

ICARUS

INTERNATIONAL JOURNAL OF SOLAR SYSTEM STUDIES

Volume 79, Number 2, June 1989

Copyright © 1989 by Academic Press, Inc.

ALL RIGHTS RESERVED

No part of this publication may be reproduced or transmitted in any form or by any means, electronic or mechanical, including photocopy, recording, or any information storage and retrieval system, without permission in writing from the copyright owner.

The appearance of the code at the bottom of the first page of an article in this journal indicates the copyright owner's consent that copies of the article may be made for personal or internal use, or for the personal or internal use of specific clients. This consent is given on the condition, however, that the copier pay the stated per copy fee through the Copyright Clearance Center, Inc. (27 Congress Street, Salem, Massachusetts 01970), for copying beyond that permitted by Sections 107 or 108 of the U.S. Copyright Law. This consent does not extend to other kinds of copying, such as copying for general distribution, for advertising or promotional purposes, for creating new collective works, or for resale. Copy fees for pre-1989 articles are as shown on the article title pages; if no fee code appears on the title page, the copy fee is the same as for current articles.

0019-1035/89 $3.00

MADE IN THE UNITED STATES OF AMERICA

ICARUS 79, 229–288 (1989)

Urey Prize Lecture: Water on Mars

STEVEN W. SQUYRES

Center for Radiophysics and Space Research, Cornell University, Ithaca, New York 14853

Received November 16, 1988; revised November 17, 1988

Geologic evidence indicates that the Martian surface has been substantially modified by the action of liquid water and that much of that water still resides beneath the surface as ground ice. The action of liquid water at the surface can be divided into an early epoch of valley system formation and a later epoch of outflow channel formation. The former might have required a climate somewhat warmer than the present one, while the latter did not. Layered deposits in the Valles Marineris may have been deposited in liquid water during the epoch of outflow channel formation, although the evidence that the deposition there was aqueous is not conclusive. Aqueous deposits were laid down in local topographic depressions during the epoch of valley system formation. Using the physics of heat transport in ice-covered lakes in the Dry Valleys of Antarctica as a model, it appears that liquid water lakes could have persisted in these depressions under a protective ice cover for significant periods even if the early Martian climate were fairly cold. Early lakes on Mars could have served as sites for precipitation of carbonates, scavenging CO_2 from the planet's atmosphere. Ancient aqueous sediments may contain a record of the climatic conditions that prevailed on the planet early in its history and are an important potential target for future sample return missions. Calculations of the thermodynamic stability of ground ice on Mars suggest that it can exist very close to the surface at high latitudes, but can persist only at substantial depths near the equator. A variety of observed Martian landforms can be attributed to creep of the Martian regolith abetted by deformation of ground ice. The most important of these, terrain softening, produces a pronounced rounding of sharp topographic features and conversion of concave or straight slope profiles to a convex shape. Finite element modeling of the flow process indicates that terrain softening is a near-surface phenomenon. Global mapping of creep features supports the idea that ice is present in near-surface materials at latitudes higher than ±30°, and suggests that ice is largely absent at lower latitudes. However, based on the rheology of terrestrial frozen ground, the Martian regolith must be thoroughly comminuted in order for significant creep to take place. Because regolith comminution is dominated by impacts, this condition is likely to be satisfied only relatively close to the surface. Substantial ground ice therefore may also exist at latitudes lower than ±30°, but at depths where materials are less thoroughly comminuted, preventing flow. It will be possible to investigate the geographic and vertical distribution of ice in the upper tens of centimeters of the Martian regolith using remote gamma-ray spectral data from the Mars Observer mission. © 1989 Academic Press, Inc.

INTRODUCTION

Water on Mars has been a subject of fascination since the days of the infamous canals of Schiaparelli and Lowell. The interest in the subject derives from several sources, including the effectiveness of water and ice as agents of geologic erosion and transport, the use of water abundance as an indicator of the total planetary volatile endowment, and the suitability of liquid water as an abode for life. Interest has been further heightened by recent thinking about eventual human exploration of the planet and the need for Martian resources. Since the Mariner 9 mission, it has been clear that

0019-1035/89 $3.00

Copyright © 1989 by Academic Press, Inc.
All rights of reproduction in any form reserved.

Mars in the present epoch is a desert planet. It also has been clear that this was not always the case. Water has played a significant role in Mars' geologic history. Just how significant that role really has been, however, has been a subject of continuing debate.

The subject has a peculiar history, Schiaparelli and Lowell notwithstanding. Many attempts to estimate the amount of water on Mars have been based on the chemical and isotopic composition of the present Martian atmosphere. When the Soviet Mars 6 lander seemed to have detected large amounts of argon in the Martian atmosphere (Istomin and Grechnev 1976), the observation was widely interpreted as an indicator of a substantial Martian H_2O endowment, based on the assumption of an Earth-like H_2O/Ar ratio on Mars. Total outgassed water amounts of as much as 10^5 g cm^{-2} were envisioned, or enough to cover the entire planet with a layer of water 1 km deep. A few years later, the Viking Landers touched down on the Martian surface and determined that the argon concentration there in fact is only 1.6% (Owen and Biemann 1976). Estimates of Martian H_2O outgassing dropped to $\sim 10^3$ g cm^{-2} or less. Then came results from the Pioneer Venus probe that showed unexpectedly large amounts of argon in the Venusian atmosphere (Hoffman *et al.* 1980) and called into question the entire concept of using argon as an indicator of H_2O outgassing. Attempts were made using other indicators like nitrogen isotopic ratios (McElroy *et al.* 1976, 1977) and inferred potassium abundance (Pollack and Black 1979), but these too involved uncertain assumptions. No real consensus emerged regarding the amount of outgassing on Mars as inferred from the composition of its atmosphere and surface materials, but the general feeling among most workers in the field seemed to be that Mars had always been a fairly dry planet.

Despite the difficulties in making geochemical inferences, there has been something of a revolution in thinking about the subject of water on Mars in the past few years. The change has come largely through the use of geologic rather than chemical evidence. To many, the low estimates of the Martian H_2O endowment always seemed at odds with the widespread geologic evidence for the action of water and ice on and beneath the Martian surface (see, e.g., Carr 1986). For example, water on Mars has carved enormous outflow channels and numerous small valley systems, and removal of subsurface water has led to formation of many deep and extensive collapse features. There still is no clear consensus regarding the amount of H_2O on Mars or its importance in Martian geologic history, and it is safe to assume that none will emerge until the planet is more thoroughly explored. Nevertheless, there has been a strong recent shift on the basis of geologic data toward the view that Mars was, and is, a "wet" planet.

This paper is about the history and distribution of water on Mars. The subject is a vast one, and I cannot deal with it all adequately in a single paper. I concentrate, therefore, on two aspects that seem to me to be of particular importance: the possible existence of standing bodies of liquid water very early in Martian history and the present distribution of Martian ground ice. In the first part of the paper, I outline the rationale behind the view that there may be water-lain sediments in some locations on Mars, and discuss the importance of such sediments as targets for future exploration of the planet. In the second, I discuss the factors that control the distribution of ground ice on Mars, and discuss ways in which the distribution may be investigated via its effects on viscous deformation of the Martian regolith and on the spectrum of planetary gamma radiation that can be detected from an orbital spacecraft.

LIQUID WATER ON EARLY MARS

A large body of work, which I shall summarize briefly below, has shown that liquid water once flowed in abundance across the surface of Mars. A subject that has received much less attention, however, is whether standing bodies of liquid water ever persisted on the Martian surface for any significant period.

The issue is one of considerable importance, stemming primarily from the fact that sediments deposited in liquid water can preserve a rich record of the physical and chemical conditions that existed in the water and in the atmosphere above it at the time of their deposition. On the Earth, because of our planet's long history of intense tectonic activity, the sedimentary record of the earliest parts of its history is very fragmentary. In fact, sedimentary evidence concerning the immediate postaccretional period when the Earth possessed its earliest atmosphere and when life was gaining its first foothold appears to be lacking altogether. The situation on Mars may be very different. Mars has undergone substantially less tectonic and volcanic activity than has the Earth and is rich in geologic terrains that date back billions of years. If we can identify aqueous sedimentary deposits in these terrains, then we can hope one day to investigate those deposits in detail and to read the record that they contain of the conditions that existed in the earliest part of Martian history.

Evidence for Liquid Water on Mars

One of the most startling and important discoveries of the Mariner 9 mission was widespread evidence for modification of the Martian surface by the action of liquid water (McCauley *et al.* 1972, Masursky 1973, Milton 1973). This evidence comes primarily in the form of channels, which often are remarkably similar to terrestrial stream, river, and flood features. Martian channels have a wide range of morphologies, but those that show the strongest evidence for a fluvial origin can be grouped in two categories: *outflow channels* and *valley systems* (Sharp and Malin 1975). Outflow channels arise fully developed from spatially limited, often clearly bounded, source regions. Valley systems, on the other hand, possess tributary systems and are more similar to conventional terrestrial drainage systems.

Outflow channels are most common along the Martian northern lowland/southern highland boundary, where they arise from source regions in the highlands and debouch onto the lowland plains. Many of the source regions show very complex topography that earns them the name "chaotic terrain." The appearance of chaotic terrain indicates removal of subsurface material and widespread collapse of topography. The channels arise fully born from these chaotic regions and may extend for many hundreds of kilometers. Their debouchments are much less distinct than their sources. In fact, they often simply fade into obscurity at their downstream ends. While there must be massive deposits of sediments at their debouchments, these materials generally cannot be identified with confidence from their morphology.

Although clearly the result of fluid flow, outflow channels bear only the most superficial resemblance to terrestrial rivers. They are much more similar to features formed by catastrophic floods on Earth. In fact, the morphologic evidence appears overwhelming that the outflow channels were formed by very rapid release of large amounts of subsurface water from their source regions (Milton 1973, Baker and Milton 1974, Baker and Kochel 1979).

A variety of release mechanisms have been proposed to account for the large discharges required by the large sizes of these channels. Perhaps the most plausible is the suggestion of Carr (1979) that ground ice was melted from below by geothermal warming and that the water was released at high pressure from an extensive and highly permeable groundwater system confined by a cap of impermeable permafrost and pressurized by tectonic tilting. Whatever the release mechanism, however, it is clear that the discharges were huge (see, e.g., Carr

1979). In fact, assuming sufficient geothermal heat to initiate the release, the discharges were so high that these floods could have proceeded their full distance across the Martian surface under the present climatic conditions (see, e.g., Wallace and Sagan 1979). Despite the fact that exposed liquid will freeze rapidly on exposure to the present Martian atmosphere, the enormous amount of latent heat present in a flood of such a magnitude would enable the water to flow for many hundreds of kilometers before being halted by freezing. So, while outflow channels tells us that water has flowed in abundance on Mars, they tell us little about the climatic history of the planet.

Valley systems are very different from outflow channels. They are superficially similar to terrestrial drainage systems, consisting of narrow, often sinuous valleys with branching tributary systems. Despite this apparent similarity, however, there are important morphologic differences between Martian valley systems and most terrestrial drainage systems (Pieri 1980). The Martian valleys commonly have steep, cliff-like walls and rounded amphitheater terminations to tributaries. The tributary systems do not show typical dendritic branching patterns, but instead are poorly developed and show little evidence for runoff erosion on the intervalley surfaces. These observations strongly suggest that precipitation was not responsible for carving most valley systems. Instead, the landforms exhibited by the valley systems are more typical of those formed by sapping, the gradual removal and flow of subsurface fluid.

Essentially all of the valley systems on Mars are found in the ancient cratered highlands (Pieri 1976, 1980, Carr and Clow 1981). The density of impact craters superimposed on the valleys is substantially higher than that for the outflow channels and indicates an age as old as the cratered highlands themselves. The formation of valley systems on Mars was almost completely limited to the earliest part of the planet's recorded geologic history.

A particularly important aspect of the valley systems' morphology is that the fluid discharges implied by their dimensions are very modest. In fact, it commonly has been assumed that they could not have formed under the present climatic conditions. It might be possible for a stream to flow as much as a few hundred kilometers on Mars under the present climate if it were protected from the atmosphere by an ice cover and if it were flowing in an established channel with a fairly steep gradient (Carr 1983). However, problems may be posed by initiating the flow and establishing the channel in the first place. Moreover, the modest discharges implied by the valley morphology seem to require a significant time to produce the volume of erosion observed and flow of water at the implied discharge for the necessary duration might not be possible under the present climate. Much more quantitative work in this area is needed, but work done to date suggests that atmospheric temperatures and pressures on Mars at the time of valley system formation may have been higher than they are today. The general lack of valley systems in terrains younger than roughly 4.0–3.5 Gy old suggests that this more clement era, if it occurred, did not extend past the earliest part of Martian history.

Possible Aqueous Sedimentation on Mars

I now turn to a discussion of the sedimentation associated with fluvial activity on Mars. I consider possible sedimentation in two environments: in the Valles Marineris canyon system during the epoch of outflow channel formation and in shallow local depressions in heavily cratered terrain during the epoch of valley system formation.

The Valles Marineris. Thick sequences of rhythmically layered deposits in the Valles Marineris first were found during the Mariner 9 mission. They were studied on

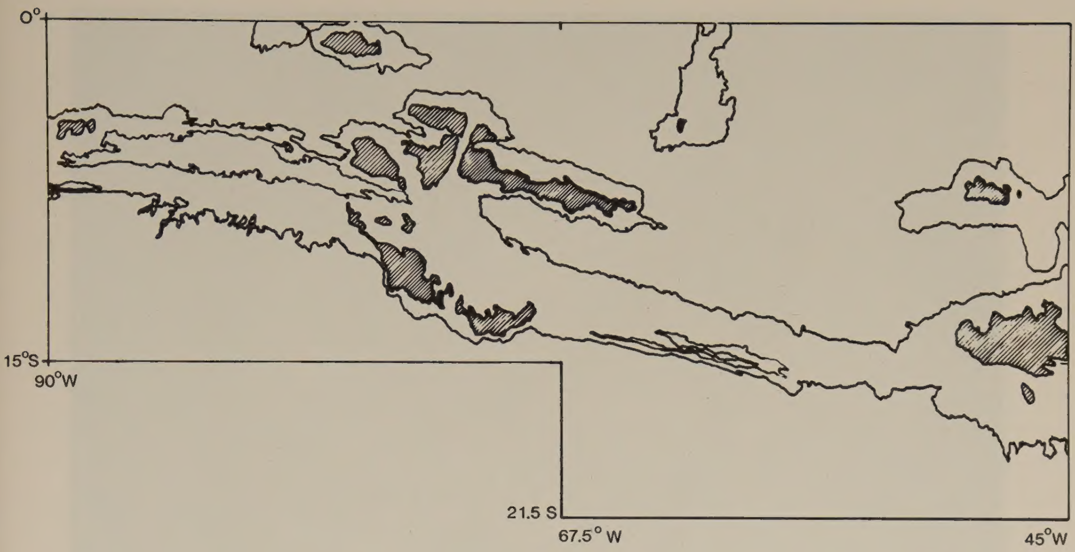

FIG. 1. Map of the Valles Marineris region, indicating the distribution of layered deposits and possible layered deposits (both shown as cross-hatched regions). Solid lines give the outlines of the major canyons (modified from Nedell *et al.* 1987a).

the basis of both Mariner 9 and Viking data by a number of investigators (Malin 1976, McCauley 1978, Peterson 1981, Lucchitta 1981, 1982, Lucchitta and Ferguson 1983). Nedell *et al.* (1987a) performed a detailed study of the layered deposits using the full Viking mission imaging data set. We used these data to investigate four hypotheses for the deposits' origin: (1) they are eolian deposits, (2) they are remnants of the same material that makes up the canyon walls, (3) they are the deposits of subaerial explosive volcanic eruptions, or (4) they were deposited in standing bodies of water.

A map giving the distribution of the deposits is shown in Fig. 1, and images presenting examples of their appearance are shown in Figs. 2 and 3. The deposits form plateaus on the floors of the Valles Marineris, rising as high as 5 km above the canyon floor. The greatest total thicknesses are found in Hebes, Ophir, and Candor chasmata. In each of these locations, the upper surface of the layered deposit plateau rises to within 500 m of the elevation of the surrounding plains. Rhythmic, nearly horizontal layers are exposed on the slopes of the plateaus, which are as steep as 22° in some places. Individual layers extend laterally for at least tens of kilometers. In some locations, the deposits lap directly against the eroded spur-and-gully topography of the canyon walls; in others, the plateaus stand alone and are separated from the canyon walls by a deep trough. Eroded surfaces of the deposits typically show a distinctive fluted topography that is strikingly different from the morphology of the canyon walls. In a few instances the plateaus clearly have undergone very deep erosion subsequent to their formation.

Several estimates of layer thicknesses have been made stereophotogrammetrically (Nedell *et al.* 1987a). Mean layer thicknesses in various measured sections ranged from a minimum of 70 m to a maximum of 300 m. Of course, it is possible that finer layering exists at a scale too small to be visible at Viking resolution (20–80 m/pixel). The measurements reveal systematic variations in layer thicknesses throughout a sequence; for example, one

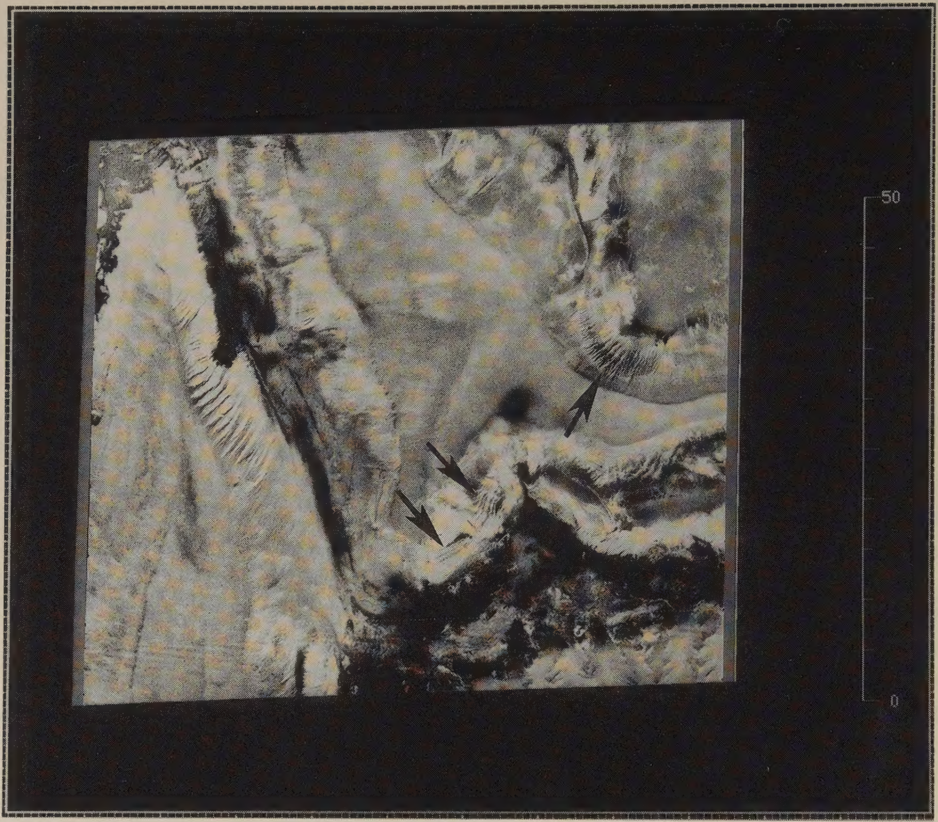

FIG. 2. A plateau composed of layered deposits in Candor Chasma in the Valles Marineris. Arrows indicate areas where layers are well exposed (Viking Orbiter image 66A25, latitude −6°, longitude 73°).

sequence in Candor Chasma has coarse (300 m) layering at its base and fine (70 m) layering at its top. Although no unequivocal angular unconformities are observed, evidence is found from the measured topography that some sequences may be tilted by a few degrees.

From the appearance of the deposits and their stratigraphic relationships with other materials in the canyons, it is possible to infer their place in the geologic history of the Valles Marineris and to evaluate the various possible hypotheses for their origin. The Valles Marineris themselves appear to have begun as extensional tectonic features. They were subsequently widened by gradual mass-wasting and development of spur-and-gully topography on their walls (Sharp 1973a, Lucchitta 1981). Liquid water may have been present in the canyons at about this time, since they merge into chaotic terrain and several large outflow channels at their eastern end. Still later, the canyons were widened further by massive landsliding of the canyon walls (Lucchitta 1979).

The layered chasma deposits clearly postdate the initial formation of the canyons. They probably date from approximately the same epoch as the enlargement of the canyons by development of the spur-and-gully topography. This timing is suggested by the fact that layered chasma deposits lap against spur-and-gully topography in some locations, but are separated from it in others. The eroded plateaus of

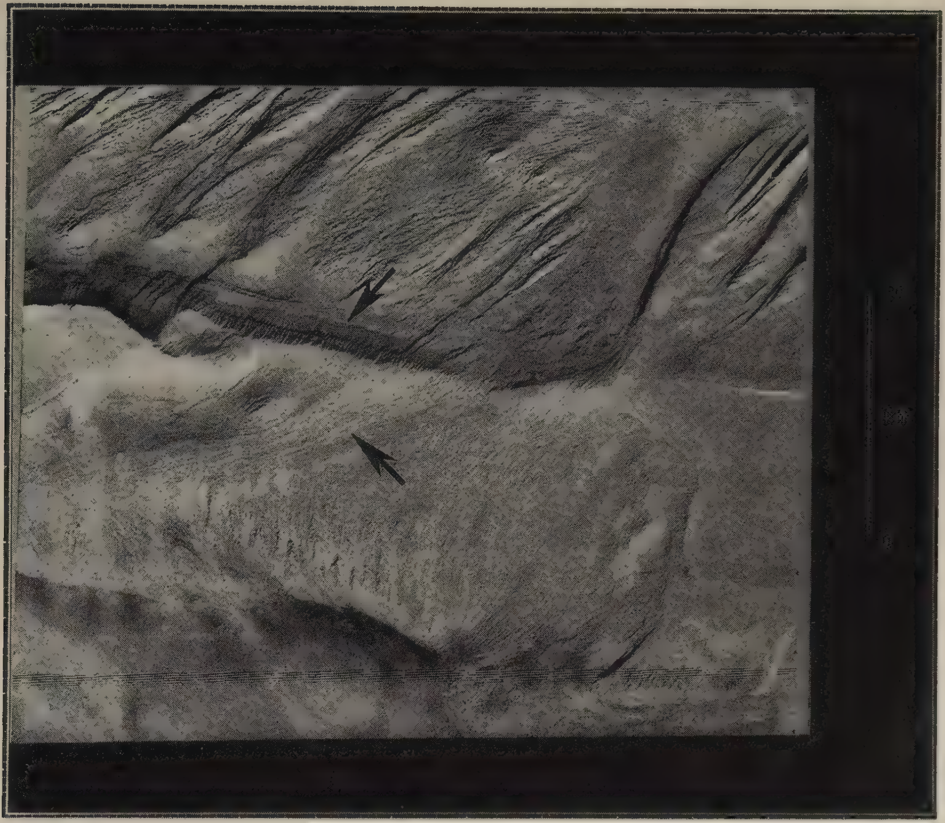

FIG. 3. Exposures of layered deposits in Candor Chasma in the Valles Marineris. Arrows indicate particularly well-exposed layers (Viking Orbiter Image 815A58, latitude −7°, longitude 70°).

layered deposits clearly divert landslides from the canyon walls, so both the formation of the deposits and their subsequent deep erosion were completed before the landsliding took place.

Two of the four hypotheses mentioned above for the origin of the deposits may be argued against with some degree of certainty. The suggestion that the deposits are eolian in origin appears flawed because the deposits are found only in the deepest parts of the canyons. There are no traces of the materials on the upper canyon walls or the plains surrounding the Valles Marineris, as would be expected for dust that has settled from the atmosphere. The hypothesis that the deposits are erosional remnants of the canyon wall material can be eliminated because of the lack of similar layering in the canyon walls and the very different erosional styles of the two materials. The volcanic and aqueous sedimentation hypotheses, however, both suffer from no obvious fatal flaws.

When considered in more detail, a volcanic origin cannot be ruled out, although several points argue against it. If the layered chasma deposits are volcanic, an ash-flow origin is much more likely than origin by air fall, for the same reasons that eolian deposition is not an attractive candidate. The characteristics of the deposits do not appear to match what one would expect for ash flows, however. The sources of the flows would have to lie on the canyon floors, but no likely calderas or other eruptive vents can be identified. Moreover, no volcanic edifices are observed nor any systematic thinning of layers away from possible sources, as would be expected for ash flows.

The hypothesis that the deposits are sediments deposited in a standing liquid water environment appears to me to be most consistent with all of the data, a conclusion also reached by a number of other investigators (McCauley 1978, Lucchitta 1981, Carr 1981). This process seems to explain best the deposits' locations, near horizontality, lateral continuity, and stratigraphic relationships with other units within the canyons. Large rift valleys are common locations for deep lakes on Earth, and there is ample evidence that, around the time of canyon formation, there was a substantial subsurface aquifer system on Mars (Sharp 1973b, Carr 1979). When deep tectonic depressions formed in this material, it is natural that water would partially fill the depressions temporarily, probably capped with a thick ice cover.

While deposition in standing water may account best for the characteristics of the layers, the actual source of the materials is an open question. Some may have originated from the canyon walls; certainly it is reasonable to expect that material mass-wasted from the walls while water was present would be deposited in that water. However, this source is inadequate to account for the full volume of the deposits. Transport of eolian sediments laid down on the lake surface through the ice cover is another possibility, and Nedell *et al.* (1987a) discussed several mechanisms by which this could take place. A final possibility is that explosive volcanic eruptions took place on the canyon floors while the canyons were filled with water; in this case the presence of the water would result in more even deposition of the materials and burial of vents, helping to take care of some of the morphologic arguments facing a subaerial volcanic origin.

Subsequent to their formation, some plateaus of layered chasma deposits appear to have been deeply eroded. A possible explanation is that lakes filling the canyons overtopped a divide to the south or east and drained rapidly, eroding some of the layered materials away as the flow took place (Lucchitta 1982). The canyons slope downhill to the east, and there are indeed large outflow channels emanating from their eastern end.

The layered deposits in the Valles Marineris appear to be reasonable candidates for sediments deposited in standing water bodies on Mars. For use as a record of the climatic changes that may have been experienced by the planet, however, these deposits suffer from two major difficulties. First, their identification as aqueous sediments is equivocal. Despite the morphologic arguments presented above, a subaerial volcanic origin cannot be ruled out. Second, the deposits date roughly from the epoch of outflow channel formation on Mars. They are significantly younger than those of the valley systems found in Mars' ancient heavily cratered terrain. While valley systems might have required a warmer climate than that which exists at the present, outflow channels did not. There is no evidence to suggest, then, that these deposits formed during climatic conditions that were in any way different from those existing on Mars now. In order to find sedimentary evidence that can be used to address the question of a possible former warmer climate on Mars, we must turn to sediments associated with the only features that actually might provide evidence for such a warmer climate: the valley systems.

The valley systems. The valley systems in Mars' ancient heavily cratered terrain show a considerable amount of variety in their lengths, their geometries, and their relationships to other valley systems. Some consist of one trunk valley hundreds of kilometers long, with only a few short, stubby tributaries. Others are nothing more than short gullies down steep slopes like crater walls. Still others show a moderately

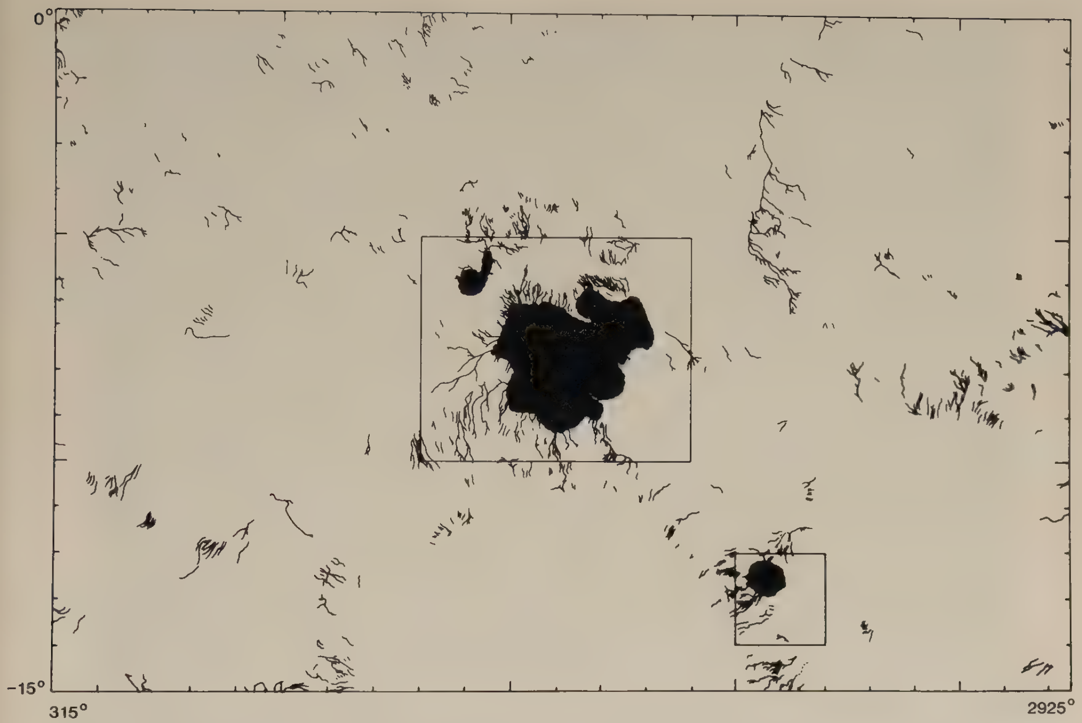

FIG. 4. Map of valley systems in the Iapygia NW quadrangle of Mars. Closed depressions that may function as sedimentation basins are shaded. Boxes outline regions searched for high-resolution coverage. Mapping by J. M. Goldspiel.

well-developed quasi-dendritic drainage pattern and drain areas upward of 10^4 km^2 in size.

The patterns of the drainage basins were established by topography that predates their formation. The topography in the ancient terrain on Mars is primarily the result of cratering, and it contains many local closed topographic depressions. Many of these, of course, are craters themselves; others are simply local topographic lows spaced among the surrounding crater rims. Many of the valley systems, including well-developed drainage networks, flow into such closed depressions. Where a large number of valleys flow into a single, small, well-defined local depression, the potential exists for significant aqueous sedimentary deposition to have taken place. Indeed, the materials eroded from the valleys could have gone nowhere else. The problem lies in ascertaining that the sediments have not been subsequently removed, buried, or modified in such a fashion that the record they might have contained is lost.

Figure 4 shows one of a series of maps of drainage systems in the ancient cratered terrain on Mars that is being compiled by J. M. Goldspiel (personal communication, 1988). It shows something of the observed variety in valley system geometry. A number of well-developed valley systems are observed, along with many small, localized valley segments. The areas shown as shaded are local closed depressions into which a number of valley systems flow. Two small ones are formed largely or entirely by impact craters; one larger one is a broad topographic depression nestled among craters. Locations like these can be recognized readily from moderate resolution images and are relatively common in the ancient heavily cratered terrain.

Figures 5 and 6 show examples of two

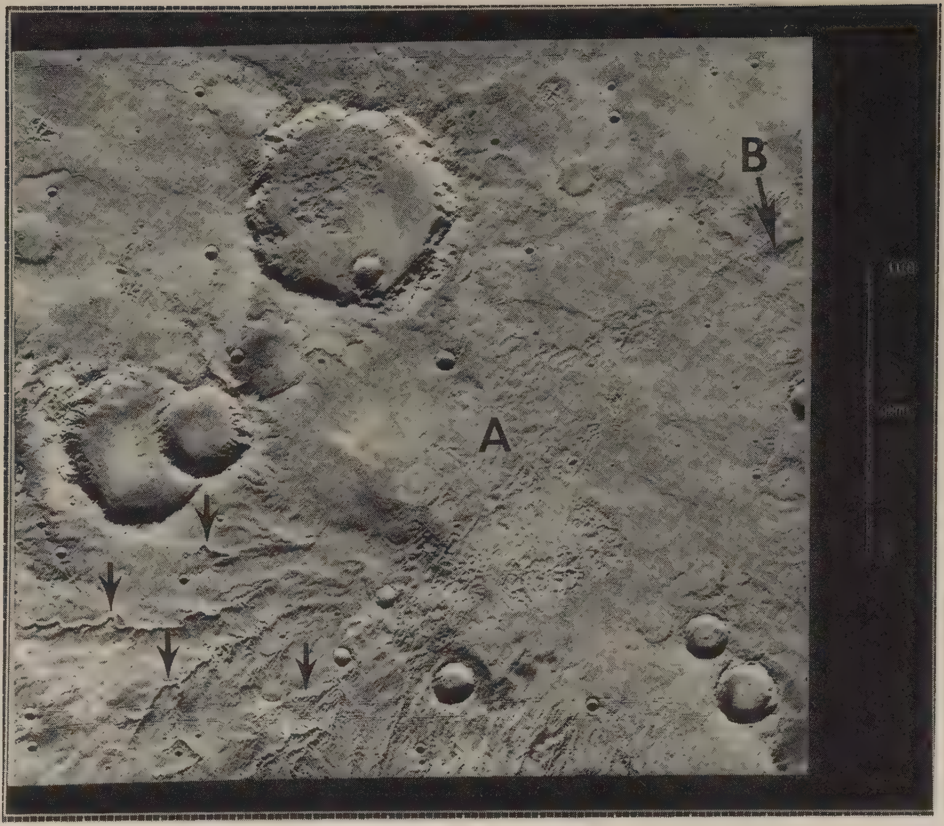

FIG. 5. A local topographic depression in heavily cratered terrain, into which a number of valley systems (arrows) drain. *A* indicates the interior of the depression, *B* indicates a single valley draining the expression (Viking Orbiter image 615A66, latitude −23°, longitude 13°).

other locations that might contain ancient water-lain sediments. Figure 5 is a moderate-resolution view of a large local topographic low into which a large number of well-developed valley systems flow. A single valley flows out of the depression and continues down a gentle regional topographic slope for more than five hundred kilometers. Clearly a substantial amount of water drained out of the depression. This configuration of valleys suggests that the depression was partially filled with water from the inflowing valley systems, overtopped a divide, and eventually drained. The topography is not sufficiently well known to determine the depth of ponding possible; it may have been quite shallow. A particularly interesting characteristic of some of the materials in the interior of the depression is that they have an unusual hummocky texture. This hummocky unit may be composed of the materials that were deposited by water from the inflowing valley systems, but the origin of the texturing is unclear.

Another possible example is shown at high resolution in Fig. 6. Here a quasi-dendritic valley system breaches and empties into an ancient and highly degraded impact crater. On the opposite side of the crater, the crater wall is again breached and a single valley drains from it and into a lower and much broader depression. The crater is nearly filled with material, and indeed it seems likely that the total volume of debris eroded from the inflowing valleys exceeded the initial capacity of the crater when it was fresh. A significant fraction of the crater-filling material therefore may be debris eroded from the upstream valleys and deposited in standing water that ponded temporarily in the crater. Further deposition would have taken place on the lowlands downstream from the crater. A particularly noteworthy (and troubling) aspect of Fig. 6 is that it shows the highly degraded nature of many valley systems that becomes evident when they are viewed at high resolution. The valley systems are very ancient features, and they and their sediments have in many cases been substantially modified by subsequent geologic activity.

Conditions in Standing Water Bodies on Early Mars

What might the conditions have been like in temporary bodies of standing water very early in Martian history? The answer, of course, depends on the climate that prevailed at the time. It is interesting to speculate on the possibility of a very warm climate—one so warm that liquid could exist even exposed directly to the atmosphere. However, while reasonable theo-

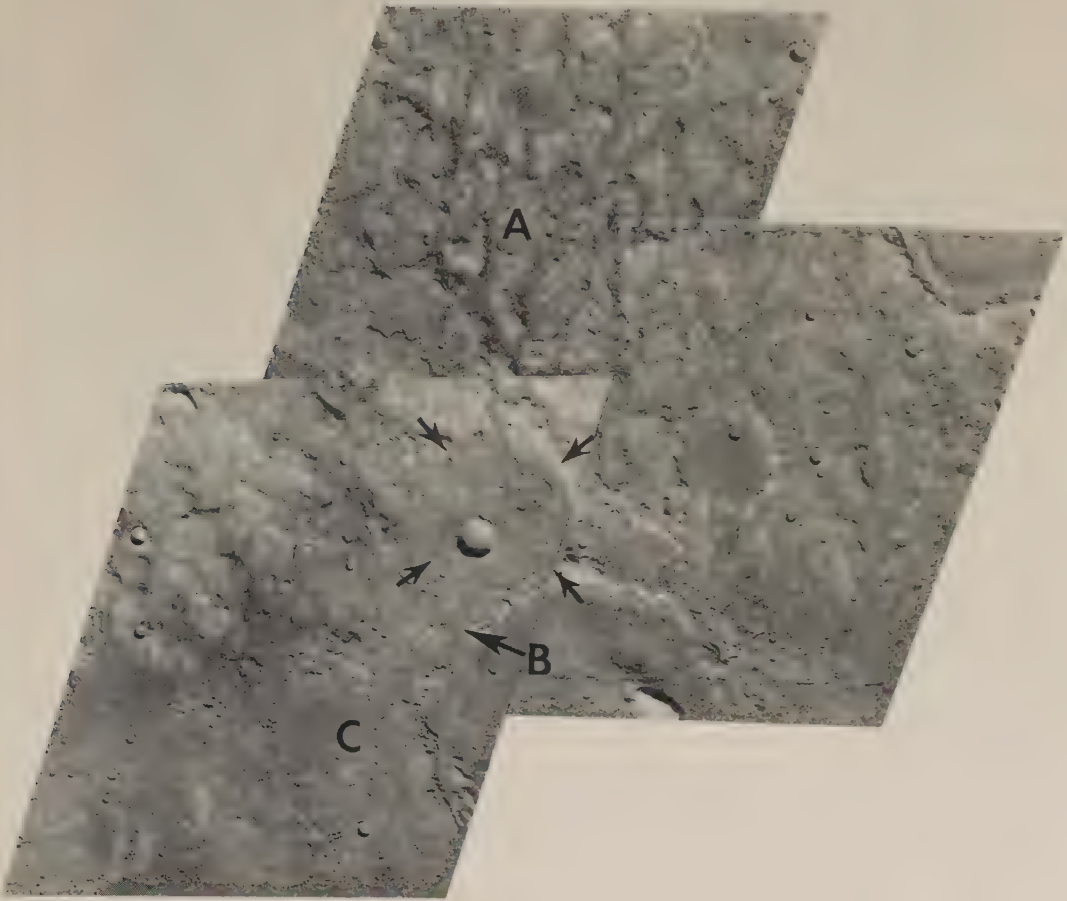

FIG. 6. High-resolution view of ancient valley systems (*A*) draining into a highly degraded, largely filled impact crater (rim indicated by arrows). A single valley drains from the crater at *B* and empties onto lowland plains at *C* (Viking Orbiter images 754A09, 754A10, and 754A11, latitude −9°, longitude 279°; scale across each frame is about 30 km).

retical arguments have been advanced supporting this view (see, e.g., Pollack *et al.* 1987), there is nothing in the geologic record that appears to require it. The valley systems might have required a climate somewhat warmer than the present one for their formation, but it is clear that substantial flow and erosion are possible in a cold climate under a protective ice cover. Also, it must be kept in mind that the Martian surface near the end of heavy bombardment was an ever-changing landscape, with frequent burial of materials by the ejecta of large impacts. The sedimentary deposits we are most likely still to be able to identify at the present are those that were laid down latest in this period. Even if there were very early conditions that allowed exposed liquid to exist, the most recent water-lain deposits (and hence the ones we are most likely to observe) would have been formed as the climate was cooling and as an ice cover was becoming a necessity for liquid to persist. The best case for aqueous sedimentation early in Martian history warranted by the geologic evidence, then, is sedimentation in a small, shallow water body covered with ice.

Insight into the physics, chemistry, and sedimentary geology of ice-covered lakes early in Martian history may be gained by studying perennially ice-covered lakes on Earth. Such lakes are rare. The best-studied examples are in the Dry Valleys of Antarctica, a relatively small glacier-free region of the continent cut off from the main Antarctic ice sheet by the Transantarctic Mountains. The Dry Valleys lie near sea level at a latitude of about −77°30′ in South Victoria Land. The climate there is among the most Mars-like on Earth. Air temperatures range from about −45°C in winter to a maximum of about +5°C in midsummer; the mean annual temperature is roughly −20°C. Precipitation is extremely low, creating a true polar desert. A number of lakes are found there (Fig. 7), with surface areas ranging up to ~10 km^2. Despite the fact that the mean annual temperature is substantially below freezing, the lakes remain mostly liquid. They are covered year-round with ice 3 to 5 m thick. The ice cover has a profound effect on the water chemistry, sedimentation, and biological activity within the lakes. Because they constitute a unique terrestrial environment, and because that environment may be in some ways analogous to aqueous environments existing on early Mars, these lakes recently have been subjected to intense study (McKay *et al.* 1985, Wharton *et al.* 1986, Nedell *et al.* 1987b, Clow *et al.* 1988, Squyres *et al.* 1989).

McKay *et al.* (1985) considered the energy terms that influence the thickness of the ice cover on these lakes. The major terms in the overall energy budget for an ice-covered lake (on Earth or Mars) are shown in Fig. 8. In general, the lakes in Antarctica have inflow streams that flow briefly in summer, but no outflow streams. The only way in which they lose water is by ablation from the ice surface. An analogous situation would have existed on Mars where valley systems empty into a closed topographic depression. If the lake is large, lateral conduction of heat from the shore is negligible. Thermal energy is added to the water in the lake by geothermal heat flow at the base and, much more importantly, by the influx of water from inflow streams or from groundwater seepage. The latent heat of fusion in this water is released at the ice/water interface when freezing takes place to form new ice. Inflowing water also can carry sensible heat; however, since the temperature of the water in Antarctica (and probably also on Mars) is near 0°C, this contribution is small. Heat is transported from the water upward through the ice cover to the cold air above by conduction. Ablation from the ice surface removes heat and H_2O to the atmosphere. Finally, sunlight shining into the ice deposits energy within it and, if it is thin enough, into the water below.

If the geothermal heat flux is small, the critical factor that allows the lakes to re-

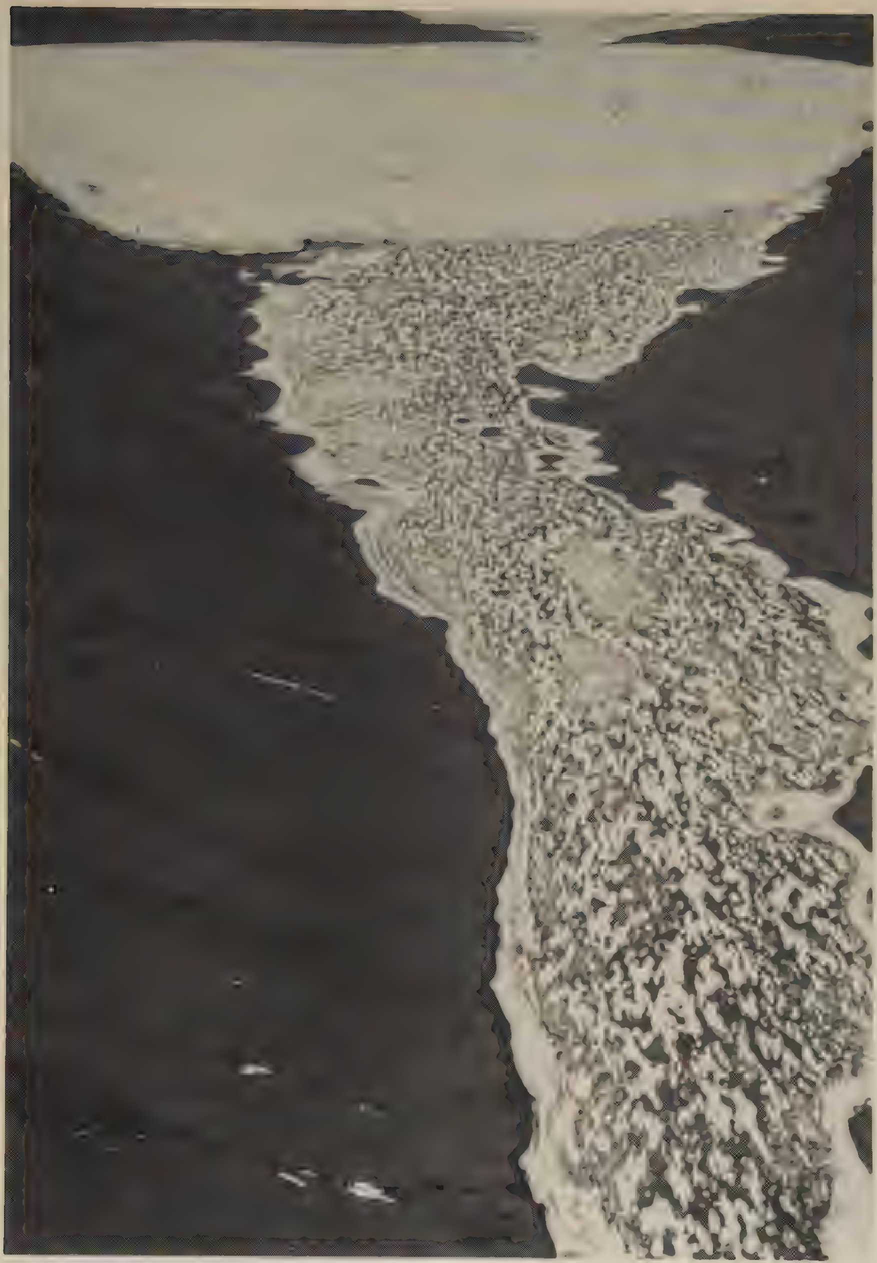

FIG. 7. Lake Hoare, in Taylor Valley, Antarctica. Despite a mean annual temperature of −20°C, liquid water persists beneath an ice cover 3.5 m thick. The lake is about 4 km long and dammed at the far end by the Canada Glacier.

main liquid despite the cold atmospheric temperatures is the latent heat in the inflowing water. Assuming a sufficient water supply, the ice cover will reach and sustain an equilibrium thickness such that the ablation from the surface is balanced by freezing at the ice/water interface. The thickness stabilizes at a value such that the conductive energy flux upward just equals the heat removed by ablation at the ice surface (with

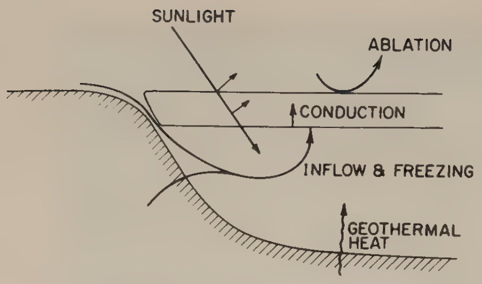

FIG. 8. The major terms in the energy budget of an ice-covered lake. See text for discussion (modified from McKay *et al.* 1985).

some adjustment for additional solar energy input). The primary factor influencing the ice thickness, then, is the ablation rate at the ice surface. If the ablation rate increases, the ice will thin until the conductive heat flux becomes large enough to balance the increased heat loss from the ice surface; if the ablation rate decreases, the ice instead will thicken.

Using measured values of the ablation rate, solar flux, ice albedo, and ice extinction path length, the model described here does a good job of predicting ice thicknesses for Antarctic dry valley lakes. Taking the best available values for these parameters, including an annual ablation rate of about 30 cm year^{-1}, we calculated an equilibrium ice thickness for dry valley lakes of about 3.6 m, very close to the measured value for most lakes (McKay *et al.* 1985).

The same kind of model may be used to consider the thickness of ice on lakes that may have formed early in Martian history. As in the Antarctic, the ablation rate exerts a strong influence on ice thickness. For Mars, of course, the ablation rates must be calculated. The treatment of the ablation rate that I have adopted here is based on Brutsaert's (1975, 1982) model of evaporation into planetary atmospheres. The same model has been used, along with meteorological data, to calculate ablation rates for Antarctic lakes that are in excellent agreement with measured values (Clow *et al.* 1988).

Ablation from the ice surface takes place by sublimation into the atmosphere, at a rate that is controlled in part by the ice temperature, but limited by upward diffusion of water vapor. At the ice surface, vapor is transported first into an interfacial sublayer of the atmosphere that is characterized by eddies that sweep recurrently downward from the fully turbulent dynamic sublayer above to contact the surface. The thickness of this interfacial sublayer is of the order of the height of roughness elements on the ice surface, which in Antarctica is ~1 m. Water vapor transport from the surface is dominated by molecular diffusion into Kolmogorov-scale eddies in the interfacial sublayer and subsequently upward by eddy diffusion in the fully turbulent dynamic sublayer. The rate of eddy transport to the top of the full atmospheric boundary layer is influenced by atmospheric stability; for the calculations presented here I consider the nominal case of a neutral atmosphere. A more complete treatment, including the effect of nonneutral conditions, will be presented in a subsequent paper.

Using this model for transport of water in the atmospheric boundary layer, I have calculated ablation rates for ice surfaces on Mars for three different sets of atmospheric conditions. The properties of the ice cover (surface roughness, albedo, extinction path length for solar radiation) are assumed to be identical to those measured for ice on the lakes in Antarctica. The atmospheric conditions considered are the present pressure of 7 mbar, a moderately dense early atmosphere of 300 mbar, and a dense early atmosphere of 1000 mbar. According to the greenhouse model of Pollack *et al.* (1987), a 300-mbar CO_2 atmosphere would contribute about 15° of greenhouse warming above the present temperature, while a 1000-mbar atmosphere would raise the temperature about 30°. For the present atmospheric pressure, I assume that the mean annual surface temperature of the ice is $T_s = 215°K$ and that the atmospheric temperature and

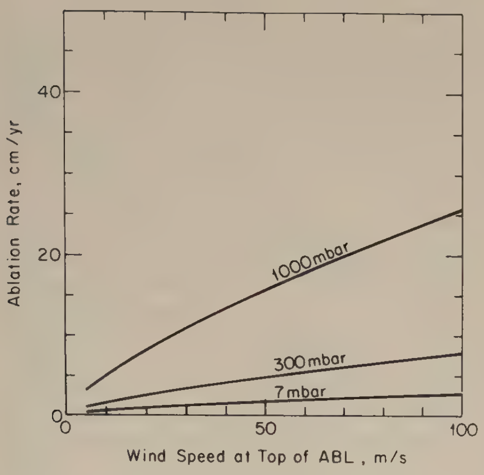

FIG. 9. Calculated ice ablation rates on Mars for three sets of atmospheric conditions: atmospheric pressure 7 mbar, mean annual surface temperature T_s = 215°K, surface and atmospheric ablation temperature T_a = 230°K; pressure 300 mbar, T_s = 230°K, T_a = 245°K; and pressure 1000 mbar, T_s = 245°K, T_a = 260°K. All ablation rates are given as a function of the wind velocity at the top of the atmospheric boundary layer.

ice surface temperature when ablation is taking place are T_a = 230°K. For 300 mbar, these values are taken to be T_s = 230°K and T_a = 245°K; for 1000 mbar, they become T_s = 245°K and T_a = 260°K. In all cases, ablation is assumed to be limited to a midday period of 6 hr/day. Atmospheric water vapor content at the top of the atmospheric boundary layer is assumed to be 50% of saturation during the daily ablation period. Solar input is taken to be that appropriate for the Martian equator. Geothermal heat is neglected.

The results of the calculation are shown in Figs. 9 and 10. Figure 9 shows the ablation rate calculated for each of the three cases as a function of the wind speed at the top of the atmospheric boundary layer. For the present atmospheric conditions, ablation rates are only about 1–2 cm year^{-1}. For a 300-mbar atmosphere, they increase to ~5 cm year^{-1}, and for a 1000-mbar atmosphere, they are about 10–20 cm year^{-1}. Figure 10 shows the ice thicknesses one obtains from these ablation rates, using the Antarctic ice model. The effects of changing the atmospheric conditions are substantial. For the present atmosphere, the equilibrium ice thickness on an ice-covered Martian lake is calculated to be hundreds of meters. Lakes could not be expected to persist in equilibrium on Mars under the present climate unless they were extremely deep. For a 300-mbar atmosphere, however, the equilibrium ice thicknesses are just tens of meters under the assumptions used here. For 1000 mbar, temperatures and ablation rates approach those found in the Antarctic, and the equilibrium ice thickness is only slightly more than 1 m. (The ice thickness under these conditions is less than that in Antarctica because the solar input at the Martian equator is actually greater than it is in the Antarctic.)

The results in Fig. 10 are crude, as they involve a number of very uncertain assumptions concerning Martian ice cover properties, atmospheric conditions, and so forth. However, some basic conclusions probably are valid. Under present Martian conditions, a lake will ice over immediately, and the ice cover will thicken until it completely solidifies any but a very deep lake. With fairly modest amounts of atmo-

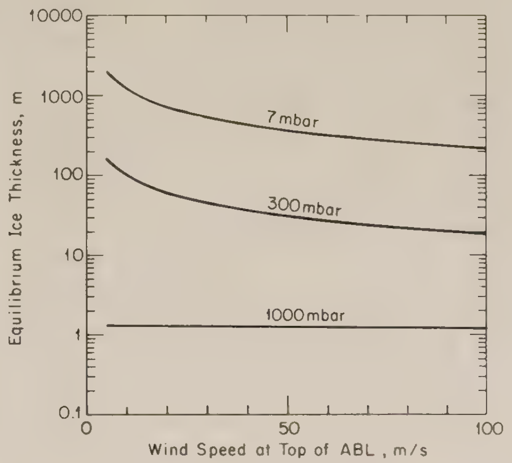

FIG. 10. Calculated equilibrium thickness of ice on an ice-covered Martian lake for the same three sets of atmospheric conditions considered in Fig. 8.

spheric greenhouse warming, however, it is possible to establish a lake that can exist in equilibrium under an ice cover meters to tens of meters thick. This equilibrium will be maintained as long as water from a subsurface aquifer/inflow stream system can replenish the slow loss of material by ablation. It is not necessary to have a very massive CO_2 atmosphere and surface temperatures in excess of 273°K in order for shallow lakes to persist for significant periods on the Martian surface.

It is also of interest to consider the chemical conditions that might have existed in lakes on early Mars. Perhaps the greatest significance that standing water bodies could have in the overall evolution of Mars is that they would form an ideal environment for the precipitation of carbonate rocks. A substantial problem may exist in accounting for all of the CO_2 originally outgassed from Mars. The total H_2O endowment of Mars inferred from geologic features is at least of the order of 10^4 g cm^{-2}, and larger values are possible (see, e.g., Carr 1986). If the CO_2/H_2O ratio for Mars was like that for the Earth, then the amount of CO_2 implied by this H_2O abundance is sufficient to produce an early atmosphere of at least 0.5 bar of CO_2, and its associated greenhouse conditions.

The quantity of outgassed CO_2 implied by this reasoning far exceeds the amount of gaseous, solid, and adsorbed CO_2 presently residing in the atmosphere–regolith–polar cap system (see, e.g., Fanale *et al.* 1982). Thermal escape of CO_2 to space is negligible over the planet's history. Therefore, some repository for a substantial amount of CO_2 seems to be necessary. Carbonate rocks are the most attractive candidate. CO_2 dissolved in surface water forms a weak acid that reacts with silicate rocks, producing a solution containing HCO_3^-, Ca^{2+}, and Mg^{2+} ions. Combination of these ions in water leads to precipitation of calcium and magnesium carbonate. Most of the originally outgassed CO_2 on Earth resides in carbonates formed in liquid water, and the same may well be true for Mars.

It seems clear that the small ancient sedimentation basins that can be identified in the present geologic record cannot account for all the CO_2 in a massive early atmosphere. A 500-mbar CO_2 atmosphere could produce about 30 moles cm^{-2} of carbonates, or enough to cover the entire planet with a layer ~10 m thick. Either the early atmosphere was less massive than this or there are other large and still unidentified sinks for Martian CO_2. One possibility might be burial in the regolith of still older aqueous carbonates. Regardless, however, the identified sedimentation basins may be climatically important for two reasons. First, they may preserve a record of the climatic conditions early in the planet's history. Second, if that climate was really a warmer one brought on by a more dense CO_2 atmosphere, they may actually be the final resting place of some fraction of that CO_2. The liquid water that would have been allowed to exist by an early more dense atmosphere would also have participated in bringing about the atmosphere's demise (and hence its own as well).

Implications for Future Martian Exploration

Both theoretical considerations and geologic evidence suggest that Mars might once have been warmer, wetter, and more Earth-like than it is at the present. However, we do not know just how much warmer and wetter it really was or what the chemistry of its atmosphere was during this early period. Nor are we likely to be able to infer this information with a high degree of confidence from remotely sensed data or from theoretical models. The only way in which we will be able to state anything with real confidence about early Martian climate and atmospheric chemistry is if we can obtain direct evidence about the conditions that prevailed during that period. By examining the sediments associated with Mars' ancient valley systems, which are the only features that provide evidence that might support an early warmer climate, we have the best chance of determining just how much more Earth-like Mars really was early in its history.

The interest in ancient aqueous sediments on Mars extends beyond paleoclimatology. A discussion of the importance of such sediments would be incomplete without mention of the possible biological implications. A major disappointment of the Viking mission was its failure to find evidence for life on Mars. The cold, dry, and highly oxidizing conditions that prevail on Mars at the present create an environment extremely hostile to life as we know it. However, early Mars and early Earth may have been more similar than present Mars and present Earth are. On Earth, life had evolved to a fair degree of sophistication within 0.8 Gy after the planet's formation. The period of time required for its origin may have been significantly less than 0.8 Gy, but the absence of a suitable sedimentary record precludes that determination. While conditions for life appear to be prohibitively harsh on Mars at the present, they may not always have been so. Moreover, there may be a much better record of the possibly more clement conditions in the first ~1.0 Gy of Martian history preserved in the geologic record and waiting to be read. For these reasons, the primary objective of the study of possible life on Mars has shifted from finding extant life (exobiology) to searching for evidence of former life ("exopaleontology") (see, e.g., McKay 1986). The best place on Mars to search for such evidence may also be in very ancient water-lain sediments.

Considerable thought now is being devoted, both in the United States and in the Soviet Union, to some form of Mars Sample Return mission. Such a mission would return samples from the Martian surface to the Earth for detailed laboratory analysis. Most scenarios for these missions involve the use of some kind of roving vehicle, so that samples could be gathered from a variety of sites. The potential scientific return from such a mission obviously is enormous. One of the things that makes Mars so attractive as a target for scientific exploration is its relatively Earth-like nature. By making an effort to include ancient water-lain sediments in the samples brought back from Mars, we might do a great deal to illuminate what was apparently the most Earth-like period of the planet's history. Such sediments should be an important target for any future sample return mission to the planet.

GROUND ICE ON MARS

I now turn to the subject of the distribution of ground ice on the planet in more recent times. This, too, is a topic of some importance. Ground ice seems to be the largest prospective reservoir for Martian H_2O. If we can determine the total amount of H_2O locked up as ground ice on Mars, then we have learned much about the planet's total water inventory. Ground ice that is close enough to the surface to be accessible for direct exploration is particularly significant. Finding and sampling ground ice would be another major objective for a Mars Sample Return mission, again because of the climatic evidence the ground ice might contain. Another significant aspect of ground ice that has been discussed very little is its potential for inhibiting diffusion processes in the Martian soil. For example, the surface conditions at the Viking Lander sites were strongly oxidizing, and no organic compounds were found at the parts-per-billion level (Biemann *et al.* 1977). Oxidants diffuse downward through the Martian regolith and may have produced such conditions to considerable depths (Chyba *et al.* 1988). However, where ground ice saturates the regolith and has been present for most of Martian history, it would substantially inhibit diffusion, perhaps preserving in and beneath it a record of earlier chemical conditions in the Martian soil. Finally, ground ice may present one of the best hopes for a water resource for future human exploration of the planet.

Ground Ice Distribution: Thermodynamic Considerations

We see in the Martian channels substantial evidence that the planet's regolith, even close to the surface, was once rich in liquid water. As the Martian climate cooled, water residing beneath the ground would have frozen, perhaps forming the large reservoir of ground ice often assumed to exist on the planet. However, even if one assumes a pervasive pole-to-pole reservoir of ground ice on Mars early in its history, it is not clear that that ice would persist to the present. In order to determine where ground ice reasonably can be expected to persist for extended periods on Mars, one must consider both its thermodynamic stability and the factors that can influence its migration.

Among the first to consider carefully the stability of ground ice on Mars on the basis of Viking data were Farmer and Doms (1979). They made three assumptions. First, they assumed that H_2O is uniformly mixed through the lower Martian atmosphere, with a mixing ratio that gives a total column abundance of 12 precipitable μm, the global mean value found by the Viking Mars Atmospheric Water Detector (MAWD) instrument. This water mixing ratio leads to a frost point temperature of 198°K. Second, they assumed subsurface temperatures in the upper 10 m of the regolith given by the thermal model of Kieffer *et al.* (1973). Third, they assumed that subsurface ice is in diffusive contact with the atmosphere, so that the atmospheric frost point temperature of 198°K can be applied to ice stability throughout the regolith.

The results of their calculations are reproduced in Fig. 11. The patterned regions in the figure show the locations where the temperature is less than 198°K throughout the year, allowing ground ice to be stable year-round. Under these assumptions, ice is stable at the surface from the poles down to a latitude of ~±85°. The top of the zone of stability descends gradually to a depth of about 1 m at a latitude of ~±50°, then drops off steeply to 10 m at ~±40°. At all other locations, temperatures in the top 10 m of the regolith exceed 198°K at some point during the year, so that ground ice is unstable and can, in principle, be lost to the atmosphere via sublimation and diffusion.

In a simpler pre-Viking calculation, Fanale (1976) made similar assumptions, but extended the calculation to depth. He obtained similar results: ground ice stable at the poles, with the top of the zone of stability descending gradually beneath the surface as one moves to progressively lower latitudes. The depth to the base of the stability zone is less certain, as it depends on the poorly known Martian geothermal gradient. Assuming a gradient of 40°K/km, he found that the base of the stability zone

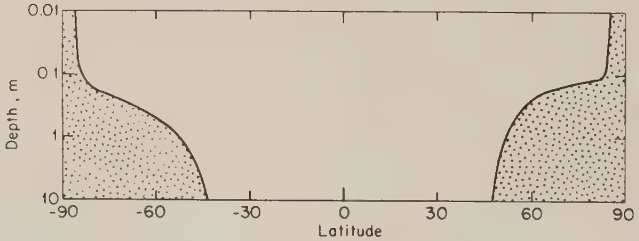

FIG. 11. Zones in the Martian regolith in which ice can exist year-round in thermodynamic equilibrium with the present Martian atmosphere (modified from Farmer and Doms 1979).

extends to a depth of 1–1.5 km at the poles and rises gradually toward lower latitudes. At latitudes lower than ~±40°, he found ice to be unstable at any depth.

Stability calculations of this sort have some severe limitations as guides to where ground ice might presently exist on Mars. One stems from the fact that they simply define zones of thermodynamic equilibrium with the atmosphere. Even at temperatures higher than the atmospheric frost point, ground ice can persist indefinitely if it is physically cut off from the atmosphere by a regolith through which it cannot diffuse (Smoluchowski 1968). Second, these calculations are for the present atmosphere only and do not take into account the substantial and complex episodic variations in Martian climate that are forced by variations in the planet's orbital and rotational elements (Murray *et al.* 1973, Ward 1973, 1974).

The first detailed calculation of loss of nonequilibrium subsurface ice from low latitudes was presented by Clifford and Hillel (1983). They estimated the time required to lose a 200-m layer of subsurface ice overlain by 100 m of ice-free regolith in the latitudes between ±30°, assuming a range of soil pore sizes and considering both Knudsen and molecular diffusion. They found that their results depended sensitively on the pore structure of the regolith. However, for most plausible soil structures, they found that such an ice layer at those low latitudes could be lost by sublimation and diffusion in a time less than 3.5 Gy.

A more detailed treatment of the loss of nonequilibrium ice from low latitudes was presented by Fanale *et al.* (1986). They began with a layer of ice uniformly distributed through the upper 200 m of the Martian regolith at all latitudes. Their model included a host of physical effects, including Knudsen and molecular diffusion, geothermal heat flow, long-term changes in solar luminosity, cyclic climatic variations, and albedo changes due to time-varying surface frost distributions. The results of one of their calculations are reproduced in Fig. 12. The curves in the figure show the position of the retreating margin of the ground ice at various times during the planet's history. The result is qualitatively similar to that of Clifford and Hillel (1983). Ice is lost gradually and inexorably from the equatorial region, diffusing upward through the regolith, escaping to the atmosphere, and recondensing at higher latitudes. Again, the depth to which the desiccation extends depends sensitively on the poorly known diffusive permeability of the regolith.

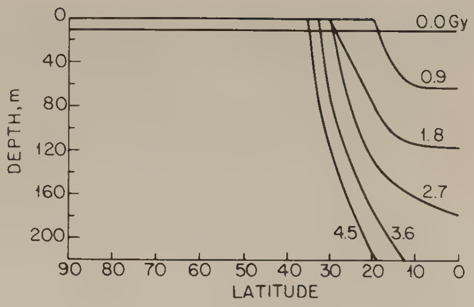

FIG. 12. A calculation of the long-term evolution of ground ice in the Martian regolith, assuming an initially homogeneous distribution. Curves give the position of the retreating ice front with time (in Gy). Above and to the right of each curve the regolith has become desiccated by the time indicated. Ice is gradually and irreversibly lost from near-surface equatorial regions (from Fanale *et al.* 1986).

Until we have substantially better information about the physical nature of the deep Martian regolith, these models probably represent the best that can be done to calculate where ground ice can exist on Mars. However, they do not tell us where ice actually *does* exist. In the following sections, I discuss two ways in which we may be able to detect the effects of ice beneath the Martian surface. The first deals with the way ice in the upper hundreds of meters affects the morphology of Martian landforms, and the second deals with the way ice in the upper tens of centimeters affects the spectrum of gamma rays emitted by the planet.

Ground Ice Distribution: Geomorphic Evidence

Subsurface ice can work in many ways to alter the appearance of a planetary surface. It can melt and flow, creating chaotic terrain and channels. It can undergo repeated freeze–thaw, producing polygonal "patterned ground" and a variety of other "periglacial" landforms (Carr and Schaber 1977, Helfenstein 1980; but see also Pechmann 1980). Ground ice can be liquefied during impacts, producing the distinctive Martian "rampart craters," with their lobed ejecta deposits. Rampart craters are very common on the planet and are one of the most certain and most often-cited pieces of evidence for subsurface H_2O. I do not discuss any of these features in detail here, although I return to the rampart craters and some of their implications below.

Another way in which subsurface ice can modify a planetary surface is by slow creep and flow in the solid state. This effect is well known and has been observed on planetary bodies ranging from the Earth to the satellites of Uranus. By geologic standards, ice is an extremely mobile material. On Earth, the mobility of ice is demonstrated dramatically by glaciers, which can flow at considerable velocities with no melting involved. It also is demonstrated by the mobility of rocky debris and soil cemented by ice.

Two terrestrial examples are particularly pertinent. The first is ice-rich permafrost. (It should be noted that "permafrost," in the strict geologic sense, simply means ground whose temperature is always less than 0°C; no ice content is necessarily implied by the term.) One of the more vexing problems in projects such as construction in the arctic is the slow deformation of ice-rich ground. The problems caused by permafrost melting of course are well known. However, even if steps are taken that prevent any melting, ice-rich permafrost still can undergo substantial deformation as the ice that cements the soil deforms and flows in the solid state (Thompson and Sayles 1972, Phukan 1983, Sadovsky and Bondarenko 1983, Weerdenburg and Morgenstern 1983). The deformation of ice-rich soil has been extensively studied in creep experiments with frozen laboratory samples (Andersland and Akili 1967, Goughnour and Andersland 1968, Sayles 1973, Haynes, 1978, Ladanyi and Paquin 1978, Zhu and Carbee 1983). Flow laws (albeit for temperatures and strain rates substantially higher than those that are appropriate for Mars) have been determined and are at least partially understood from a theoretical standpoint (Ladanyi 1972, Vyalov 1978, Zaretskiy and Shchobolev 1983).

The second pertinent terrestrial example is rock glaciers, which are found in many arctic and alpine environments. They consist of particles, ranging in size from boulders to silt, that have been loosened from their original locations and have become cemented by interstitial ice. They tend to develop immediately below steep rocky slopes characterized by rapid mass-wasting. These rock–ice masses deform and flow due to solid-state creep in the ice; again, no thawing is involved (Ives 1940, Wahrhaftig and Cox 1959, Thompson 1962, White 1976). The mobility of the materials is substantial. Representative effective viscosities calculated for terrestrial rock glaciers are 2 to 9 × 10^{14} P (Wahrhaftig and Cox 1959) and 5 to 9 × 10^{15} P (White 1971).

Examples of solid-state deformation of ice-rich materials also abound in the outer Solar System. The clearest evidence for such deformation comes from the relaxed topography of impact craters on many icy bodies. An example is shown in Fig. 13. This is a photoclinometrically derived topographic profile across a 40-km crater on Ganymede (Squyres 1981). The crater rims are sharp and prominent, and the central pit characteristic of craters in this size range on Ganymede is well shown. However, the crater is in other ways markedly different

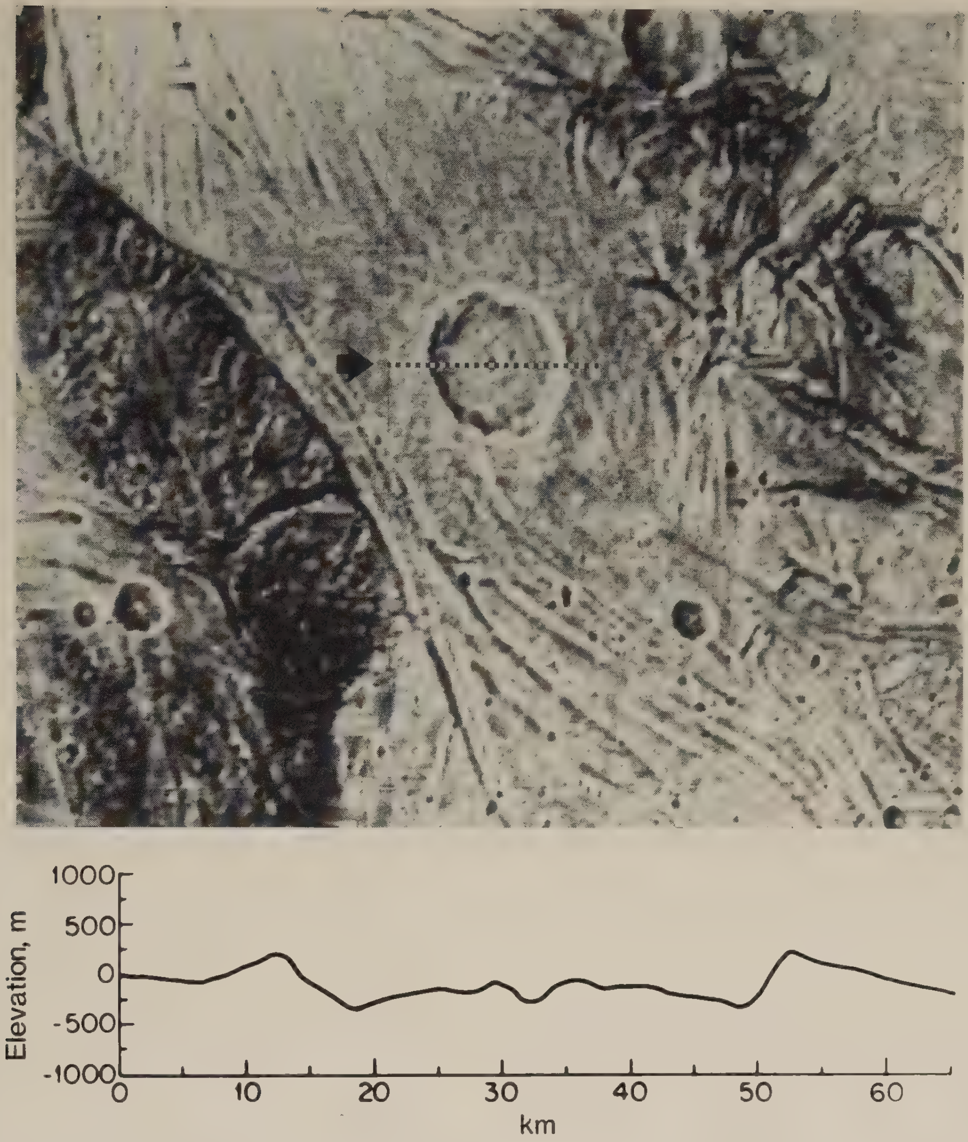

FIG. 13. Photoclinometric profile across an impact crater on Ganymede. The floor of the crater has been bowed upward by viscous relaxation, i.e., solid-state creep of Ganymede's icy crustal material (from Squyres, 1981).

from comparable-sized craters on other bodies. Instead of being concave or flat, the floor of the crater is bowed distinctly upward. The crater is extremely shallow, with a depth/diameter ratio (with depth measured at the center point) of no more than about 1/80. Deformation of the crater floor has taken place by viscous flow of Ganymede's icy crust. Isostatic forces favor subsidence of crater rims and upwarping of the floor, and the crustal material, in spite of its low temperature, has been able to deform in response to these forces over the course of Ganymede's history. The temperature at which the deformation has taken place is a subject of some debate, but it is clear that it was at most comparable to (and in fact probably substantially lower than) typical temperatures found in the Martian regolith.

Relaxation of impact craters is not restricted to Ganymede, and has been identified on at least Callisto, Enceladus, Tethys, and Rhea (Passey and Shoemaker 1982, Passey 1983, Thomas and Squyres 1988). There also are observations of what appear to be surface extrusions of ice on Miranda and Ariel in the Uranian system (Jankowski and Squyres 1988), although these had such low viscosities that they may have been mobilized by inclusion of volatiles other than H_2O.

The observations of solid-state deformation on cold outer Solar System bodies has led to a renewed interest in the rheology of ice, particularly at low temperatures, in the past several years. Important advances have been made via experimental deformation of samples of ice I (and other high-pressure polymorphs) at temperatures far lower than typically were investigated in the past (see, e.g., Durham *et al.* 1983, Kirby *et al.* 1985, Kirby *et al.* 1987). Even at the (geologically) very high strain rates of laboratory experiments, ductile creep of pure polycrystalline H_2O ice I has been observed at temperatures as low as 165°K (Kirby *et al.* 1987).

To summarize these points, H_2O ice is known to undergo ductile deformation at and below Martian temperatures and is observed on Earth effectively to mobilize highly comminuted erosional debris or soil that it cements. Given these facts, it is reasonable to search for Martian landforms modified or formed by viscous deformation of ice-rich regolith. In fact, such landforms may be identified fairly readily. Moreover, their distribution agrees extremely well with the aforementioned thermodynamic considerations of where ground ice would be expected to persist on the planet.

Landforms Produced by Viscous Creep

I discuss here two classes of Martian landforms that appear to result from viscous creep of near-surface materials. The first class is formed of materials that have been loosened from their original locations, transported down an escarpment by mass-wasting, and accumulated at the base of the escarpment. Depending on the location in which they have accumulated, I have termed these accumulations *lobate debris aprons, lineated valley fill,* and *concentric crater fill* (Squyres 1978, 1979). The landforms produced are inferred to be directly analogous to rock glaciers and are morphologically very similar to their terrestrial counterparts. The second class is really a style of landform degradation produced by viscous deformation of material *in situ.* It affects all manner of landforms, including craters, ridges, channels, and in fact almost any sort of topographic relief. It is referred to here and elsewhere as *terrain softening* (Squyres and Carr 1986). It is more directly analogous to the solid-state deformation observed in terrestrial permafrost or to relaxation of impact craters on icy satellites. As I will show, however, the details of the relaxation are quite different from what is observed on icy satellites and have important implications for the nature of the deep Martian regolith.

Because these features, particularly terrain softening, have been illustrated only sketchily in previous papers on the subject, I provide very detailed morphologic arguments and numerous illustrations here for the benefit of the truly interested reader. The casual reader may gain the gist of this section of the paper from the photographs and captions of Fig. 14 through 33 to follow.

Lobate debris aprons, lineated valley fill, and concentric crater fill. A simple example of lobate debris aprons is shown in Fig. 14. They are thick accumulations of debris at the bases of escarpments. Their most noteworthy morphologic characteristic is their pronounced convex topography. The surface of the debris apron slopes gently away from the source escarpment and then steepens to form a distinct flow terminus. This

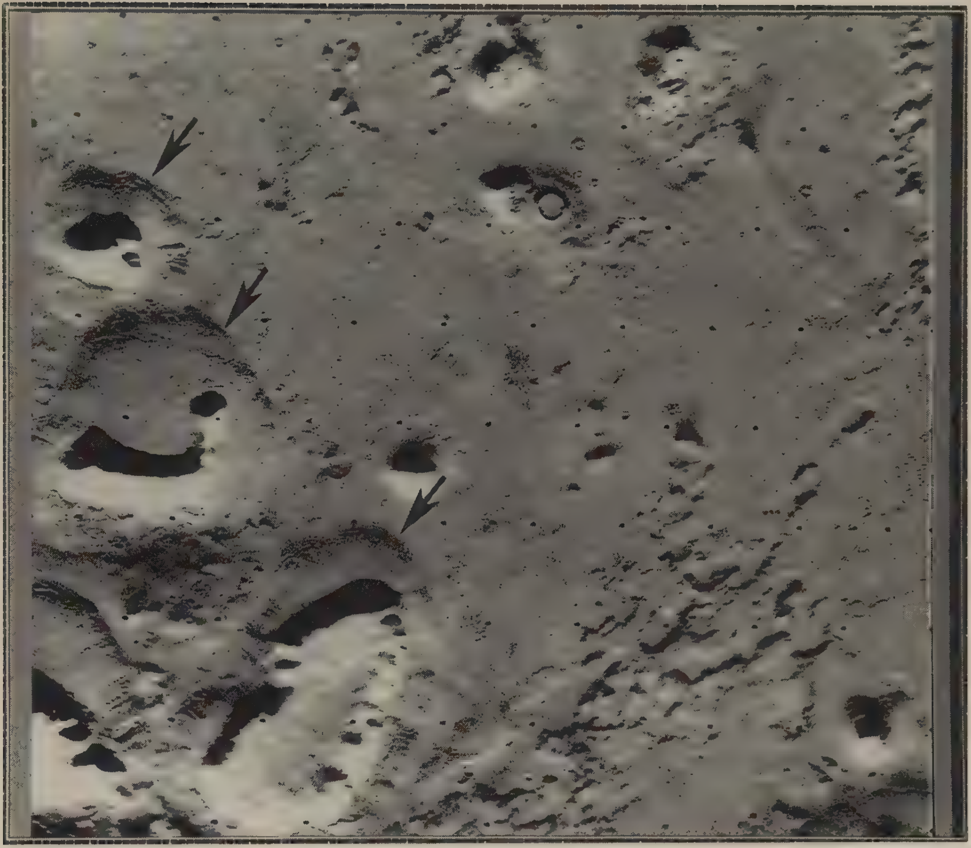

FIG. 14. Lobate debris aprons (arrows), showing the convex topographic profiles commonly exhibited by these features (Viking Orbiter image 58B51, latitude 47°, longitude 325°; scale across frame is about 90 km).

morphology is a clear indication that deformation and flow have taken place throughout a substantial thickness of the deposits.

A somewhat more complex example is shown in Fig. 15. This figure shows two classes of lineations found on the surfaces of the flows. Both have counterparts in terrestrial rock glaciers (Wahrhaftig and Cox 1959). At *A*, lineations composed of parallel ridges and troughs begin at the source escarpment and extend directly outward from it. They probably approximate flow lines. On terrestrial rock glaciers, such lineations form due to lateral inhomogeneities in the rock supply at the source, which are preserved as ridges and troughs paralleling the flow. At *B*, lineations have developed perpendicular to the flow direction. The flow here has met an obstruction, which has led to compressional stresses and surface folding on the obstruction's ''upstream'' side. Such compressional lineations also commonly are observed on terrestrial rock glaciers. Both classes of lineations provide strong evidence for the formation of lobate debris aprons by flow.

Lobate debris aprons are very common in some areas, particularly in the fretted terrain separating the northern lowlands from the southern highlands between 280° and 350° long. In some locations, the lobate debris aprons are packed together so closely that they cover nearly all of the lowlands over a broad region (Fig. 16). In

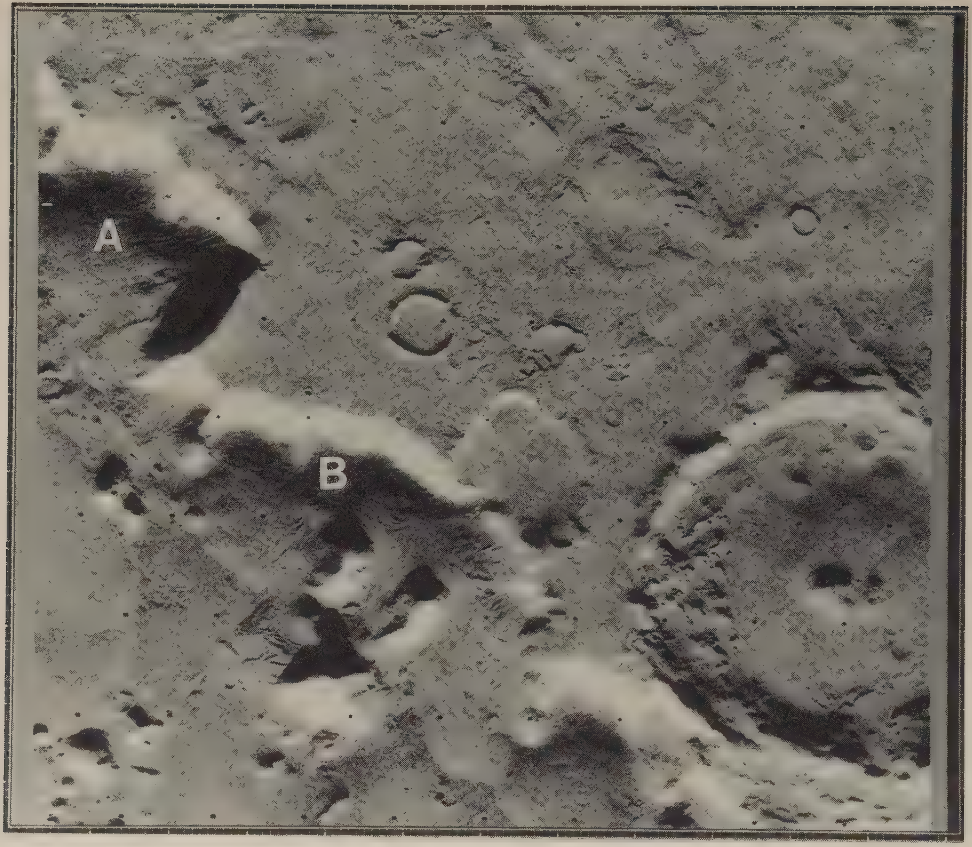

FIG. 15. A lobate debris apron, showing the two classes of lineations found on the surface of these features. At *A*, flow lineations originating at the source escarpment show the direction of flow. At *B*, lineations are formed perpendicular to the direction of flow by compressional folding as the flow runs up against an obstacle (Viking Orbiter image 58B56, latitude 44°, longitude 332°; scale across frame is about 90 km).

such locations, where flows commonly run up against opposing escarpments or against one another, complex patterns of flow and compressional lineations can form. A relatively simple example is shown in Fig. 17. In part of this figure, unobstructed flow has produced simple flow lineations. However, where an obstruction produces a small valley confining the flow, lineations are formed parallel to the valley walls by compressional stresses. These stresses are generated by movement of material from the walls of the valley toward its center. A more extreme case is shown in Fig. 18, also in fretted terrain. Here the debris has been confined entirely in narrow valleys. The pervasive obstruction of flow outward from the valley walls has produced many compressional lineations parallel to those walls. However, with the exception of one small lobate flow front, no clear lobate debris apron morphology (which requires less obstructed flow) has been allowed to develop. These valley-floor deposits are what I have previously termed "lineated valley fill." They are composed of the same material that forms the lobate debris aprons and are simply the other end-member of a continuum of landforms produced by this material in the fretted terrain. That both are the result of the kind of flow evident in the lobate debris aprons is demonstrated

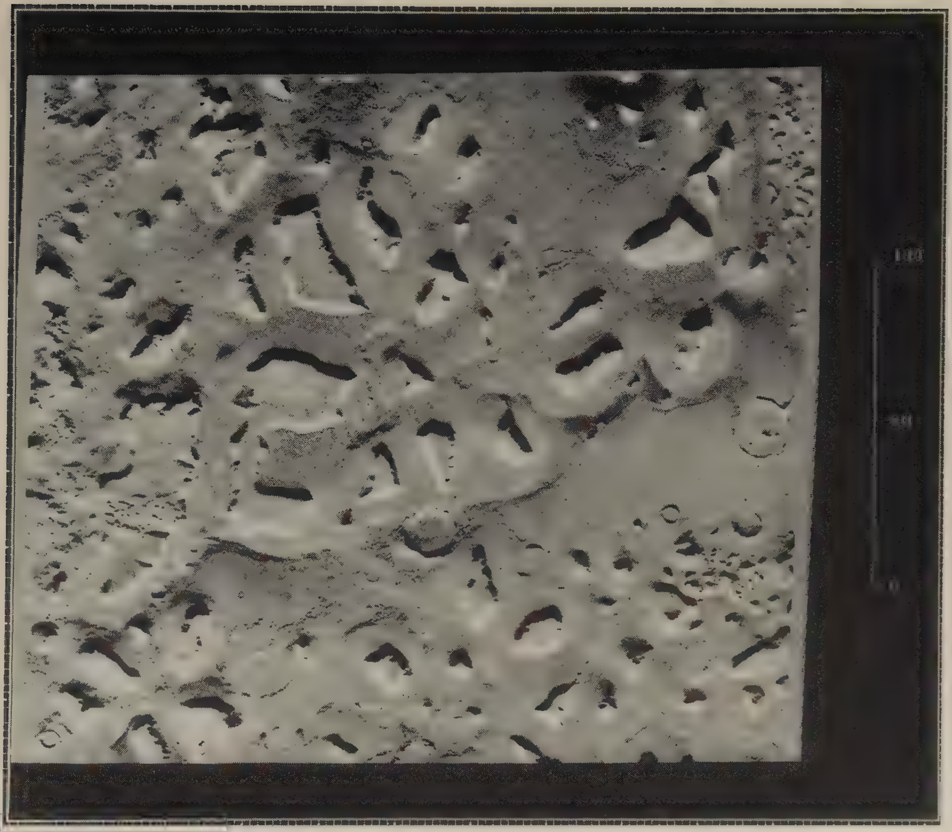

FIG. 16. A broad area of fretted terrain in which the lowlands are largely covered by lobate debris apron material (Viking Orbiter image 675B42, latitude 46°, longitude 332°).

clearly by the gradation of one type of landform into the other (as in Fig. 17).

Further information about the nature of these flows can be gained from examination of very high-resolution Viking Orbiter images of them. Examples are shown in Figs. 19a and b. In (a), lobate debris aprons are observed at moderate resolution and show clear morphologic evidence for flow, including one flow that has overtopped a crater rim and partially filled the crater. In (b), small subareas of these flows are shown at an image resolution approaching 10 m pixel^{-1}. The improved resolution brings about a striking change in the appearance of the flows. They are observed to be highly textured at a scale down to the image resolution. The surface is distinctly etched in appearance, and it is likely that the etching was produced by eolian erosion. Eolian etching may have been aided by sublimation of thermodynamically unstable ice from the uppermost portion of the flow, removing the cementing agent and allowing the finest material to be removed by deflation. In some instances the etching has progressed to a common level, giving the appearance of layering in the flow material.

(A remark is in order here concerning the significance of this eolian etching for the formation of the deposits themselves. It has been pointed out recently that, in the highest resolution Viking images, the surface of Mars commonly is dominated by eolian landforms (Zimbelman 1987, Zimbelman *et al.* 1988). This observation appears to hold for lobate debris aprons, just as it does for lava flows, tectonically disrupted terrains,

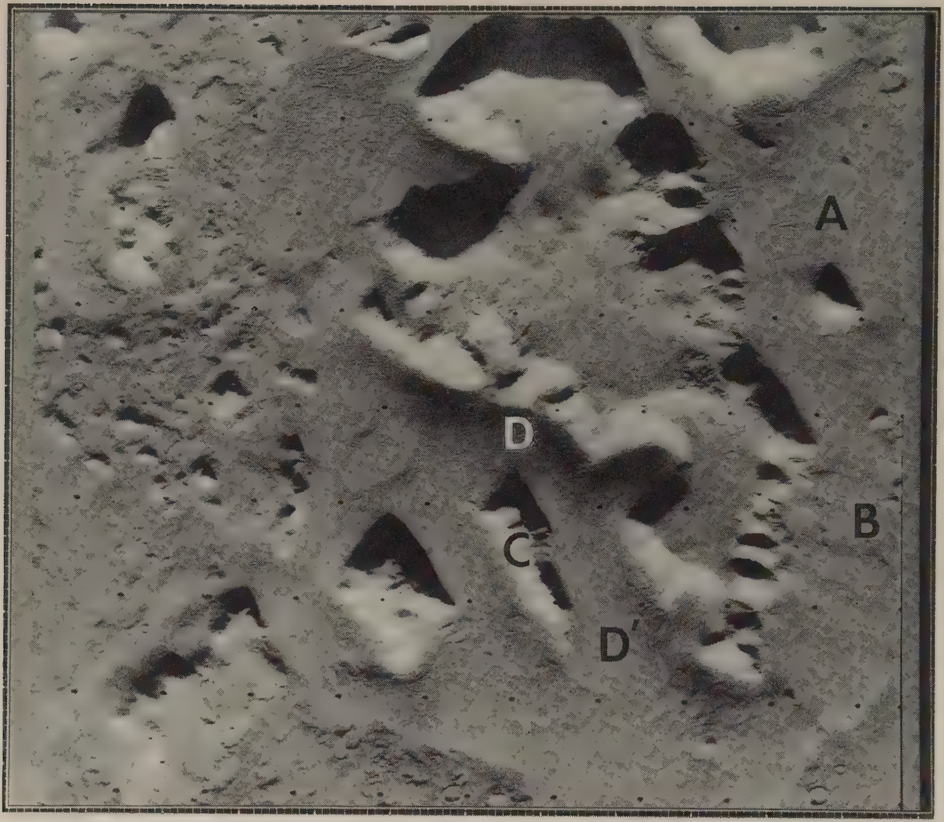

FIG. 17. A lobate debris apron showing flow lineations. At *A* and *B*, flow lineations are formed by unobstructed motion outward from the source escarpment. An obstruction at *C* creates a valley from *D* to *D*′. Within the valley, lineations have formed parallel to the valley walls in response to compressive stresses generated by flow of debris toward the center of the valley (Viking Orbiter image 58B55, latitude 46°, longitude 322°; scale across frame is about 90 km).

and many other materials. However, it should not be concluded from this observation that the materials that have been etched or otherwise modified by the wind are themselves eolian in origin if the morphology observed at moderate resolution clearly indicates otherwise. There is an optimum size scale and resolution for observing any geologic phenomenon. For many types of eolian features on Mars, the small size of the features makes them visible only near the highest resolution presently available. However, the true nature of the material on which they lie may only be evident at larger scales in lower resolution images. Such is the case for the lobate debris aprons and lineated valley fill, whose origin by flow can be discerned clearly only in images of large enough scale to show the geometry of flow lineations and the topography of flow fronts.)

The final class of landforms that I have interpreted to be formed from flow of ice-cemented erosional debris is shown in Fig. 20. Material is observed on the floors of craters with a distinctive, roughly concentric pattern of ridges and troughs. I have called such deposits "concentric crater fill" and have interpreted the topography as resulting from compressional stresses generated by inward flow of ice-rich material from the crater walls.

In general, the interpretation of most concentric crater fill as having resulted

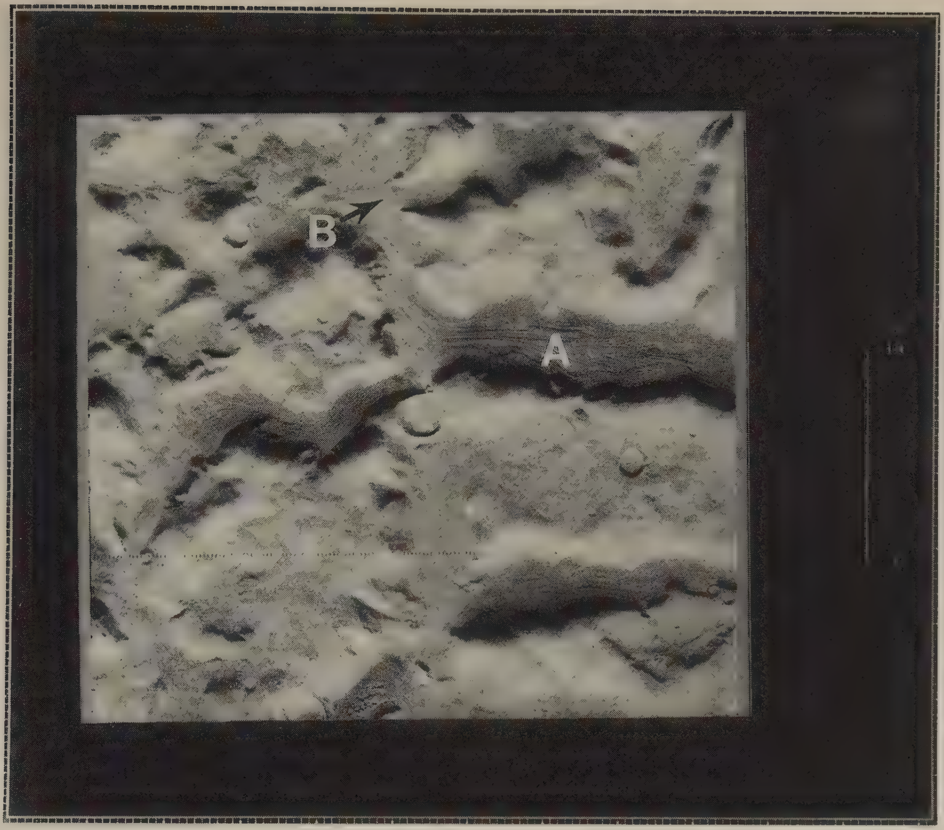

FIG. 18. Lineated valley fill (*A*). The valley-filling deposits are composed of the same kind of material that makes up lobate debris aprons. *B* indicates a small lobate flow front (Viking Orbiter image 84A73, latitude 34°, longitude 290°).

from ice-aided flow is less clear-cut than is the case for lobate debris aprons and lineated valley fill. In fact, an eolian origin for these materials has been advocated (Zimbelman *et al.* 1988), and it is clear that concentric crater fill (like lobate debris aprons and lineated valley fill) commonly has been subjected to eolian erosion. However, there are three arguments that support the view that concentric crater fill also owes its morphology largely to flow processes. The first is the general morphologic similarity between concentric crater fill and the portions of the other types of flows that possess compressional lineations. The similarity at moderate resolution can be seen by comparison of Fig. 20 with earlier figures showing lobate debris aprons and lineated valley fill. The similarity also extends to high resolution, as shown in Fig. 21. Concentric crater fill shows the same kinds of large-scale morphology and small-scale eolian etching of lineations as are observed on the other types of flows. The second (and most powerful) argument is that landforms transitional between lobate debris aprons and concentric crater fill are common in some regions. Examples are shown in Figs. 22a and b. Here, material with the characteristic convex topographic profile of lobate debris aprons has flowed inward from the crater walls, but has not completely covered the crater floor. The result is, in effect, an inward-facing annular lobate debris apron that, were it to cover the entire crater floor, would form more typical concentric crater fill. The final argument is that, as shown below, the geographic distributions of lobate debris aprons, lineated valley fill, and concentric crater fill are all strikingly similar and all consistent with the thermodynamically expected distribution of mobile, near-surface ground ice.

Terrain softening. Terrain softening is a distinctive style of landform degradation observed in some regions on Mars. It affects landforms of all types, but one type of landform on which it is particularly evident is impact craters. Four examples are given in Figs. 23 through 26. In each of these figures, a pair of Viking Orbiter images is presented. The first image of each pair shows craters in "normal," i.e., unsoftened, terrain. The second presents a similar scene, with similar illumination geometry and resolution, in softened terrain. The differences are striking. In the unsoftened terrain, the topography is crisp and rugged. Crater rims are sharp. Crater walls are blocky and angular, with slope profiles that are dominantly straight or concave upward. Between large craters are low but angular ridges and hills. In the softened terrain, however, crater rims are broad and gently rounded. Crater walls preserve their blocky nature to some degree, but the individual blocks are softly rounded rather than angular. Slope profiles are dominantly convex upward. The terrain between large craters

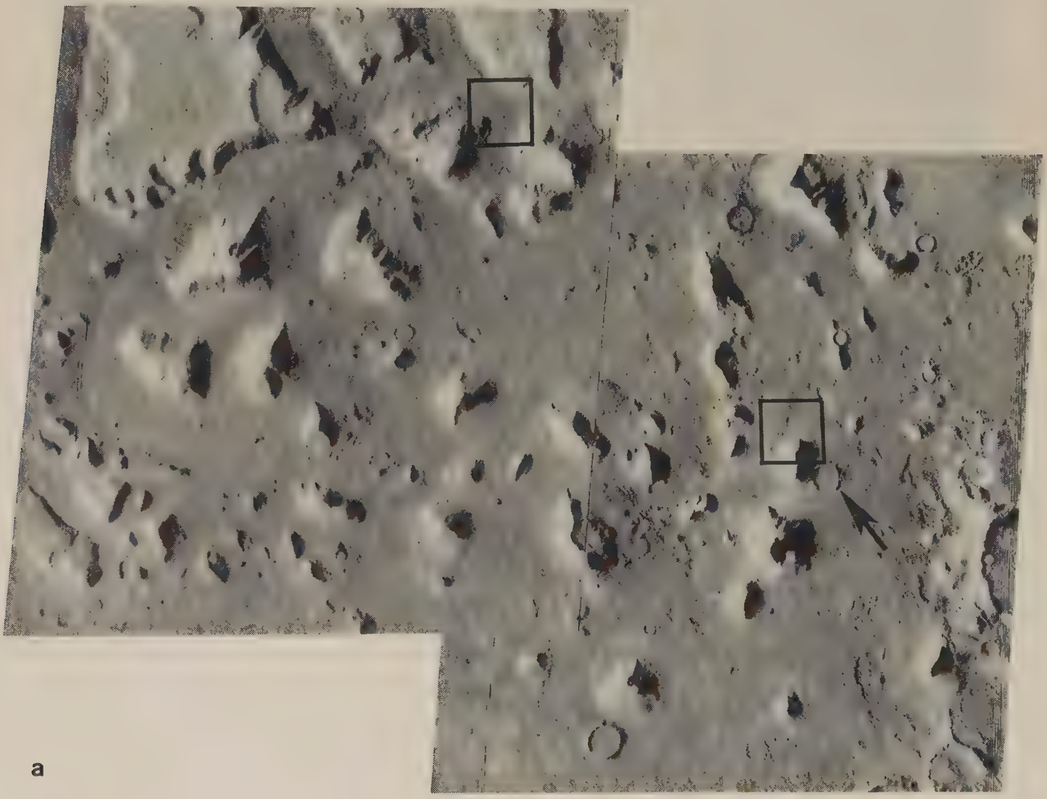

FIG. 19. (a) A region with widespread lobate debris apron and lineated valley fill deposits. One flow has partially filled a small impact crater (arrow). Insets show the location of high-resolution images (Viking Orbiter images 338S86 and 338S88, latitude 45°, longitude 317°). (b) Two high-resolution views of lobate debris apron and lineated valley fill material. The deeply etched appearance of the flows at this resolution suggests that their surfaces have suffered significant eolian erosion (Viking Orbiter images 461B08 and 461B14).

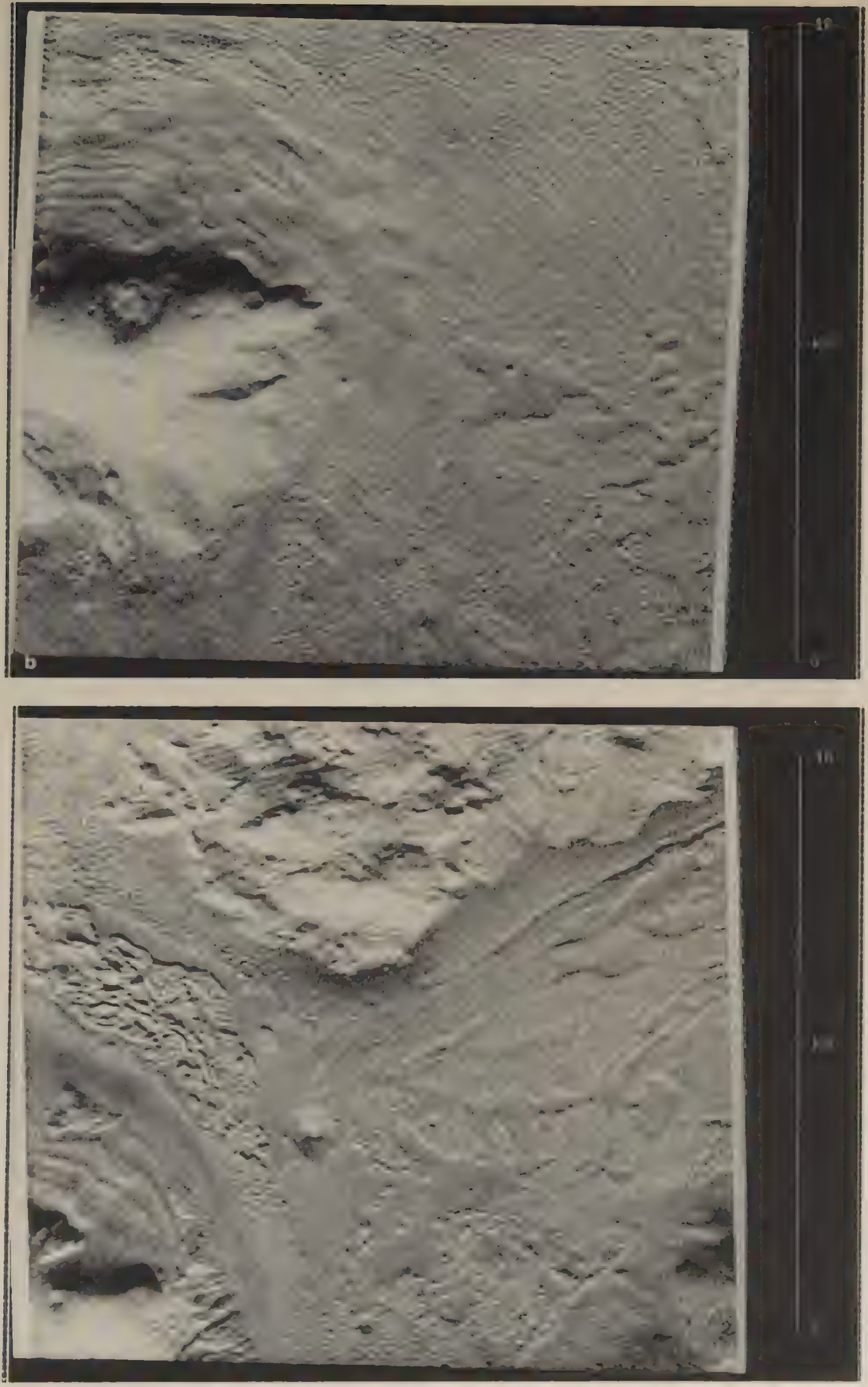

FIG. 19—*Continued*

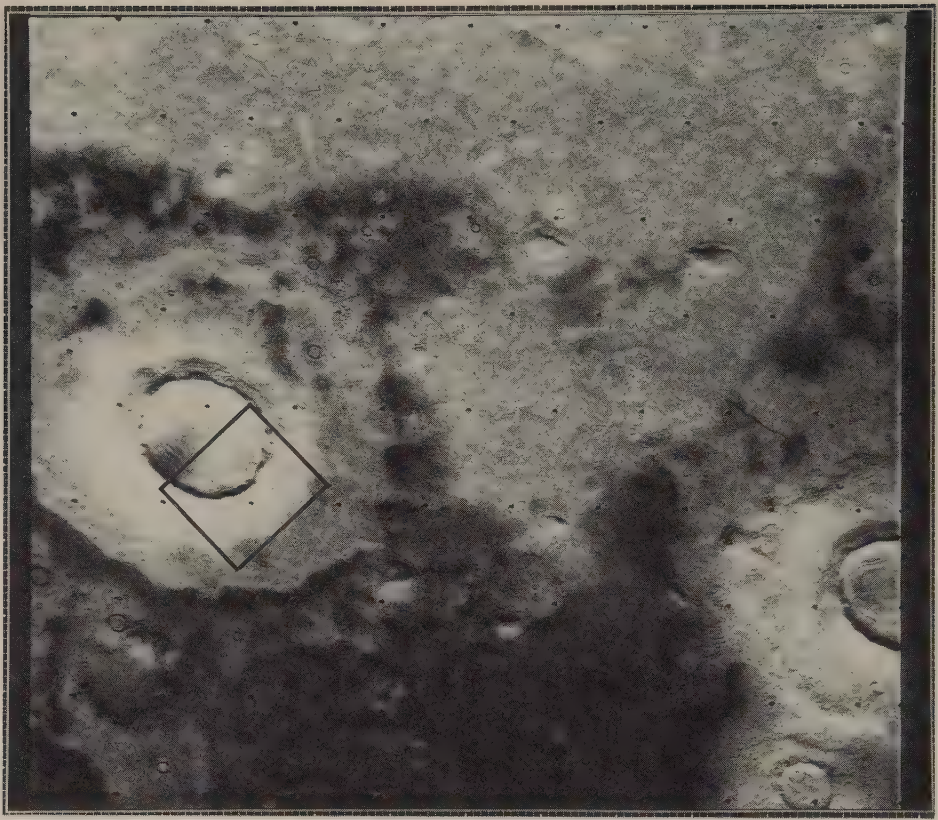

FIG. 20. Impact craters in Utopia Planitia containing concentric crater fill. Inset shows the location of the high-resolution image in Fig. 21 (Viking Orbiter image 10B70, latitude 42°, longitude 272°).

has a smooth rolling character and lacks the angular ridges and hills characteristic of unsoftened terrain.

The differences between unsoftened and softened terrain are shown somewhat more quantitatively in Fig. 27, which presents photoclinometrically derived topographic profiles across craters in softened and unsoftened terrain. No attempt was made in constructing the profiles to remove the effects of contrast reduction in the images by atmospheric scattering, so the absolute elevation differences are inaccurate and probably significantly too small. However, the slope shapes and inflections are correct as shown, within the limits of the image resolution and the photoclinometric technique itself. The sharp crater rims and concave crater wall slopes of the unsoftened terrain are shown clearly, as are the broad crater rims and convex crater wall slopes of the softened terrain.

Terrain softening is by no means limited to impact craters. Figures 28, 29, and 30 show, respectively, how terrain softening can affect channels, ridges, and complex terrain containing a variety of landforms. In all cases, the effects are the same: terrain softening produces broad rather than sharp slope infections and convex rather than concave slope segments.

What is the evidence that terrain softening results from viscous creep of near-surface materials? It seems intuitive that viscous creep, if it took place, could produce the rounded topography observed. I show quantitatively below that this intuition is correct. However, other possible sources

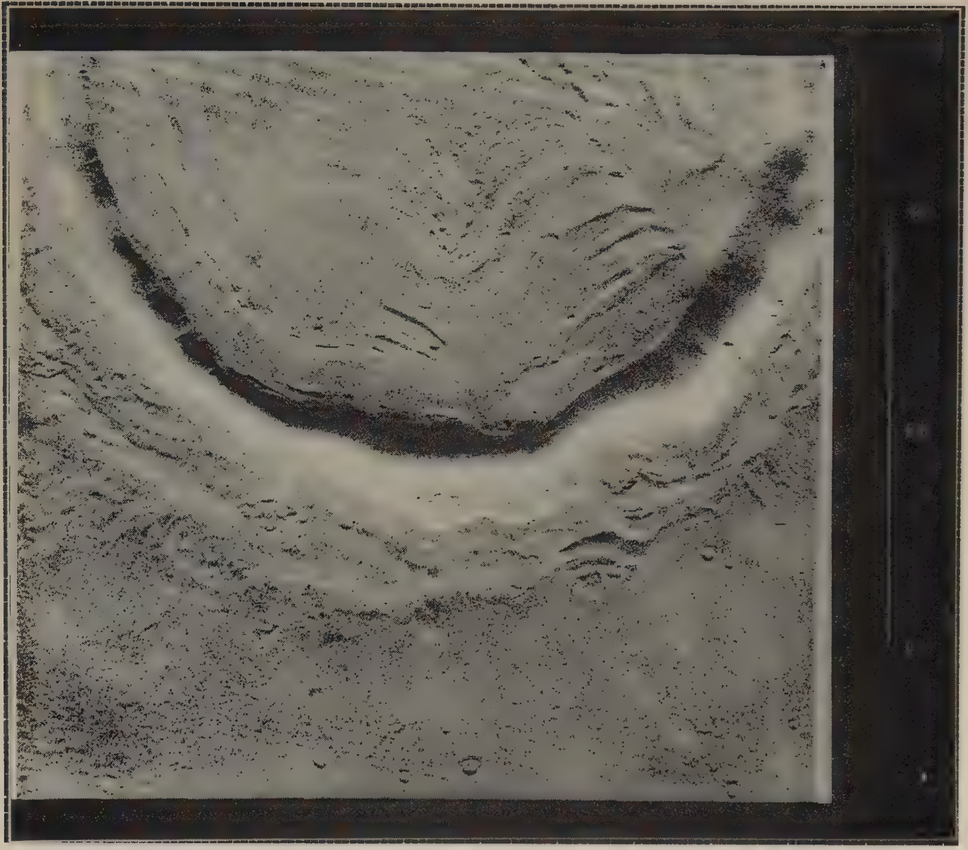

FIG. 21. High-resolution image of concentric crater fill, showing apparent eolian etching of the deposits (Viking Orbiter image 425B07).

of the apparent softening must be considered carefully. The two that seem most likely to be significant are blurring of surface detail by atmospheric obscuration and mantling of the surface by eolian debris. Upon close consideration, both of these possibilities can be argued against with some degree of certainty.

One observation that supports an origin by viscous creep rather than obscuration or mantling is the fact that, in extreme cases of terrain softening, evidence for downhill flow of materials is observed. An example is shown in Fig. 31. Highly softened terrain is shown, with a number of separated outcrops of dark material. Extending downhill from these outcrops are distinct streamers of dark debris that appear to trace downhill movement of the material.

Atmospheric obscuration as a cause can be ruled out with confidence by observation of images of unsoftened terrain at times when there was a significant amount of dust in the atmosphere. An example is shown in Fig. 32. Even with a great deal of atmospheric dust obscuring the scene, the unsoftened nature of the topography is clearly evident. Despite the fact that many small-scale details of the image are obliterated, the sharpness of the crater rims and the concavity of the crater walls are still very obvious.

Eolian mantling can be ruled out by two arguments. The first deals with the nature

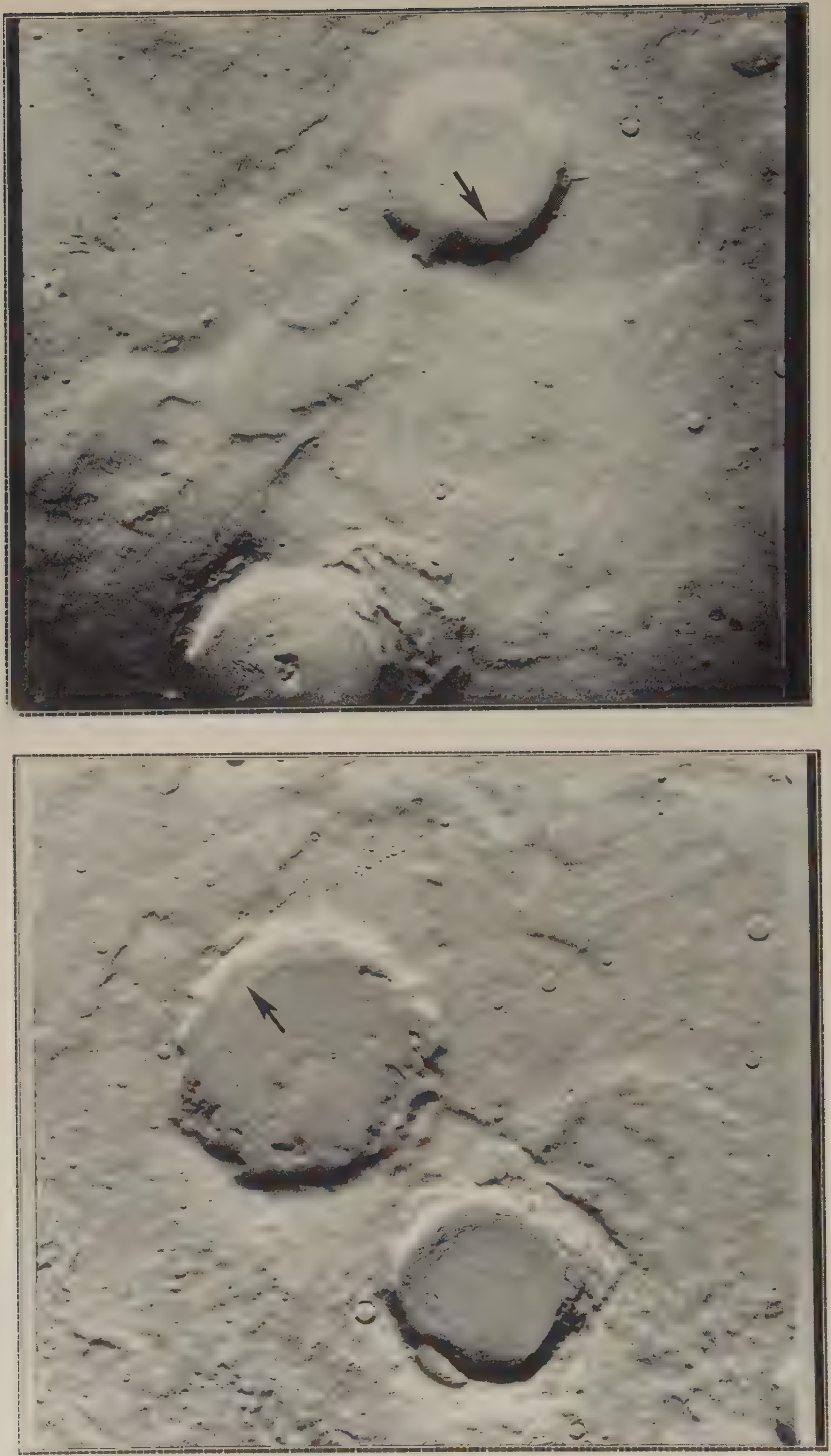

FIG. 22. Two images showing lobate debris aprons within impact craters (arrows). If the aprons completely covered the crater floor, they would form concentric crater fill (Viking Orbiter images 196S03, latitude 31°, longitude 319°, and 199S11, latitude 32°, longitude 325°; scale across each frame is about 50 km).

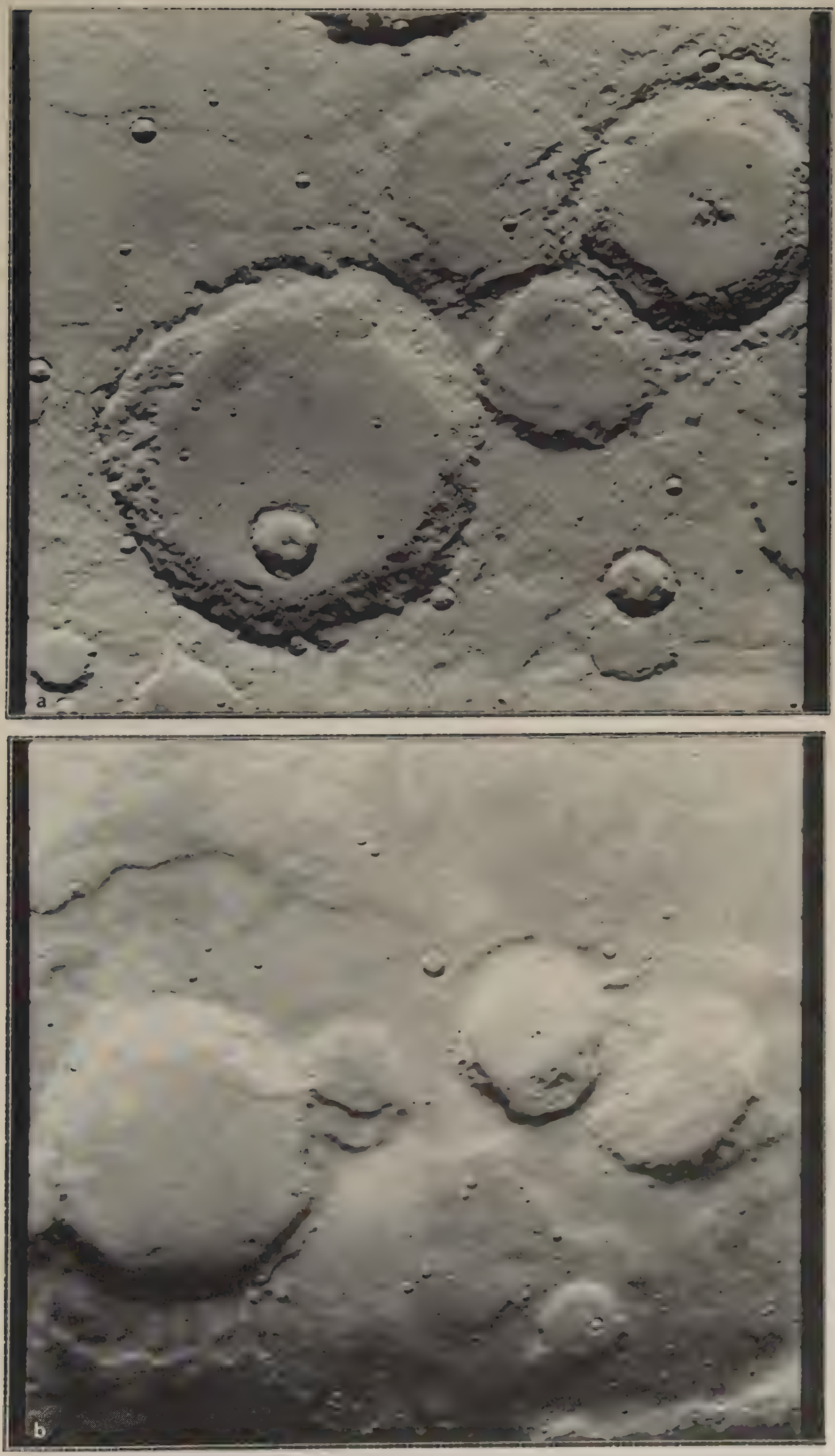

FIG. 23. Images showing unsoftened (a) and softened (b) cratered terrain (Viking Orbiter images 423S10, latitude −32°, longitude 227°, scale across frame is about 160 km; and 195S20, latitude 33°, longitude 313°, scale across frame is about 60 km).

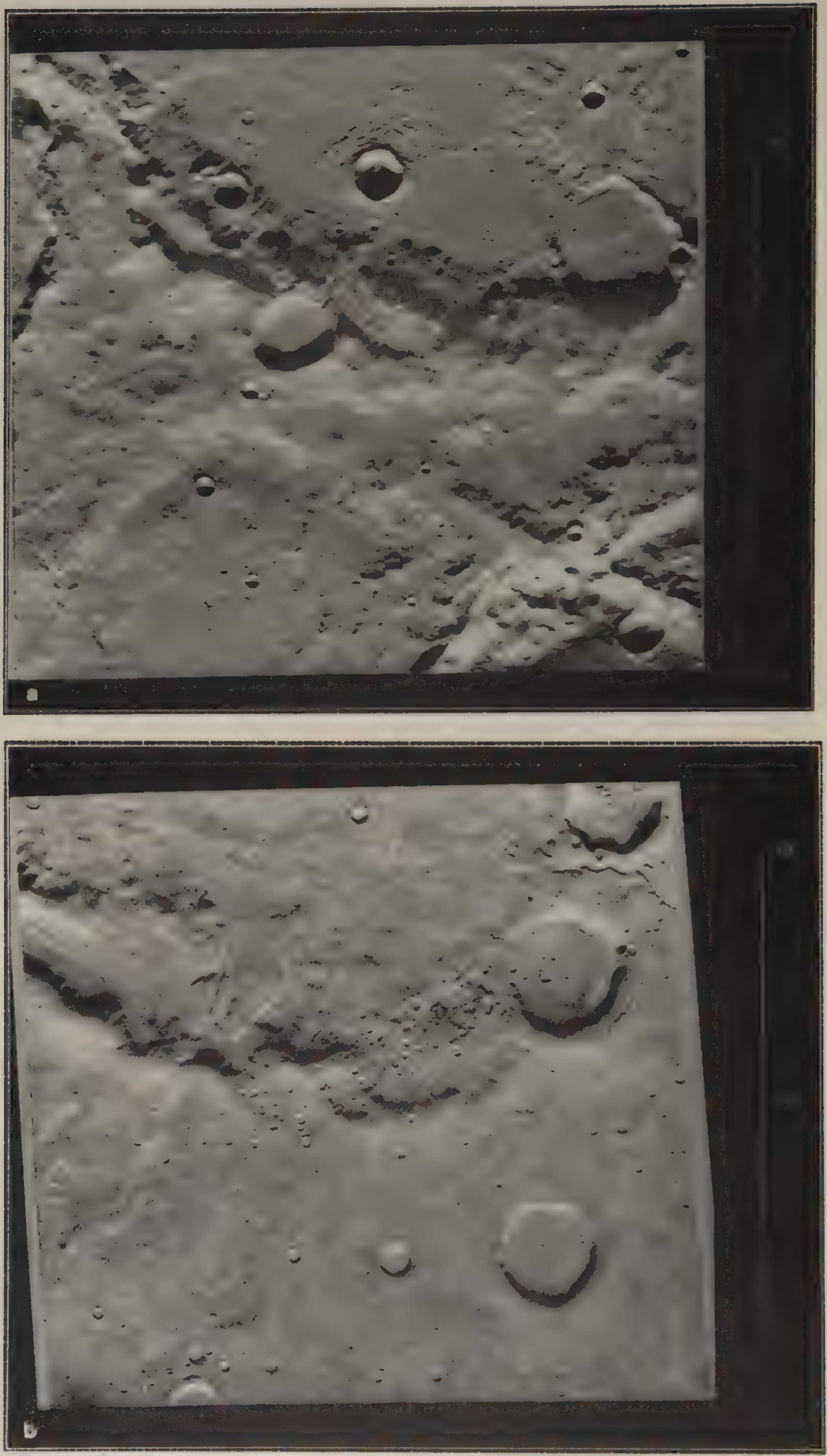

FIG. 24. Unsoftened (a) and softened (b) cratered terrain (Viking Orbiter images 432S23, latitude −19°, longitude 181°, and 192S23, latitude 32°, longitude 307°).

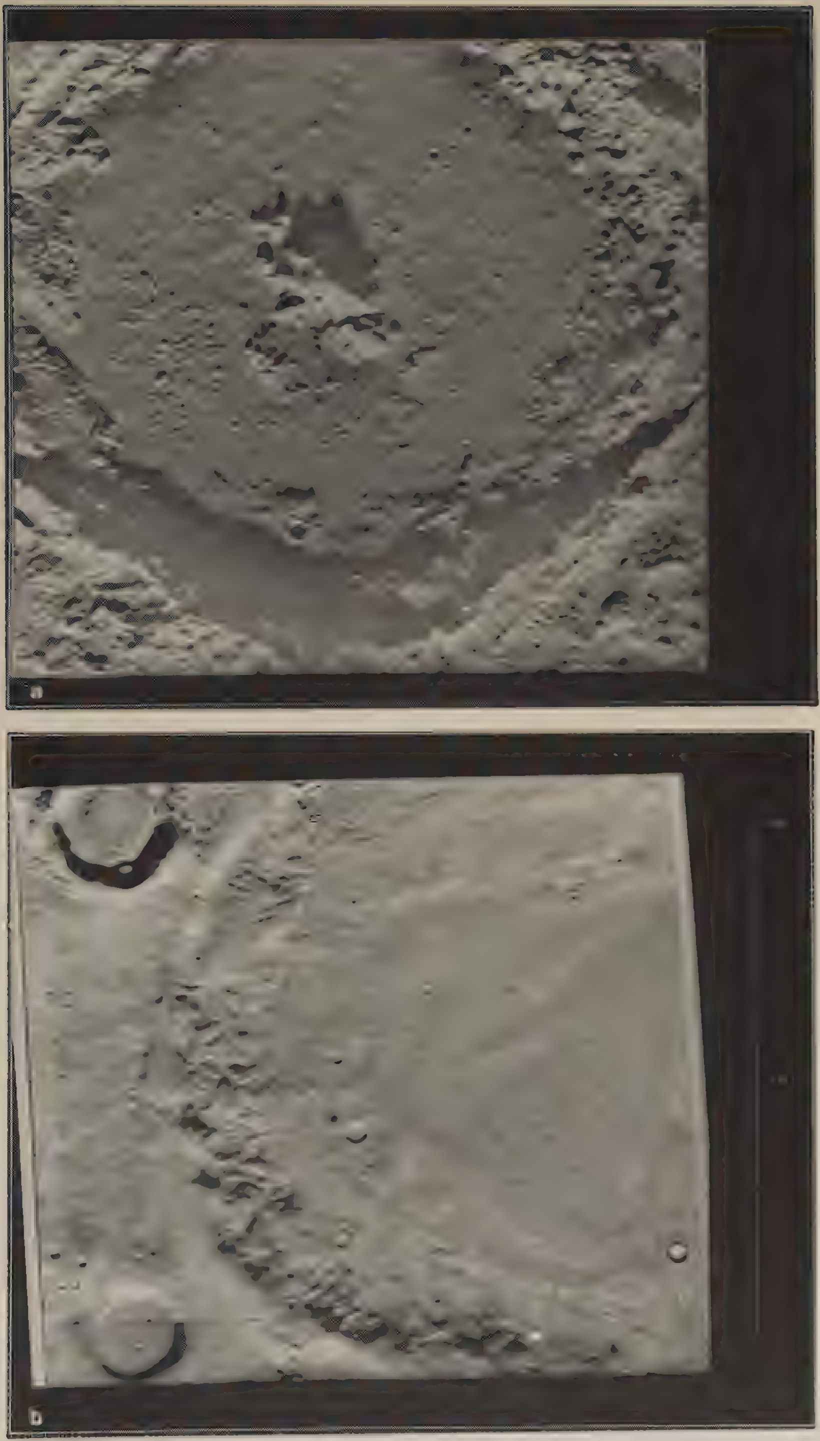

Fig. 25. Unsoftened (a) and softened (b) cratered terrain (Viking Orbiter images 427S32, latitude −25°, longitude 194°, and 191S18, latitude 32°, longitude 309°).

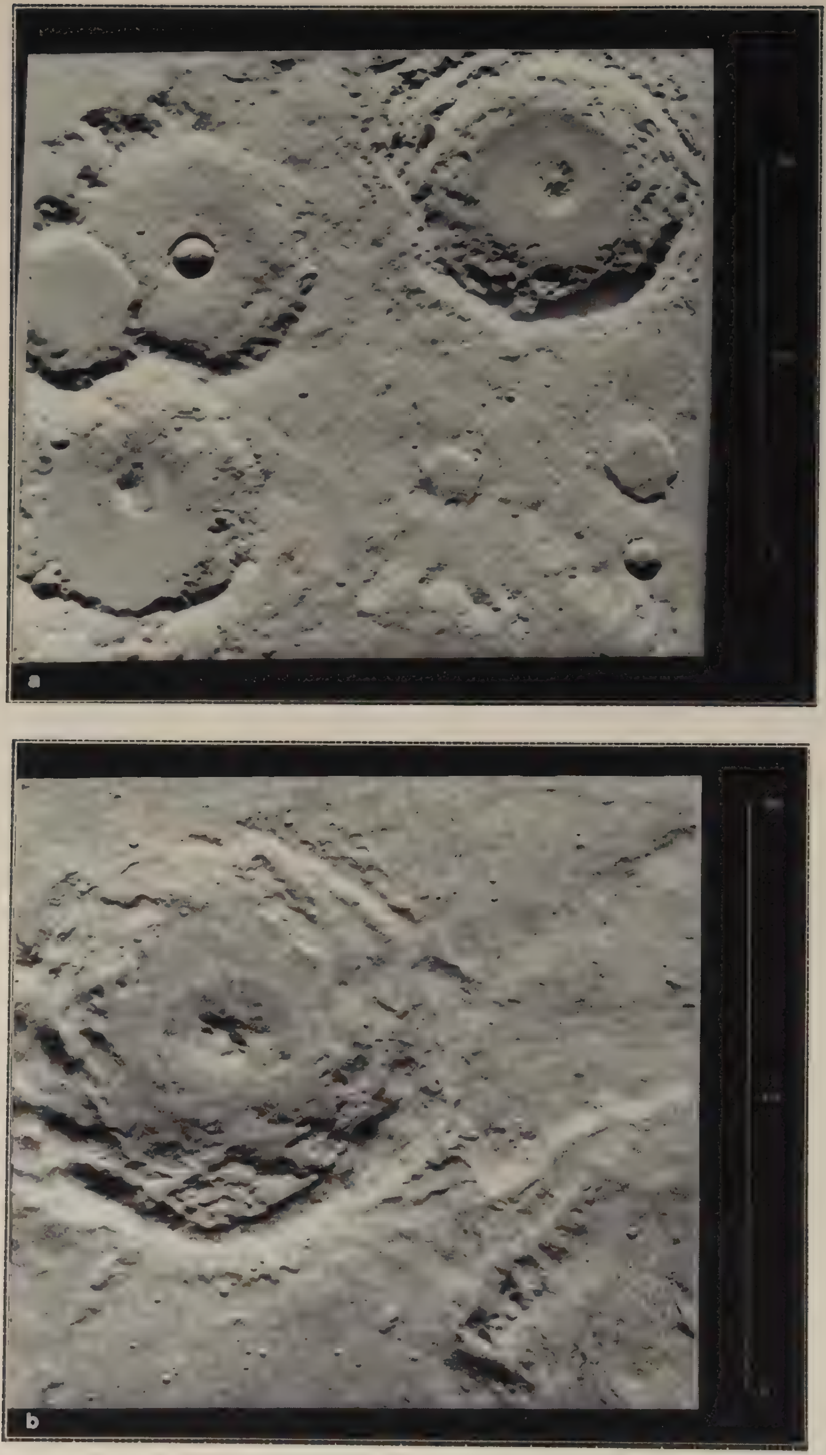

FIG. 26. Unsoftened (a) and softened (b) cratered terrain (Viking Orbiter images 432S09, latitude −15°, longitude 187°, and 641A19, latitude 34°, longitude 305°).

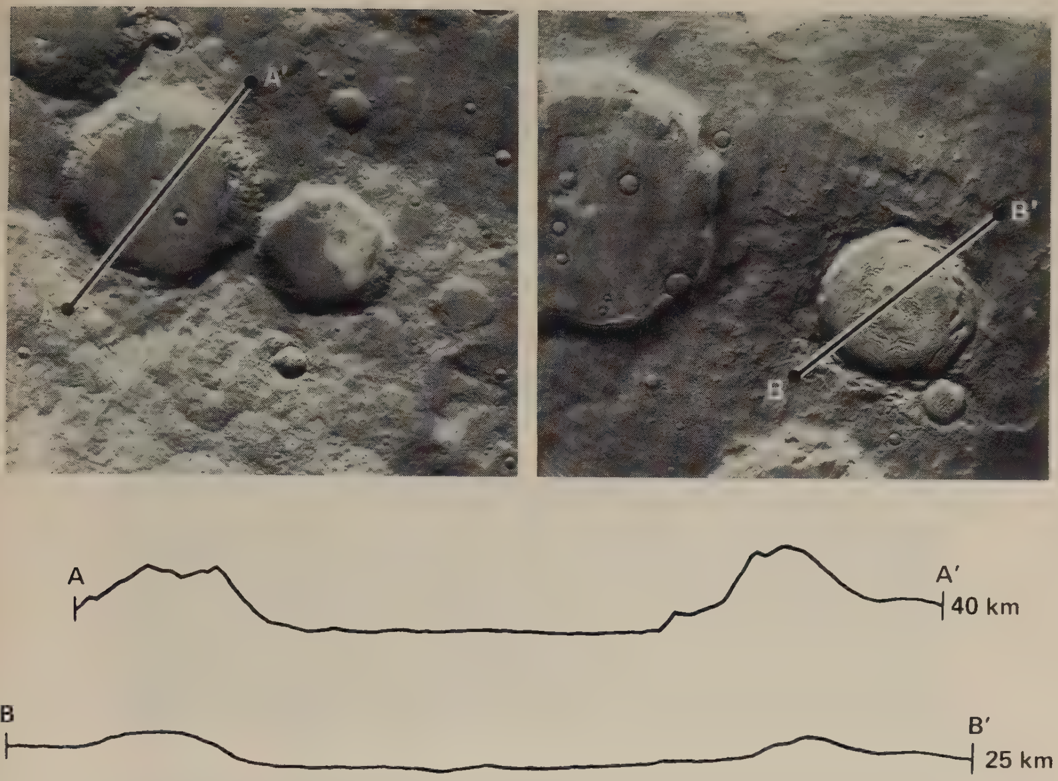

FIG. 27. Photoclinometric profile across impact craters in unsoftened (*A*) and softened (*B*) terrain. In the unsoftened terrain, the crater rims are sharp and the crater walls have straight or concave profiles. In softened terrain, the crater rims are broad and rounded, and the crater walls have convex profiles. Vertical exaggeration in the profiles is 4×; however, the photoclinometric technique used did not correct for scene contrast reduction due to atmospheric scattering. While the slope shapes are qualitatively correct, the true absolute height of the topography is probably greater than that shown (Viking Orbiter images 441S01, latitude −10°, longitude 170°, and 196S11, latitude 32°, longitude 316°; from Squyres and Carr 1986).

of the topography produced by mantling. In general, eolian mantling of sharp, rugged topography does not produce broadened ridge crests and convex slope segments. Eolian debris, because it is by definition readily transported by winds, tends not to accumulate on sharp, exposed ridge crests. Instead, it tends to accumulate preferentially in the lowest-lying regions, leaving the slopes concave and the ridge crests sharp. This effect is shown in Fig. 33. A rugged surface here has been blanketed by debris that is probably eolian in origin, but the effect produced is markedly different from that of terrain softening, with sharp ridge crests protruding through the smooth deposits that fill the hollows. The second argument deals with the scale of features affected by the mantling process. Eolian mantling, by its nature, tends most effectively to obliterate the smallest-scale topographic features in a scene, for example, very small craters. Large features simply require more dust to be buried than do small features. In contrast, viscous relaxation tends preferentially to preserve very small-scale features because the isostatic forces associated with them are small. Figure 33 again demonstrates the point well. Small-scale features here, particularly in

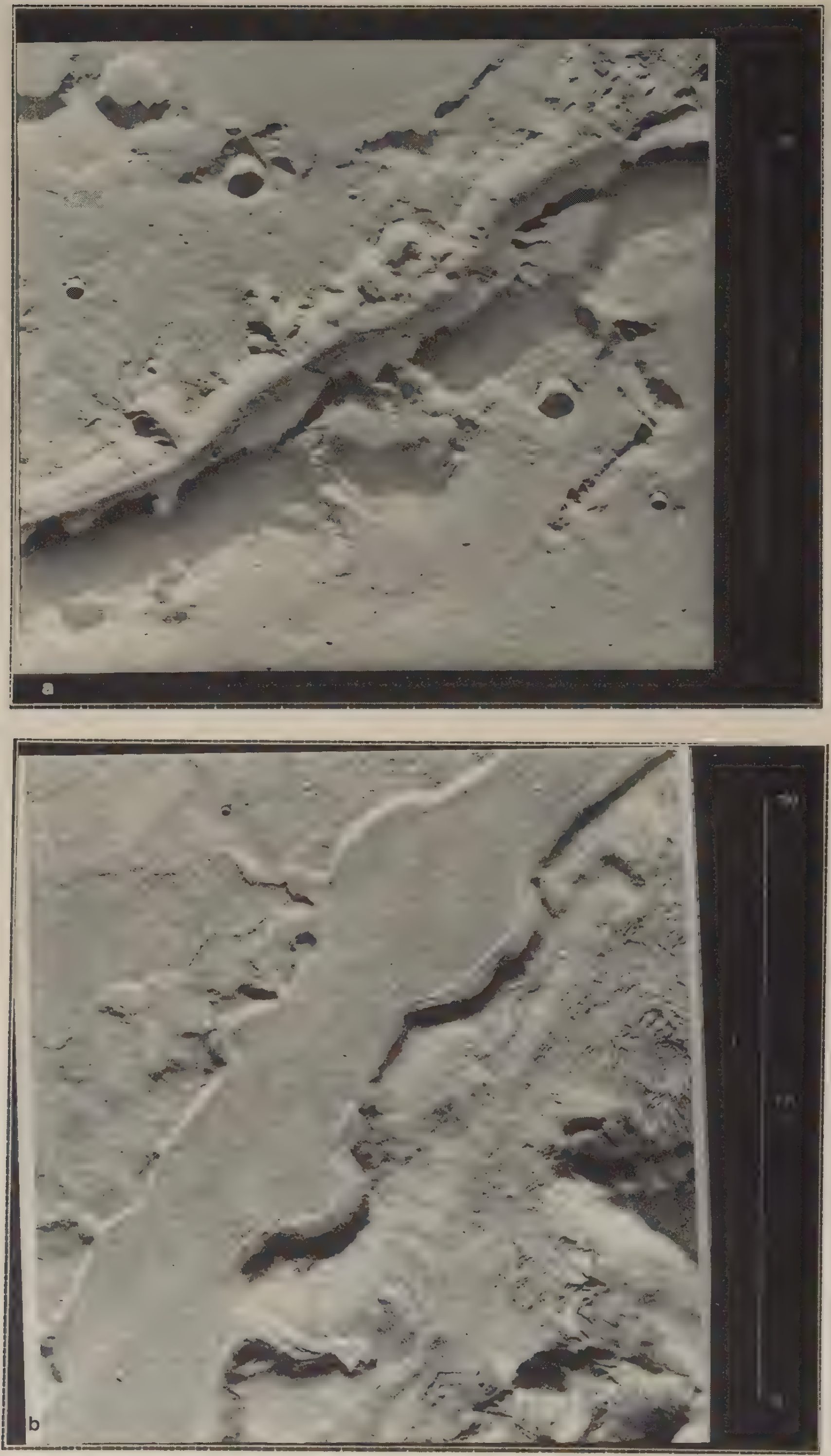

FIG. 28. Channels in unsoftened (a) and softened (b) terrain (Viking Orbiter images 431S28, latitude −22°, longitude 183°, and 584B22, latitude −43°, longitude 254°).

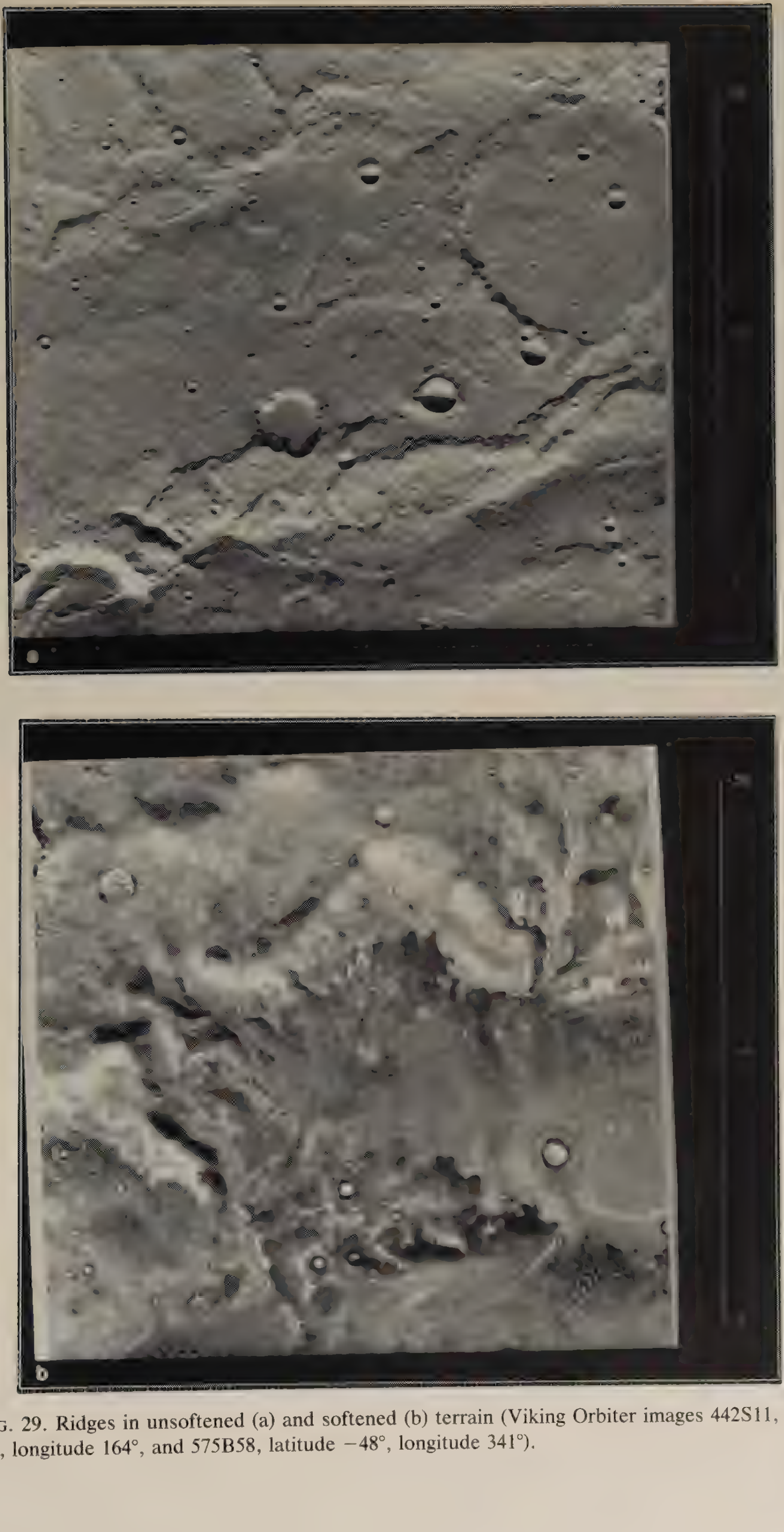

FIG. 29. Ridges in unsoftened (a) and softened (b) terrain (Viking Orbiter images 442S11, latitude −12°, longitude 164°, and 575B58, latitude −48°, longitude 341°).

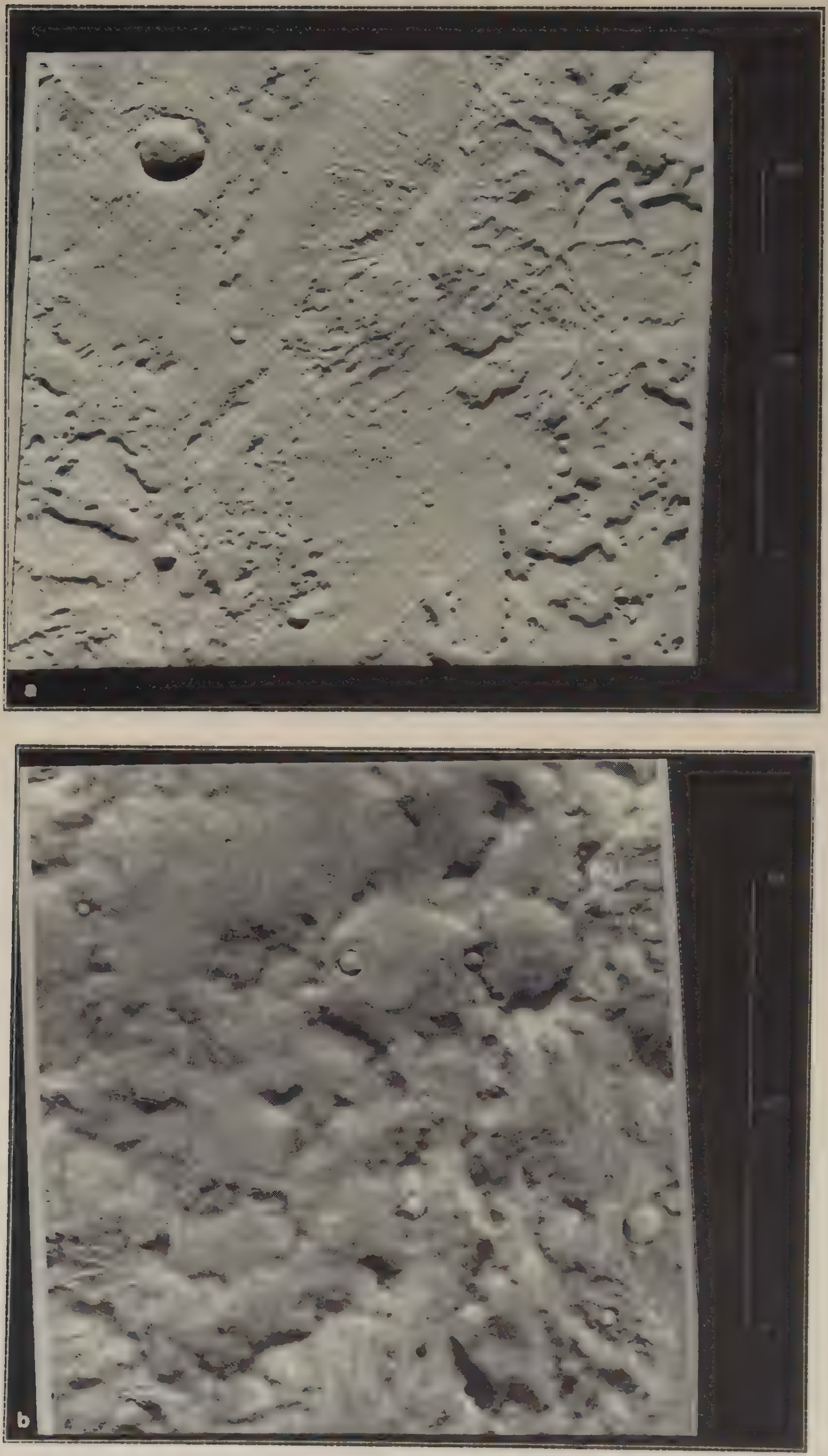

FIG. 30. Unsoftened (a) and softened (b) terrain in complex regions containing a variety of landforms (Viking Orbiter images 432S04, latitude −15°, longitude 89°, and 575B36, latitude −48°, longitude 338°).

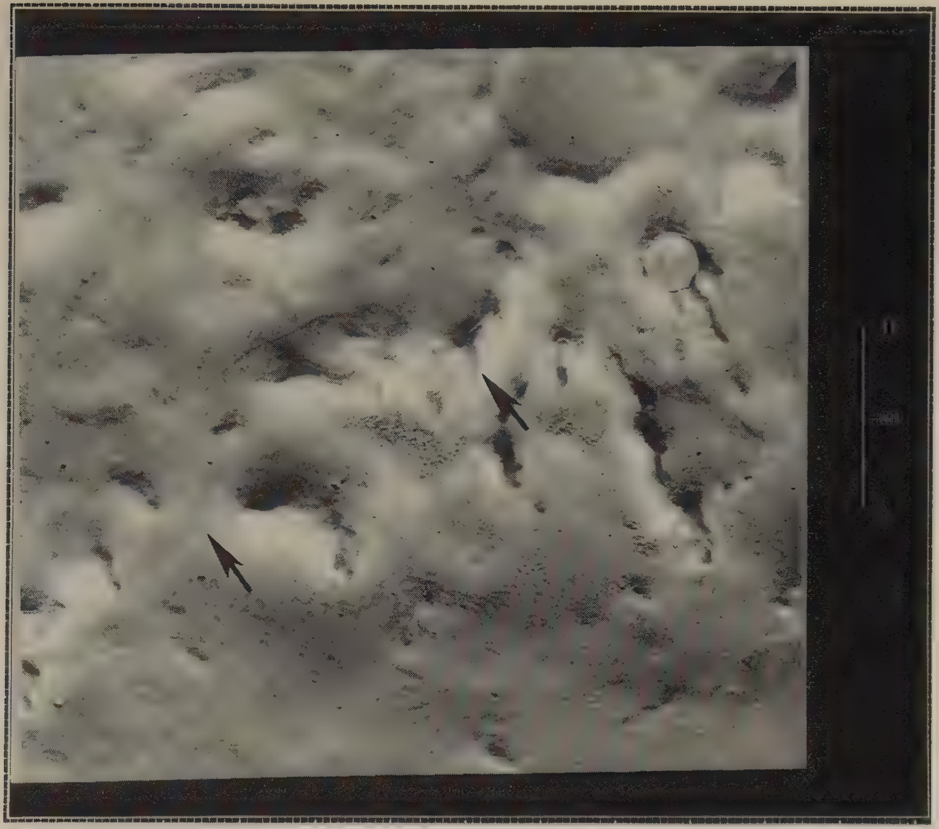

FIG. 31. An area of extreme terrain softening, with streamers of dark material (arrows) showing the direction and extent of downhill flow of surface materials (Viking Orbiter image 585B01, latitude −49°, longitude 248°).

the low-lying regions, have been buried by eolian debris, leaving a smooth, nearly featureless surface. In contrast, small-scale features like impact craters and channels, even near the limit of image resolution, are preserved very well in softened terrain. Figure 24b shows this particularly well.

I conclude, then, that neither atmospheric obscuration nor eolian mantling can account for terrain softening and that the preferred explanation is that it results from viscous creep of near-surface materials. As in the case of the more dramatic flow features like the lobate debris aprons, the agent I believe most likely to have allowed such creep is ground ice. If this inference is correct, then it is useful to compare the global distribution of all of these creep features to thermodynamic predictions of where subsurface ice is most likely to persist on Mars.

Distribution of Viscous Creep Features

Figure 34 presents a map of the distribution of viscous creep features on Mars (Squyres and Carr 1986). In producing the map, we divided the planet into 1° × 1° lat.–long. boxes, and the presence or absence of features was noted in each box. We examined all of the approximately 24,000 Viking Orbiter images obtained while the spacecraft was within 5000 km of the planet's surface. The creep features in the images were grouped into three classes: (1) lobate debris aprons and lineated valley fill, (2) concentric crater fill, and (3) terrain

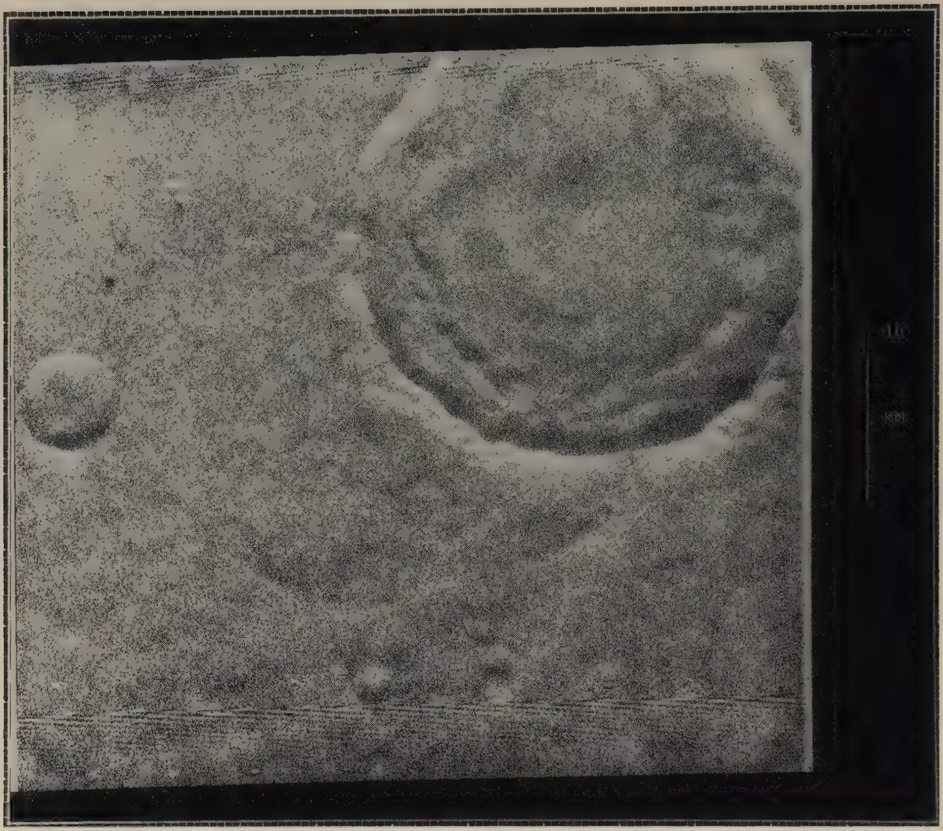

FIG. 32. Image of unsoftened terrain obtained when there was a large amount of dust in the atmosphere. There is substantial contrast reduction and obscuration of small detail in the scene. However, the sharp, unsoftened nature of the topography still is quite evident, and the appearance is very different from that produced by terrain softening (Viking Orbiter image 418A17, latitude −11°, longitude 155°).

softening. The data were digitized, subjected to a 3 by 3 low-pass boxcar filter for smoothing, transformed to a Mercator projection, and displayed with different colors indicating the location of each class of creep features.

The distribution of the features shows a pronounced variation with latitude. Virtually no creep features are found within 30° of the equator. In the northern hemisphere, lobate debris aprons and lineated valley fill are most common in Tempe Fossae, Mareotis Fossae, the Phlegra Montes, in a small region of old cratered terrain north of Olympus Mons, and particularly in the region of fretted terrain discussed earlier. Concentric crater fill is found in most of these areas and also is common on Utopia Planitia. In the southern hemisphere, lobate debris aprons/lineated valley fill and concentric crater fill are most common in regions adjacent to the Hellas and Argyre basins.

In the northern hemisphere, terrain softening is present in all areas where the ancient cratered highlands extend north of 30° lat. Cratered highlands dominate the southern hemisphere, and most regions observed south of −30° lat. exhibit some degree of terrain softening. It is ubiquitous in the midlatitudes and becomes less pronounced toward the south pole.

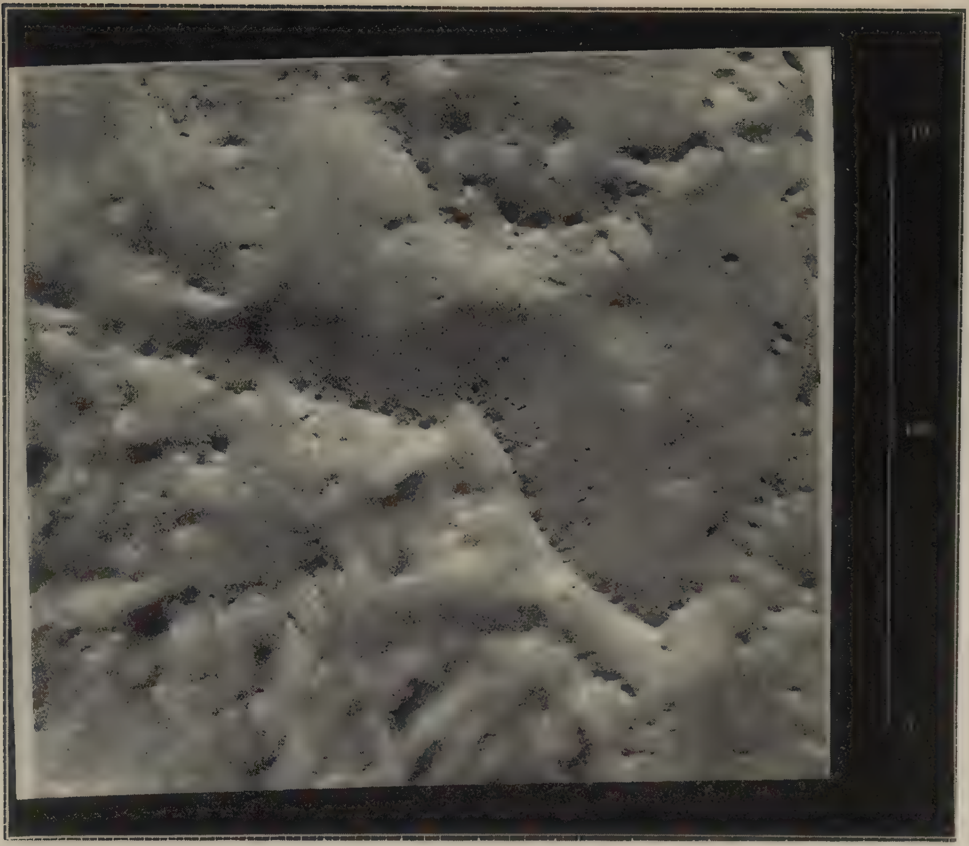

FIG. 33. Dust mantling of sharp, rugged terrain. Fine details in low-lying regions are obscured; ridge crests remain sharp, and slope profiles remain straight to concave. The appearance is very different from that produced by terrain softening (Viking Orbiter image 575B71, latitude −10°, longitude 335°).

The significance of this distribution can be seen immediately by comparing the map of creep features with the thermodynamic predictions of ground ice stability in Figs. 11 and 12. Where the calculations indicate that ground ice should be stable close to the Martian surface, creep features are observed in abundance. Where they indicate that ice is unstable, creep features are essentially absent. If the creep features indeed result from ground ice, then, their distribution provides strong support for the view that the near-surface Martian regolith is rich in ice at high and middle latitudes and depleted in ice at low latitudes. It perhaps also is noteworthy that the creep features are particularly common in the ancient cratered terrain, although this observation may be a simple result of the fact that relaxation of topography is most easily recognized in areas where the topography is initially rugged.

Vertical Extent of Viscous Creep in the Martian Regolith

Once the geographic distribution of viscous creep on Mars has been determined, it is of equivalent importance to establish the depth to which the deformation extends. Both must be known to establish the total volume of ice-rich material involved and on this basis to make any kind of sensible estimate of the amount of ice present. The thickness of the deformation involved in

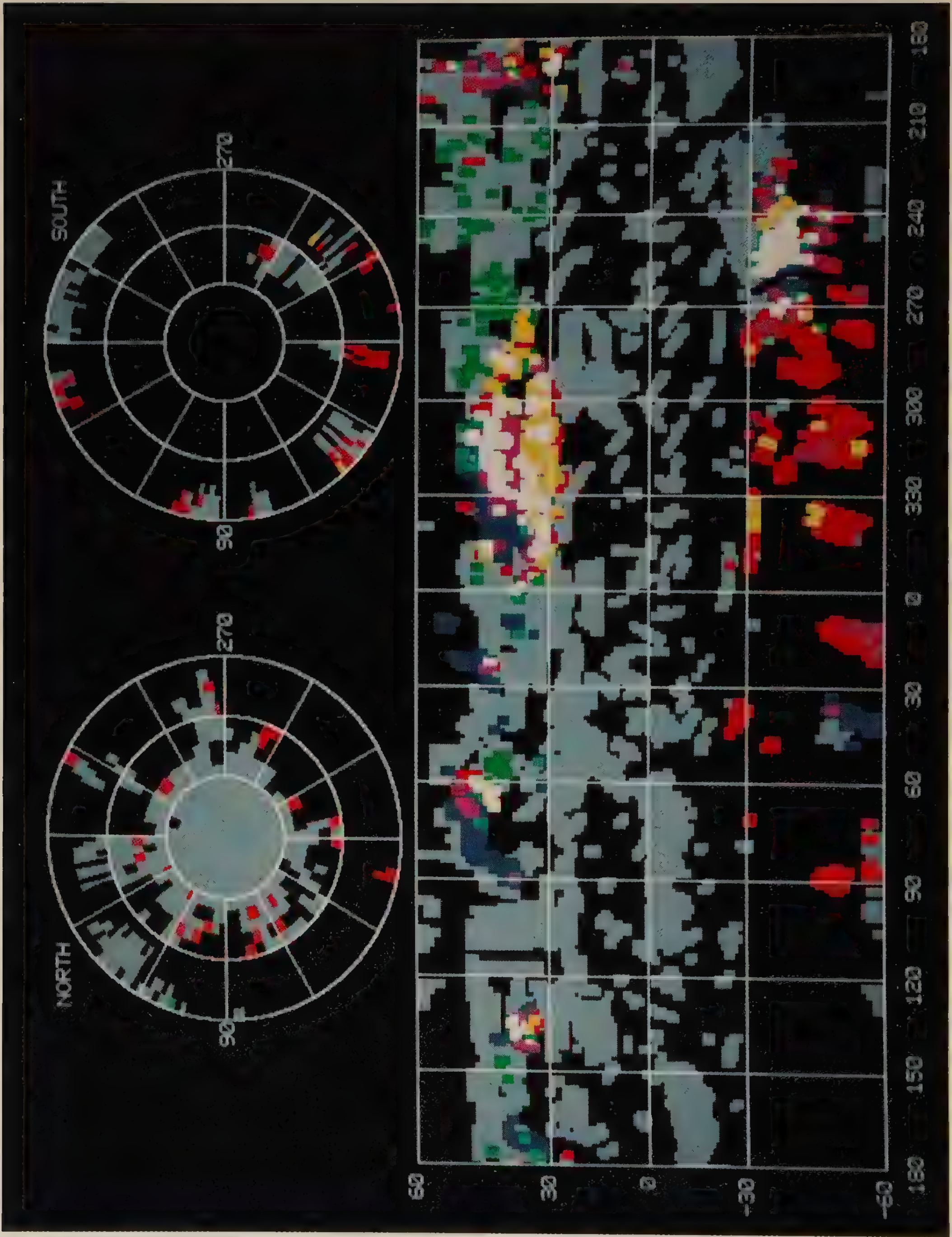
NORTH
SOUTH
270
90
270
90
60
30
0
-30
-60
180
210
240
270
300
330
0
30
60
90
120
150
180

lobate debris aprons, lineated valley fill, and concentric crater fill is in some cases fairly easy to estimate: it is simply the thickness of the flows themselves. I have made three estimates of thicknesses of lobate debris aprons in the fretted terrain based on shadow length measurements (Squyres 1978), obtaining values of 500, 800, and 900 m. More measurements could be made productively. However, it is unlikely that these flows constitute a major Martian H_2O reservoir.

A much more important issue is the depth to which the deformation involved in terrain softening extends. Images of terrain softening convey the impression that it is a relatively near-surface phenomenon. The correctness of this impression can be demonstrated with simple quantitative consideration of the process, using a model of solid-state deformation of a crater in the Martian regolith.

The approach I have taken is to use the MANTLE finite element code to model the flow (Thompson *et al.* 1969, Thompson and Haque 1973, Thompson 1975, Dawson and Thompson 1978). The code uses a two-dimensional grid of triangular elements containing six nodal points each, allowing quadratic interpolation of velocities and linear interpolation of pressure. The grid is shown schematically in Fig. 35. It solves the Navier–Stokes equations for incompressible, noninertial (i.e., creeping) flow. Symmetry is rotational about the midpoint of the crater. The crater has a diameter of 20 km, and the total width of the grid is 100 km. This ratio of grid size to crater size has been demonstrated in other numerical models of crater relaxation to be sufficient to eliminate grid edge effects (Thomas and Schubert 1986). The upper boundary condition of the model is that of a free surface, and the lower boundary condition is that of a rigid surface; i.e., flow velocities are unconstrained at the upper surface and are fixed at zero in both the horizontal and vertical directions at the lower surface. The model therefore simulates relaxation of a viscous layer overlying and fixed to a rigid substrate. The thickness *D* of the deforming layer is variable. The flow is modeled as Newtonian, although I discuss the likelihood and possible significance of non-Newtonian deformation below.

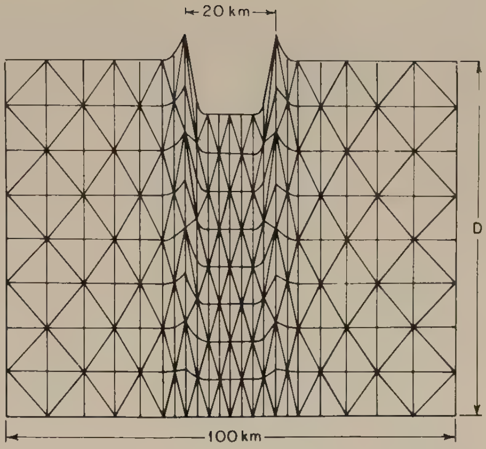

FIG. 35. Schematic representation (doubled about the center of symmetry) of the finite element grid used for calculations of relaxation of a crater in a viscous material overlying a rigid substrate.

Results of the calculations are shown in Fig. 36. At the top of the figure is the profile of the fresh 20-km crater before deformation. The crater rims are 0.75 km high, and the depth from the rim crest to the crater floor is 2.25 km (the actual crater depth with respect to surrounding plains hence is

FIG. 34. Map showing the distribution of viscous creep features on Mars. (Blue) lobate debris aprons and lineated valley fill; (green) concentric crater fill; (red) terrain softening. Where two or more classes of features occur together, colors are added: (Yellow) terrain softening plus concentric crater fill; (magenta) terrain softening plus lobate debris aprons/lineated valley fill; (cyan) lobate debris aprons/lineated valley fill plus concentric crater fill; (white) all three. Gray indicates areas where no creep features are observed, and black indicates where no adequate data are available (from Squyres and Carr 1986).

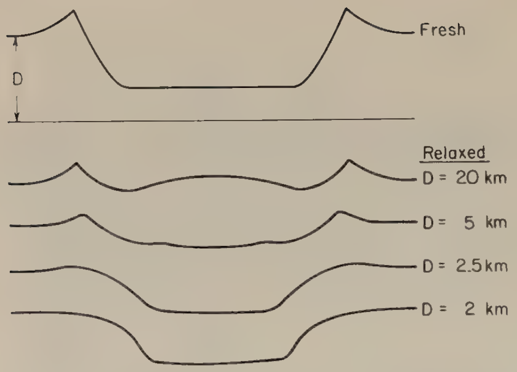

FIG. 36. Results of calculations of relaxation of a crater in a viscous material overlying a rigid substrate. Upper profile shows the topography of the initial crater, with a vertical exaggeration of 2.5×. Lower four profiles show topography at the same vertical exaggeration after comparable amounts of relaxation for four different thicknesses of the viscous layer. For a thick viscous layer ($D = 20$ km), the topography is similar to that observed on icy satellites (see Fig. 13), but unlike softened terrain. In order to produce topography like that observed in softened terrain, the viscous layer thickness must be a small fraction of the crater diameter.

1.5 km). The crater walls are slightly concave, and the crater floor is flat. These shapes are well represented by the finite-element grid; five nodal points comprise the crater wall. The lower part of Fig. 36 shows the crater after roughly equivalent amounts of relaxation for four thicknesses of the deforming layer: 20, 5, 2.5, and 2 km. In the first, then, the deformation is taking place through a layer equivalent in thickness to the crater diameter, while in the last the rigid substrate lies only 500 m beneath the crater floor. The differences in final morphology are striking. With relaxation in a deep viscous layer, the longest topographic wavelengths are removed most rapidly, producing a pronounced upwarping of the crater floor and leaving the crater rims sharp. The crater walls retain their convexity. This is exactly the style of deformation observed for craters on the icy satellites, as shown in Fig. 13 above. However, it is not the style of deformation observed on Mars.

Important changes take place as the deforming layer in the model is made thinner. The flow that produces upwarping of the crater floor extends to a depth comparable to the crater diameter, and intersects the surface in the vicinity of the crater's center with a substantial upward component. As the depth to the rigid substrate becomes smaller, this deep rim-to-bowl flow is suppressed, and the crater floor remains flat. However, substantial changes take place in the shape of the crater's rim. The rim is lowered and is broadened significantly. Moreover, the profile of the crater walls is altered markedly, from concave to distinctly convex. This is the style of deformation observed in terrain softening.

This numerical relaxation model is far too simple to allow a quantitative determination of the thickness of the deforming layer on Mars. However, it does demonstrate two things. First, viscous relaxation of a deformable material overlying a rigid substrate can qualitatively reproduce the morphology of impact craters observed in softened terrain on Mars. Second, the thickness of the deforming layer must be a very small fraction of the diameter of the relaxed crater. Terrain softening indeed seems, then, to be readily attributable to viscous creep and to be a relatively near-surface phenomenon.

Rheology of the Martian Regolith

Further insight into the nature of creep deformation in the Martian regolith may be gained by more detailed consideration of the rheology of the material involved. The rheologic properties of ice and ice-rich soil are known from laboratory experiments performed with natural and prepared samples of these materials. Both constant stress and constant strain rate tests commonly are performed. After an initial period of transient creep, quasi-steady-state creep is established, in which there is a time-invariant functional dependence of strain rate on stress. A severe complication of all such tests is that, by necessity, they must be conducted at strain rates orders of magnitude higher than those that are appropriate for investigation of slow geologic processes like terrain softening. With this limitation in mind, however, they can be a useful guide to the likely behavior of the Martian regolith. In general, three factors have been found to influence strongly the strain rate of frozen ground undergoing steady-state creep: stress, temperature, and regolith structure.

The stress dependence of the rheology of ice depends on the deformation mechanism operating at the atomic scale. Two fundamental deformation mechanisms are possible: diffusion and movement of dislocations. Diffusion creep can involve diffusion of atoms both along grain boundaries (at low temperatures) and within individual grains (at higher temperatures). Deformation via either type of diffusion creep is essentially Newtonian. Dislocation creep takes place by the movement of various types of dislocations through the crystal lattice and produces non-Newtonian deformation. For dislocation creep, the strain rate is proportional to stress to some power n, where n is typically about 3.

Whether diffusion or dislocation creep dominates in ice depends on stress, on temperature, and on grain size (Shoji and Higashi 1978). Both mechanisms could operate in the Martian regolith during the relaxation of a given topographic feature, perhaps at different times and at different depths. For example, for typical Martian regolith temperatures, the shear stress required for (Newtonian) diffusion creep is 10^5–10^6 dyn cm^{-2}; at higher shear stresses, (non-Newtonian) dislocation creep will dominate. Taking Martian gravity, a soil + ice density of 1.8 g cm^{-3}, and a topographic slope α such that $\sin \alpha = 0.05$, a shear stress of 10^5–10^6 dyn cm^{-2} will be found at a depth of 30–300 m. Above this level (in this simple example), deformation would be Newtonian, below it, non-Newtonian. Stress levels decrease during the relaxation of a feature, so topographic relaxation may be dominated by non-Newtonian flow in its early stages and by Newtonian flow in its later stages. When flow is non-Newtonian, then, other things being equal, lower viscosities and higher strain rates will be found at greater depths. However, it may not make a great deal of difference for the shape of the final topography whether the flow is Newtonian or non-Newtonian. Detailed numerical models of Newtonian and strongly non-Newtonian crater relaxation on icy satellites show only very subtle differences in the shapes of the final landforms (Thomas and Schubert 1988).

The temperature dependence of ice and frozen soil rheology is relatively well understood. The rate of steady-state creep generally is proportional to $\exp(-Q/kT)$, where T is temperature, k is Boltzmann's constant, and Q is the activation energy of the deformation mechanism. The effect of the Martian geothermal gradient therefore will be qualitatively similar to the effect that would be produced by non-Newtonian rheology: warmer temperatures at depth lead to lower viscosities and higher strain rates. The effect is, however, less pronounced than the effect of non-Newtonian rheology would be. For example, for a geothermal gradient of 40° K km^{-1}, thermal effects would lower the viscosity by a factor of about 1.7 in going from a depth of 100 m down to 200 m; non-Newtonian viscosity (for an isothermal material) would cause a decrease by a factor of about 8 over the same depth range.

The temperature dependence of viscosity should have a significant influence on regolith rheology as a function of latitude, however. There is indeed a change in the style and prevalence of terrain softening over the latitudes where it is observed (Squyres and Carr 1986). At middle latitudes (30° to ~55°), terrain softening is common and has the morphologic characteristics already described. At higher latitudes, however, a change takes place. Terrain softening becomes much less prevalent, and the other creep features (lobate debris aprons, etc.) disappear alto-

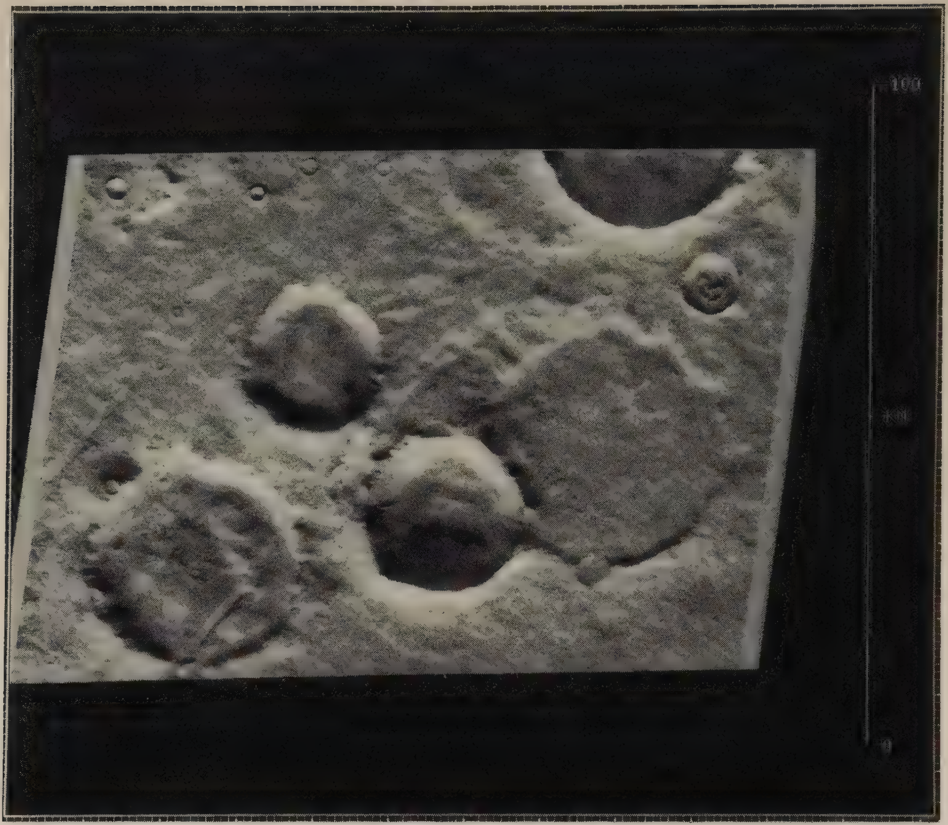

FIG. 37. Typical view of cratered terrain at high latitudes. Terrain softening is much less evident than at midlatitudes (Viking Orbiter image 555B13, latitude −61°, longitude 134°).

gether. Moreover, the little terrain softening that is observed is much less pronounced. Crater rims are sharper than at the middle latitudes, and intercrater areas are rougher (Fig. 37).

The decrease in the observed frequency and extent of terrain softening at high latitudes is most likely due to the colder temperatures and higher viscosities found there. In fact, the exponential dependence of rheology on temperature may mean that creep is essentially negligible under most conditions at high latitudes. The present annual average surface temperature on Mars at 45° lat., where terrain softening is common, is about 205°K. The cyclic changes in Martian climate, of which the most important are caused by obliquity variations, have essentially no effect on mean annual temperature at this latitude, so this temperature applies thoroughout the obliquity cycle. At a latitude of 75°, where terrain softening is uncommon and minor, a typical mean annual surface temperature at the present obliquity is about 160°K. At this latitude, however, the thermal effects of obliquity variations are substantial. At the lowest obliquity, the mean annual temperature drops to about 145°K (Fanale *et al.* 1986), while at the highest obliquity, it rises to nearly 180°K.

The approximate viscosity of ice at the midlatitude temperature of 205°K will be lower than the high latitude viscosity by factors of 10^2 (for 180°K), 10^5 (for 160°K), and 10^6 (for 145°K). It is easy to see, then, why terrain softening is so much less pronounced at high latitudes: the material there is very much stiffer than at the lower latitudes. Moreover, it is evident that significant viscous creep, if it takes place at all, probably will be limited to the brief periods when the obliquity is highest and the temperatures warmest. The dominant periodicity of the obliquity variation is 1.2×10^5 years, so the thermal skin depth to which the episodic warming penetrates (and hence to which the deformation will extend) will be at most a few hundred meters (Squyres and Carr 1986).

The most important determinant of the rheology of an ice–silicate mixture can be the structure of the mix; that is, the relative proportions of ice and silicate and the way in which the grains interact. Depending on structure, the material can be as mobile as pure ice or as rigid as pure rock. More than any other factor, structure may dominate the depth dependence of the rheology of the Martian regolith.

At small silicate concentrations in an ice/silicate mixture, grains of rock act as particles in suspension in the ice. Their presence acts to increase the viscosity of the mixture. They do not deform appreciably in response to stress, and a comparatively higher strain rate in the ice is required to provide a given bulk deformation rate for the mix as a whole. Theoretical treatments exist for describing the viscosity of such suspensions, and they are fairly successful at low to moderate particle fractions (Thomas 1965). However, once the particle volume concentration exceeds about 0.5–0.6, simple theory breaks down because the particles begin to ''lock'' together.

(Another effect that may or may not be important in increasing the viscosity of ice/rock mixtures is dispersion hardening, which increases the apparent activation energy for diffusion creep. This will be substantial only if silicate grains are of the same size or smaller than the ice grains, a possibility that is difficult to evaluate.)

When the volume fraction of silicates exceeds about 0.5–0.6, the physical manner in which the grains and ice come into contact (the regolith ''structure'') becomes crucially important in controlling the rheology of the mix. If the silicate material is thoroughly comminuted and disaggregated, forming a true soil, then significant mobility still is possible at very high silicate fractions. Numerous experiments have been conducted with natural and fabricated frozen soils in which ice-abetted creep takes place at silicate volume concentrations as high as 0.8 (see, e.g., Andersland and Akili 1967, Ersoy and Togrol 1978, Haynes 1978). Physically, the ice acts as a lubricant, decreasing the inherent grain-to-grain frictional resistance of the soil to flow. However, there are other possible structures that can have substantial ice content, but that have rheologic properties completely controlled by the rheology of the rocky component. An extreme example would be a lava flow unit. Lava flows can have substantial porosity, with a blocky fractured structure and internal lava tubes. However, no matter how full the lava tubes and fractures become with ice, the structural integrity of the lava will prevent any creep deformation. Fractured bedrock, in which large fractures have been produced but complete disaggregation, comminution, and reorientation of blocks has not taken place, can have the same characteristics.

Dependence on stress, temperature, and structure all will affect the rheology of the Martian regolith. Structure aside, stress and temperature effects will tend to make mobility increase with depth at a given latitude. However, as the transition is made from comminuted soil near the surface to solid bedrock below, structural effects will cause mobility to decrease with depth, dropping it to zero at some depth where the rheology becomes controlled by rock rather than ice.

Terrain Softening, Rampart Craters, and the Distribution of Ground Ice on Mars

Terrain softening appears to be a useful indicator of the distribution of ground ice on Mars. However, there is another equally plausible indicator that seems at first glance to give a different result: rampart craters. These are craters surrounded by lobed ejecta that appears to have been emplaced as a low-viscosity mud flow. The most commonly accepted interpretation of their morphology is that the water lubricating the flow was present as subsurface ground ice and was melted and mobilized by the impact event (Carr *et al.* 1977, Gault and Greeley 1978, Mouginis-Mark 1987). It has been suggested that some aspects of rampart crater morphology could be attributable to atmospheric effects independent of subsurface H_2O (Schultz and Gault 1979, Schultz 1986). However, the details of rampart crater morphology, particularly in the common cases where several overlapping flow lobes are present, argue persuasively for an origin related to subsurface H_2O.

There have been several studies of rampart craters that have documented the variability in their morphology, their geographic distribution, and their relation to crater size (see, e.g., Johansen 1979, Mouginis-Mark 1979, 1981, Kargel 1986, Horner and Barlow 1988). While the findings of these studies differ in some details, they agree conclusively on at least one thing: rampart craters are found at all latitudes on Mars. So, if both rampart craters and terrain softening are indicators of ground ice, a fundamental problem appears to exist: one indicates ground ice at all latitudes, while the other indicates ground ice only at latitudes higher than 30°.

One important aspect of rampart craters as an indicator of subsurface H_2O is that they, too, may provide information about the depth distribution of H_2O. In any given region on Mars, not all impact craters have flow ejecta. There usually is some critical crater diameter below which ramparts are not observed and above which they are common. The obvious interpretations of this observation is that H_2O is present at depth, but absent close to the surface. An impactor must penetrate through the dry surface layer to the H_2O-rich layer underneath for ramparts to form.

It has been recognized for some time from the various global surveys of rampart craters that they are best developed, and appear at smaller critical crater diameters, at high latitudes. The dependence of critical diameter on latitude has been documented in detail in a recent study of Kuzmin *et al.* (1988). They examined approximately 10,500 craters over almost the entire planet and noted the onset diameter for crater ramparts as a function of geographic position. They then took a reasonable depth for the transient cavity of a Martian crater as a function of crater diameter and assumed that ramparts would form once the depth to the transient cavity became greater than the depth to the top of a H_2O-rich layer.

Their mapping showed a striking latitudinal variation in the interpreted depth to H_2O. At latitudes less than ±30°, the depth was substantial—from 300 to more than 400 m. At about ±30° the depth was found to rise fairly abruptly to 200 m and by ±50° to just 50–100 m.

The exact values of these depths perhaps should not be taken too literally. Several factors will work to complicate the picture. As pointed out by S. Clifford (personal communication, 1988), penetration of the transient cavity just to the top of a H_2O-rich layer may not be sufficient for ramparts to develop; deeper penetration into the layer probably is required. The depth to the H_2O-rich layer undoubtedly has changed with time, and older craters may give depths substantially shallower than the true value at the present, particularly at low latitudes. The appropriate value to use for the depth of the transient cavity of Martian craters is not entirely certain. There also could be significant variations in the H_2O content of the subsurface layer as a function of latitude, further complicating the problem. However, the general trend is clear: Interpretation of rampart craters as the result of subsurface ice indicates that ice is present close to the surface at high latitudes and is substantially deeper at low latitudes, with a fairly steep dropoff at a latitude of ~±30°.

In order to form a consistent picture of the distribution of ground ice on Mars, we need to resolve the apparent differences between the implications of rampart craters and the implications of terrain softening. To do this, we must keep in mind that terrain softening is not an indicator of ground ice, per se. It is an indicator of solid-state creep of the regolith. The presence of ice is a necessary but not sufficient condition for significant creep to take place. Heavily fractured bedrock can contain substantial amounts of ice while remaining immobile over geologic time scales. When both the presence of ground ice and the structure of the regolith/ice matrix are considered together, the apparent conflict between terrain softening and rampart craters is resolved in a straightforward manner.

The Martian regolith in the heavily cratered terrain where terrain softening is observed is primarily a product of intensive impact bombardment coupled with volcanic activity. Most of what is known about the structure of such materials on ancient planetary surfaces comes from seismic data for the Moon (see, e.g., Kovach and Watkins 1973, Toksöz *et al.* 1973). The lunar crust shows a pronounced increase of seismic velocity with depth in the upper few kilometers. Materials in the upper several hundred meters have *P*-wave velocities of just 100–300 m $\sec^{-1}$, indicating a highly disaggregated granular structure. By a depth of 1 km the velocity has increased to about 1 km $\sec^{-1}$, typical of a highly fractured bedrock. Below depths of 1–2 km, velocities are 4 km $\sec^{-1}$ or more, indicating solid rock. This velocity structure is due largely to the effects of the impact process. Near the surface, materials in heavily cratered terrains are dominated by disaggregated and pulverized impact ejecta. This grades downward into bedrock that has been extensively fractured in place, and, finally, into solid bedrock below. A qualitatively similar structure is to be expected in heavily cratered terrains on Mars.

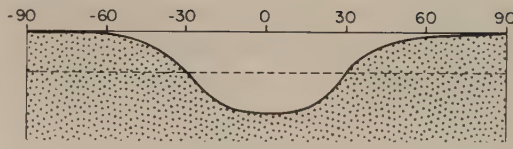

FIG. 38. Schematic representation of the distribution of ice in the Martian subsurface, as deduced from both terrain softening and rampart craters. Ice in the equatorial region has been removed to a substantial depth by sublimation and diffusion. Dashed line indicates the depth above which the crustal material has been sufficiently disaggregated by impacts that it is able to flow and produce terrain softening. Current understanding is inadequate to allow accurate labeling of the depth scale on the vertical axis.

Figure 38 shows a schematic pole-to-pole cross section through the Martian regolith that I believe to be broadly consistent with all the current data and theoretical considerations that bear on the issue of ground ice distribution. The patterned region indicates the locations where ground ice is present. Ice extends very close to the surface at high latitudes. The top of the ground ice becomes deeper with decreasing latitude, dropping off fairly sharply in the vicinity of ±30°. Ground ice is present at equatorial latitudes, but only at substantial depths. This ice distribution is in agreement with both theoretical considerations and observations of rampart craters.

The dashed line in Fig. 38 shows the depth at which an effective transition takes place from pulverized, thoroughly disaggregated debris near the surface to fractured bedrock below. The transition of course will be gradual rather than abrupt, but the effect on the mobility of materials will be qualitatively the same. Both materials are porous and can contain significant amounts of ice, but only the upper one has a structure that will allow creep deformation to occur. At latitudes higher than ±30°, ice is present in near-surface, thoroughly disaggregated materials, and terrain softening can take place. At lower latitudes, ice only persists in deep, heavily fractured bedrock, still allowing rampart craters to form for large impacts, but preventing terrain softening. This picture is consistent with the observed distribution of terrain softening, with our knowledge of the rheology of ice–silicate mixtures, and with the expected vertical structure of the upper few kilometers of the Martian surface.

The vertical scale on Fig. 38 is left unlabeled intentionally. We do not know the depth to which terrain softening extends with any real accuracy. Neither can we determine the depth to the top of the ice-rich layer with any certainty. While a consistent general picture can be identified, it will be left to future investigations to determine its regional variability and its quantitative details.

Investigation of Near-Surface Ground Ice via Gamma-Ray Spectroscopy

There is one future technique that offers the possibility of direct detection of shallow Martian ground ice: gamma-ray spectroscopy. A gamma-ray spectrometer will be part of the payload of the Mars Observer mission scheduled for launch to the planet in 1992. Referring back to Fig. 11, it can be seen that ground ice may exist within tens of centimeters of the Martian surface at latitudes greater than roughly ±50–60°. The power of the gamma-ray technique for investigation of ground ice is that it can see tens of centimeters below the Martian surface and can detect the hydrogen in this ice directly if it is there. Moreover, data analysis techniques are being developed that will enable determination of quantitative information about both the concentration and the depth distribution of ice present in that depth range.

Planetary gamma-ray remote sensing is a technique that first was used with real success on the Apollo 15 and 16 missions (Metzger *et al.* 1973, 1974, Harrington *et al.* 1974). It is based on the fact that several processes can lead to emission of gamma radiation by a planet's surface. This emission consists of discrete spectral lines superimposed on a background continuum. The lines have energies characteristic of the atomic nucleus from which they were emitted, and the strengths of identified lines can be used to infer quantitative elemental abundances. The spatial resolution of the technique typically is low and on the Mars Observer will be ~300 km in most cases.

The primary sources of gamma-ray emissions from the Martian surface are decay of natural radionuclides, decay of radionuclides produced by solar cosmic-ray and galactic cosmic-ray bombardment, and inelastic scatter and neutron capture reactions caused by secondary neutrons from galactic cosmic-ray interactions with the surface. The third process is the most important for the study of subsurface H_2O. It begins when galactic cosmic rays bombard the Martian surface. Most incident particles undergo nuclear interactions before they are stopped by ionization energy losses. Many secondary particles are produced by these interactions and in the resulting particle cascade, including neutrons, protons, π-mesons, and others. Most charged particles are stopped quickly, but the neutrons are able to undergo further nuclear interactions of interest.

Because of the limited depth of cosmic-ray penetration, most neutrons are produced at depths of no more than a few hundred grams per square centimeter. These neutrons typically have energies of several MeV and up. They can undergo inelastic scattering $(n, n'\gamma)$ interactions with a variety of nuclei, producing many of the gamma-ray emissions of geochemical interest. They also can undergo elastic scattering from nuclei, losing kinetic energy through collisions and eventually reaching thermal speeds. Thermal neutrons can be captured to produce a new nuclide in an excited state that decays via emission of gamma rays; these interactions are called capture (n, γ) reactions. Because of its low atomic weight and relatively large scattering/absorption cross section ratio, H is by far the most important nucleus for neutron moderation. The neutron energy spectrum and the variation with depth in the regolith of the total neutron flux therefore depend strongly on the concentration and vertical distribution of H (Lapides *et al.* 1980, Haines and Metzger 1984, Evans *et al.* 1986, Drake *et al.* 1988).

There are two ways in which hydrogen in the Martian regolith can be detected using gamma-ray spectral data. The first is direct. Thermal neutrons can interact with H nuclei via the (n, γ) reaction: ${}^{1}_{1}\mathrm{H} + {}^{1}_{0}n \rightarrow {}^{2}_{1}\mathrm{H}^{*} \rightarrow {}^{2}_{1}\mathrm{H} + \gamma$. As the deuterium nucleus produced by neutron capture returns to its ground state, it emits a γ ray with an energy of 2.223 MeV. Detection of a discrete line at 2.223 MeV provides unambiguous evidence for the presence of H.

The second gamma-ray technique for detection of H is indirect. The special effectiveness of H for thermalizing neutrons means that the neutron energy spectrum also carries information about subsurface H. Capture reactions are caused primarily by thermal neutrons, while inelastic scatter reactions are caused primarily by fast neutrons. Some elements emit strong lines of both types. For example, Si has a strong inelastic scatter line at 1.779 MeV and strong capture lines at 4.934 and 3.539 MeV. One may therefore examine ratios of inelastic scatter to capture line strengths for elements like Si and acquire direct information about the neutron fast/thermal ratio. This information in turn provides an indirect measure of subsurface H.

The real power of gamma-ray spectroscopy for investigation of near-surface ground ice comes when both techniques are applied together. The e^{-1} absorption length for 2.223-MeV gamma rays is about 20 g cm^{-2}. The strength of the 2.223-MeV line therefore provides information about H concentration in the upper few tens of g cm^{-2}. The distance traveled by neutrons is substantially greater, and the neutron energy spectrum provides information about H concentration in the upper 100 g cm^{-2} or more. So, when the two independent techniques are used together, information can be obtained about both the concentration of subsurface H and its vertical distribution in near-surface materials.

(It should be noted that the Mars Observer gamma-ray spectrometer also will include a neutron mode capable of determining information about the energy spectrum of leakage neutrons from the planet's surface in the thermal and epithermal energy ranges. This capability will not be discussed in detail here, but will add an additional, independent, and powerful capability for investigation of ground ice (Drake *et al.* 1988).)

The application of gamma-ray spectroscopy to the problem of Martian ground ice was considered in detail by Evans and Squyres (1987). We used a simple two-layer model of the Martian surface. The upper layer consists of dry soil of arbitrary thickness with an elemental composition like that observed at the Viking landing sites (Clark *et al.* 1982). The lower layer consists of soil intermixed uniformly with an arbitrary amount of ice, and is semi-infinite. Two parameters therefore describe the model: the thickness of the upper dry soil layer and the ice mass fraction of the lower ice-rich layer. In both cases, the regolith was taken to be overlain by an atmosphere of Martian composition (Owen *et al.* 1977), with a thickness of 20 g cm^{-2}.

The calculation begins with the primary cosmic-ray spectrum and the resulting secondary neutron source distribution. These were taken to be like those inferred for the Moon from lunar data (Lingenfelter *et al.* 1972, Kornblum *et al.* 1974). Neutron transport calculations were then used to determine the neutron energy and spatial distributions resulting from the scattering processes that take place in the regolith. The code used for the calculations was ANISN (Engle 1967), which is a one-

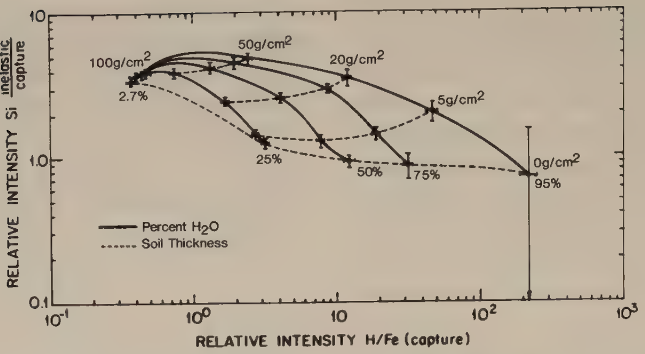

FIG. 39. Results of gamma-ray production and transport calculations for a layer of pure soil overlying a layer of mixed soil and H_2O. Vertical axis gives the measured Si (inelastic scatter/capture) line strength ratio, horizontal axis gives the measured H(capture)/Fe(capture) ratio (see text for discussion). Solid curves are contours of constant H_2O mass fraction in the lower layer, and dashed curves are contours of constant thickness of the upper layer. For data falling in much of this region, it will be possible to determine uniquely both the thickness of the upper layer and the ice mass fraction of the lower layer. Uncertainties (1σ) are shown for an integration time of 38 hr.

dimensional discrete ordinate code that solves the neutron transport equation by evaluating the flux for discrete directions, positions, and energies. The gamma-ray line fluxes were calculated from the resultant neutron distribution. For the capture lines, the thermal flux was used with the appropriate thermal neutron capture cross sections and gamma-ray yields and was integrated from each depth, with the appropriate attenuation value, to the top of the atmosphere. Inelastic scatter line fluxes were calculated in a similar manner, with the inelastic scatter cross sections integrated over energy at each depth. These calculations together yielded the gamma-ray line fluxes for each model configuration.

The gamma-ray background continuum results from cosmic-ray cascade processes, Compton scattering, and electron bremsstrahlung from the planet; emission from natural radionuclides on the planet; cosmic-ray interactions with the detector and the spacecraft; and cosmic gamma rays (Bielefeld *et al.* 1976). Of these, the dominant one is scattering from the planet. We estimated the background from the shape of this component of the lunar spectrum, scaled from our gamma-ray transport results. Finally, detection of the discrete lines and background at the spacecraft was modeled using the measured energy resolution and efficiency of a 120-cm^3 high purity Ge detector similar to the one that will be flown on Mars Observer.

The results of the calculation are shown in Fig. 39. The horizontal axis of this figure gives the intensity of the 2.223-MeV capture line of H, ratioed for convenience to the sum of the 7.632- and 7.647-MeV capture lines of Fe. The vertical axis gives the ratio of the Si 1.779-MeV inelastic scatter line to the sum of the Si 3.539- and 4.934-MeV capture lines. Solid curves give contours of constant H_2O mass fraction in the lower ice-rich layer of the model, and dashed curves give contours of constant thickness of the upper dry layer. Error bars are shown for an integration time at the spacecraft of 38 hr, a typical number for a single high-latitude gamma-ray spectrometer spatial resolution element over the expected duration of the Mars Observer mission. The important point is that the calculations yield two well-separated sets of curves. Within reasonable limits, for any measurement that falls on this plot, there is only one combination of upper layer thickness and lower layer ice concentration that will fit the data. If we are willing to accept this simple two-layer model as a representation of the true vertical distribution of ice in the near-surface Martian regolith, then, we can use gamma-ray data to determine both the depth to the ice-rich layer and the concentration of ice in that layer. This technique will be applied to the data returned by the Mars Observer gamma-ray spectrometer and may help determine whether the ground ice inferred to be close beneath the surface at high latitudes in fact is present.

CONCLUSIONS

There are suggestions in the Martian geologic record, as yet unproven, that the climate of the planet may have changed significantly over its history. Conclusive evidence concerning the long-term changes that may have taken place in a planet's climate can be preserved in water-lain sediments. The liquid water that once flowed across the Martian surface and carved the erosional features observed there also must have produced sedimentary deposits. Layered deposits in the Valles Marineris may have been laid down in lakes dating from the epoch of outflow channel formation, but their identification as aqueous sediments on the basis of their present morphology is not certain. In Mars' ancient heavily cratered terrain, however, many water-carved valleys empty into local topographic depressions that acted as catchment basins for the water and the sediments washed from the valleys. Under plausible early Martian conditions, ice-covered lakes could have existed in these depressions for significant periods. These water bodies could have provided sites for formation of carbonate rocks, permanently sequestering CO_2 from the planet's atmosphere. It is the valley systems that have led some to the conclusion that Mars was once warmer, wetter, and more Earth-like than it is at the present. Water-lain sediments associated with the valley systems may hold the evidence to support or refute this view, and I believe should be considered important targets for future in-depth exploration of the planet.

Thermodynamic considerations may be used to infer the locations where ice can persist beneath the Martian surface. If enough ice is present in the Martian regolith, one can expect solid-state creep of the regolith to take place. Such flow should produce deformation of topographic features on the planet's surface and is observed in Viking Orbiter images. The most widespread form of deformation leads to production of convex topographic profiles from concave or straight slopes and broadening of originally sharp slope inflections. Simple numerical models show that the creep must be a near-surface phenomenon to produce the style of deformation observed. When the distribution of creep features is mapped, the results provide strong support for the conclusions derived from thermodynamic calculations: ice is common in the near-surface Martian regolith poleward of ±30° lat and largely lacking from the near-surface regolith at lower latitudes.

Rampart craters, another frequently cited indicator of subsurface H_2O on Mars, at first glimpse appear to give a different result, since they are observed at all latitudes. This apparent conflict may be resolved by consideration of all the factors that influence the rheology of the Martian regolith. At sufficient depth, transition from a thoroughly comminuted regolith to a more coherent fractured bedrock will prevent solid-state deformation, while still allowing significant H_2O content. It is likely, then, that ice is present beneath the surface at all latitudes on Mars, but that it only lies at shallow enough depths to allow significant regolith deformation at latitudes higher than ±30°.

Thermodynamic calculations predict that ice should be stable to within a meter or less of the surface at latitudes higher than about ±50–60°. Ice at depths this shallow will produce a distinctive signal in the spectrum of gamma radiation from the planet's surface that is stimulated by cosmic-ray interactions and emitted to space. The details of this spectrum can be measured by an orbital gamma-ray spectrometer and can be used to investigate both the concentration and vertical distribution of ice in the near-surface Martian soil.

In the minds of some, including many who have hopes for the eventual detailed exploration of the Solar System, Mars has come to occupy a special place. What makes Mars special are its Earth-like qualities, and foremost among these is the role that water appears to have played in the planet's history. Water can shape a planet's surface into distinctive and familiar forms; its history holds clues to the evolution of a planet's climate; it is believed to be a prerequisite for the emergence of life and certainly will be a necessity for long-term human habitation. However, we still lack the knowledge necessary to describe the history or distribution of water on Mars with anything approaching confidence. Most of the conclusions I have drawn in this paper are based on conjecture and inference from incomplete data; many may be wrong. Aristotle, in *On Generation and Corruption,* wrote

> Lack of experience diminishes our power of taking a comprehensive view of the admitted facts. Hence those who dwell in intimate association with nature and its phenomena grow more and more able to formulate, as the foundations of their theories, principles such as to admit of a wide and coherent development; while those whom devotion to abstract discussions has rendered unobservant of the facts are too ready to dogmatize on the basis of a few observations.

We really have only "a few observations" of Mars, too few to answer many of the most basic questions about the planet. What is needed now is further exploration: a comprehensive set of spacecraft missions to perform global mapping, to deploy networks of surface stations, to move about the planet's surface, and to bring samples of Martian materials back to Earth for analysis. These missions are within our technological reach; all that is needed is the will to carry them out. Only if they are flown can we ever hope really to understand Mars and the ways in which it may be unlike or like our own planet.

ACKNOWLEDGMENTS

It is a pleasure to thank a number of colleagues with whom I have worked on problems concerning Mars, including Larry Evans, Chris McKay, Don Wilhelms, Sue Nedell, Gary Clow, Bob Wharton, Dave Andersen, and, especially, Mike Carr. Most of the work described here arose out of those collaborations, and this paper owes a great deal to the contributions of those individuals. I am also grateful to Steve Clifford and Fraser Fanale for numerous thought-provoking discussions on the Martian ground ice problem and to Jim Zimbelman for a careful review of part of the paper. The recent work on aqueous sedimentation early in Martian history was done with Jules Goldspiel, and the finite-element modeling of viscous relaxation on Mars was done with Paul Thomas and Dave Jankowski. Jack Trombka taught me most of what I know and much that I have already forgotten about the arcana of gamma-ray spectroscopy. Finally, I owe special thanks to Joe Veverka and Ray Reynolds for years of instruction, encouragement, and patience. This work was supported by the NASA Planetary Geology and Geophysics Program.

REFERENCES

ANDERSLAND, O. B., AND W. AKILI 1967. Stress effect on creep rates of a frozen clay soil. *Geotechnique* **17,** 27–39.

BAKER, V. R., AND R. C. KOCHEL 1979. Martian channel morphology: Maja and Kasei Valles. *J. Geophys. Res.* **84,** 7985–7993.

BAKER, V. R., AND D. MILTON 1974. Erosion by catastrophic floods on Mars and Earth. *Icarus* **23,** 27–41.

BIELEFIELD, M. J., R. C. REEDY, A. E. METZGER, J. I. TROMBKA, AND J. R. ARNOLD 1976. Surface chemistry of selected lunar regions. *Proc. Lunar Sci. Conf. 7th,* 2661–2676.

BIEMANN, K., J. ORÓ, P. TOULMIN III, L. E. ORGEL, A. O. NIER, D. M. ANDERSON, P. G. SIMMONDS, D. FLORY, A. V. DIAZ, D. R. RUSHNECK, J. E. BILLER, AND A. L. LAFLEUR 1977. The search for organic substances and inorganic volatile compounds in the surface of Mars. *J. Geophys. Res.* **82,** 4641–4658.

BRUTSAERT, W. 1975. A theory for local evaporation (or heat transfer) from rough and smooth surfaces at ground level. *Water Resour. Res.* **11,** 543–550.

BRUTSAERT, W. 1982. *Evaporation into the Atmosphere*. Reidel, Dordrecht.

CARR, M. H. 1979. Formation of Martian flood features by release of water from confined aquifers. *J. Geophys. Res.* **84,** 2995–3007.

CARR, M. H. 1981. *The Surface of Mars*. Yale Univ. Press, New Haven, CT.

CARR, M. H. 1983. Stability of streams and lakes on Mars. *Icarus* **56,** 476–495.

CARR, M. H. 1986. Mars: A water-rich planet? *Icarus* **68,** 187–216.

CARR, M. H., AND G. D. CLOW 1981. Martian channels and valleys: Their characteristics, distribution, and age. *Icarus* **48,** 91–117.

CARR, M. H., L. S. CRUMPLER, J. A. CUTTS, R. GREELEY, J. E. GUEST, AND H. MASURSKY 1977. Martian impact craters and emplacement of ejecta by surface flow. *J. Geophys. Res.* **82,** 4055–4065.

CARR, M. H., AND G. G. SCHABER 1977. Martian permafrost features. *J. Geophys. Res.* **82,** 4039–4054.

CHYBA, C. F., S. W. SQUYRES, AND C. SAGAN 1988. Oxidant diffusion in the Martian regolith (Abst.). *Bull. Amer. Astron. Soc.*, in press.

CLARK, B. C., A. K. BAIRD, R. J. WELDON, D. M. TSUSAKI, L. SCHNABEL, AND M. P. CANELARIA 1982. Chemical composition of Martian fines. *J. Geophys. Res.* **87,** 10,059–10,067.

CLIFFORD, S. M., AND D. HILLEL 1983. The stability of ground ice in the equatorial region of Mars. *J. Geophys. Res.* **88,** 2456–2474.

CLOW, G. D., C. P. MCKAY, G. M. SIMMONS, JR., AND R. A. WHARTON, JR. 1988. Climatological observations and predicted sublimation rates at Lake Hoare, Antarctica. *J. Climate* **1,** 715–728.

DAWSON, P. R., AND E. G. THOMPSON 1978. Finite element analysis of steady-state elasto-visco-plastic flow by the initial stress-rate method. *Int. J. Num. Meth. Eng.* **8,** 3–16.

DRAKE, D. M., W. C. FELDMAN, AND B. JAKOSKY 1988. Martian neutron leakage spectra. *J. Geophys. Res.* **93,** 6353–6368.

DURHAM, W. B., H. C. HEARD, AND S. H. KIRBY 1983. Experimental deformation of polycrystalline H_2O at high pressure and low temperature: Preliminary results. *J. Geophys. Res.* **88,** 377–392.

ENGLE, W. W. 1967. *ANISN, Multigroup One-Dimensional Discrete Ordinates Transport Code with Anisotropic Scattering*, ORNL Rep. K-1693. Oak Ridge Nat. Lab., Oak Ridge, TN.

ERSOY, T., AND E. TOGROL 1978. Temperature and strain rate effects on the strength of compacted frozen silty-clay. In *Third International Conference on Permafrost*, pp. 643–647.

EVANS, L. G., AND S. W. SQUYRES 1987. Investigation of Martian H_2O and CO_2 via orbital gamma-ray spectroscopy. *J. Geophys. Res.* **92,** 9153–9167.

EVANS, L. G., J. I. TROMBKA, AND W. V. BOYNTON 1986. Elemental analysis of a comet nucleus by passive gamma ray spectrometry from a penetrator. *J. Geophys. Res. Suppl.* **91,** D525–D532.

FANALE, F. P. 1976. Martian volatiles: Their degassing history and geochemical fate. *Icarus* **28,** 179–202.

FANALE, F. P., J. R. SALVAIL, W. B. BANERDT, AND R. S. SAUNDERS 1982. Mars: The regolith–atmosphere–cap system and climate change. *Icarus* **50,** 381–407.

FANALE, F. P., J. R. SALVAIL, A. P. ZENT, AND S. E. POSTAWKO 1986. Global distribution and migration of subsurface ice on Mars. *Icarus* **67,** 1–18.

FARMER, C. B., AND P. E. DOMS 1979. Global seasonal variation of water vapor on Mars and the implications for permafrost. *J. Geophys. Res.* **84,** 2881–2888.

GAULT, D. E., AND R. GREELEY 1978. Exploratory experiments of impact craters formed in viscous-liquid targets: Analogs for Martian rampart craters? *Icarus* **34,** 486–495.

GOUGHNOUR, R. R., AND O. B. ANDERSLAND 1968. Mechanical properties of a sand–ice system. *J. Soil Mech. Found. Div. (ASCE)* **94,** 923–950.

HAINES, E. L., AND A. E. METZGER 1984. Measuring planetary hydrogen by remote gamma-ray sensing. *Nucl. Instrum. Methods* **226,** 509–516.

HARRINGTON, T. M., J. H. MARSHALL, J. R. ARNOLD, L. E. PETERSON, J. I. TROMBKA, AND A. E. METZGER 1974. The Apollo gamma-ray spectrometer. *Nucl. Instrum. Methods* **118,** 401–411.

HAYNES, D. F. 1978. Strength and deformation of frozen silt. In *Third International Conference on Permafrost*, pp. 656–661.

HELFENSTEIN, P. 1980. Martian fractured terrain: Possible sequences of ice-heaving. In *Reports of Planetary Geology Program*, NASA-TM 82385, pp. 373–374.

HOFFMAN, J. H., R. R. HODGES, T. M. DONAHUE, AND M. B. MCELROY 1980. Composition of the Venus lower atmosphere from the Pioneer Venus mass spectrometer. *J. Geophys. Res.* **85,** 7882–7890.

HORNER, V. M., AND N. G. BARLOW 1988. Martian craters: Changes in the diameter range for ejecta fluidization with latitude (Abst.). *Lunar Planet. Sci. XIX*, 505–506.

ISTOMIN, V. G., AND R. V. GRECHNEV 1976. Argon in the Martian atmosphere: Evidence from the Mars 6 descent module. *Icarus* **28,** 155–158.

IVES, R. L. 1940. Rock glaciers in the Colorado Front Range. *Bull. Geol. Soc. Amer.* **51,** 1271–1294.

JANKOWSKI, D. G., AND S. W. SQUYRES 1988. Solid-state ice volcanism on the satellites of Uranus. *Science* **241,** 1322–1325.

JOHANSEN 1979. The latitude dependence of Martian splosh cratering and its relationship to water. In *Reports of Planetary Geology Program 1978–1979*, NASA TM-80339, pp. 123–125.

KARGEL, J. S. 1986. Morphologic variations of Martian rampart crater ejecta and their dependencies and implications (Abst.). *Lunar Planet. Sci. XVII*, 410–411.

KIEFFER, H. S., S. C. CHASE, JR., E. MINER, G. MUNCH, AND G. NEUGEBAUER 1973. Preliminary report on infrared radiometric measurements from the Mariner 9 spacecraft. *J. Geophys. Res.* **78,** 4291–4312.

KIRBY, S. H., W. B. DURHAM, M. L. BEEMAN, H. C. HEARD, AND M. A. DALEY 1987. Inelastic processes of ice I_h at low temperatures and high pressures. *J. Phys.* **48,** C1-227–C1-232.

KIRBY, S. H., W. B. DURHAM, AND H. C. HEARD 1985. Rheologies of H_2O ices I_h, II and III at high pressures: A progress report, in *Ices in the Solar System* (J. Klinger and D. Benest, Eds.). Reidel, Dordrecht.

KORNBLUM, J. J., E. L. FIREMAN, M. LEVINE, AND A. ARONSON 1974. Neutrons in the Moon. *Proc. Lunar Sci. Conf. 4th,* 2171–2182.

KOVACH, R. L., AND J. S. WATKINS 1973. The structure of the lunar crust at the Apollo 17 site. *Proc. Lunar Planet. Sci. Conf. 4th,* 2549–2560.

KUZMIN, R. O., N. N. BOBINA, E. V. ZABALUEVA, AND V. P. SHASHKINA 1988. The structure of the Martian cryolithosphere upper levels. In *Workshop on Mars Sample Return Science,* LPI Technical Report 88-07, p. 108.

LADANYI, B. 1972. An engineering theory of creep of frozen soils. *Canad. Geotech. J.* **9,** 63–80.

LADANYI, B., AND J. PAQUIN 1978. Creep behavior of frozen sand under a deep circular load. In *Third International Conference on Permafrost,* pp. 680–686.

LAPIDES, J. R., M. S. SPERGEL, O. W. LAZARETH, P. W. LEVY, R. C. REEDY, AND J. I. TROMBKA 1980. The effects of hydrogen on gamma-ray emission from planetary surfaces. *Lunar Planet. Sci. XI,* 605–607.

LINGENFELTER, R. E., E. H. CANFIELD, AND V. E. HAMPEL 1972. The lunar neutron flux revisited. *Earth Planet. Sci. Lett.* **15,** 355–369.

LUCCHITTA, B. K. 1979. Landslides in Valles Marineris, Mars. *J. Geophys. Res.* **84,** 8097–8113.

LUCCHITTA, B. K. 1981. Valles Marineris—Faults, volcanic rocks, channels, basin beds. In *Reports of Planetary Geology Program,* NASA-TM 84211, pp. 419–421.

LUCCHITTA, B. K. 1982. Lakes or playas in Valles Marineris. In *Reports of Planetary Geology Program,* NASA-TM 85127, pp. 233–234.

LUCCHITTA, B. K., AND H. M. FERGUSON 1983. Chryse basin channels: Low gradients and ponded flows. *J. Geophys. Res.* **88,** 553–568.

MALIN, M. C. 1976. *Nature and Origin of Intercrater Plains on Mars.* Ph.D. thesis, California Institute of Technology, Pasadena.

MASURSKY, H. 1973. An overview of geological results from Mariner 9. *J. Geophys. Res.* **78,** 4009–4030.

MCCAULEY, J. F. 1978. *Geologic Map of the Copreates Quadrangle of Mars.* U.S. Geol. Survey Misc. Inv. Series Map I-897, scale 1 : 5,000,000.

MCCAULEY, J. F., M. H. CARR, J. A. CUTTS, W. K. HARTMANN, H. MASURSKY, D. J. MILTON, R. P. SHARP, AND D. E. WILHELMS 1972. Preliminary Mariner 9 report on the geology of Mars. *Icarus* **17,** 289–327.

MCELROY, M. B., T. Y. KONG, AND Y. L. YUNG 1977. Photochemistry and evolution of Mars' atmosphere: A Viking perspective. *J. Geophys. Res.* **82,** 4379–4388.

MCELROY, M. B., Y. L. YUNG, AND A. O. NIER 1976. Isotopic composition of nitrogen: Implications for the past history of Mars' atmosphere. *Science* **194,** 70–72.

MCKAY, C. P. 1986. Exobiology and future Mars mission: The search for Mars' earliest biosphere. *Adv. Space Res.* **6,** 269–285.

MCKAY, C. P., G. D. CLOW, R. A. WHARTON, JR., AND S. W. SQUYRES 1985. Thickness of ice on perennially frozen lakes. *Nature (London)* **313,** 561–562.

METZGER, A. E., J. I. TROMBKA, L. E. PETERSON, R. C. REEDY, AND J. R. ARNOLD 1973. Lunar surface radioactivity: Preliminary results of the Apollo 15 and 16 gamma-ray spectrometer experiments. *Science* **179,** 800–803.

METZGER, A. E., J. I. TROMBKA, R. C. REEDY, AND J. R. ARNOLD 1974. Element concentrations from lunar orbital gamma-ray measurements. *Proc. Lunar Sci. Conf. 5th,* 1067–1078.

MILTON, D. J. 1973. Water and process of degradation in the Martian landscape. *J. Geophys. Res.* **78,** 4037–4047.

MOUGINIS-MARK, P. J. 1979. Martian fluidized crater morphology: Variations with crater size, latitude, altitude, and target material. *J. Geophys. Res.* **84,** 8011–8022.

MOUGINIS-MARK, P. J. 1981. Ejecta emplacement and modes of formation of Martian fluidized ejecta craters. *Icarus* **45,** 60–76.

MOUGINIS-MARK, P. J. 1987. Water or ice in the Martian regolith?: Clues from rampart craters seen at very high resolution. *Icarus* **71,** 268–286.

MURRAY, B. C., W. R. WARD, AND S. C. YEUNG 1973. Periodic insolation variations on Mars. *Science* **180,** 638–640.

NEDELL, S. S., S. W. SQUYRES, AND D. W. ANDERSEN 1987a. Origin and evolution of the layered deposits in the Valles Marineris, Mars. *Icarus* **70,** 409–441.

NEDELL, S. S., D. W. ANDERSEN, S. W. SQUYRES, AND F. G. LOVE 1987b. Sedimentation in ice-covered Lake Hoare, Antarctica. *Sedimentology* **34,** 1093–1106.

Owen, T., and K. Biemann 1976. Composition of the atmosphere at the surface of Mars: Detection of Argon-36 and preliminary analyses. *Science* **193,** 801–803.

Owen, T., K. Biemann, D. R. Rushneck, J. E. Biller, D. W. Howarth, and A. L. Lafleur 1977. The composition of the atmosphere at the surface of Mars. *J. Geophys. Res.* **82,** 4635–4639.

Passey, Q. R. 1983. Viscosity of the lithosphere of Enceladus. *Icarus* **53,** 105–120.

Passey, Q. R., and E. M. Shoemaker 1982. Craters and basins on Ganymede and Callisto: Morphological indicators of crustal evolution. In *Satellites of Jupiter* (D. Morrison, Ed.), pp. 379–434. Univ. of Arizona Press, Tucson.

Pechmann, J. C. 1980. The origin of polygonal troughs on the northern plains of Mars. *Icarus* **42,** 185–210.

Phukan, A. 1983. Long-term creep deformation of roadway embankment on ice-rich permafrost. In *Permafrost—Fourth International Conference Proceedings,* pp. 994–999.

Peterson, C. P. 1981. A secondary origin for the central plateau of Hebes Chasma. *Proc. Lunar Planet. Sci. Conf. 12th,* 1459–1471.

Pieri, D. C. 1976. Martian channels: Distribution of small channels on the Martian surface. *Icarus* **27,** 25–50.

Pieri, D. C. 1980. Martian valleys: Morphology, distribution, age, and origin. *Science* **210,** 895–897.

Pollack, J. B., and D. C. Black 1979. Implications of the gas compositional measurements of Pioneer Venus for the origin of planetary atmospheres. *Science* **205,** 56–59.

Pollack, J. B., J. F. Kasting, S. M. Richardson, and K. Poliakoff 1987. The case for a wet, warm climate on early Mars. *Icarus* **71,** 203–224.

Sadovsky, A. V., and G. I. Bondarenko 1983. Creep of frozen soils on rock slopes. In *Permafrost—Fourth International Conference Proceedings,* pp. 1101–1104.

Sayles, F. 1973. Triaxial and creep tests on frozen Ottawa sand. In *North American Contribution—Permafrost—Second International Conference*, pp. 384–391.

Schultz, P. H. 1986. Crater ejecta morphology and the presence of water on Mars (Abst.). In *Symposium on Mars: Evolution of Its Climate and Atmosphere,* LPI Contrib. No. 599, pp. 95–97.

Schultz, P. H., and D. E. Gault 1979. Atmospheric effects on Martian ejecta emplacement. *J. Geophys. Res.* **84,** 7669–7687.

Sharp, R. P. 1973a. Mars: Troughed terrain. *J. Geophys. Res.* **78,** 4063–4072.

Sharp, R. P. 1973b. Mars: Fretted and chaotic terrains. *J. Geophys. Res.* **78,** 4074–4083.

Sharp, R. P., and M. C. Malin 1975. Channels on Mars. *Geol. Soc. Amer. Bull.* **86,** 593–609.

Shoji, H., and A. Higashi 1978. A deformation mechanism map of ice. *J. Glaciol.* **21,** 419–427.

Smoluchowski, R. 1968. Mars: Retention of ice. *Science* **159,** 1348–1350.

Squyres, S. W. 1978. Martian fretted terrain: Flow of erosional debris. *Icarus* **34,** 600–613.

Squyres, S. W. 1979. The distribution of lobate debris aprons and similar flows on Mars. *J. Geophys. Res.* **84,** 8087–8096.

Squyres, S. W. 1981. The topography of Ganymede's grooved terrain. *Icarus* **46,** 156–168.

Squyres, S. W., D. W. Andersen, S. S. Nedell, and R. A. Wharton, Jr. 1989. Lake Hoare, Antarctica: Sedimentation through a thick perennial ice cover. Submitted. *Sedimentology.*

Squyres, S. W., and M. H. Carr 1986. Geomorphic evidence for the distribution of ground ice on Mars. *Science* **231,** 249–252.

Thomas, D. G. 1965. Transport characteristics of suspensions. VIII. A note on the viscosity of Newtonian suspensions of uniform spherical particles. *J. Colloid. Sci.* **20,** 267–277.

Thomas, P. J., and G. Schubert 1986. Crater relaxation as a probe of Europa's interior. *J. Geophys. Res.* **91,** 453–459.

Thomas, P. J., and G. Schubert 1988. The power-law rheology of ice and the retention of craters on Ganymede. *J. Geophys. Res.* **93,** 13755–13762.

Thomas, P. J., and S. W. Squyres 1988. Relaxation of impact basins on icy satellites. *J. Geophys. Res.* **93,** 14919–14932.

Thompson, E. G. 1975. Average and complete incompressibility in the finite element method. *Int. J. Num. Meth. Eng.* **9,** 925–932.

Thompson, E. G., and M. I. Haque 1973. A high order finite element for completely incompressible creeping flow. *Int. J. Num. Meth.* **6,** 315–321.

Thompson, E. G., R. M. Lawrence, and F.-S. Lin 1969. Finite element method for incompressible slow viscous flow with a free surface. *Dev. Mech.* **5,** 93–111.

Thompson, E. G., and F. H. Sayles 1972. In situ creep analysis of room in frozen soil. *J. Soil Mech. Found. Div. (ASCE)* **98,** 899–915.

Thompson, W. F. 1962. Preliminary notes on the nature and distribution of rock glaciers relative to true glaciers and other effects of the climate on the ground in North America. In *Symposium at Obergurgl,* pp. 212–219. Internat. Assoc. Scientific Hydrology Publ. No. 58, Obergurgl, Austria.

Toksöz, M. N., A. M. Dainty, S. C. Solomon, and K. R. Anderson 1973. Velocity structure and evolution of the Moon. *Proc. Lunar Planet. Sci. Conf. 4th,* 2529–2547.

Vyalov, S. S. 1978. Kinetic theory of deformation of frozen soils. In *Third International Conference on Permafrost,* pp. 751–755.

WAHRHAFTIG, C., AND A. COX 1959. Rock glaciers in the Alaska Range. *Bull. Geol. Soc. Amer.* **70,** 383–436.

WALLACE, D., AND C. SAGAN 1979. Evaporation of ice in planetary atmospheres: Ice-covered rivers on Mars. *Icarus* **39,** 385–400.

WARD, W. R. 1973. Large-scale variations in the obliquity of Mars. *Science* **181,** 260–262.

WARD, W. R. 1974. Climatic variations on Mars. I. Astronomical theory of insolation. *J. Geophys. Res.* **79,** 3375–3386.

WEERDENBERG, P. C., AND N. R. MORGENSTERN 1983. Underground cavities in ice-rich frozen ground. In *Permafrost—Fourth International Conference Proceedings,* pp. 1384–1389.

WHARTON, R. A., JR., C. P. MCKAY, G. M. SIMMONS, JR., AND B. C. PARKER 1986. Oxygen budget of a perennially ice-covered antarctic lake. *Limnol. Oceanogr.* **31,** 437–443.

WHITE, S. E. 1971. Rock glacier studies in the Colorado Front Range, 1961 to 1968. *Arctic Alpine Res.* **3,** 43–64.

WHITE, S. E. 1976. Rock glaciers and block fields, review and new data. *Quat. Res.* **6,** 77–97.

ZARETSKIY, Y. K., AND A. G. SHCHOBOLEV 1983. A mathematical model for the viscoplastic deformation of frozen soils. In *Permafrost—Fourth International Conference Proceedings,* pp. 1457–1462.

ZHU, Y., AND D. L. CARBEE 1983. Creep behavior of frozen silt under constant uniaxial stress. In *Permafrost—Fourth International Conference Proceedings,* pp. 1507–1512.

ZIMBELMAN, J. R. 1987. Spatial resolution and the geologic intrepretation of Martian morphology: Implications for subsurface volatiles. *Icarus* **71,** 257–267.

ZIMBELMAN, J. R., S. M. CLIFFORD, AND S. H. WILLIAMS 1988. Concentric crater fill on Mars: An aeolian alternative to ice-rich mass wasting. *Proc. Lunar Planet. Sci. Conf. 19th,* in press.

ICARUS **79**, 289–310 (1989)

Radar Altimetry of Large Martian Craters

L. E. ROTH AND R. S. SAUNDERS

Jet Propulsion Laboratory, California Institute of Technology, Pasadena, California 91109

G. S. DOWNS

Lincoln Laboratory, Massachusetts Institute of Technology, Lexington, Massachusetts 02173

AND

G. SCHUBERT

Department of Earth and Space Sciences, University of California, Los Angeles, California 90024

Received August 10, 1987; revised November 4, 1988

Mars topography in the 23 to −22° latitude band has been measured by the Goldstone λ13-cm radar during the 1971–1982 oppositions. A total of 108 scans were produced. Each scan spans several tens of degrees in longitude. The longest scan spans 133° (~8000 km). The vertical resolution generally is better than 200 m. With some exceptions, the areal resolution is 0.16° (~8 km) in longitude and 1.30° (~80 km) in latitude. On regional scales, elevation differences of as much as 3 km over less than 10° longitude have been observed (Aeolis, Memnonia). Most local relief is provided by structural elements of impact craters. One hundred fifty-two complex, degraded craters, some as small as 25 km in diameter, have been identified in this data set. Repeated scans of the same craters yield nearly identical elevation profiles. Measured crater depths rarely exceed 2.5 km. Depths of the most degraded craters in the sample are a weak function of crater diameter. Depths of the largest craters ($D > 125$ km) show no functional relationship to diameters. Measured rim heights rarely exceed several hundred meters. Structures with no discernible rim (e.g., Ladon) have retained a basin shape. Low exterior relief rather than overall low relief seems to be the distinguishing characteristic of large, degraded craters included in the Goldstone sample. Craters or basins that serve as sinks for major channel systems (e.g., Gusev, Ladon) appear to be as deep as comparable structures not associated with such systems, suggesting that processes other than fluvial sedimentation contributed to crater shallowing. © 1989 Academic Press, Inc.

I. INTRODUCTION

Mars has been the target of observations by the Goldstone λ13-cm radar since the early sixties. The experiments resulted in the acquisition of topographic and scattering information for the planet's equatorial regions (Goldstein *et al.* 1970, Downs *et al.* 1971, 1973, 1975, 1978, 1982). The most extensive observations were carried out during the perihelic opposition of 1971 and the intermediate opposition of 1973 (68 scans). The program of observations was less extensive for the intermediate and aphelic oppositions of 1975 through 1982 (40 scans). No observations were conducted during the 1984 opportunity. The single range-doppler observation carried out during the opposition of 1986 has not been processed.

Goldstone data furnish evidence of detection of topographic features on Mars by observers on the Earth. The possibility that Earth-based radars might detect topographic features on Mars was first recog-

0019-1035/89 $3.00

Copyright © 1989 by Academic Press, Inc.
All rights of reproduction in any form reserved.

nized by Pettengill *et al.* (1971), working with the Haystack instrument, and by Downs *et al.* (1971), working with the Goldstone facility. Schubert *et al.* (1977) identified echoes from 12 impact craters in the Goldstone data. Malin and Dzurisin (1977), employing R. J. Terrile's results, identified echoes from 32 such objects. We have confirmed the findings of both groups of investigators and have identified, with varying degrees of confidence, echoes from 152 craters. The Goldstone Mars data are of sufficient quality to offer complete elevation profiles along lines of constant latitude for a number of prominent craters or basins on Mars. They also provide synoptic views of landscape segments at a regional scale. Under favorable circumstances the Goldstone λ13-cm radar permits morphometric analysis of craters as small as 25 km in diameter and routinely on craters of 80–100 km in diameter. In the present context, "morphometry" means quantitative determination of the morphological characteristics of impact craters (Baldwin 1963). Radar morphometry of lunar impact craters, based on bistatic data and following an objective different from the one pursued here, was carried out by Simpson *et al.* (1977). High-resolution radar interferometry of lunar craters was carried out by Zisk (1972, 1978). Elevation profiles of the equatorial topography of Mercury, analogous to the Goldstone Mars profiles, were produced by Harmon *et al.* (1986).

Here we use the Goldstone Mars radar results to reconstruct topography in some of the subequatorial quandrangles and to compile depth–diameter (d/D) curves for craters in three degradation classes. Errors associated with elevation measurements are discussed in the text and in the Appendix. The Goldstone data imply that large Martian craters are rarely deeper than about 2.5 km, regardless of the crater size. The unexpected variety of the profiles of large craters or basins indicates either a considerable spatial and temporal nonuniformity in the action of the surface-modification processes on Mars throughout much of its history or the presence of large-scale lateral crustal nonuniformities, or both.

The following conventions are observed here: An arc of constant latitude on the planet, traversed by the subradar point during one ranging session, is referred to as the radar scan. Individual scans are identified by the nominal Martian latitude, date, and the Earth–Mars distance. The latitudes and distances were derived from the Jet Propulsion Laboratory Ephemeris DE-118. The triaxial ellipsoid of Standish (1973) serves as the elevation reference surface for the 1971–1973 data. The 1975–1982 elevations were reduced relative to the 6.1-mbar datum. Craters are identified by longitude and latitude of their center and by the rim-crest diameter D (km). The coordinates and the diameters were estimated from the Mars 1:5M charts (Batson *et al.* 1979).

II. RADAR DATA

We review here information pertinent to radar altimetry of large Martian craters. For further details refer to Downs *et al.* (1973, 1975) and to Roth *et al.* (1980).

Location of the subradar point on Mars is dictated by the circumsolar orbital positions of Mars and Earth, by the inclinations of their respective spin axes, and by the spin-rates of Earth and Mars. Over one 15-year cycle of oppositions a discontinuous distribution of latitudes within the band from ~−25° to ~25° is visible to Earth-based radar. This band constitutes slightly over 40% of the total surface area of the planet. Subradar tracks lie in areas close to the northern boundary of the radar-visible band during the aphelic oppositions and in areas close to the southern boundary during the perihelic oppositions.

A latitude band between −14° and −22°, corresponding to about 7% of the planet's surface area, was visible to radar during the 1971–1973 oppositions. About 15% of this band, i.e., about 1% of the planet's surface area, was actually scanned. The 1975–1982 coverage is spotty, scattered mostly in the northern latitudes. It represents a much smaller fraction of the planet's area. Thus, the 1971–1973 Goldstone data, despite their limited coverage, constitute the most comprehensive radar altimetry of Mars currently available.

The range (i.e., the distance to the target) component of the radar echo provides, after the requisite processing (Pettengill *et al.* 1969, Downs *et al.* 1973, 1975), an elevation measurement for a point, or a patch of the ground, located somewhere within the resolution cell. The average uncertainty in the determination of the echo delay in the Goldstone Mars data is less than 100 m (Downs *et al.* 1975). This uncertainty governs the precision of the data. Global accuracy depends on the accuracy of the planetary ephemeris and on the choice of the reference figure. Uncertainty in the planetary ephemeris in the 1971–1973 data is 1800 m peak-to-peak over 180° long (Downs *et al.* 1975). The data acquired at the subsequent apparitions have a lower ephemeris uncertainty. Neither this uncertainty nor the choice of datum is expected to affect the relative elevations at the scales we are concerned with here. The size of the resolution cell in the 1971, 1973, 1978, 1980, and 1982 data is 0.16° (~8 km) in longitude (or 1/2250 of the planet's circumference) and about 1.30° (~80 km) in latitude. The resolution cell in the 1975 data is 0.50° (~30 km) in longitude and about 2° (~110 km) in latitude.

Additional uncertainties in the data affect local altimetric accuracy. First, there is an uncertainty that originates with the ranging algorithm. The algorithm selects the peak in the echo power to represent the point closest to the Earth. In this manner, high elevations within the footprint are favored over the low ones. On the other hand, a situation can be visualized when the high-lying segments of a resolution cell, rough at scales comparable to, or smaller than, the radar wavelength, would scatter the reflected power to the point of becoming undetectable. In such a case, the ranging algorithm would select as the highest segment of the resolution cell that segment which returns the strongest echo. This segment may not represent the highest point in the cell or it may be located off the subradar track (cf. Figs. 18, 19, and 20 in Roth *et al.* 1980; also cf. Harmon *et al.* 1986). For this reason we refer to the ephemeris latitude of a scan as the nominal latitude. In a related context, and with reference to the results of Dyce *et al.* (1967), Pettengill *et al.* (1969) noted that "if the Martian surface were not uniformly rough, a locally rough region appearing at the subradar point could remove the specular echo contribution with no associated compensation from smooth areas lying outside that region." In a similar manner, "anomalously high returns could be created by the inverse situation." Thus the radar-estimated elevation of the positive relief should always be considered a minimum elevation and the radar-estimated elevation of the negative relief a minimum depth. In other words, radar yields a lower bound on positive or negative relief. A second source of uncertainty, the "range bias," is discussed in the Appendix. The bias is associated with nonuniform roughness of the reflecting surface and with contributions to the echo from nonnormal angles of incidence.

The complex interaction between the radar pulse and the planet's surface also means that the depths of craters smaller than the length of the resolution cell or of craters located off the nominal subradar track can be estimated. In those cases the strongest return comes from the low-lying, apparently smooth floor, rather than from the elevated, rough rim. We stress that the radar-derived interior/exterior relief of concave/convex landforms has to be viewed as the minimum estimated relief.

III. TOPOGRAPHY OF THE CRATERED TERRAIN

At the scale of Goldstone resolution, the general character of the highlands topography tends to be bland. In the 1971–1973 data, no elevation difference is detectable along the line of contact between the highlands and the plains. Thus, in the latitude interval from −14 to −22° the two physiographic provinces do not appear to be separated by a detectable topographic discontinuity. Radar topography generally does not distinguish between the coarse geological subdivisions, e.g., between units Hprg (ridged plains), Nplc (cratered plateau materials), and Nhc (hilly and cratered materials) of Scott and Carr (1978). Exceptions might exist at smaller scales (cf. Schaber 1977). Systematic elevation differences are associated with the variable-albedo features within craters and perhaps with some topographic lows. On a regional scale, albedo and elevation appear to be unrelated, in agreement with earlier observations (Pettengill *et al.* 1969).

Among the continuous elevation profiles of large craters or basins, produced by the Goldstone radar, the profile of Ladon basin (Figs. 1 and 2) is of particular interest. The basin was detected, but not recognized, by the Mariner 6 IRS (Herr *et al.* 1970) and Viking IRTM (Kieffer *et al.* 1977) experiments. It was tentatively recognized in the Mariner 9 images (Saunders 1979) and confirmed in the Goldstone data (Figs. 3 and 4). Positive-relief protrusions (unit m in Saunders 1979) that are best discernible in the northwest quadrant of the basin plan delineate a roughly circular, 475-km-diameter (inner) ring of a (possibly) multiring structure, with the outermost ring 1200 km in diameter (Schultz and Glicken 1979, Schultz *et al.* 1982). Besides the isolated mounds mapped by Saunders (1979), the basin has no discernible rim. The radial pattern of a drainage system that probably discharged into the basin hints at the existence

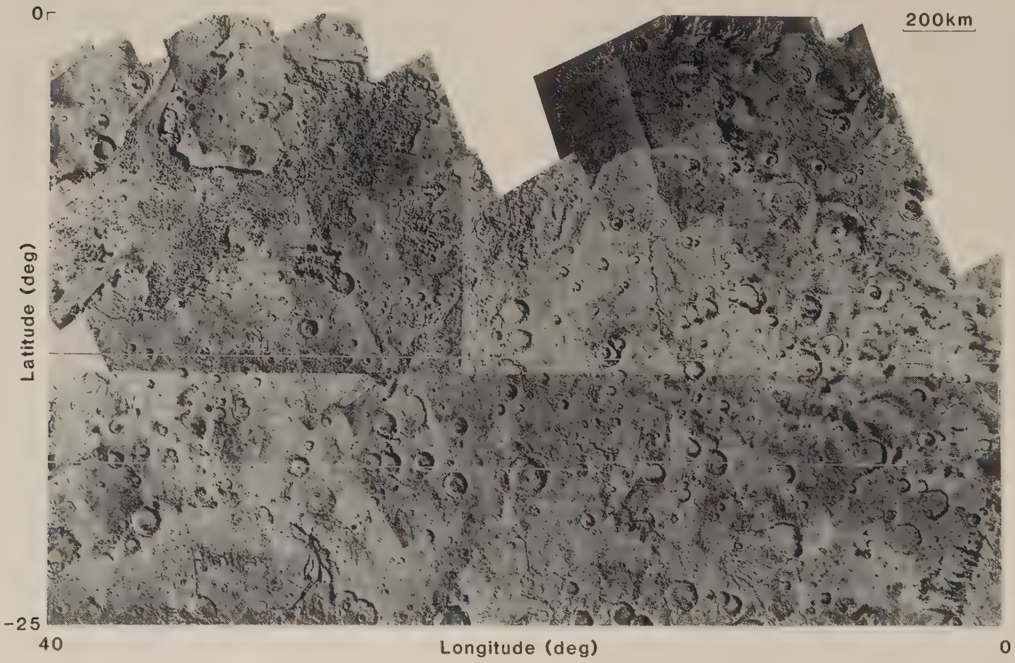

FIG. 1. Composite photomosaic of the Margaritifer Sinus quadrangle (MC-19). A highly degraded, probable impact basin extending between approx. −14° and −22° lat and between approx. 25° and 33° long has been designated Ladon (Schultz and Glicken 1979). Reconstruction of the topography enclosed in the box is presented in Fig. 2. Assignment of coordinates and scales in all photo frames and the uncontrolled photomosaics is approximate. (Viking Medium Resolution Photomosaics: (MC-19) NW, NE, SW, SE; USGS, Flagstaff.)

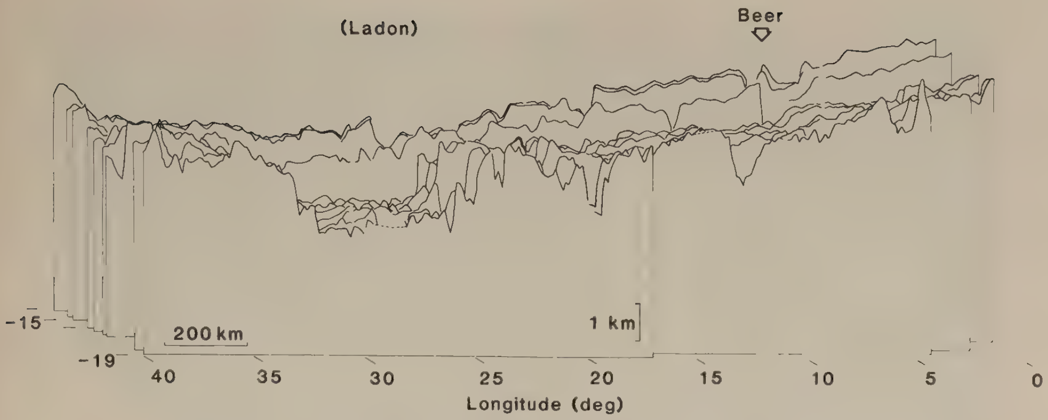

FIG. 2. Reconstruction of topography in the Margaritifer Sinus quadrangle. The most prominent structure visible in the panorama is the Ladon basin. Vertical exaggeration is 100×. (12 Radar scans between −14.13° and −18.97° lat.)

of a watershed extending far beyond the basin limits. Ladon Valles, the most prominent component of the system, intersects the basin from the south through a breach in the partially exposed remnants of the inner ring (?) of a hypothetical multiring basin centered in Pyrrhae Regio (Schultz and Glicken 1979), about 350 km southwest of Ladon. The presently available radar data cannot confirm the existence of the Pyrrhae basin. Considering the virtual absence of any positive relief, Ladon basin has a sur-

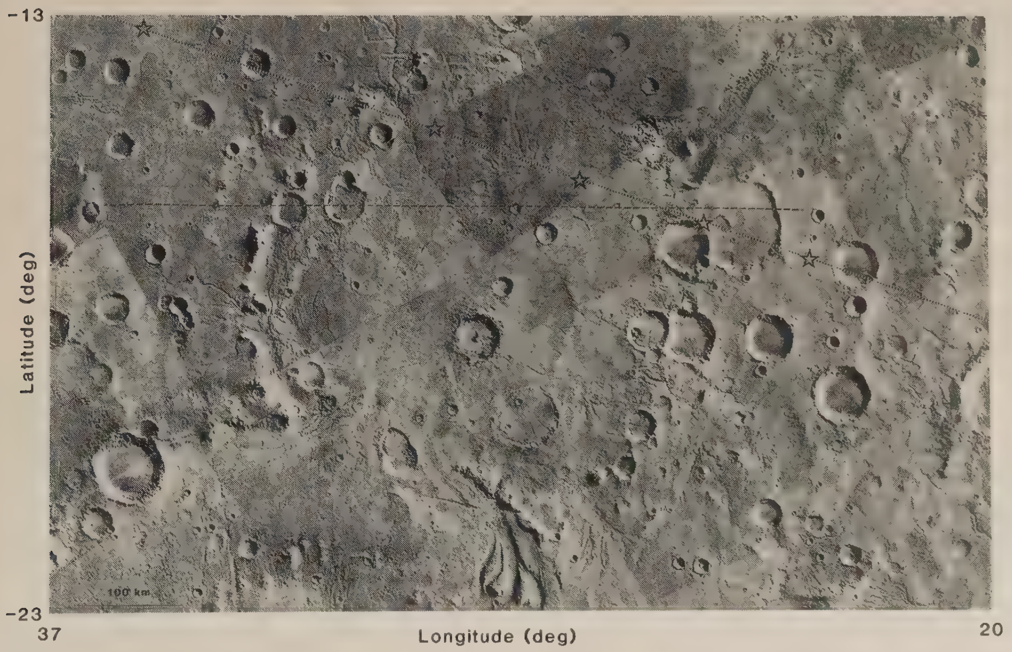

FIG. 3. Photomosaic of the Ladon basin. Diameter of the basin: ~475 km. The oblique line denotes the Mariner 6 suborbital track. Stars denote the locations over which the Mariner 6 IRS altimetry readings were taken (Herr *et al.* 1970). (Radar scan: −16.73°. VOIT photomosaic: 211-5821.)

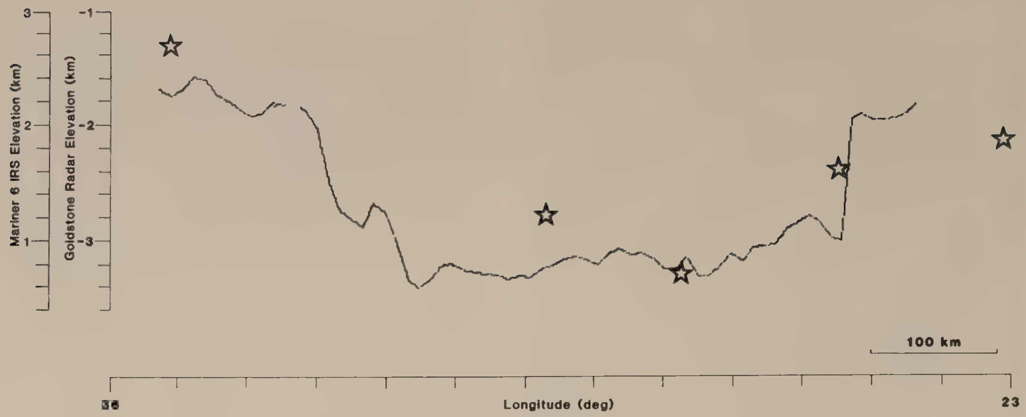

FIG. 4. Goldstone elevation profile (line) and Mariner 6 IRS elevations (stars) of basin Ladon. Mariner 6 IRS data were taken from Herr *et al.* (1970). The absolute elevation scales refer to the respective datum surfaces (cf. Herr *et al.* 1970, Standish 1973). In the Viking IRTM data (Kieffer *et al.* 1977) the presence of the basin is marked by an oval-shaped 400-km patch of positive predawn residual temperatures. In telescopic observations, the location of the basin has been identified as a site from which "possible dust clouds" originate (Hartmann 1978). Vertical exaggeration is 100×. (Radar scan: −16.73°, 12 Oct 73, 0.438 AU.)

prisingly large apparent depth. (The term "apparent depth" designates the depth below the level of the surrounding terrain, cf. Pike 1977a.) The Ladon Valles discharge appears to have entered the basin along the southwest segment of the inner wall, tangentially to the basin floor plan. The basin was scanned five times. All scans show the structure to be deepest along its southwest perimeter, the lowest point apparently being the point of contact between the basin cavity and the Ladon Valles channel entering the basin.

A relatively sharp elevation increase has been observed immediately west of crater Williams (164.0°, −18.0°, 125 km) (Figs. 5 through 7). As in the case of the radar-identified Coprates rise (Figs. 14 and 16 in Roth *et al.* 1980), the sudden elevation change may be accompanied by a north–south-trending, low-albedo trough (Fig. 5). The elevation gradient of the topographic rise west of Williams appears to be orthogonal to the same gradient in Mutch and Morris (1979). The floor of Williams (Fig. 7) tilts in concordance with the rise. The crater was scanned twice; a virtually identical floor slope was obtained on both occasions.

Crater Gusev (184.5°, −14.7°, 170 km) (Figs. 8 and 9) is the terminus of the Ma'adim Vallis channel system. Low-albedo material, visible in both the Viking Orbiter and Mariner 9 images (Fig. 8), covers the southwest half of the crater floor. The crater was scanned six times. All six scans cut across the low-albedo region and, to various degrees, all six show the crater to have an inclined floor, with the dark segment of the floor always at a higher elevation than the light segment. The two best scans (Fig. 9) suggest the floor slope to be uniform and equal to less than 0.05 km/km (~3.0°), with no observable discontinuity over the albedo boundary.

In contrast to crater Williams, the tilt of the Gusev floor appears to be associated with the tonal differences between materials that constitute the floor, rather than with the regional topographic trends. Variable-albedo, wedge-shaped floors have been reported for the Saharan craters Temimichat–Ghallaman, Tenoumer, and Aouelloul (Smith 1972). In the Saharan craters the order of the albedo effects is reversed, with the high-albedo (wind-blown sand?) floor segments at the higher eleva-

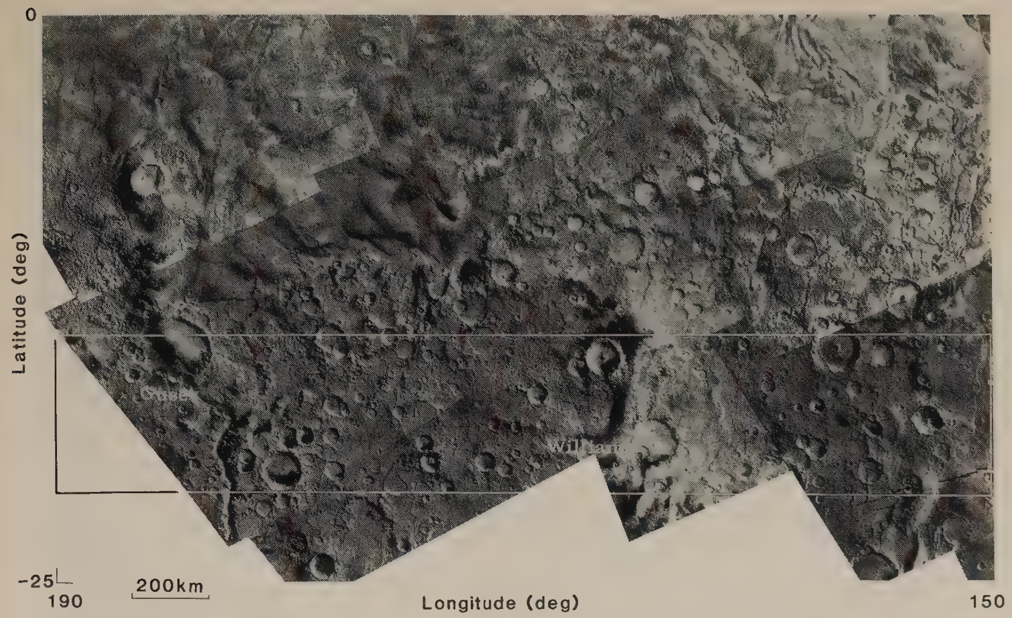

FIG. 5. Composite photomosaic of segments of the Memnonia (MC-16) and Aeolis (MC-23) quadrangles. Radar coverage ends at the northern edge of the Memnonia-Mare Sirenum fault fields (Mutch and Morris 1979). Reconstruction of the topography enclosed in the box is shown in Fig. 6. Profiles of structures named in this figure are shown in Figs. 7 and 9. (Uncontrolled, partially completed VOIT photomosaic.)

tion. In analogy to Ladon basin, the floor of Gusev appears to be tilted toward the point where a major runoff channel (the Ma'adim Vallis) is entering the crater. If this is the lowest point of the crater floor, then the dark wedge superimposed on the light background material must have evolved since the time of cessation of the Ma'adim Vallis flows. An eolian origin would imply entrapment of the material of the dark surface to a depth of about 400 m. Goldstone C-parameter data (Downs *et al.* 1975) indi-

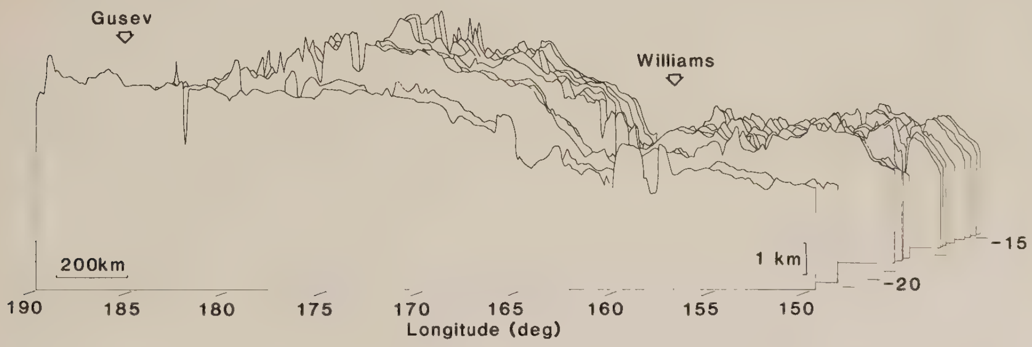

FIG. 6. Reconstruction of topography in the Memnonia and Aeolis quadrangles. The figure provides a setting for craters Williams and Gusev. The sharp negative-relief spike at 182° long represents the echo from the floor of the south–north-trending channel Ma'adim Vallis. Detection was possible because of the alignment of the channel trunk with the radar resolution cell. Vertical exaggeration is 100×. (14 Radar scans between $-14.80°$ and $-21.23°$ lat.)

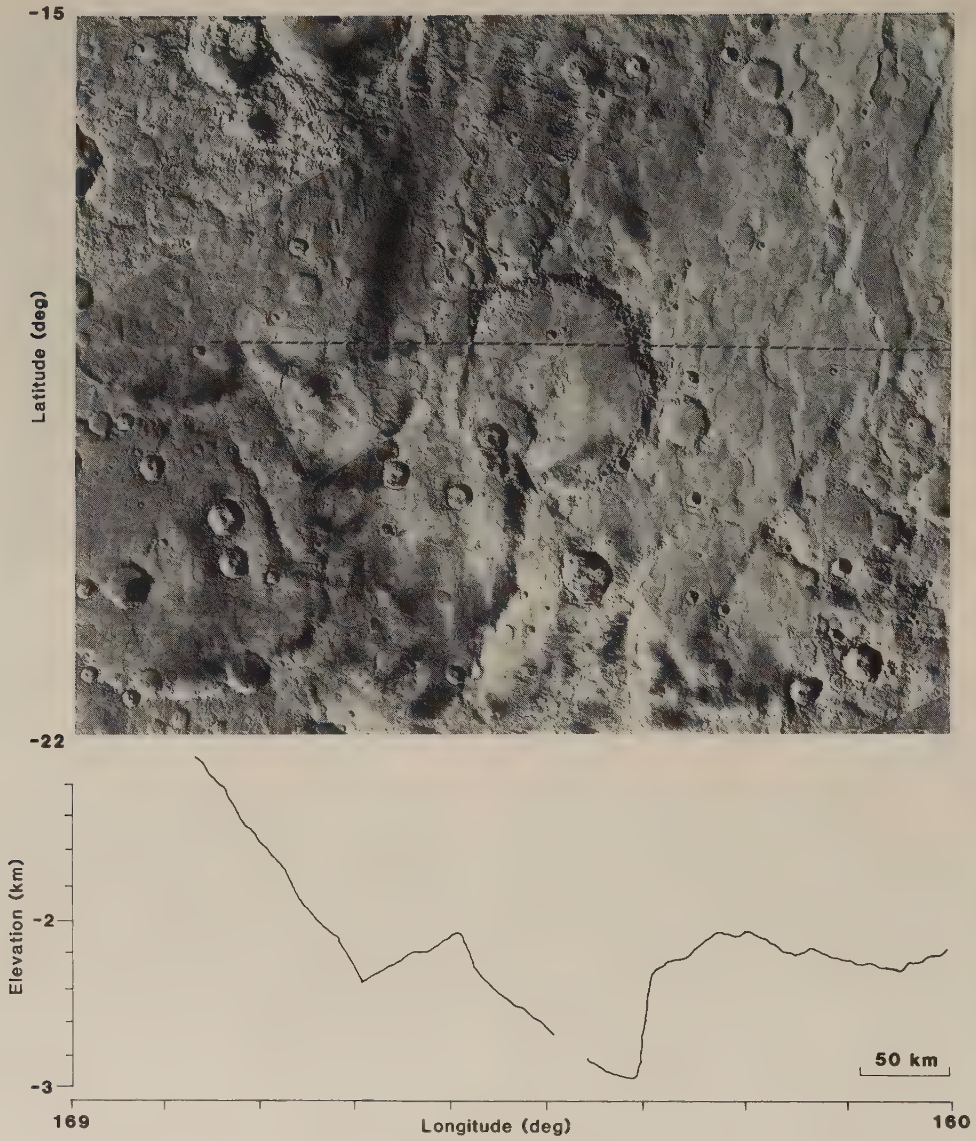

FIG. 7. Photomosaic (top) and a profile (bottom) of crater Williams (164.0°, −18.0°, 125 km). Williams belongs to the category of Martian craters with tilted floors. Vertical exaggeration is 100×. (Radar scan: −17.94°, 2 Jul 71, 0.484 AU. Viking frames: 599A25, 637A53, 55–58.)

cate the dark material to be radar-smooth and the light surface to be radar-rough. The combined elevation uncertainty due to differences in radar roughness and to possible contributions from the neighboring Doppler cells (cf. Appendix) is less than the measured elevation difference. We conclude that the difference is probably real. Albedo-associated elevation differences are perhaps also present in crater Boeddicker (197.3°, −15.0°, 110 km) (Figs. 10 and 11), scanned five times. All scans indicate the dark southwest segment of the crater floor to be about 200 m above the light northeast segment, with a gradual elevation transition between the two segments.

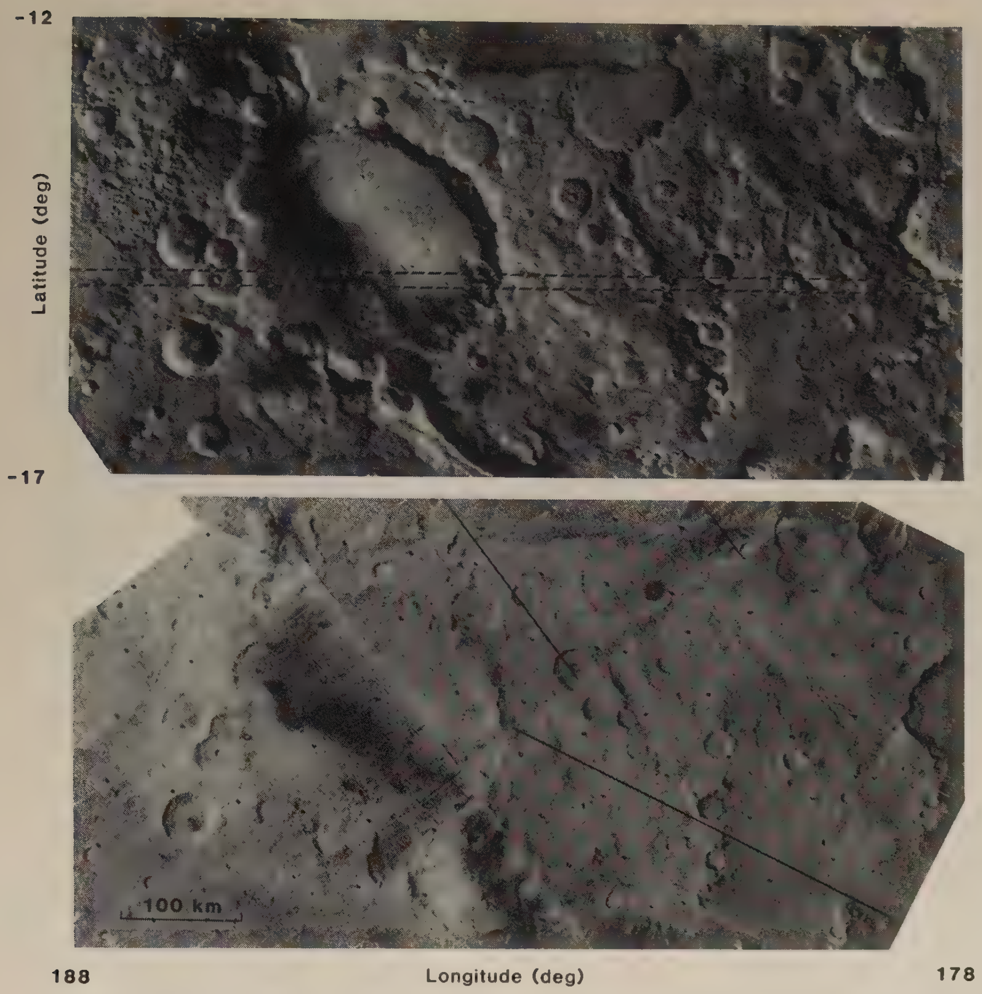

FIG. 8. Viking (top) and Mariner 9 (bottom photomosaic of crater Gusev (184.5°, −14.7°, 170 km). (Radar scans: −14.80°, −14.89°. Viking frame: 603A41. Mariner 9 frames: DAS 06606848, 06606778, 08009648, 08009718.)

The variety of elevation profiles for large craters or basins surveyed here seems to suggest that each object has its own development history (Schultz and Glicken 1979, Schultz *et al.* 1982, Stam *et al.* 1984), not necessarily shared by comparable objects in the same latitude band. Basin Ladon has retained a cavity with an apparent depth of about 2 km, despite almost complete absence of a raised rim. Thus we have a case of a major basin that has no positive relief and a considerable negative relief. Crater Denning (Figs. 12 and 13) represents a reverse case to that of Ladon and Gusev. It has a measurable rim height, but a negligible apparent depth. No significant fluvial activity appears to have been associated with the crater. Plains material perhaps responsible for the reduction in the apparent depth of Denning is probably of volcanic origin (Moore 1980). The attributes common to all the craters or basins scanned by the Goldstone radar are a variable apparent depth, absence of floor doming, and, excepting basin Huygens (Figs. 14 and 15), a low-exterior relief. The virtual absence of a

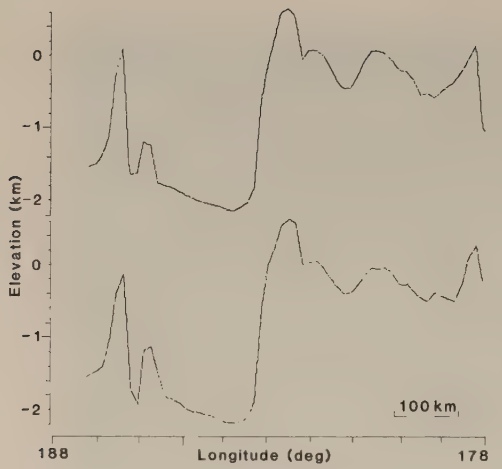

FIG. 9. Elevation profiles of crater Gusev. Gusev is another example of a crater with an inclined floor. The height of the west rim is less than about 400 m above the level of the surrounding plains. The prominent topographic spike masquerading as the west rim is probably a composite profile of the rims of a swarm of superimposed craters located outside the Gusev perimeter. Vertical exaggeration is 100×. (Radar scans: −14.80°, Sep 71, 0.442 AU; −14.89°, 10 Aug 71, 0.376 AU.)

pronounced exterior relief and the presence or absence of the interior relief do not seem to be coupled.

IV. MORPHOMETRY OF LARGE MARTIAN CRATERS

Morphology of impact craters provides clues to the evolution of surfaces of terrestrial planets. Compilation of telescopically obtained morphological parameters of lunar craters was initiated two centuries ago (cf. Baldwin 1963). Even through radar morphometry of large lunar craters is, in principle, possible (Zisk 1972, 1978), most modern work relies on Lunar Orbiter and Apollo photography (Pike 1974, 1976, Schubert *et al.* 1977). The first information on depths of Martian craters was obtained through photoclinometric processing of the Mariner 4 images (Leighton 1966, Leighton *et al.* 1967). Martian impact craters were noted to be shallower and to have lower rims than the lunar craters. These phenomena were confirmed by visual inspection of the Mariner 6 and 7 images (Murray *et al.* 1971) and by the subsequent observations. Mariner 9 UV spectrometer data (Hord *et al.* 1974) enabled determination of depths for a number of craters of all classes, larger than about 15 km across (Burt *et al.* 1976, Cintala *et al.* 1976). Both the areal and the elevation resolutions of the Mariner 9 UVS data were too coarse for the depth measurements to be considered definite. Contemporary morphometry of impact craters on the Moon, Mars, and other planets concentrates on fresh craters, and it mostly relies on shadow-length measurements and on photoclinometry (Gault *et al.* 1975, Cintala and Mouginis-Mark 1980, Pike 1980, Squyres 1981, Passey and Shoemaker 1982, Davis and Soderblom 1984, Lee 1984, Pike and Davis 1984). When viewing smaller craters on Mars ($D < 100$ km), the Earth-based radar morphometry cannot match these techniques in accuracy or resolution. However, radar has an ability to view large objects *in toto,* within their regional context (cf. Section III). Furthermore, radar can produce continuous elevation profiles (not necessarily along strictly straight lines) of those objects. Accordingly, the Goldstone data permit determination of morphological parameters of large craters only. In this respect, the Goldstone altimetry of Mars and the Arecibo altimetry of Mercury (Harmon *et al.* 1986) are of comparable utility.

We have identified in the combined 1971–1982 Goldstone data echoes from 152 craters. We have measured rim-to-floor depths d of 100 craters and rim heights h of 29 craters (Table I). If an object was scanned more than once, the largest measurement was retained (because of the aforementioned tendency of radar to underestimate the topographic relief). The depth measurements allowed construction of depth vs diameter (d/D) curves for three classes of large Martian craters (Fig. 16).

Depth/Diameter Ratios

The diameter range, from ~25 to ~475 km, of 100 objects comprising the higher

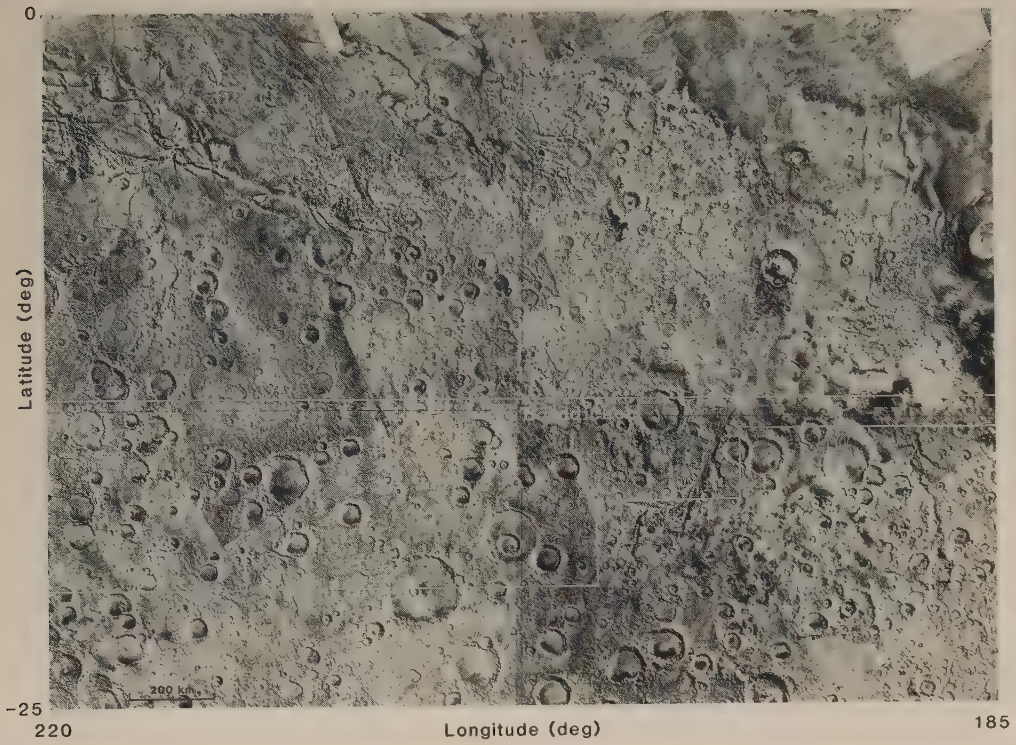

FIG. 10. Composite photomosaic of the Aeolis quadrangle (MC-23). Radar coverage centers on the area W of crater Boeddicker. The area has been mapped mostly as cratered plateau and hilly and cratered materials (units plc and hc in Scott *et al.* 1978). Reconstruction of the topography enclosed in the box is presented in Fig. 16. (Viking Medium Resolution Photomosaics: (MC-23) NW, NE, SW, SE; USGS, Flagstaff.)

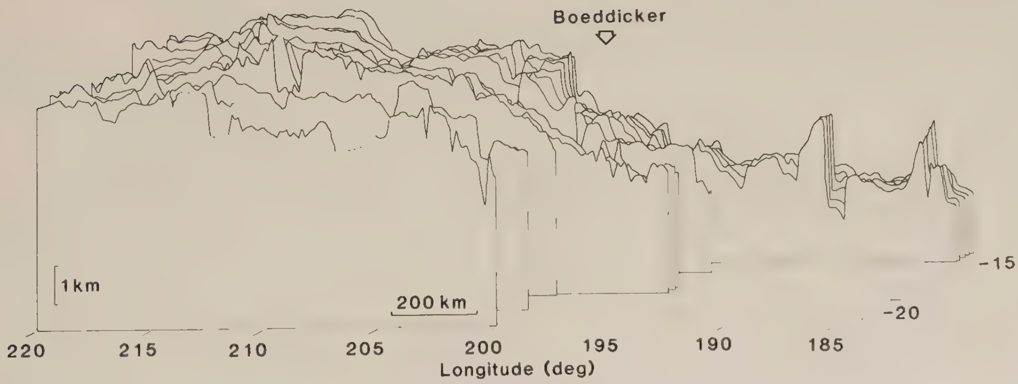

FIG. 11. Reconstruction of topography in the Aeolis quadrangle. Low-lying areas in the Gusev–Boeddicker corridor appear to be flanked by sub-craton-sized blocks characterized by approximately 3 km of topographic relief. The relief roughly corresponds to the transition from the unit hc to the unit plc (Scott *et al.* 1978). Vertical exaggeration is 100×. (18 Radar scans between −14.35° and −21.03° lat.)

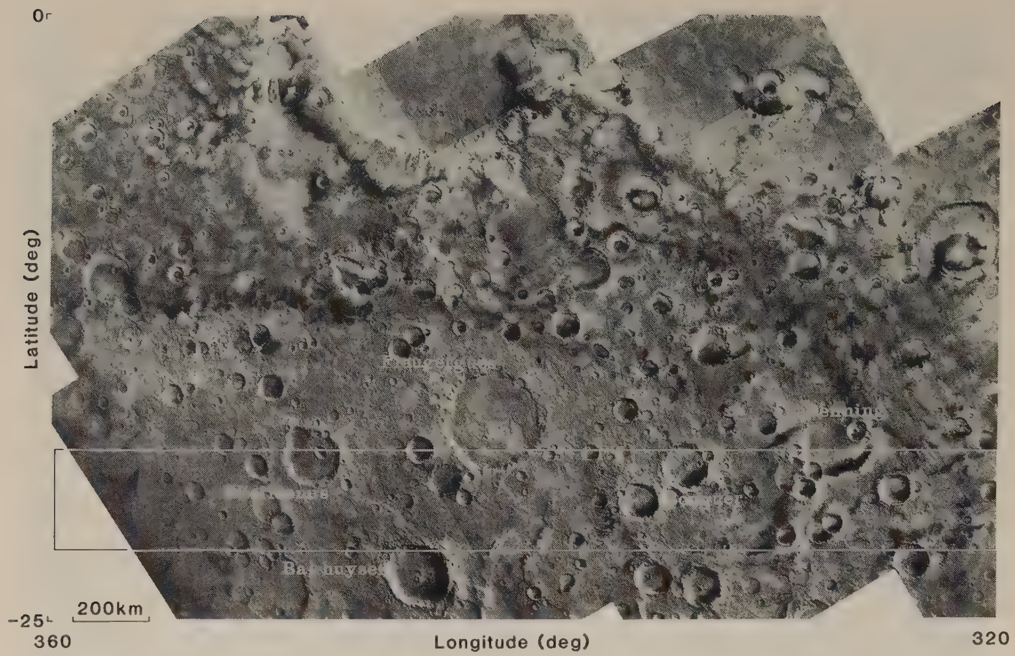

FIG. 12. Photomosaic of the Sinus Sabaeus (MC-20) quadrangle. The radar coverage is restricted mostly to the classical high-albedo Deucalionis Regio (Moore 1980). Reconstruction of topography enclosed in the box is presented in Fig. 13. (Viking frames 623A62, 64, 68, 70, 624A21–26.)

confidence grouping of the depth measurements corresponds to the branch of the Martian d/D curves past the inflection point that marks the transition from the simple to the complex crater morphologies (Pike 1971, 1974, 1980). In terms of the USGS classification, the scanned craters fall in three classes: c1 (highly degraded), c2 (degraded), c3 (subdued). The least-squares fits to the d vs D relationship for these classes are given below (unclassified craters not included):

c1 $d = (0.413 \pm 1.740)D^{(0.211 \pm 0.085)}$,
$(N = 37,\ r = 0.389)$

c2 $d = (0.365 \pm 1.643)D^{(0.321 \pm 0.121)}$,
$(N = 42,\ r = 0.387)$

c3 $d = (0.303 \pm 1.634)D^{(0.389 \pm 0.113)}$,
$(N = 17,\ r = 0.665)$

d and D are in kilometers and r is the corre-

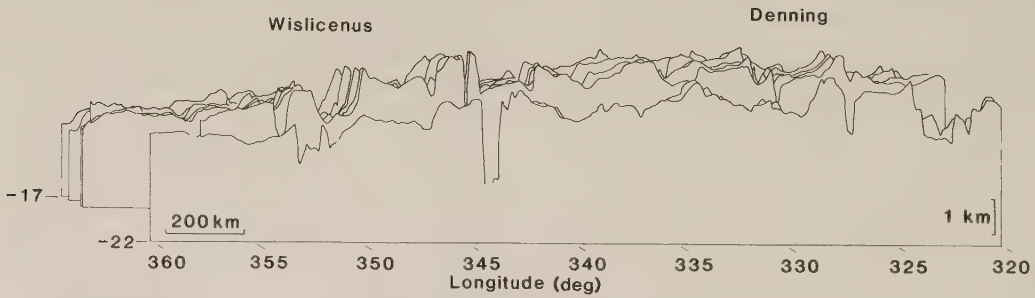

FIG. 13. Reconstruction of topography in the Sinus Sabaeus quadrangle. No elevation differences have been observed in the area of transition (around 320° long) from the high-albedo Deucalionis Regio to the low-albedo Sinus Sabaeus. Vertical exaggeration is 100×. (11 Radar scans from −17.13° to −22.17° lat.)

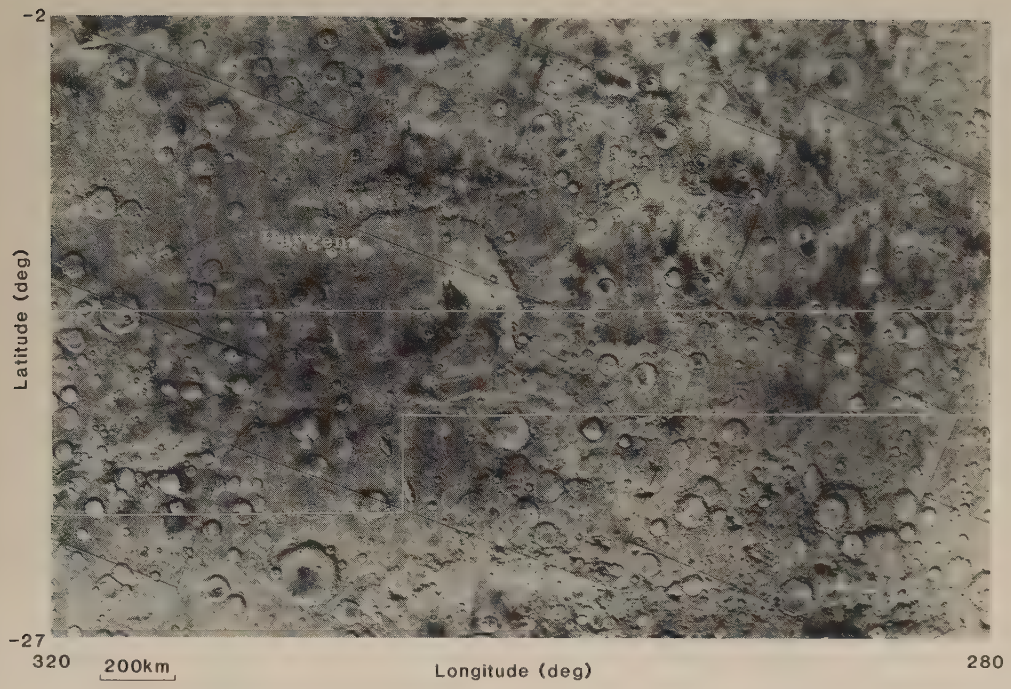

FIG. 14. Photomosaic of the Iapygia (MC-21) quadrangle, with its most prominent structure, basin Huygens. Most of the area within the radar coverage has been mapped as hilly and cratered materials and cratered plains materials (units hc and pc in Schaber 1977). Reconstruction of the topography enclosed in the box is presented in Fig. 20. (VOIT mosaic 211-5918.)

lation coefficient. Despite a considerable scatter and the poor correlation between *d* and *D*, the fits are consistent with progressive shallowing of Martian craters with age and the corresponding weakening of the functional relationship between *d* and *D* (Figs. 16a through 16c). Most craters larger than 125 km across, contained in the Gold-

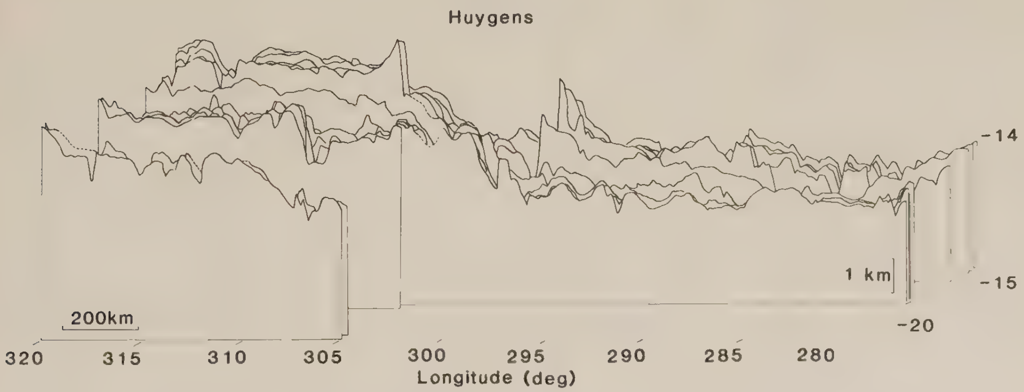

FIG. 15. Reconstruction of topography in the Iapygia quadrangle. In contrast to Ladon, with its nonexistent rims (Figs. 2 and 4), the positive relief associated with Huygens dominates the local topography. No other impact structure in the Goldstone sample possesses comparably commanding rims. Vertical exaggeration is 100×. (14 Radar scans between −14.13° and −22.17° lat.)

TABLE I

RADAR MEASUREMENTS FOR CRATERS IN THE HIGHER CONFIDENCE GROUPING OF THE GOLDSTONE SAMPLE

	Long (deg)	Lat (deg)	D (km)	d (km)	h (km)	Class	Distance (AU)	Name
1	4.0	−21.4	70	0.8			0.554	
2	5.5	−18.3	80	1.6	0.25	2	0.439	
3	6.6	−14.4	25	0.7		3	0.393	
4	7.1	−13.9	60	0.7		1	0.393	
5	8.0	22.0	155	2.4		2	0.679	Becquerel
6	8.1	−14.8	82	1.8	0.10	3	0.442	Beer
7	9.2	−21.5	85	1.4		3	0.554	
8	12.8	−18.2	48	1.8		2	0.554	
9	14.0	10.8	95	1.8		3	0.837	
10	15.7	−13.9	30	1.0		2	0.403	
11	16.2	−14.3	60	1.0	0.30	2	0.403	
12	19.5	−19.2	90	1.7	0.15	3	0.695	Jones
13	20.2	23.5	90	2.5		2	0.820	
14	22.5	21.7	85	3.0		2	0.679	McLaughlin
15	23.8	−18.5	53	1.6		2	0.717	
16	24.8	−16.5	90	0.6		1	0.504	
17	25.5	−18.5	52	1.5		2	0.717	
18	28.0	−17.0	475	1.9	0.00	1	0.438	Ladon
19	29.3	−18.7	45	1.4		3	0.695	
20	39.4	−22.2	100	2.0	0.30		0.554	
21	52.4	10.3	60	1.9		2	0.706	
22	86.6	22.0	87	1.6		2	0.689	Fesenkov
23	142.8	−15.0	63	1.4	0.35	2	0.454	
24	152.5	−16.8	40	1.6		2	0.490	
25	154.3	−14.3	56	1.0		2	0.377	
26	155.5	−15.6	37	1.6		2	0.471	
27	156.2	−14.0	112	2.0	0.20	2	0.442	Burton
28	157.3	−18.0	38	1.0		2	0.444	
29	158.3	−21.8	39	1.6			0.492	
30	159.2	−21.8	65	1.1			0.492	
31	164.0	−18.0	125	0.8		2	0.484	Williams
32	166.5	−15.0	100	2.5	0.15	3	0.460	
33	177.6	−14.6	35	1.6		3	0.442	
34	178.0	−14.3	72	1.3		3	0.442	
35	180.3	−19.7	95	1.6	0.45	1	0.766	
36	184.5	−14.7	170	1.6		1	0.442	Gusev
37	186.2	−14.9	40	1.8	1.00	3	0.442	
38	186.5	−19.5	40	1.3		2	0.455	
39	187.8	−20.3	45	0.8		2	0.766	
40	191.8	−15.6	55	0.6		1	0.598	
41	193.5	−16.6	82	0.6		1	0.598	
42	194.7	−16.4	60	1.2		2	0.598	
43	197.3	−15.0	110	1.9	0.30	3	0.431	Boeddicker
44	201.6	−20.2	60	1.2		1	0.750	
45	203.0	−19.5	115	0.6		1	0.750	Hadley
46	206.0	−21.5	150	0.9	1.00		0.750	Graff
47	211.0	−17.2	90	1.5		1	0.470	
48	211.5	−17.5	30	1.8		2	0.470	
49	212.0	−18.5	42	1.4		2	0.484	

TABLE I—(*Continued*)

	Long (deg)	Lat (deg)	*D* (km)	*d* (km)	*h* (km)	Class	Distance (AU)	Name
50	215.6	−14.1	62	1.2		2	0.417	
51	217.4	−14.2	50	0.6		1	0.417	
52	217.8	−14.3	35	1.0		1	0.417	
53	222.2	−5.5	145	2.4		3	~0.600	Gale
54	225.1	−15.3	25	0.7		1	0.378	
55	226.8	−6.6	130	3.0		2	~0.600	Knobel
56	229.6	−18.0	53	2.0	0.30	2	0.484	
57	230.0	−15.0	340	1.5	0.20	1	0.417	Herschel
58	236.5	−19.8	90	2.0	0.30	2	0.750	
59	240.6	−15.4	60	1.4			0.378	
60	261.8	−15.0	80	1.5	0.25	2	0.417	
61	270.0	−15.5	55	0.8		2	0.381	
62	270.5	−6.5	65	1.9		2	~0.600	
63	277.5	−18.8	44	1.4		2	0.580	
64	283.3	−17.3	35	0.8		1	0.468	
65	284.0	−14.3	75	1.2		2	0.506	
66	286.3	−14.5	60	0.9		2	0.506	
67	286.5	−15.5	50	1.0	0.35	2	0.381	
68	294.5	22.8	175	1.8		2	0.752	Baldet
69	295.0	−16.7	70	1.4	0.10	1	0.504	
70	299.0	22.0	380	0.7		1	0.677	Antoniadi
71	299.5	−17.0	58	1.0	0.15		0.468	
72	300.6	−18.8	95	1.6		1	0.436	
73	303.5	−18.7	50	1.2	0.50	1	0.515	
74	304.0	−14.0	400	2.0	1.20	1	0.408	Huygens
75	309.3	−18.4	77	1.6		2	0.436	
76	312.3	−22.0	70	1.0		2	0.554	
77	315.5	−21.5	80	1.4		3	0.834	
78	317.0	−13.7	95	1.2		1	0.393	
79	322.5	2.5	150	1.7		3	0.678	Janssen
80	323.0	−22.3	80	1.0		2	0.554	
81	325.6	−16.9	38	1.2	0.15		0.648	
82	326.7	−17.8	140	0.6	0.50	1	0.674	Denning
83	327.0	−21.0	56	1.2		2	0.834	
84	328.0	23.5	400	1.4		1	0.678	Cassini
85	328.8	−17.0	35	1.3		2	0.674	
86	331.6	−13.6	90	1.3		1	0.403	
87	331.7	−18.0	30	0.5		2	0.440	
88	332.6	−18.5	95	0.8	0.10	1	0.549	Bouguer
89	335.0	−16.3	65	1.0	0.15	3	0.412	
90	340.5	−16.8	225	1.5	0.20	1	0.504	Flaugergues
91	343.6	−18.0	60	1.4		1	0.674	
92	343.8	−13.5	47	1.2		1	0.393	
93	344.0	−23.0	140	2.5	0.20	3	0.554	Bakhuysen
94	344.4	−14.0	55	0.8		1	0.387	
95	348.5	−18.3	130	1.6	0.30	1	0.541	Wislicenus
96	349.0	−17.5	58	1.2		1	0.541	
97	350.0	−15.4	65	1.1		2	0.534	
98	351.2	−18.5	59	1.3	0.10	1	0.440	
99	351.5	−17.5	32	0.9		1	0.674	
100	358.2	−16.7	50	1.0		2	0.403	

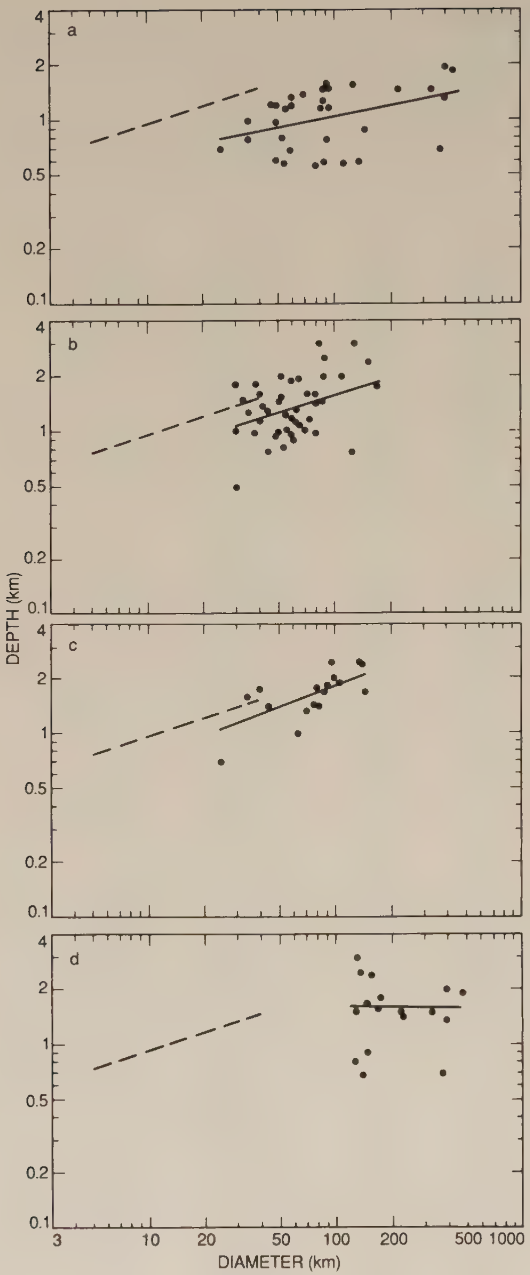

FIG. 16. Depth vs diameter for degraded complex Martian craters contained in the Goldstone sample. Dashed line: *d*/*D* least-squares fit for fresh complex Martian craters (Table I in Pike (1980). Solid lines: *d*/*D* least-squares fits for crater categories considered in the text. (a) Craters in the c1 class. Diameter range: 25–475 km. (b) Craters in the c2 class. Diameter range: 30–175 km. (c) Craters in the c3 class. Diameter range: 30–150 km. (d) Craters with diameters larger than 125 km.

stone sample, belong to the c1 class. The least-squares fit of the *d*/*D* ratios for the subgroup of craters with $D > 125$ km,

$$d = (2.216 \pm 3.785)D^{(-0.072\pm0.250)},$$
$$(N = 17,\ r = -0.074)$$

indicates that the average depth of largest craters in the Goldstone sample is about 2 km, virtually independent of the crater size. (Note, however, the large standard errors in both the slope and the intercept.) The separation of the largest, degraded craters from the remaining sample results in the disappearance of the linear (log *d*) vs (log *D*) relationship or, alternately, in the appearance of a second break in slope of the *d*/*D* curves (Fig. 16d). Because the 125-km-diameter division was arbitrarily chosen, we cannot be certain that a change in the *d*/*D* relation actually occurs at this diameter. However, a change may exist somewhere in the diameter range from 100 to 200 km. This range may correspond to the threshold of the passage from peak-ring basins to center peak basins or, in general, from complex craters to ringed basins (Stuart-Alexander and Howard 1970). Because the accuracy of the radar range measurements decreases as the size of the scanned object approaches the size of the resolution cell, the least-squares fits that include smaller craters may suffer from contamination by the less reliable points, while the fit valid for $D > 125$ km gives a more accurate representation of the *d*/*D* relationship. Thus a customary power-law fit when taken over the full range of diameters past the 3- to 8-km transition diameter (Pike 1980) may obscure the fact that the depths of the large, mostly senescent, Martian craters tend to be very weakly dependent on the crater diameter. However, the limited size of the Goldstone sample, the large scatter in the data, and the concomitant poor correlation between the paired variables may also hide the fact that unrecognized crater subpopulations are sampled. This possibility requires further investigation.

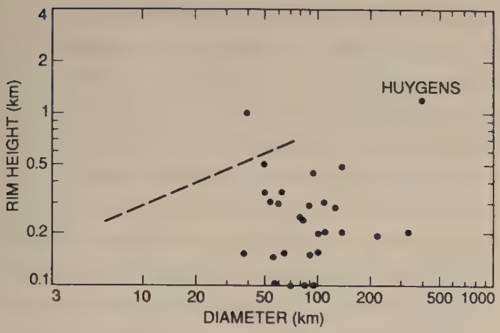

FIG. 17. Rim height vs diameter for degraded complex Martian craters contained in the Goldstone sample. Dashed line: h/D least-squares fit for fresh complex Martian craters (Eq. 1b in Lee (1984)).

Pike (1977a) has detected the existence of a limiting apparent depth, 3.4 km, independent of crater size, in the Apollo metric-camera morphometry of the fresh lunar craters. Because the apparent depth is at most equal to the rim-to-floor depth, the limiting apparent depth in the Goldstone Mars data is about 2.0 km, with few exceptions.

Rim-Height/Diameter Ratios

Another parameter of interest is the crater rim height h. For fresh craters the plots of log (rim height) vs log (rim-crest diameter), the h/D curves, follow a pattern similar to that followed by the d/D curves, i.e., they describe an isometric h/D relationship below the transition diameter and a power-law relationship above it (Pike 1977b, Lee 1984, Pike and Davis 1984). The Goldstone data permit measurement of rim heights for craters above the transition diameter (Fig. 17; Table I). It should be noted, however, that the crater rim-height measurements are intrinsically less reliable than the corresponding depth measurements. The relative errors are large because radar determines the topographic relief along one direction only and most craters were scanned only once. Furthermore, "there will be a tendency to underestimate crater rim heights if the rim crest fills only a small fraction of the area of the radar resolution cell" (Harmon *et al.* 1986). If an *ad hoc* assumption is made that the width of rims is about 10% of crater diameter, then, under an ideal viewing geometry, a rim of a ~125-km crater would fill the Goldstone resolution cell. Thus, in the present Goldstone Mars data the diameter of ~125 km probably constitutes the lower limit on the size of a crater for which radar measurements of rim heights might be sufficiently accurate. Rim heights for smaller craters (Fig. 17) may still be acceptable but, as in the case of depths of craters smaller than ~100 km across, they have to be viewed with caution.

Keeping in mind the stated qualifications, it is confirmed here that "the (large, degraded) Martian craters have rims that rise about 100 meters above the surrounding surface" (Leighton 1966) (Fig. 17). While separation of the measured rim-heights sample into the three degradation-class subsamples yields faint suggestions of trends in the h/D relationships, the subsamples are too small (c1: $N = 11$; c2: $N = 8$; c3: $N = 6$) to give credence to those suggestions. This matter is not pursued any further here.

It is evident that the large lunar craters have more prominent rims than do the Martian craters surveyed here. Compare, e.g., the rim-height data from Baldwin (1963) ($\langle h \rangle = 1.47$ km, $\sigma = 0.67$ km, $D > 50$ km; $N = 23$; all classes) to the Goldstone data ($\langle h \rangle = 0.26$ km, $\sigma = 0.23$ km, $D > 50$ km; $N = 25$; all classes). On the moon, "the topographic expression of a crater above the surrounding surface typically decreases to one-tenth of the estimated rim height at a range of 1.3 to 1.7 R (crater radius)" (Settle and Head 1977). The topographic expression of craters in the Goldstone sample rarely extends beyond the immediate vicinity of the crater cavity. Low rims in small Martian craters may genetically be related to an impact into a volatile-rich upper crust (Cintala and Mouginis-Mark 1980). While gravity scaling of the initial shapes has certainly been important (Pike 1980), excavation of large craters into a volatile-poor lower crust should not result in anomalously low rims (Fig. 17). Modeling exercises (Ramberg 1963, Danes 1965, R. F. Scott 1967, Hall *et al.* 1981) indicate that the advanced stage of structural adjustment of large craters would presumably be accompanied by the simultaneous loss of much or all of both the interior and the exterior relief. Because it is mostly the exterior relief that appears to be absent, while the interior relief, although reduced, has been largely retained, neither the rapid post-impact rebound nor the protracted relaxation is the likely principal contributor to the present low-rimmed appearance of large Martian craters. Eolian-erosion-induced disappearance of the competent exterior relief is improbable (Arvidson 1986). Likewise, fluvial erosion is an unlikely agent of the exterior relief suppression (Baker and Milton 1974). Thus, while Martian craters were certainly subjected to the action of all the commonly considered modification processes, the emergence of a low-rimmed, flat-floored crater is perhaps related to the intermittent (volcanic?/eolian?) plains-resurfacing episode(s) (Chapman 1974, Chapman and Jones 1977, Greeley and Spudis 1978). Erosion due to impacts during the waning stages of the epoch of heavy bombardment may have also been significant in rim obliteration. However, as the example of Ladon (Figs. 1 and 3) shows, the effects of the early impact-induced erosion are easily masked by the more recent plains deposits.

V. CONCLUDING REMARKS

The Goldstone data demonstrate the overall blandness of Martian topography at the scale of the radar resolution cell (8 km east–west, ~80 km north–south). The data confirm the shallowness of large craters in the cratered highlands and the subdued character of exterior relief in those craters. The floors of large craters are flat. The doming observed in some lunar craters is absent. In some instances (Huygens, Williams) the crater floors may have responded to an external topographic control and tilted. In others (Flaugurgues, Herschel) such a control was probably inoperative. Volcanic resurfacing may have been significant in reducing rims of most craters and raising floors in some craters. Fluvial deposition does not appear to have been significant (Gusev, Ladon). Craters and basins with or without associated channel systems seem to be equally deep. Nonuniform eolian deposition may have modified the floors of some structures (Boeddicker, Gusev). If the limited Goldstone sample is representative of the population of Martian craters, then (volcanic?/eolian?/impact-induced?) suppression of the positive relief has perhaps been the most notable phenomenon associated with the evolution of large craters on Mars. The tentative nature of these conclusions underscores the need for reliable topographic information when attempting to reconstruct the geologic history of terrestrial planets.

In a different context, the results presented here demonstrate that it is possible to acquire acceptable quality altimetry of Mars from the Earth. (Acceptable in the sense that it permits a first-order morphometry on large craters.) Uncertainty as to the exact latitude of the subradar point diminishes the merit of the good range resolution, but λ3.5-cm ranging with an upgraded Goldstone antenna would ameliorate this situation and would also prolong the Goldstone ranging season. This, in turn, would result in a denser coverage within the radar-visible band of latitudes. Achieving this goal is of considerable importance since the areal coverage in the extant Goldstone data (about 1% of surface area) barely corresponds to the TV-imaging coverage at the beginning of the era of spacecraft reconnaissance of Mars (about 0.5% of area, after the Mariner 4 mission (Pollack and Sagan 1970)). With a denser areal coverage and a reduced footprint, Goldstone Mars altimetry along constant-latitude tracks and the spacecraft altimetries along polar and subpolar tracks would provide complementary data sets.

APPENDIX: MEASUREMENT ERRORS

This discussion is based on a series of simulations of actual radar data as part of a study for the Viking Project (Jurgens 1974, Downs and Reichley 1975). Although the study was in terms of the Goldstone λ3.5-cm system rather than the λ13-cm system, a particular result of that study applies here. The pertinent result is that systematic biases in the measured delay (or elevation) change with the angle-of-incidence of the signal and with the surface roughness, and these effects are larger than the rms measurement error when the signal-to-noise ratio (SNR) is large.

The desired effects are illustrated in Figs. 18 and 19. To understand these figures, consider first how the radar system samples the planetary surface. Planes of constant range and planes of constant Doppler shift (parallel to the apparent spin axis of the planet and to the line of sight) intersect to sample the surface. The only ambiguity occurs between the northern and southern hemispheres where two distinct regions can have the same range and the same Doppler shift. We avoid this problem by working at the Doppler equator, where two regions merge into one. The signal is in fact the measured reflected power vs time delay at a fixed Doppler shift. We label this signal a delay function. The reflected power corresponds to a range of longitudes and angles of incidence θ, where θ is a function of the Doppler shift. As the planet rotates, a series of delay functions corresponding to particular values of θ become available for a particular longitude. With the extra delay due to curvature of the nearly spherical surface removed, the collection of delay functions is usually added to produce a composite delay function with a higher SNR. We confine the measurements to the Doppler equator by measuring the range corresponding to the signal peak.

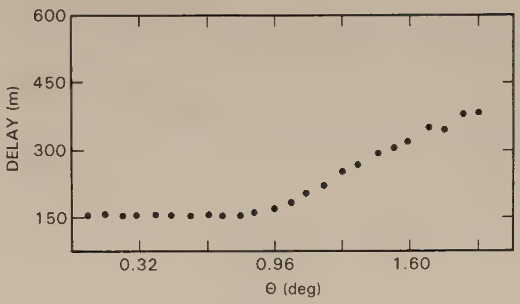

FIG. 18. Echo delay vs angle of incidence for a smooth (C = 5000) reflecting surface.

A particular data frame is considered in Fig. 18. The delay of the peak of each delay function is presented as a function of θ. Here, at Hagfors parameter $C = 5000$, the magnitude of the backscatter function decreases rapidly with θ. (For a discussion of backscatter functions as modeled by the Hagfors scattering law, see Downs *et al.* 1975 and references therein.) A positive drift in the delay of the signal occurs as Doppler slices are taken further back on the backscatter function, and the magnitude of the peak decreases as well. The positive drift is readily observed in the figure for $\theta >$ 1°. Clearly, a bias in the measurement is present, varying from a minimum 150 m up to 350 m. In practice, one cannot probe the surface on a continuous basis since the transmitter must be turned off one-half of the time to allow for reception. Hence, a given longitude will be sampled at one-half the available values of θ. The actual bias in range will depend on which values of θ are available for the construction of the composite delay function. In an extreme case one might observe elevation to vary periodically no more than 200 m peak to peak as the radar view window slides over the surface. In general, we would expect this effect to be $\leq$100 m or less peak to peak due to averaging over a range of θ.

A rougher surface (C = 150) is represented in Fig. 19. The minimum bias (relative to the closest point on the assumed spherical surface) is now ~300 m, but the increase is less. This is due to the slower

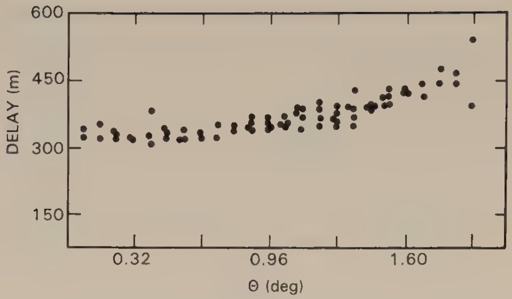

FIG. 19. Echo delay vs angle of incidence for a rough ($C = 150$) reflecting surface.

variation in the backscatter function with θ. (The effects of a weaker signal are present, so several simulated data frames were combined for this illustration.) Therefore, as we traverse a surface of widely varying roughness we might expect the elevation to change by no more than 150 m due to this effect. Also, in comparing regions that are characterized by single but different values of C we might expect a bias in the elevation difference. Thus, for example, the difference between a low, bright region and a high, rough region will be biased toward a smaller elevation difference (a positive change in delay or range is a negative change in elevation.) This situation may occur when comparing smooth crater floors with rough crater rims.

Downs and Reichley (1975) estimated absolute measurement errors for the case of the λ3.5-cm radar. We are dealing here with the λ13-cm radar. Scaling results between the two systems is not simply a matter of scaling various constants with operating frequency. Estimates of the measurement as a function of C for a reasonable set of Earth–Mars distances can be obtained for the λ13-cm system only by repeating simulations reported by Downs and Reichley (1975). Therefore we only reiterate the experience reported in Downs *et al.* (1973, 1975). Under the best conditions (Earth–Mars distance ~0.36 AU, $C > 5000$) the observed measurement error was about 40 m. Typical errors were about 150 to 200 m. Errors much larger than the typical errors usually corresponded to a loss of signal, so the measurement was usually eliminated. Distance to the planet is included in Table I as a guide to estimating the accuracy of the listed depth and rim-height measurements.

ACKNOWLEDGMENTS

We thank R. Mehlman, without whose help this work would not have been possible. We appreciate the critical comments of R. J. Pike and the anonymous referees. We thank T. H. Dixon, C. Elachi, D. L. Evans, D. L. Matson, D. B. Nash, S. J. Ostro, F. D. Palluconi, N. A. Renzetti, and T. W. Thompson for support. N. Evans furnished the mosaics used in Figs. 5 and 12. V. Arriola, K. J. Banwart, T. Kiriyama, A. H. Richardson, and S. M. Salas provided technical assistance. The research described in this paper was carried out at the Jet Propulsion Laboratory, California Institute of Technology, under contract with the National Aeronautics and Space Administration.

REFERENCES

ARVIDSON, R. E. 1986. On the rate of formation of sedimentary debris on Mars (abstract). *Lunar Planet. Sci. XVII,* 17.

BAKER, V. R., AND D. J. MILTON 1974. Erosion by catastrophic floods on Mars and Earth. *Icarus* **23,** 27–41.

BALDWIN, R. B. 1963. *The Measure of the Moon.* Univ. of Chicago Press, Chicago.

BATSON, R. M., P. M. BRIDGES, AND J. L. INGE 1979. *Atlas of Mars.* National Aeronautics and Space Administration, Washington, DC.

BURT, J., J. VEVERKA, AND K. COOK 1976. Depth–diameter relation for large Martian craters determined from Mariner 9 UVS altimetry. *Icarus* **29,** 83–90.

CHAPMAN, C. R. 1974. Cratering on Mars. I. Cratering and obliterating history. *Icarus* **22,** 272–291.

CHAPMAN, C. R., AND K. L. JONES 1977. Cratering and obliteration history of Mars. *Annu. Rev. Earth Planet. Sci.* **5,** 515–540.

CINTALA, M. J., J. W. HEAD, AND T. A. MUTCH 1976. Martian crater depth/diameter relationships: Comparisons with the Moon and Mercury. *Proc. Lunar Sci. Conf. 7th,* 3575–3587.

CINTALA, M. J., AND P. J. MOUGINIS-MARK 1980. Martian fresh crater depths: More evidence for subsurface volatiles? *Geophys. Res. Lett.* **7,** 329–332.

DANES, Z. F. 1965. Rebound processes in large craters. In *Astrogeol. Studies Ann. Progress Rep.,* July 1, 1964 to July 1, 1965. United States Geological Survey.

DAVIS, P. A., AND L. A. SODERBLOM 1984. Modeling crater topography and albedo from monoscopic Viking Orbiter images. I. Methodology. *J. Geophys. Res.* **89,** 9449–9457.

Downs, G. S., R. M. Goldstein, R. R. Green, and G. A. Morris 1971. Mars radar observations, a preliminary report. *Science* **174,** 1324–1327.

Downs, G. S., R. M. Goldstein, R. R. Green, G. A. Morris, and P. E. Reichley 1973. Martian topography and surface properties as seen by radar: The 1971 opposition. *Icarus* **18,** 8–21.

Downs, G. S., R. R. Green, and P. E. Reichley 1978. Radar studies of the Martian surface at centimeter wavelengths: The 1975 opposition. *Icarus* **33,** 441–453.

Downs, G. S., P. J. Mouginis-Mark, S. H. Zisk, and T. W. Thompson 1982. New radar-derived topography for the northern hemisphere of Mars. *J. Geophys. Res.* **82,** 9747–9754.

Downs, G. S., and P. E. Reichley 1975. *Radar Ranging of the Planet Mars at 8495 MHz.* JPL DSN Prog. Rep. 42-29.

Downs, G. S., P. E. Reichley, and R. R. Green 1975. Radar measurements of Martian topography and surface properties: The 1971 and 1973 oppositions. *Icarus* **26,** 273–312.

Dyce, R. B., G. H. Pettengill, and A. D. Sanchez 1967. Radar observations of Mars and Jupiter at 70 cm. *Astron. J.* **72,** 771–777.

Gault, D. E., J. E. Guest, J. B. Murray, D. Dzurisin, and M. C. Malin 1975. Some comparisons of impact craters on Mercury and the Moon. *J. Geophys. Res.* **80,** 2444–2460.

Goldstein, R. M., W. G. Melbourne, G. A. Morris, G. S. Downs, and D. A. O'Handley 1970. Preliminary radar results of Mars. *Radio Sci.* **5,** 475–478.

Greeley, R., and P. D. Spudis 1978. Volcanism in the cratered terrain hemisphere of Mars. *Geophys. Res. Lett.* **5,** 453–455.

Hall, J. L., S. C. Solomon, and J. W. Head 1981. Lunar floor-fractured craters: Evidence for viscous relaxation of crater topography. *J. Geophys. Res.* **86,** 9537–9552.

Harmon, J., K., D. B. Campbell, D. L. Bindschadler, J. W. Head, and I. I. Shapiro 1986. Radar altimetry of Mercury: A preliminary analysis. *J. Geophys. Res.* **91,** 385–401.

Hartmann, W. K. 1978. Mars: Topographic control of clouds, 1907–1973. *Icarus* **33,** 380–387.

Herr, K. C., D. Horn, J. M. McAfee, and G. C. Pimentel 1970. Martian topography from the Mariner 6 and 7: Infrared spectra. *Astron. J.* **75,** 883–894.

Hord, C. W., K. D. Simmons, and L. K. McLaughlin 1974. Mariner 9 ultraviolet spectrometer experiment: Pressure–altitude measurement on Mars. *Icarus* **17,** 292–302.

Jurgens, R. F. 1974. *A Survey of Ground-Based Radar Astronomical Capabilities Employing 64 and 128 Meter Antenna Systems at S- and X-Band.* JPL Tech. Rep. 890-44.

Kieffer, H. H., T. Z. Martin, A. R. Peterfreund, B. M. Jakosky, E. D. Miner, and F. D. Palluconi 1977. Thermal and albedo mapping during the Viking primary mission. *J. Geophys. Res.* **82,** 4249–4291.

Lee, S. W. 1984. Mars: Wind streak as related to obstacle type and size. *Icarus* **58,** 339–357.

Leighton, R. B. 1966. The photographs from Mariner IV. *Sci. Am.* **214,** 54–68.

Leighton, R. B., B. C. Murray, R. B. Sharp J. D. Allen, and R. K. Sloan 1967. *Mariner IV Pictures of Mars.* JPL Tech. Rep. 32-884.

Malin, M. C., and D. Dzurisin 1977. Landform degradation on Mercury, the Moon, and Mars: Evidence from crater depth/diameter relationships. *J. Geophys. Res.* **82,** 376–388.

Moore, H. J. 1980. *Geologic Map of the Sinus Sabaeus Quadrangle of Mars.* USGS map I-1196 (MC-20).

Murray, B. C., L. A. Soderblom, R. P. Sharp, and J. A. Cutts 1971. The surface of Mars: The cratered terrain. *J. Geophys. Res.* **76,** 313–330.

Mutch, T. A., and E. C. Morris 1979. *Geologic Map of the Memnonia Quadrangle of Mars.* USGS Map I-1137 (MC-16).

Passey, Q. R., and E. M. Shoemaker 1982. Craters and basins on Ganymede and Callisto: Morphological indicators of crustal evolution. In *Satellites of Jupiter* (D. Morrisson, Ed.), Univ. of Arizona Press, Tucson.

Pettengill, G. H., C. C. Counselman, L. P. Rainville, and I. I. Shapiro 1969. Radar measurement of Martian topography. *Astron. J.* **74,** 461–482.

Pettengill, G. H., A. E. E. Rogers, and I. I. Shapiro 1971. Martian craters and a scarp as seen by radar. *Science* **174,** 1321–1324.

Pike, R. J. 1971. Genetic implications of the shapes of Martian and lunar craters. *Icarus* **15,** 384–395.

Pike, R. J. 1974. Depth/diameter relations of fresh lunar craters: Revision from spacecraft data. *Geophys. Res. Lett.* **1,** 291–294.

Pike, R. J. 1976. Crater dimensions from Apollo data and supplementary sources. *Moon* **15,** 463–477.

Pike, R. J. 1977a. Apparent depth/apparent diameter relation for lunar craters. *Proc. Lunar Sci. Conf. 8th,* 3427–3436.

Pike, R. J. 1977b. Size-dependence in the shape of fresh impact craters on the moon. In *Impact and Explosion Cratering* (D. J. Roddy, R. O. Pepin, and R. B. Merrill, Eds.). Pergamon, New York.

Pike, R. J. 1980. Formation of complex impact craters: Evidence from Mars and other planets. *Icarus* **43,** 1–19.

Pike, R. J., and P. A. Davis 1984. Toward a topographic model of Martian craters from photoclinometry (abstract). *Lunar Planet. Sci. XV,* 645–646.

Pollack, J. B., and C. Sagan 1970. Studies of the surface of Mars (very early in the era of spacecraft reconnaissance). *Radio Sci.* **5,** 443–464.

Ramberg, H. 1963. Experimental study of gravity tectonics by means of centrifuged models. *Bull. Geol. Inst. Univ. Uppsala* **42,** 1–97.

Roth, L. E., G. S. Downs, R. S. Saunders, and G. Schubert 1980. Radar altimetry of South Tharsis, Mars. *Icarus* **42,** 287–316.

Saunders, R. S. 1979. *Geologic Map of the Margaritifer Sinus Quadrangle of Mars*. USGS Map I-1144 (MC-19).

Schaber, G. G. 1977. *Geologic Map of the Iapygia Quadrangle of Mars*. USGS Map I-1020 (MC-21).

Schubert, G., R. E. Lingenfelter, and R. J. Terrile 1977. Crater evolutionary tracks. *Icarus* **32,** 131–146.

Schultz, P. H., and H. Glicken 1979. Impact crater and basin control of igneous processes on Mars. *J. Geophys. Res.* **87,** 8033–8047.

Schultz, P. H., R. A. Schultz, and J. Rogers 1982. The structure and evolution of ancient impact basins on Mars. *J. Geophys. Res.* **87,** 9803–9820.

Scott, D. H., and M. H. Carr 1978. *Geologic Map of Mars*. USGS Map I-1083.

Scott, D. H., E. C. Morris, and M. N. West 1978. *Geologic Map of the Aeolis Quadrangle of Mars*. USGS Map I-1111 (MC-23).

Scott, R. F. 1967. Viscous flow of craters. *Icarus* **7,** 139–148.

Settle, M., and J. W. Head III 1977. Radial variations of lunar craters rim topography. *Icarus* **31,** 123–135.

Simpson, R. A., G. L. Tyler, and H. T. Howard 1977. Crater morphometry from bistatic radar. In *Impact and Explosion Cratering* (D. J. Roddy, R. O. Pepin, and R. B. Merrill, Eds.), pp. 481–487. Pergamon Press, New York.

Smith, H. T. U. 1972. Aeolian deposition in Martian craters. *Nature* **238,** 72–74.

Squyres, S. W. 1981. The topography of Ganymede's grooved terrain. *Icarus* **46,** 156–168.

Stam, M., P. H. Schultz, and G. E. McGill 1984. *Martian Impact Basins: Morphology Differences and Tectonic Provinces (abstract)*. NASA TM 86246, pp. 818–819.

Standish, E. M. 1973. The figure of Mars and its effect on radar ranging. *Astron. Astrophys.* **26,** 463–466.

Stuart-Alexander, D. E., and K. A. Howard 1970. Lunar maria and circular basins: A review. *Icarus* **12,** 440–456.

Zisk, S. H. 1972. Lunar topography: First radar-interferometer measurements of the Alphonsus–Ptolemaeus–Arzachel region. *Science* **178,** 977–988.

Zisk, S. H. 1978. Mare Crisium area topography: A comparison of Earth-based radar and Apollo mapping camera results. In *Mare Crisium: The View from Luna 24* (R. B. Merrill and J. J. Papike, Eds.), pp. 75–80. Pergamon Press, New York.

ICARUS **79**, 311–327 (1989)

Recharge of the Early Atmosphere of Mars by Impact-Induced Release of CO_2

MICHAEL H. CARR

U.S. Geological Survey, Menlo Park, California 94025

Received May 16, 1988; revised September 6, 1988

Channels on the Martian surface suggest that Mars had an early, relatively thick atmosphere. If the atmosphere was thick enough for water to be stable at the surface, CO_2 in the atmosphere would have been fixed as carbonates on a relatively short time scale, previously estimated to be 1 bar every 10^7 years. This loss must have been offset by some replenishment mechanism to account for the numerous valley networks in the oldest surviving terrains. Impacts could have released CO_2 into the atmosphere by burial, by shock-induced release during impact events, and by addition of carbon to Mars from the impacting bolides. Depending on the relationship between the transient cavity diameter and the diameter of the resulting crater, burial rates as a result of impact gardening at the end of heavy bombardment are estimated to range from 20 to 45 m/10^6 years, on the assumption that cratering rates on Mars were similar to those of the Nectarian Period on the Moon. At these rates 0.1–0.2 bar of CO_2 could have been released every 10^7 years as a result of burial to depths where dissociation temperatures of carbonates were reached. Modeling of large impacts suggests that an additional 0.01 to 0.02 bar of CO_2 could have been released every 10^7 years during the actual impacts. In the unlikely event that all the impacting material was composed of carbonaceous chondrites, a further 0.3 bar of CO_2 could have been added to the atmosphere every 10^7 years by oxidation of meteoritic carbon. Even when supplemented by the volcanically induced release of CO_2, these release rates are barely sufficient to sustain an early atmosphere if water were continuously present at the surface. The results suggest that water may have been only intermittently present on the surface early in the planet's history. © 1989 Academic Press, Inc.

INTRODUCTION

The question addressed by this paper is whether high impact rates early in Mars's history could have helped maintain a relatively thick CO_2 atmosphere at that time. Thicker atmospheres in Mars's past have been suggested because of evidence of warmer climatic conditions. The arguments in favor of previous warmer climates (Masursky 1973, Sagan *et al.* 1973, Pollack 1979) are based largely on the presence of branching valley networks throughout the old terrains of Mars. At present, mean surface temperatures are close to 210°K, liquid water is unstable everywhere on the surface, and the planet is covered with a thick permafrost zone. The branching valley networks have been widely interpreted as having formed by slow erosion of running water (see summaries in Baker 1981, Carr 1981). If this interpretation is correct, then at times in the past, climatic conditions were probably warmer than at present. For conditions to have been warmer, the atmosphere must have been thicker. Greenhouse calculations show that for the mean global surface temperatures to reach 273°K, and so allow liquid water at the surface at low latitudes, the atmospheric pressure at the surface must have been at least 1 bar, and possibly as high as 5 bars (Pollack 1979, Toon *et al.* 1980, Cess *et al.* 1980, Postawko and Kuhn 1986). However, a CO_2

0019-1035/89 $3.00
Copyright © 1989 by Academic Press, Inc.
All rights of reproduction in any form reserved.

atmosphere thick enough to stabilize liquid water at the surface would have been itself unstable (Fanale *et al.* 1982, Kahn 1985, Pollack *et al.* 1987) because the CO_2 would have reacted with rock materials to form carbonates at a relatively rapid rate. Pollack *et al.* (1987) and Fanale *et al.* (1982) estimate that, with water present on the surface, 1 bar of CO_2 would be fixed in carbonates every 10^7 years. Thus, if formation of valley networks requires water to be stable at the surface, the presence of valley networks on surfaces that formed hundreds of millions of years after the planet formed implies that some mechanisms existed for recharging the atmosphere with CO_2.

Most of the valley networks appear to be very old. They are present almost everywhere in the ancient, heavily cratered highlands, at least at latitudes below 30° (Pieri 1976, Carr and Clow 1981). In contrast, there are only a few, relatively rare, examples of valley networks on younger terrains (Masursky *et al.* 1987). The lower Hesperian plains of Lunae Planum, for example, which are among the oldest surfaces that formed after heavy bombardment, are almost devoid of branching valley networks, whereas most upper Noachian surfaces, which formed during the waning phases of heavy bombardment, have numerous valley networks. The relative scarcity of valley networks on the heavily cratered terrains at high latitudes may be due to a variety of causes. Fewer valleys may have formed at these latitudes for climatic reasons. Alternatively, just as many valleys may have formed at high latitude as at low latitude, but many were subsequently destroyed as a result of the enhanced mobility of the surface materials at high latitudes (Squyres and Carr 1986) or as a result of burial by eolian deposits (Soderblom *et al.* 1973). The almost complete restriction of the valley networks to the oldest terrains can be explained in at least three ways. (1) The conditions required for channel formation were commonly met very early in Mars's history but only rarely at later times. (2) The networks formed by groundwater seepage, and groundwater could access the surface only in the cratered highlands. (3) Channels form more easily in the cratered highlands because the highlands are more easily erodible than the plains. While (2) and (3) may be true in part, intersection relations throughout the cratered highlands appear to indicate that the dominant reason that most valley networks are restricted to the oldest terrains is that most of the valleys themselves are old (Carr and Clow 1981). This, then, is the basis for suspecting that Mars experienced a relatively warm period early in its history.

However, the climatic conditions required for formation of valley networks are poorly understood. In this context, the distinction between valley networks and large flood features must be emphasized. The flood features have a wide range of ages, and many appear to have formed by eruption of groundwater under enormous hydrostatic pressures (Carr 1979). To contain such high pressures, a thick permafrost zone and climatic conditions similar to those that currently prevail may have been required. The general morphology of the valley networks suggests that they also formed from groundwater (Pieri 1980, Laity and Pieri 1980, Baker 1981). However, their small size, the presence of tributaries, and the increase in size of the valleys downstream suggest that the valley networks formed as a result of seepage at modest discharges rather than as a result of short-lived catastrophic events. Although the climatic conditions required for groundwater seepage have not been firmly established, it has generally been supposed that surface temperatures could not have been below freezing. If they were, groundwater would have been hindered from reaching the surface by the frozen ground, and if water did reach the surface, it would have frozen before it could flow far and cause appreciable erosion (Carr 1983). Thus, we can reasonably conclude that during the time period represented by the heavily cratered highlands, that is, at the end of and immediately following heavy bombardment, Mars experienced conditions much more conducive to groundwater seepage than it did in later times. One such condition was probably a thicker atmosphere to maintain higher surface temperatures.

Pollack *et al.* (1987) addressed this problem in some detail, discussing how rapidly atmospheric CO_2 might be fixed as carbonates and how CO_2 might be returned to the atmosphere. Volcanism is their favored agent for recharging the atmosphere. They suggest that early in Mars's history, the rates of volcanism were higher than at later times. Volcanism would have released CO_2 in three ways: by release of juvenile CO_2, by burial of carbonates to depths where they dissociate, and by near-surface interaction between the hot volcanics and carbonates.

While all these mechanisms may operate, several lines of evidence suggest that impact may play a significant, if not dominant, role. First, there appears to be a connection between the impact rates and the rates of valley formation. When the impact rates declined so did the rate of valley formation. Second, if the recharge were connected with volcanism we would expect only a slow decline in recharge efficiency because of the slowly changing global heat flow. The heat flow has probably changed by a factor of no more than 5 over the last 4 Ga (Davies and Arvidson 1981), whereas, if the impact history of Mars was similar to that of the Moon, the impact rate declined over two orders of magnitude at the end of heavy bombardment. Third, the morphology of the cratered uplands demonstrates that rates of volcanism were small compared with the rate of crater production. Although intercrater plains are common, and most of these plains are probably volcanic, at least half of the visible impact craters retain rims. The rate of modification of the terrain by volcanism fell far short of the rate of modification of the terrain by impacts. As will be demonstrated later in the paper, the rates of burial by volcanics that are required to transport carbonates down to depths where temperatures would be high enough for carbonates to dissociate would result in burial of most of the craters within a short period of their formation. The dominance of impacts over volcanism is clear for the cratered highlands. However, on about one-third of the planet's surface the heavily cratered terrain is buried, and rates of volcanism in these areas (Tharsis, for example) could have been much larger.

The above reasoning, particularly the seeming correlation between the rate of formation of valley networks and the impact rates, suggests that impacts might have been a major factor in sustaining an early thick CO_2 atmosphere, and that when the impact rates declined, the atmosphere dissipated, and the rate of valley formation declined. Impacts could introduce CO_2 into the atmosphere in at least three ways: (1) carbonates that formed on the surface could have been folded so deeply into the megaregolith that they reached dissociation temperatures, (2) CO_2 could have been released from carbonates during impacts as a result of shock loading and heating, and (3) CO_2 could have been introduced onto the planet by the impacting meteorites. These three mechanisms are explored below, on the assumption that impact rates on Mars at the tail end of heavy bombardment were comparable to those on the Moon at the end of its heavy bombardment.

The intent of the paper is to make order of magnitude calculations to assess whether recharge of the atmosphere with CO_2 as a result of impacts is quantitatively plausible. Conditions on Mars during heavy bombardment are very uncertain so that precise estimates of the recharge rates should not be expected. The impact rates during this time are particularly uncertain. Lunar Nectarian rates are assumed in all the calculations.

This is a major assumption. There is some uncertainty in the age of the Nectaris basin (Wilhelms 1987) which leads directly to uncertainties in the Nectarian impact rate for the Moon, but more importantly, we do not know how cratering rates on Mars and the Moon compared during the first several hundred million years of Solar System history. Thus, while some of the models used below are simple, it is not clear that more complex models would lead to more accurate estimates of how effective impacts might have been in maintaining an early, thicker atmosphere on Mars.

BURIAL BY IMPACT EJECTA

The first mechanism to be explored is that, during heavy bombardment, mixing of the near-surface materials as a result of repeated impacts could have caused burial of carbonates to such depths that they dissociated. Burial depths were estimates on the assumption that impact rates at the end of heavy bombardment on Mars were comparable to the Nectarian rates on the Moon. The Nectarian period is at the tail end of heavy bombardment. It starts with formation of the Nectaris basin and ends with formation of the Imbrium basin. The best estimates of the ages of the Imbrium and Nectaris basins are 3.85 and 3.92 Ga, respectively, so that the Nectarian period lasted approximately 0.07 Ga (Wilhelms 1987). However, analytical errors permit time intervals that range from 0.02 to 0.13 Ga. Wilhelms (1987) derived the cratering rate during the Nectarian period by counting craters on the ejecta blankets of the Imbrium and Nectaris basins. The crater counts are restricted to craters larger than 20 km because of mutual crater destruction and the difficulty of recognizing small craters on these heavily bombarded surfaces. Basins larger than 300 km were not included in the crater data but were listed individually. Wilhelms' crater curves were divided into two linear segments,

$$\log N_c = 2.552 - 1.928 \log (D) \qquad (D < 100 \text{ km}) \quad (1)$$

$$\log N_c = 2.790 - 2.050 \log (D) \qquad (D > 100 \text{ km}), \quad (2)$$

where N_c is the cumulative number of craters larger than diameter D that formed in an area of 10^6 km^2 every 10^6 years. D is expressed in kilometers. Equation (1) was used to extrapolate below 20 km where there are no data.

Two simple models were used to calculate burial rates, the purpose being to get a sense of the magnitude of the effect. While elaborate Monte Carlo models have been used to assess various effects of impact gardening (see, for example, Woronow 1978, Hörtz *et al.* 1976), for the present purposes such elaboration was not thought justified in view of the large uncertainties in the impact rates. Moreover, the concern here is with assessing globally averaged burial rates, not local variations. The first model follows Short and Foreman (1972), and takes the rate at which craters are excavated and assumes the excavated volume is spread evenly over the whole planet. This gives an upper limit on the burial rate for it does not take into account reexcavation of ejecta. The second model, which attempts to take into account reexcavation of material that had previously been deposited in the time interval of interest, gives a lower limit on burial rates.

In order to determine the volume excavated during formation of a crater we must know the shape and diameter of the transient cavity. Following Melosh (1977), a paraboloid transient cavity was assumed to form during an impact event such that

$$r = (C/2)[1 - z/\lambda C]^{1/2}, \qquad (3)$$

where C is the diameter of the transient cavity, r is the radius of the cavity at depth z, and λ is the depth/diameter ratio, taken as 0.2. The transient cavity is assumed to have collapsed into a crater of diameter D such that $C = D/c_f$. The volume of material excavated is sensitive to the collapse factor c_f. Two cases were examined. In the first case, the collapse factor was assumed to be 1.3 and independent of the crater diameter (Shoemaker 1977, Shoemaker *et al.* 1979, Shoemaker and Wolfe 1982). In the second case the collapse factor was assumed to be dependent on crater diameter. Following Short and Foreman (1972) and Hörtz *et al.* (1976), the value of c_f was assumed to be 1.25 for craters diameters less than 50 km, 1.5 for diameters between 50 and 300 km, and 2.0 for craters larger than 300 km. From (3) the volume of the transient cavity is $(\pi\lambda D^3)/8$. To determine the rate of production of ejecta the volumes of the transient cavities corresponding to the crater production function described by Eqs. (1) and (2) were summed from 100 m to 1500 km. The burial rate is then simply this volume normalized to the surface area of the planet. The results, expressed in terms of the time taken for burial to a given depth, are shown in Fig. 1.

The procedure just outlined does not to take into account the fact that material is repeatedly turned over, particularly at shallow depths. To account for this, burial rates were calculated in a second way. It was assumed that, at any given depth, the average burial rate due to impact is the rate at which material accumulates above that depth (the rate of deposition of ejecta on the surface) less the rate at which material is removed from above that depth (the volume excavated from above that depth in forming all the craters). At any given depth d, therefore, the average burial rate B is given by

$$B = (V_c - V_a)/At = V_b/At, \tag{4}$$

where V_c is the volume of ejecta deposited on the surface during time t, in other words, the volume of all the transient cavities associated with the craters that formed; V_a is the volume of material excavated above depth d, that is that fraction of the total transient cavity volume that lies above depth d; V_b is that fraction of the total crater volume that lies below depth d; and A is the area of the planet. According to the model, the rate of burial at any given depth is affected only by craters that extend below that depth; shallower craters merely stir the overlying material. At the depth of the deepest crater the average burial rate is zero. At this depth the volume of material deposited on the surface exactly equals the amount removed to form the craters so that there is no net burial in a globally averaged sense.

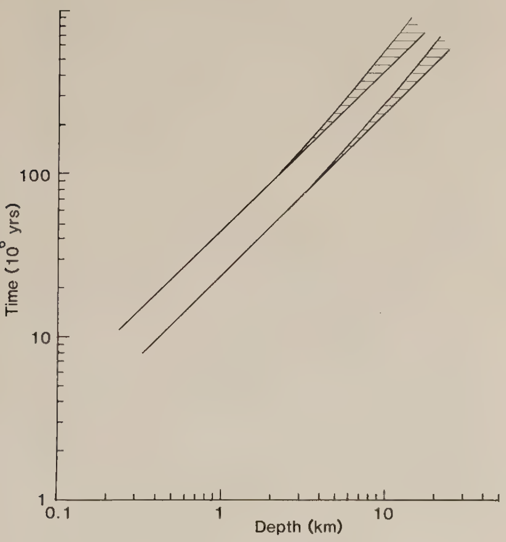

FIG. 1. Time taken for material to be buried to different depths as a result of Nectarian impact rates. The lower curves are for a constant c_f. The upper curves are for a diameter-dependent c_f. For each assumption for c_f two models are shown, as described in the text.

To determine burial rates from Eq. (4), the volume, V, excavated from below the depth of interest d is derived by integrating Eq. (3) from d to the base of the crater:

$$V = (\pi C^2/4)[(\lambda C - d) - (\lambda^2 C^2 - d^2)/2\lambda C]. \tag{5}$$

Volumes were calculated for every one-tenth incremental increase in crater diameter from 100 m to 1500 km using the cratering rate given in Eqs. (1) and (2), and for depths up to 60 km. As before, C was calculated by using both a constant c_f and a diameter-dependent c_f. The results are shown in

Fig. 1. As can be seen from Fig. 1, burial rates calculated by the two methods are essentially identical for depths less than a few kilometers; they only diverge significantly for depths greater than around 10 km.

Burial rates are sensitive to the assumed relation between the transient cavity diameter and the crater diameter. For the constant c_f model used by Shoemaker and coworkers, the burial rate calculated from the total ejecta volume for the Wilhelms' Nectarian impact rate is 4.3×10^{-2} km/10^6 years. For the variable c_f model, the equivalent burial rate is 2.3×10^{-2} km/10^6 years. At these rates it would take material deposited on the surface 230 and 430 myr, respectively, to reach a depth of 10 km.

To assess whether this effect could result in significant recycling of CO_2 we need to know the near-surface temperature gradients at this time. Thermal modeling of Mars's interior suggests that global surface heat fluxes could have ranged from 50 to 150 mW m^{-2} (Davies and Arvidson 1981, Basaltic Volcanism Study Project 1981, Schubert *et al.* 1979). What thermal conductivities are appropriate is unclear. In Fig. 2, possible temperature profiles are shown for two extreme assumptions for the thermal conductivities. The shallow thermal gradients are based on the Schatz and Simmons (1972) thermal conductivity $k = k_L + k_R$, where

$$k_L = 10^2/(7.4 + 0.05T) \text{ W m}^{-1}\,°\text{K}^{-1}$$

and

$$k_R = 0.0023(T - 500) \text{ W m}^{-1}\,°\text{K}^{-1}.$$

k_L is the lattice conductivity, k_R is the radiative term, and T is the temperature (°K). These conductivities are almost certainly too high. They are for solid basalt with zero porosity, whereas the cratered highlands must have been brecciated. Like the lunar highlands, they would have had significant porosity, and hence a lower conductivity, at least in the upper few kilometers.

The low-conductivity model is based on the assumption that fracturing by impact would have had a significant effect on the thermal conductivity (Horai and Winkler 1980, Warren and Rasmussen 1987). On the Moon, an incompetent, megaregolith with an estimated porosity of 5–20% extends down to a depth of about 2–3 km. According to seismic data, this is underlain by a low porosity layer extending down to about 20 km, below which the porosity is effectively zero. A similar model is used here for Mars except that, because of the higher gravity, the high porosity layer would be only 1 km thick and the base of low porosity layer would be at 10 km. Mitzutani and Osako (1974) determined the conductivity of an anorthositic breccia with 15% porosity to be 0.194 W m^{-1} °K^{-1}, under vacuum

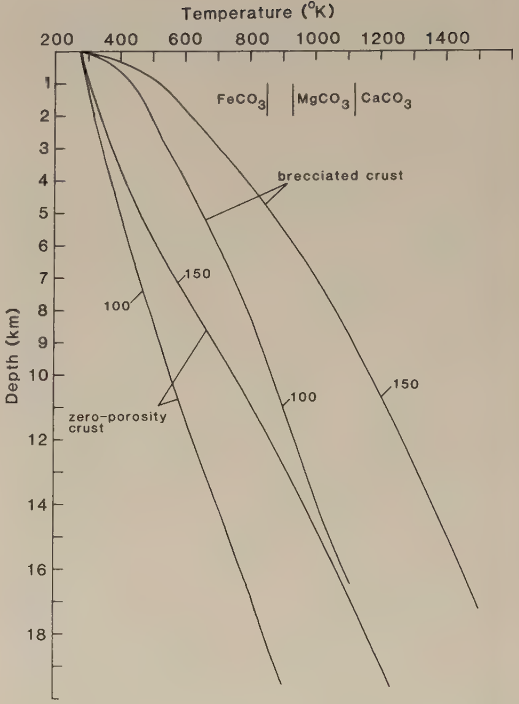

FIG. 2. Possible thermal profiles at the end of heavy bombardment when heat flows are estimated to be between 100 and 150 mW m^{-2} sec^{-1}. The two curves on the right are for the low conductivity model; the two on the left are for the high conductivity model. The most plausible profiles are believed to be close to the two center profiles. The profile on the right is unlikely because it results in a lithosphere that is too thin. The profile on the left combines an implausibly high conductivity with the lower bound on the heat flow. Also shown are the dissociation temperatures of the three most probable carbonates.

conditions. Mars's breccias are likely to be composed of more conducting Fe/Mg silicates, which would increase the conductivity by a factor of about 2.2, and have its pores filled with CO_2 gas, further increasing its conductivity by a factor of 1.3–1.5 (Horai and Winkler 1980). A thermal conductivity of 0.6 W m^{-1} $°K^{-1}$ was accordingly used for the upper porous layer. This is probably un underestimate of the conductivity, because on Mars the pores are likely to be partly filled with water. For the low porosity layer, the Schatz and Simmons conductivity, given above, was used except for a modification for microfracturing. On the basis of the experimental work of Robertson and Peck (1974), the Schatz and Simmons conductivity was reduced by 50% at 1 km depth and the correction reduced linearly to zero at 10 km depth. Below 10 km the unmodified Schatz and Simmons conductivity was used. The resulting thermal profiles are shown in Fig. 2.

To assess the efficacy of burial in recycling CO_2, the dissociation temperatures for the three most likely carbonates are shown in Fig. 2. These are calcite (860°C), magnesite (660°C), and siderite (585°C) (Hutchison 1974). It can be seen that dissociation temperatures for all three carbonates are reached at depths shallower than 10 km only for the improbable combination of an upper limit on the heat flow and a low near-surface conductivity. This combination results in an implausibly thin lithosphere of 20 km. In the other models $FeCO_3$ would not dissociate at depths less than 10 km, and $CaCO_3$ would not dissociate at depths less than about 17 km.

Enough CO_2 could have outgassed from the planet to form an atmosphere with a surface pressure of 10 bars or to form a carbonate layer 250 m thick (Pollack and Black 1979, Carr 1986). If this were distributed evenly throughout the upper 10 km of the crust as a result of impact gardening, then the megaregolith would contain 2.5% carbonate. At the burial rate calculated for a constant c_f, the equivalent of 0.043 bar of CO_2 would have been transported to 10 km depth every 10^6 years. Thus, in the unlikely event that the right-hand curve in Fig. 2 is correct, 0.43 bar of CO_2 could be released every 10^7 years, enough to almost offset the 1 bar estimated to have been fixed every 10^7 years. For the diameter-dependent c_f model, the equivalent figure is 0.23 bar. As can be seen from Fig. 1, burial to 10 km also requires that the Nectarian impact rate be sustained for most of the period between planet formation and emergence of the geologic record around 3.8 byr ago.

For the more probable thermal profiles for 3.8 byr ago, burial to depths of 15–20 km is required for $MgCO_3$ and $CaCO_3$ to dissociate. If the 10 bars of CO_2 were distributed evenly throughout the upper 15 km, the megaregolith would contain 1.7% carbonate. The equivalent of 0.29 and 0.15 bar of CO_2 in carbonates would be delivered to a depth of 15 km every 10^7 years for the two models being considered. However, only for the constant c_f model is there sufficient time for the carbonates to reach this depth. Earlier in the heavy bombardment period, thermal gradients would have been steeper (Schubert *et al.* 1979) and dissociation depths correspondingly shallower. Thus carbonates may have been delivered to depths where they could dissociate continuously throughout heavy bombardment, despite relatively slow rates of burial.

The above reasoning can be applied to volcanism. If we assume that burial to depths of 15 km is needed for release of CO_2, and this must be done in a time no longer than 500 myr, then a burial rate of 30 m/10^6 years is required. This would produce CO_2 at a rate of 0.2 bar every 10^7 years if 10 bars were distributed evenly throughout the overlying materials. However, such a rate of volcanism is quite implausible for the two-thirds of the planet on which the old cratering record has survived. Fully half the visible craters in the Martian highlands retain crater rims. The crater density on the highlands is roughly equivalent to the density on the rim of the Nectaris basin on the Moon. If we assume the Nectarian rates apply to Mars, the entire population of craters visible in the highlands formed in about 10^8 years. The vast majority of the highland craters are less tha 100 km in diameter. A fresh 100-km-diameter crater on Mars would have a rim height of about 800 m (Pike and Davis 1984). Thus, from all causes, rims were eroded or buried at a rate of 800 m every 5×10^7 years, or 16 m/10^6 years. Part of the rim destruction must be due to burial by impact and eolian debris and to erosion, so an upper limit of 10 m/10^6 years for volcanic burial appears reasonable. Even this rate is likely to be an overestimate since the rims of all the craters 100 km in diameter and smaller would have been buried within 80 myr of the end of heavy bombardment. This clearly did not happen over the surviving cratered terrain. If these high volcanic rates are valid, therefore, the rates of volcanism must have declined at the same time that the impact rates declined. The above argument, of course, only applies to the surviving cratered terrain. In the areas now covered by volcanics, higher rates were obviously sustained. Nevertheless, in order to replenish atmospheric CO_2 by volcanic burial alone, implausibly high rates of volcanism must be invoked to deliver material to the depths needed in the times required.

We can conclude from this section that if the diameter-dependent c_f model is approximately correct, impact gardening alone is unlikely to have resulted in burial of carbonates to depths where they would dissociate. If the constant c_f model is correct, carbonates could be delivered to depths required for dissociation, and CO_2 could be released at a rate of a few tenths of a bar every 10^7 years. Volcanic burial rates of up to 10 m/10^6 years are compatible with observations. If added to the impact burial rates, the resulting burial rate, even for the variable c_f model, may be just sufficient to deliver carbonates fixed at the surface to the 15–20 km depths. All these conclusions assume that a Nectarian impact rate is maintained from the time of formation of the planet until around 3.8 Ga years ago when the impact rates are believed to have declined to close to their present rate.

SHOCK-INDUCED DECOMPOSITION OF CARBONATES

The second way that CO_2 could be introduced into the atmosphere is as a direct result of impacts into carbonate-bearing surface materials. Kieffer and Simonds (1980) suggested that the observed deficiency of impact melts around large terrestrial impacts in carbonate rocks may result from dispersion of the melt by release of CO_2 formed by decomposition of the carbonates. Lange and Ahrens (1986) showed that during experimental impacts into calcite crystals, CO_2 gas starts being released at peak shock pressures of 100 kbar, and that approximately 50% of the CO_2 in the calcite is released at peak shock pressures of 200 kbar. In addition, impacts leave a thermal anomaly. This anomaly, when superimposed on the geothermal gradient, could raise ambient temperatures at depths well below the surface such that carbonates could dissociate. Thus, while the CO_2 in Mars's early atmosphere would have tended to become fixed as carbonates in the soil, impacts would have tended to break down the carbonates and introduce CO_2 back into the atmosphere. As will be shown below, the mechanism is significant only at the high impact rates expected during heavy bombardment. Only trivially small amounts of CO_2 could be reinjected into the atmosphere with the small impact rates experienced for most of the planet's history.

In order to assess the magnitude of direct release by impact, the Nectarian cratering rate on the Moon (Wilhelms 1987) was again taken as an indication of what the cratering rates might have been like on Mars at the end of heavy bombardment. These cratering rates were transposed into frequencies of different energy events by means of appropriate scaling laws; then the size of the impacting body was determined for different assumed meteorite densities and impact velocities. The volume of material shocked to 200 kbars was calculated using the impact model of Kieffer and Simonds (1980), which is itself an outgrowth of the models of Shoemaker (1963) and Gault and Heitowit (1963). Models of Kieffer and Simonds (1980) and Gault and Heitowit (1963) were also used to calculate residual temperatures after the impact. The CO_2 released is determined from the volume of target material that either is shocked to 200 kbar or is left with a residual temperature in excess of the dissociation temperature of carbonates, taken as 1030°K. The Kieffer and Simonds paper is referred to as K and S in the remainder of this paper.

Following Shoemaker and Wolfe (1982) the energy yield for each crater diameter was determined from

$$D = (g_e/g_m)^{1/6} c_f k_n W^{1/3.4}, \qquad (6)$$

where g_e and g_m are the accelerations due to gravity on the Earth and Mars, c_f is the collapse factor, $k_n = 0.074$ km/(kiloton TNT equivalent), and W is the yield in kilotons of TNT (4.185×10^{19} ergs). As in the previous section, models assuming a constant c_f and a diameter-dependent c_f were examined. The density of the Martian surface was assumed to be the same as that for alluvium at the Nevada test site, where the above relationship was formulated. The yield gives the meteorite radius directly for assumed values of the meteorite density and impact velocity. In most cases examined, a meteorite density of 2.98, equivalent to basalt, was assumed. A range of impact velocities was examined, but, as will be shown below, the final volume subject to 200 kbars pressure or temperatures high enough to cause dissociation is relatively insensitive to the impact velocity, provided the velocity is large enough that the 200 kbars pressure is initially achieved.

Given the meteorite size, density, and impact velocity, and assuming specific properties for the target materials, the volume subject to 200 kbars pressure can be calculated following the procedure of K and S, which is briefly outlined here. At impact, shock waves move from the meteorite–target interface both back up into the meteorite and down into the target, enclosing between them material at uniform particle velocity and shock pressure. Shock and particle velocities are linearly related such that

$$U = c_0 + su, \qquad (7)$$

where U and u are the shock and particle velocities, respectively, and c_0 and s are constants for a specific material. (For values of c_0 and s for different materials, see K and S, Table B1.) From conservation of mass and momentum, the particle velocity during the initial stages of impact can be derived from the following quadratic equation:

$$\rho_{0m}[c_{0m} + s_m(v_i - u_t)](v_i - u_t) = \rho_{0t}(c_{0t} + s_t u_t)u_t. \qquad (8)$$

The subscript 0 refers to unshocked material, the subscripts t and m refer to the target and meteorite, respectively, and v_i is the impact velocity. ρ is the density. The initial peak pressure is determined from the relation

$$P - P_0 = \rho_{0t} U_t u_t, \qquad (9)$$

where P_0 is the pressure before impact. By the time the shock wave in the meteorite propagates to the back face of the meteorite, the fraction of the impact energy transferred to the target (f_t) is

$$f_t = 1 - [(v_i - u_t)^2 + u_t^2]/v_i^2. \qquad (10)$$

Assuming spherical geometry, the total energy transferred to the target at this stage can be used to determine the radius (r_{0t}) of the target volume moving into the ground at particle velocity u_p:

$$(r_{0t}/r_{0m})^3 = (f_t/2)(v_i/u_t)^2(\rho_{0m}/\rho_{0t}). \qquad (11)$$

After the shock wave in the meteorite hits the back face of the meteorite, energy still continues to be transferred to the target as the rarefaction wave moves down into the meteorite. Following K and S, it was assumed that when the rarefaction wave reached the interface between the meteorite and the target all the initial energy had been transferred to the target, in which case the radius of the target at pressure P is given by

$$r_0 = r_{0t}(f_t)^{-1/3}. \tag{12}$$

The penetration depth (p) is approximated by

$$p = 4r_{0m}u_t/U_m \tag{13}$$

on the assumption that the shock wave into the unshocked meteorite and the rarefaction wave back into the shocked meteorite have the same velocity U_m. For all cases considered, the penetration depth was greater than r_0 (Fig. 3).

The above procedure allows the calculation of the penetration depth p to the center of a volume of radius r_0 that is shocked to pressure P, at the time that all the energy of impact has been transferred to the target. All three parameters depend on the assumed impact velocity. For example, for a 1-km-diameter crater, formed by a basaltic meteorite hitting basalt at 5 km/sec, $p = 54$ m, $r_0 = 45$ m, and $P = 467$ kbars. For a 25 km/sec impact velocity, $p = 27$ m, $r_0 = 16$ m, and $P = 8082$ kbars. As the shock wave moves outward from this initial volume, the peak pressure, experienced by the newly engulfed materials, decays. Following the preferred model of K and S, a -3.6 decay law was assumed, and the radius of material subject to a peak shock pressure of 200 kbars is

$$r_{200} = r_0(200/P)^{-1/3.6}. \tag{14}$$

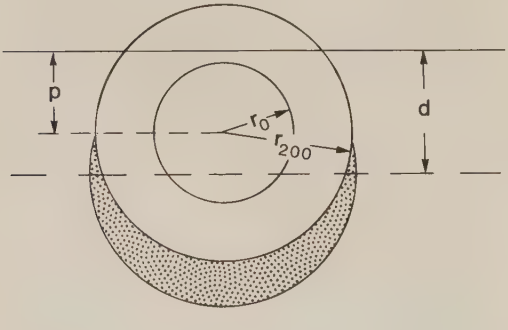

FIG. 3. The geometry of impact, showing various parameters referred to in the text. The shaded area represents material left after the impact event with temperatures above the dissociation temperatures of carbonates.

In the examples above r_{200} for a 5-km/sec impact velocity is 57 m, whereas for a 25-km/sec impact velocity, r_{200} is 43 m. Thus, a fivefold difference in impact velocity results in less than a factor of 2 difference in the total volume of material subject to the critical pressure.

To calculate the volume shocked to 200 kbars, the surface was divided into 50-m-thick slabs. The intersection of any slab at depth d, with the sphere radius r_{200} about the impact point, defines a disk of material shocked to 200 kbars. We saw in the previous section that, on a time scale of tens of millions of years, the carbonates could be buried to depths of several kilometers by impact gardening and volcanism. For very large craters the volume subject to pressures over 200 kbars extends well below where the carbonates could reasonably be expected. Volumes shocked to 200 kbars were summed down to different depths below the surface, and values of 1, 2, 4, 8, and 16 km for this limiting depth were examined.

This procedure was modified slightly to take into account irreversible heating of the target materials. After the impact event is over, a thermal anomaly remains. If the target materials were already at elevated temperatures as a result of their burial, dissociation temperatures of carbonates could be achieved. The effect is trivial for shallow depths where ground temperatures are well below the dissociation temperatures, but at depths greater than 8 km this effect can be significant. Heating results because different P–V paths are taken for compression and rarefaction (Fig. 4). Compression follows the Rayleigh line, whereas rarefaction is adiabatic and follows a path similar to the Hugoniot (K and S, Fig. 5; Gault and Heitowit 1963). The energy available for heating is determined from the area under between the two curves.

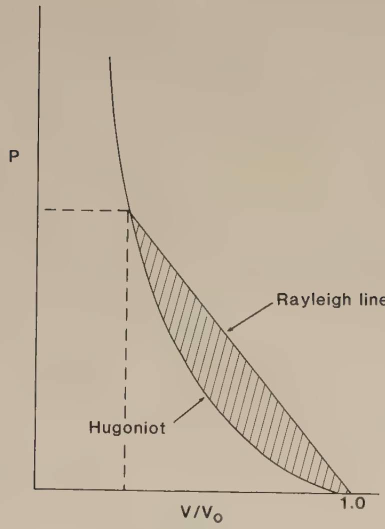

FIG. 4. Typical plot of shock pressure P against the change in volume V/V_0. Irreversible heating is computed from the shaded area between the two lines, representing different paths for compression and rarefaction.

At each depth, the temperature increase (T_{ex}) that the impact must cause in order to reach dissociation temperatures was determined. This is simply 1030°K − T_g, where T_g is the temperature due to the thermal gradient. As before, the 100 mW m^{-2} curve for porous near-surface materials was used to determine T_g. The temperature of 1030°K was chosen because it is the mean between the dissociation temperatures of $CaCO_3$ and $MgCO_3$. The shock pressure required to cause such a temperature increase was calculated as follows. The Hugoniot was determined from

$$P = (K_0/n)[(V_0/V)^n - 1], \tag{15}$$

where K_0 is the adiabatic bulk modulus, V_0 is the volume at zero pressure, V is the volume at pressure P, and n is a constant. Values for different materials are given in K and S, Table B1. The area between this curve and the Rayleigh line gives the heat produced per unit volume, for any given pressure, from which temperature is determined directly. The amount of heating that can result from impact depends strongly on the porosity of the materials. Two materials were examined. Basalt, which is relatively incompressible, and so minimizes heating effects, and ice-saturated sand which is more compressible. (It was recognized that ice-saturated sand is unrealistic for depths of 10–15 km, but the appropriate shock parameters are known for this material, and the results could be taken as an upper limit for the effect of shock heating. Other candidates which result in more extreme heating, such as Cononino Sandstone, were considered even more unreasonable analogs for the relatively large depths at which this process becomes significant.) For basalt and ice-saturated sand, the shock pressures required to heat the materials to the dissociation temperature are, respectively,

$$P = 3.279 + 0.9135\, T_{ex} - 2.142 \times 10^{-3}\, T_{ex}^2 + 1.748 \times 10^{-6}\, T_{ex}^3 \tag{16}$$

$$P = 3.439 + 0.4644\, T_{ex} - 5.829 \times 10^{-4}\, T_{ex}^2 + 2.813 \times 10^{-7}\, T_{ex}^3, \tag{17}$$

where T_{ex} is the difference between pre-impact temperature and the carbonate dissociation temperature. (These curves are valid only for T_{ex} less than 850°K.) The distance from the impact center out to where the pressure falls to these values was determined from Eq. (14), substituting the appropriate pressure for 200 kbars.

The procedure just outlined was followed for craters starting at 1 km in diameter and continuing in one-tenth of a diameter increments up to 1500 km for the crater distributions given in Eqs. (1) and (2). Impact velocities ranging from 5 to 25 km/sec were examined but the results are insensitive to impact velocity. Results for a 15 km/sec impact velocity are shown in Fig. 5 where volumes of material that experienced conditions that would cause release of CO_2 are expressed in terms of the crater diameter and depth below the surface. At depths less than 8 km about 0.01% of the material present is shocked to the appropriate conditions for CO_2 release every 10^6 years. Because of the dominance of large craters in

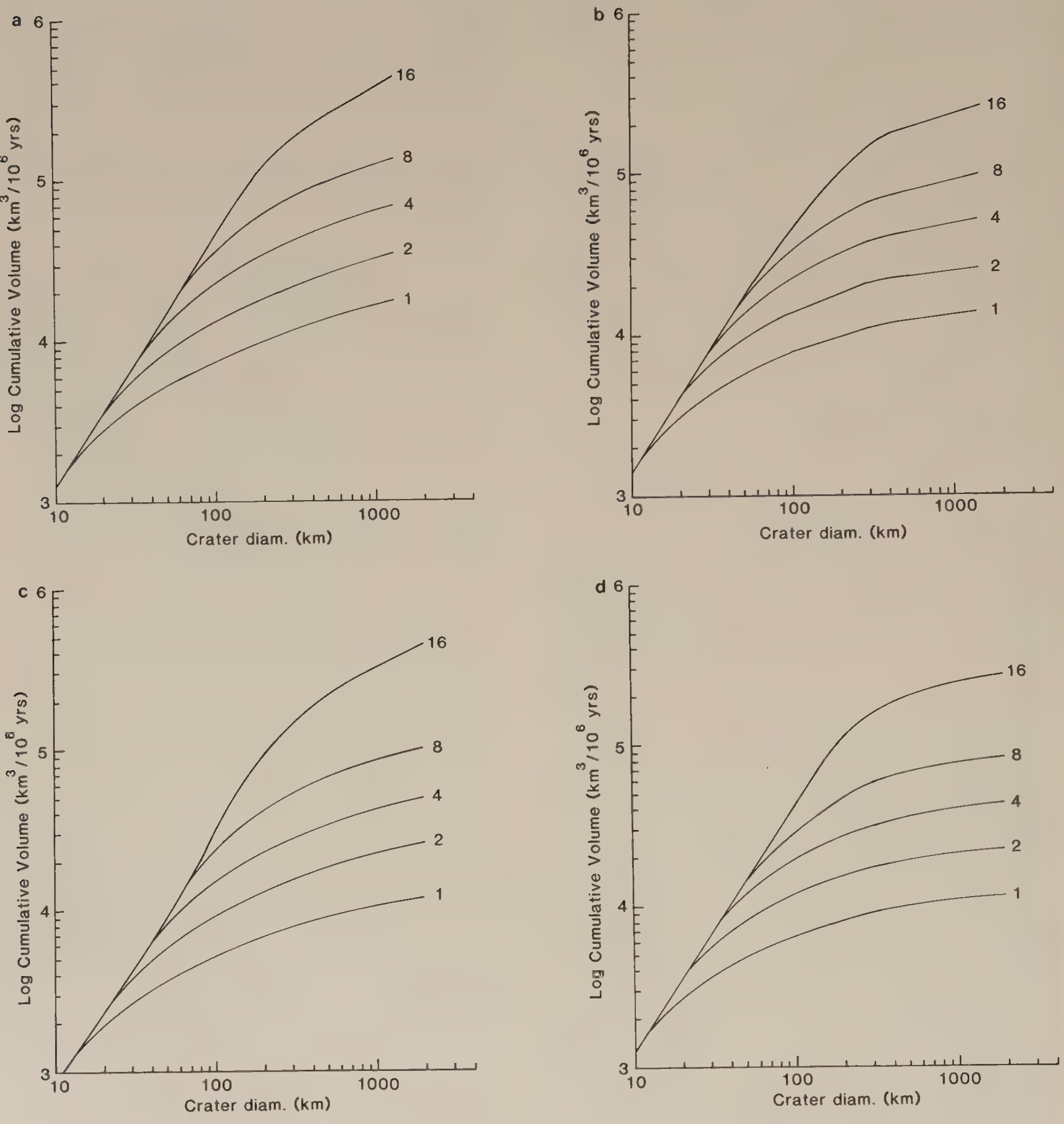

FIG. 5. The cumulative volume of material that experienced conditions which would cause dissociation of a calcite as a function of crater diameter, assuming Nectarian impact rates. The different curves show the volume summed to the different depths in kilometers below the surface as shown. The impact velocity is 15 km/sec. The divergence of the 16-km curve from the others indicates the importance of irreversible heating at larger depths. (a) Basaltic meteorite impacting a basaltic crust, constant c_f. (b) Basaltic meteorite impacting a basaltic crust, diameter-dependent c_f. (c) Basaltic meteorite impacting ice-saturated sand, constant c_f. (d) Basaltic meteorite impacting ice-saturated sand, diameter-dependent c_f.

the Nectarian crater distribution, this faction is almost independent of depth. It is also almost independent of the materials assumed and the model for c_f. For the four models shown the range is 0.0083 to 0.013%. At larger depths, irreversible heating becomes important and a greater fraction of the material experiences conditions that would cause release of CO_2. For the more realistic basalt model, the fraction increases to about 0.02% of the material down to a depth of 16 km. At depths much greater than this the heating model falls apart because the normal temperatures due to the geothermal gradient approach dissociation temperatures.

Thus, assuming a Nectarian impact rate, every 10^6 years, 0.01 to 0.02% of the materials within 16 km of the surface were subject to conditions that would have released CO_2. If most of the 10 bars of CO_2 estimated to have been outgassed (Pollack and Black 1979, Carr 1986) were distributed as carbonates throughout the upper 16 km, then CO_2 would be released at a rate of 0.01 to 0.02 bar every 10^7 years. If we take into account the analytical errors for the Imbrium and Nectaris basin ages, then the range increases to 0.005 to 0.07 bar.

This result suggests that the shock-induced release of CO_2 was not significant in sustaining an early thick atmosphere, if the estimates of fixation of CO_2 at a rate of 1 bar every 10^7 years are correct (Pollack *et al.* 1987, Fanale *et al.* 1982). Three factors could have led to an underestimate of the CO_2 released. First, a Nectarian impact rate was assumed. Between the time of formation of the Nectaris basin, 3.92 Ga until about 3.5 Ga ago, the impact rate on the Moon appears to have been decreasing exponentially (Wilhelms 1987, Wetherill 1981, Shoemaker 1981). Thus, the impact on the Moon prior to the time of formation of the Nectaris basin could have been significantly higher than that assumed. Second, a lunar impact rate was assumed for Mars. Since we have no age data for Mars, we have no plausible alternative to using lunar impact rates. Furthermore, since the source of the objects that caused the heavy bombardment on the Moon is not known, we have no satisfactory way of extrapolating from the Moon to Mars, so this assumption could involve significant errors. A third concern is the applicability of the experimental data on CO_2 release to large impacts. The shock experiments are conducted with centimeter-scale projectiles, whereas the large planetary impacts are by kilometer-size objects. For the same impact velocities and target materials, the peak pressures are independent of scale. However, the time that the peak pressures are sustained depends directly on the scale, and the 10^5 to 10^6 longer duration of the natural impacts may have resulted in release of CO_2 at lower pressures than were detected in the laboratory experiments. Despite these factors, it appears unlikely that CO_2 released simply by shock could have been as high as a few tenths of a bar every 10^7 years, although a few tenths of a bar every 10^8 years is plausible.

ACCRETION OF METEORITIC CARBON

The last hypothesis to be considered is that carbon could be directly added to the atmosphere from the impacting meteorites. Disequilibrium between the Earth's upper mantle and core suggests that the Earth accreted a late veneer of volatile-rich material (Turekian and Clark 1969, Anders and Owen 1977, Ringwood 1979, Wänke 1981). The composition of the veneer is believed to have been similar to that of carbonaceous chondrites. It has also been suggested that a significant fraction of the volatiles in the Earth's atmosphere could be derived from cometary ices and clathrates (Oro 1961, Sill and Wilkening 1978, Chyba 1987). While most meteoritic carbon is reduced, the carbon could become oxidized after deposition on the surface, as reduced carbon is at the present day. The magnitude of this effect for Mars is difficult to assess because the composition of the impacting bodies and their velocities are not known. The distribution of events of different energies was calculated for the Nectarian cratering rate from Eq. (6). For an impact velocity of 10 km/sec, the rate of infall of material at the end of heavy bombardment is estimated to be approximately 10^{21} g/10^6 years, summing over all the craters and basins. For comparison, one bar of CO_2 on Mars is 3.88×10^{21} g. The most carbon-rich meteorites are C1 carbonaceous chondrites, which contain, on average, 3% carbon (Mason 1971). Thus, if all the crater-forming bolides at the end of heavy bombardment were carbonaceous chondrites, CO_2 could accumulate at a rate of about 0.3 bar every 10^7 years. The potential contribution from ices is more difficult to assess. While there is abundant spectral evidence of carbon compounds in comets, the fraction that might be present in ices, and what fraction of the cometary material is ice, are both unknown. Accordingly, no estimates were made of the contribution from ices. We can conclude, however, that at the end of heavy bombardment, cometary and meteoritic material could potentially add CO_2 to the atmosphere at about the same rate as CO_2 is released from the ground by burial and shock loading.

SUMMARY AND IMPLICATIONS

If impact rates on Mars throughout the early period of heavy bombardment were comparable to Nectarian rates on the Moon, burial of carbonates by impact debris to depths where dissociation may occur could result in the release of 0.1 to 0.3 bar of CO_2 every 10^7 years. However, dissociation probably required burial to depths in excess of 15 km, and there is barely time for this to occur between the time of formation of the planet and the end of heavy bombardment, assumed to be around 3.8 Ga ago. Nectarian impact rates had to be maintained for this entire period, and if the available c_f model is correct, the impact burial rates must be supplemented by volcanic burial. The amount of CO_2 that could be released directly by impacts is small, estimated to be only 0.01 to 0.02 bar every 10^7 years. At most, an additional 0.3 bar of CO_2 could be introduced into the atmosphere every 10^7 years by oxidation of meteoritic carbon in the impacting meteorites. Fanale *et al.* (1982) and Pollack *et al.* (1987) estimate that, if small amounts of liquid water were present on the surface, CO_2 in the atmosphere would be fixed as carbonates at a rate of approximately 1 bar every 10^7 years. Thus, the estimated recharge rates appear to fall somewhat short of those needed. Recharge by impact would fail completely to replace the fixed CO_2 if Nectarian-like impact rates were not maintained throughout the period between planet formation and the end of heavy bombardment and if the average meteorite contained much less carbon than carbonaceous chondrites.

Several factors could have resulted in the underestimation of the atmospheric recharge. First, the impact rates assumed could be in error. Nectarian rates were assumed. The Nectarian period is at the end of heavy bombardment on the Moon and earlier rates may have been higher. Also, the Nectarian rates may be inappropriate for Mars. Third, the effect of volcanism may have been underestimated. While release of CO_2, as a result of volcanic burial as proposed by Pollack *et al.* (1987), is judged here to have been only a minor effect for the surviving cratered terrain because of severe limits on the amount of volcanism that could have occurred there, release of juvenile CO_2 may have been significant, particularly when the vast volcanic pile represented by the Tharsis ridge is taken into account. Despite these qualifications, it appears unlikely that the combined release of CO_2 by impact and volcanism was as high as 1 bar every 10^7 years.

More probably the rate of fixation of CO_2 as carbonates has been overestimated. As emphasized previously, the estimates of a fixation rate of 1 bar every 10^7 years by Fanale *et al.* (1982) and Pollack *et al.* (1987) are based on the assumption that small amounts of liquid water were continuously present at the surface. As they recognized, this may be a false assumption. The fixation rate is very sensitive to the presence of liquid water. If liquid water is absent, carbonates can form only at extremely slow rates. A possible explanation of the discrepancy between the estimated fixation rates and recharge rates is, therefore, that water was only intermittently present on the surface at the time in question. This is reasonable on other grounds. Erosion rates at the end of heavy bombardment appear to have been very low. Survival of crater rims in the highlands suggests that erosion rates could have been no more than 20 m/10^6 years (unpublished data), which is low compared with terrestrial rates, and on the Earth vegetation plays a major role in arresting erosion. Indeed, there is very little evidence of enhanced erosion and infilling in the cratered highlands other than the valley networks themselves. In addition, as pointed out by Carr and Clow (1981), the drainage system on the old cratered terrain is very immature. Fluvial erosion has not been sufficiently sustained for major trunk streams to develop and dominate large drainage basins, as occurs relatively rapidly on Earth. Either erosion rates were very low or fluvial action occurred only intermittently.

One possible explanation of the presence of water-worn valley networks, low overall erosion rates, and low rates of fixation of CO_2 as carbonates is that the atmosphere during heavy bombardment was maintained such that temperatures remained just below those required for liquid water to be stable at the surface. If CO_2 released by volcanism and impacts caused the atmosphere to thicken and temperatures to rise, thereby allowing liquid water to be stable at the surface, CO_2 would be lost and temperatures would fall below freezing again. With temperatures close to freezing, groundwater would be close to the surface, and could seep onto the surface, given the right hydrostatic conditions. Seepage could also occur as small climatic changes, occurring in response to the obliquity cycle. At high obliquities CO_2 could have been driven off the polar caps to cause temperatures to temporarily rise above freezing. Thus, during heavy bombardment the atmosphere may have been in quasi-equilibrium, with mean temperatures just below freezing. When the impact rates declined, the equilibrium could no longer be maintained. Recharge could not keep pace with even the low CO_2 fixation rates that apply when mean temperatures fall well below freezing. The atmosphere, therefore, slowly thinned, global temperatures fell, groundwater could only rarely access the surface, and the planet assumed its present frigid state.

ACKNOWLEDGMENTS

I am particularly indebted to J. Gooding who suggested I pursue the idea of shock release of CO_2, in addition to release by burial. G. Clow calculated possible thermal profiles in the crust. R. Baldwin provided preliminary estimates of burial rates of craters in the highlands. The work was supported by NASA Grants W 15,814 and W 16,433.

REFERENCES

ANDERS, E., AND T. OWEN 1977. Mars and Earth: Origin and abundance of volatiles. *Science* **198,** 453–465.

BAKER, V. R. 1981. *The Channels of Mars*. Univ. of Texas Press, Austin, TX.

Basaltic Volcanism Study Project 1981. *Basaltic Volcanism on the Terrestrial Planets*. Pergamon, New York.

CARR, M. H. 1979. Formation of Martian flood features by release of water from confined aquifers. *J. Geophys. Res.* **84,** 2995–3007.

CARR, M. H. 1981. *The Surface of Mars*. Yale Univ. Press, New Haven, CN.

CARR, M. H. 1983. The stability of streams and lakes on Mars. *Icarus* **56,** 476–495.

CARR, M. H. 1986. Mars: A water-rich planet? *Icarus* **68,** 187–216.

CARR, M. H., AND G. D. CLOW 1981. Martian channels and valleys: Their characteristics, distribution and age. *Icarus* **48,** 91–117.

CESS, W. G., V. RAMANATHAN, AND T. OWEN 1980. The Martian paleoclimate and enhanced atmospheric carbon dioxide. *Icarus* **41,** 159–165.

CHYBA, C. F. 1987. The cometary contribution to the oceans of primitive Earth. *Nature (London)* **330,** 632–635.

DAVIES, G. F., AND R. E. ARVIDSON 1981. Martian thermal history, core segregation and tectonics. *Icarus* **45,** 339–346.

DENCE, M. R., R. A. F. GRIEVE, AND P. B. ROBERTSON 1977. Terrestrial impact structures: Principal characteristics and energy considerations. In *Impact and Explosion Cratering* (D. J. Roddy, R. O. Pepin, and P. B. Merrill, Eds.), pp. 247–275. Pergamon, New York.

FANALE, F. P., J. R. SALVAIL, W. B. BANERDT, AND R. S. SAUNDERS 1982. The regolith–atmosphere–cap system and climate change. *Icarus* **50,** 381–407.

GAULT, D. E., AND E. D. HEITOWIT 1963. The partition of energy for hypervelocity impact craters formed in rock. *Proc. 6th Sympos. Hypervelocity Impact,* 419–456.

Horai, K., and J. L. Winkler 1980. Thermal diffusivity of two Apollo 11 samples 10020,44 and 10065,23: Effect of petrofabrics on the thermal conductivity of porous lunar rocks under vacuum. *Proc. Lunar Sci. Conf. 11th,* 1777–1788.

Hörtz, F., R. V. Gibbons, R. E. Hill, and D. E. Gault 1976. Large scale cratering of the lunar highlands: Some Monte Carlo model considerations. *Proc. Lunar Sci. Conf. 7th,* 2931–2945.

Hutchison, C. S. 1974. *Laboratory Handbook of Petrographic Techniques.* Wiley–Interscience, New York.

Kahn, R. 1985. The evolution of CO_2 on Mars. *Icarus* **62,** 175–190.

Kieffer, S. W., and C. H. Simonds 1980. The role of volatiles and lithology in the impact cratering process. *Rev. Geophys. Space Phys.* **18,** 143–181.

Laity, J. E., and D. C. Pieri 1980. *Sapping Processes in Tributary Systems,* pp. 271–273. NASA Tech. Memo 81776.

Lange, M. A., and T. J. Ahrens 1986. Shock-induced CO_2 loss from $CaCO_3$: Implications for early planetary atmospheres. *Earth Planet. Sci. Lett.* **77,** 409–418.

Mason, B. 1971. *Handbook of Elemental Abundances in Meteorites.* Gordon & Breach, New York.

Masursky, H. 1973. An overview of geologic results from Mariner 9. *J. Geophys. Res.* **78,** 4037–4047.

Masursky, H., M. G. Chapman, P. A. Davis, A. L. Dial, and M. E. Strobell 1987. Mars Lander/Rover/Returned sample sites. In *Lunar and Planetary Science XVIII,* pp. 600–601. Lunar and Planet. Inst., Houston, TX.

Melosh, H. J. 1977. Crater modification by gravity: A mechanical analysis of slumping. In *Impact and Explosion Cratering* (D. J. Roddy, R. O. Pepin, and R. B. Merrill, Eds.), pp. 1245–1260.

Mizutani, H., and M. Osako 1974. Elastic wave velocities and thermal diffusivities of Apollo 17 rocks and their geophysical implications. *Proc. Lunar Sci. Conf. 5th,* 2891–2901.

Oro, J. 1961. Comets and the formation of biochemical compounds on the primitive Earth. *Nature (London)* **190,** 389–390.

Pieri, D. C. 1976. Martian channels: Distribution of small channels on the Martian surface. *Icarus* **27,** 25–50.

Pieri, D. C. 1980. Martian valleys: Morphology, distribution and age. *Science* **210,** 895–897.

Pike, R. J., and P. A. Davis 1984. Toward a topographic model of Martian craters from photoclinometry. *Lunar Planet. Sci. XV,* 645–646.

Pollack, J. B. 1979. Climate change on the terrestrial planets. *Icarus* **37,** 479–453.

Pollack, J. B., and D. C. Black 1979. Implications of the gas compositional measurements of Pioneer Venus for the origin of planetary atmospheres. *Science* **205,** 56–59.

Pollack, J. B., J. F. Kasting, S. M. Richardson, and K. Poliakoff 1987. The case for a wet, warm, climate on early Mars. *Icarus* **71,** 203–224.

Postawko, S. E., and W. R. Kuhn 1986. Effect of greenhouse gases (CO_2, H_2O, SO_2) on Martian paleoclimates. *J. Geophys. Res.* **91,** D431–D438.

Ringwood, A. E. 1979. *Origin of the Earth and Moon.* Springer-Verlag, Berlin.

Robertson, E. C., and D. L. Peck 1974. Thermal conductivity of vesicular basalt from Hawaii. *J. Geophys. Res.* **79,** 4875–4888.

Sagan, C., O. B. Toon, and P. J. Gierasch 1973. Climate change on Mars. *Science* **181,** 1045–1049.

Schatz, J. F., and G. Simmons 1972. Thermal conductivity of Earth materials at high temperatures. *J. Geophys. Res.* **77,** 6966–6983.

Schubert, G., P. Cassen, and R. E. Young 1979. Subsolidus convective cooling histories of the terrestrial planets. *Icarus* **38,** 192–211.

Shoemaker, E. M. 1963. Impact mechanics at Meteor Crater, Arizona. In *The Moon, Meteorites and Comets* (B. M. Middlehurst and G. P. Kuiper, Eds.), pp. 301–336. Univ. of Chicago Press, Chicago.

Shoemaker, E. M. 1977. Astronomically observable crater forming projectiles. In *Impact and Explosion Craters* (D. J. Roddy, R. O. Pepin, and R. B. Merrill, Eds.), pp. 617–628. Pergamon, New York.

Shoemaker, E. M. 1981. The collision of solid bodies. In *The New Solar System* (J. K. Beatty, B. O'Leary, A Chaikin, Eds.), pp. 33–44. Sky Publishing, Cambridge, MA.

Shoemaker, E. M., J. G. Williams, E. F. Helin, and R. F. Wolfe 1979. Earth-crossing asteroids: Orbital classes, collision rates with the Earth, and origin. In *Asteroids* (T. Gehrels, Ed.), pp. 253–282. Univ. of Arizona Press, Tucson.

Shoemaker, E. M., and R. F. Wolfe 1982. Cratering time scales for the Galilean satellites. In *Satellites of Jupiter* (D. Morrison, Ed.), pp. 277–339. Univ. of Arizona Press, Tucson.

Short, N. M., and M. L. Foreman 1972. Thickness of impact crater ejecta on the lunar surface. *Modern Geology* **3,** 69–91.

Sill, G. T., and L. L. Wilkening 1978. Ice clathrate as a possible source of the atmospheres of the terrestrial planets. *Icarus* **33,** 13–22.

Soderblom, L. S., T. J. Kriedler, and H. Masursky 1973. Latitudinal distribution of a debris mantle on the martian surface. *Icarus* **34,** 622–637.

Squyres, S. W., and M. H. Carr 1986. Geomorphic evidence for the distribution of ground ice on Mars. *Science* **231,** 249–252.

Toon, O. B., J. B. Pollack, W. Ward, J. A. Burns, and K. Bilski 1980. The astronomical theory of climate change on Mars. *Icarus* **44,** 552–607.

TUREKIAN, K. K., AND S. P. CLARK 1969. Inhomogeneous accretion of the Earth from the primitive solar nebula. *Earth Planet. Sci. Lett.* **6,** 346–348.

WÄNKE, H. 1981. Constitution of the terrestrial planets. *Philos. Trans. R. Soc. London Ser. A* **303,** 287–302.

WARREN, P. H., AND K. L. RASMUSSEN 1987. Megaregolith insulation, internal temperatures and bulk uranium content of the Moon. *J. Geophys. Res.* **92,** 3453–3465.

WETHERILL, G. W. 1981. Nature and origin of basin-forming projectiles. *Lunar Planet. Sci. Conf. 12th A,* 1–18.

WILHELMS, D. J. 1987. *The Geologic History of the Moon.* U.S. Geological Survey Prof. Paper 1348.

WORONOW, A. 1978. A general cratering history model and its implications for the lunar highlands. *Icarus* **34,** 76–88.

ICARUS **79**, 328–349 (1989)

Titan's Atmosphere and Hypothesized Ocean: A Reanalysis of the *Voyager 1* Radio-Occultation and IRIS 7.7-μm Data

E. LELLOUCH,* A. COUSTENIS,* D. GAUTIER,* F. RAULIN,† N. DUBOULOZ,† AND C. FRÈRE†

**Département de Recherches Spatiales, Observatoire de Paris-Meudon, 92195 Meudon Principal Cedex, France; and †Laboratoire de Physico-Chimie de l'Environnement, Université Paris-Val de Marne, Av. du Gal de Gaulle, 94010 Créteil, France*

Received June 15, 1988; revised September 12, 1988

***Voyager 1* radio-occultation refractivity profiles of Titan in the 0–200 km altitude range are reanalyzed in order to derive limiting profiles for the equatorial thermal structure, taking into account uncertainties on the mean molecular weight m. The major atmospheric constituents are assumed to be N_2 and CH_4 (already detected) and Ar which is a plausible additional constituent when m is greater than 28. The stratospheric abundance of CH_4 is assumed to be limited by saturation at the tropopause. Spectra calculated from the infrared thermal profiles in the CH_4 ν_4 band at 7.7 μm are compared with the *Voyager* IRIS observations. This allows us to constrain both the abundances of major atmospheric components and the stratospheric temperatures. The methane mole fraction is between 0.5 and 3.4% in the stratosphere but may be as high as 21% at the surface, whereas the atmospheric Ar/N_2 ratio can be anything between 0 and 0.27. The temperature is between 92.5 and 101°K at the ground level, and between 70.5 and 74.5°K at the tropopause. The maximum uncertainty (±4°K) occurs between 150 and 200 km altitude. A "nominal" temperature and composition profile of Titan's atmosphere between the ground and 200 km is given with tabulated values. The implications of composition and surface temperature uncertainties on the abundances of the expected major oceanic constituents are discussed, as well as the consequences for the solubility of noncondensable atmospheric constituents (H_2 and CO) and organic compounds raining out from the atmosphere.** © 1989 Academic Press, Inc.

1. INTRODUCTION

Since the *Voyager 1* flight through the Saturn system in November 1980, much information is available on Titan's thermal structure. The radio-occultation experiment has provided two vertical pressure and temperature profiles in the equatorial region between the ground and an altitude of 200 km (Lindal *et al.* 1983). These profiles are now generally used as reference profiles for most of the studies related to Titan's lower atmosphere, and a number of authors have discussed the implications for Titan's atmosphere composition and meteorology (e.g., Samuelson *et al.* 1981, Flasar 1983, Hunten *et al.* 1984). To this date, however, no extensive analysis of the uncertainty which lies on Titan's thermal profile has been performed. Evaluation of this uncertainty is very important for the following reasons: first, it is necessary for a proper determination of the abundances of the minor gaseous components as well as for the understanding of the physicochemical processes of the atmosphere; second, within the framework of the joint ESA–NASA *Cassini* space mission to the Saturn system, a Titan Probe mission analysis, which includes estimates of the descent profile of the Probe through Titan's atmosphere down to the surface, requires ther-

0019-1035/89 $3.00
Copyright © 1989 by Academic Press, Inc.
All rights of reproduction in any form reserved.

mal and density profiles with adequate error bars; third, should Titan's surface be covered by an ethane–methane–nitrogen ocean (Lunine *et al.* 1983), a number of important physical parameters of the medium (phase equilibrium constants, solubility of minor components, etc.) depend on the local temperature, which must be close to the atmospheric temperature just above the surface.

Assuming a uniformly mixed atmosphere, the radio-occultation measurements provide the ratio of the temperature to the mean molecular weight, *m*, as a function of altitude. Temperature constraints from infrared spectra (Hanel *et al.* 1981) suggest a value of *m* close to 28, and since the *Voyager* ultraviolet experiment (UVS) establishes N_2 as the major component in Titan's atmosphere (Broadfoot *et al.* 1981), a pure N_2 atmosphere was assumed in the nominal radio-occultation temperature profiles derived by Lindal *et al.* (1983). Spectra recorded by the infrared interferometer spectrometer and radiometer (IRIS) aboard *Voyager 1*, however, exhibit a strong feature at 7.7 μm due to the ν_4 band of CH_4, which implies the presence of a substantial amount of methane in Titan's stratosphere. Preliminary analyses of *Voyager* spectra suggested a CH_4 mixing ratio of about 1% (Hanel *et al.* 1981), but this estimate is elusive, because it was based on a somewhat arbitrary thermal profile. In fact, the observed methane emission permits the inference of the CH_4 mixing ratio (assumed constant with height) if the thermal profile is known, or, alternatively, the retrieval of the thermal structure if the methane mixing ratio is known. In principle, the comparison of radio-occultation profiles, derived for various values of the mean molecular weight, with thermal profiles retrieved from the ν_4 band of CH_4, allows the determination of both *m* and the thermal structure (Hunten *et al.* 1984). Of course, this is only possible within a limited altitude range ($z \sim$ 100–200 km), and if experimental uncertainties are not too large. If the major components of Titan's atmosphere were only CH_4 and N_2, the stratospheric methane mixing ratio could then be unambiguously evaluated (with some residual uncertainty due to the intrinsic errors of the measurements).

A further analysis of the *Voyager* infrared spectra shows, however, that the presence of an atmospheric component heavier than nitrogen cannot be ruled out. The minimum of the brightness temperature observed around 200 cm^{-1} (74 ± 0.5°K) indicates that the equatorial tropopause temperature cannot exceed 74.5°K (Samuelson *et al.* 1981). Comparison with the radio-occultation profile leads to $m \leq 29.36$. If *m* is higher than 28, then a heavier component is required, and on the basis of cosmological considerations (Owen 1982), argon is the most likely candidate. A lower limit of *m* (assumed to be constant *throughout* the atmosphere) could be inferred in principle from the radio-occultation-derived temperature at the ground level using the lower limit of the surface temperature, if such a lower limit can be determined. Samuelson *et al.* (1981), advocating that the atmosphere is fairly transparent at 540 cm^{-1}, derived a lower limit of the ground temperature of 94.1°K from *Voyager* IRIS spectra. The surface temperature can in principle be different from the atmospheric temperature just above it. Considering the possibility of turbulence effects, Hunten *et al.* (1984) deduced a lower value of 93.6°K for the gas temperature at the surface, leading to $m \geq 27.80$, if the atmosphere is uniformly mixed. Such a lower limit is compatible with a CH_4–N_2 atmosphere (with no argon) if the CH_4 abundance does not exceed 1.6% at the surface (Gautier 1985). On the other hand, ground-based observations at 1.2 and 1.6 μm (Fink and Larson 1979, de Bergh *et al.* 1988) suggest methane abundances significantly higher than 1.6%, in the lower atmosphere, which would tend to confirm the presence of argon. However, from a recent reanalysis of the physical properties of Titan's atmosphere, Toon *et* *al.* (1988) find the H_2 and haze opacities to be too important between 500 to 600 cm^{-1} to allow for surface observations, and stress that all previous inferences of surface temperature are incorrect, and that the presence of argon is not demonstrated. The question is thus still open.

To our knowledge, the complete information on both the thermal structure in the 0–200 km altitude range and the relative abundances of N_2, CH_4, and Ar, which can be extracted from a simultaneous analysis of the *Voyager 1* radio-occultation data and IRIS 7.7-μm spectra, has not yet been considered. This is the purpose of the present work. Radio-occultation data are reanalyzed in Section 2. In Section 3, constraints imposed by the ν_4 emission of methane are investigated and final envelope profiles for the equatorial thermal structure and molecular abundances are given. We show in particular that Titan's stratospheric thermal profile is probably warmer than Lindal *et al.*'s (1983) profile, and we propose a "nominal" profile from the ground to 200 km, satisfying all experimental data. Section 4 discusses the implications of the remaining composition and surface temperature uncertainties on the bulk composition of the possible Titan ocean, and on the solubility of noncondensable atmospheric constituents and organic compounds raining out from the atmosphere.

2. REANALYSIS OF RADIO-OCCULTATION DATA

The first step of the analysis is to define a nominal and two "extreme" equatorial thermal profiles corresponding to Lindal *et al.*'s (1983) analysis assuming pure nitrogen. The ingress and egress occultation points were located at 6.2°N lat and 258°E long (evening), and 8.5°S lat and 76°E long (morning). The two corresponding profiles are almost identical under 150 km. The quoted uncertainty on the temperature, which includes noise in the refractivity data, and uncertainties in the gas equation of state and ephemeris, is 0.7% at the surface. Above 150 km, as the signal-to-noise ratio becomes poorer, ingress and egress profiles do not match perfectly, but no noticeable feature differentiates them. At each level, the difference between ingress- and egress-derived temperatures is well within the final quoted temperature uncertainty (6 and 9% at 200 km for ingress and egress, respectively). This indicates no significant variation of the thermal profile with longitude or solar time. Considering that the equatorial IRIS spectra were taken at the same latitude as the occultation points, but at another longitude, we start with a nominal pure N_2 profile which is level by level the weighted average of the ingress and egress profiles (the relative weights depending on the noise). The uncertainty on this profile, which is taken to be 0.5% in the troposphere, increasing linearly to 5% at 200 km, defines the "hot" and "cold" pure N_2 equatorial profiles. The three profiles, hereafter referenced as LN, LC, and LH (which stand, respectively, for "Lindal: nominal," "Lindal: cold," and "Lindal: hot") are shown in Fig. 1 and described in Table I.

We now reanalyze the refractivity data in terms of various atmospheric compositions. Nitrogen and methane are the only gases to have been positively detected in Titan's atmosphere with sufficient abundance to contribute significantly to the

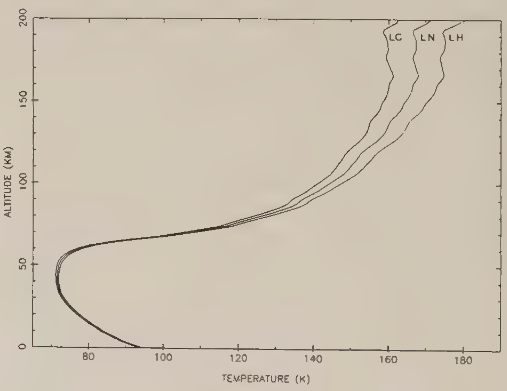

FIG. 1. The three occultation-derived profiles for a pure N_2 atmosphere. LN, LC, LH refer to nominal, cold, and hot profiles, respectively.

TABLE I

DESCRIPTION OF THE VARIOUS THERMAL PROFILES

Profile	Stratospheric composition	Stratospheric molecular mass	Inversion temperature (°K)	Temperature at the surface (°K)
LN[a]	100% N_2	28	71.4	94
LC[b]	100% N_2	28	71.0	93.5
LH[c]	100% N_2	28	71.8	94.5
OC[d]	98.5% N_2 + 1.5% CH_4	27.82	70.5	93.1
OH[e]	Various possibilities	29.07	74.5	100.6

[a] Nominal pure N_2 profile.
[b] Cold pure N_2 profile.
[c] Hot pure N_2 profile.
[d] Coldest profile allowed by the occultation data.
[e] Hottest profile allowed by the occultation data.

mean molecular refractivity and mass (hydrogen, with a mixing ratio of 0.002 (Samuelson *et al.* 1981) is negligible). Methane has been detected in various wavelengths and at various altitudes, but its mixing ratio is highly uncertain. We have mentioned above the observation of the ν_4 band of CH_4 at 7.7 μm. The ultraviolet spectrometer detected CH_4 at about 1125 km alt, with a 8 ± 3% relative abundance to nitrogen (Smith *et al.* 1982). This value, however, results from a competition between UV photodissociation of CH_4, which occurs above 600 km (Friedson and Yung 1984) and relative enrichment of CH_4 due to gravitational separation above the homopause (which lies at about 925 km above Titan's surface (Smith *et al.* 1982)). Thus, it is not possible to use it to evaluate the amount of CH_4 in the lower stratosphere (40–200 km). Methane was also detected in the troposphere in the near infrared (Fink and Larson 1979, de Bergh *et al.* 1988). Interpretation of the spectra in terms of CH_4 abundance is difficult and requires the presence of a cloud layer, but the measurements seem to agree on a 2 km-am methane column density between the ground and the cloud layer, which corresponds to an average mixing ratio of 2–2.5%. On the other hand, from a reanalysis of the far-infrared (150–600 cm^{-1}) IRIS spectra, Toon *et al.* (1988) infer a CH_4 mixing ratio at the surface of at least 6.5%, and evidence for methane clouds in the 10 to 30 km range. Therefore, we assume no a priori observational constraint on the CH_4 abundance, in the stratosphere as well as in the troposphere. We assume that under the cold trap, the maximal amount of methane is defined at each level by the local saturation law (either for condensation or sublimation). Since the convection occurring in Titan's troposphere seems modest, we assume that the methane abundance above the cold trap is limited by the cold trap saturation mixing ratio. For evaluation of the saturation pressure, we use the Thek–Stiel equation (Reid *et al.* 1977), which fits experimental data in the range 70–100°K to an accuracy always better than 3% (see Appendix). We note, however, that methane on Neptune has a stratospheric concentration which is larger than the cold trap saturation value (Courtin *et al.* 1979, Appleby 1986, Lellouch *et al.* 1986), and a similar behavior of CH_4 in Titan's stratosphere cannot be definitely excluded. On the other hand, methane may well be undersaturated in Titan's atmosphere, as is the case for water in Earth's lower stratosphere (Houghton 1984).

As mentioned previously, the presence

of argon in the atmosphere of Titan is still an open question. If indeed the atmosphere is not transparent at 540 cm^{-1} (Toon *et al.* 1988), then the idea of a large argon abundance has no observational basis. Toon *et al.* (1988) point out that the *Voyager* ultraviolet spectrometer did not detect argon emission lines, which sets an upper limit of 0.06 for Ar/N_2 at about 4000 km distance from Titan's center (Broadfoot *et al.* 1981), and use it as an additional argument against the presence of argon. Argon, however, may be depleted in the thermosphere due to mass separation. Assuming an homopause level at a distance of 3500 km from Titan's center and a mean temperature of 170°K between 3500 and 4000 km (Smith *et al.* 1982), the upper limit of the argon abundance corresponds to a maximum $Ar/N_2 = 0.40$ in the uniformly mixed atmosphere. We conclude that, although the possibility of a large argon abundance is questionable, it cannot be excluded on an observational basis. Therefore, we reanalyze the occultation data in terms of a N_2–Ar–CH_4 atmosphere. In our analysis, we assume a constant Ar/N_2 mixing ratio throughout the homosphere. Argon is considered as a 4:1 mixture of ^{36}Ar and ^{38}Ar (Gautier 1985) and its molecular mass is thus taken as 36.4. Values used for the molar refractivity are 294, 277, and 430 × 10^{-6} for nitrogen, argon, and methane, respectively. Conversion of refractivity profiles into thermal profiles can be performed by using the simple equations

$$N(z) = \frac{R(z)}{\alpha(z)}$$

$$p(z) = \int_z^{+\infty} m(z')N(z')g(z')dz',$$

where $N(z)$ is the concentration, $p(z)$ the pressure, $R(z)$ the experimental observed refractivity, $\alpha(z)$ the mean molar refractivity, $m(z)$ the mean molecular mass, and $g(z)$ the gravity at altitude z. The temperature profile can be inferred from the number density and pressure profiles under an assumption on the gas equation of state. If the gas is perfect and the atmosphere uniformly mixed, the temperature is given by

$$T(z) = \frac{m}{kR(z)} \int_z^{+\infty} R(z')g(z')dz'$$

and is thus proportional to the mean molecular mass. Departure from uniform mixing causes significant alteration of this proportionality, even if the gas is perfect.

2.1. The Stratosphere

Above the methane condensation level (the "cold trap"), which occurs between 30 and 32 km, depending on the composition of the atmosphere, the three gases are assumed to be uniformly mixed. At these low pressures, the gas mixture is perfect, and the temperatures are simply proportional to the mean molecular mass. The maximum stratospheric methane mixing ratio depends on the cold trap temperature, which is itself a function of the composition. Therefore, for a given Ar/N_2 ratio, this maximum CH_4 abundance must be found by iteration. In this frame, it is possible to easily derive a few constraints on the abundances of the gases and on the thermal profile in the stratosphere:

(i) The stratosphere methane mixing ratio cannot exceed 3.4%. This value is obtained by scaling any of the pure N_2 profiles (LN, LC, LH, or any other between) allowed by the uncertainty of the radio-occultation data to a maximum inversion temperature of 74.5°K (Samuelson *et al.* 1981). The methane condensation level temperature is then 75.4°K. The quantity of argon which is required depends on the assumed initial pure N_2 profile. The maximum possible Ar/N_2 mixing ratio, 0.27, is obtained by starting with the "cold" N_2 profile (LC). This case corresponds to the upper limit of the molecular mass, 29.36. As will be shown in Section 3, it is not possible to constrain the argon mixing ratio any further.

(ii) If argon is absent, the maximum methane mixing ratio is 1.7%. This case corresponds to the lower limit of the stratospheric molecular mass, 27.80.

(iii) The hottest of all possible thermal profiles is the one obtained by scaling the "hot" pure N2 profile (LH) to an inversion temperature of 74.5°K. This profile (which we will call OH) can be obtained for various CH_4 and Ar abundances. In this case, the molecular mass is 29.07. It may appear surprising that the hottest profile is not obtained for the maximal value of the molecular mass, but one should remember that the molecular mass is equal to $m = 28 \times 74.5/T_i$, where T_i is the inversion temperature of the initial pure N_2 profile. All profiles obtained by rescaling a pure N_2 profile to an inversion temperature of 74.5°K coincide (by definition) at the inversion. The fact that the hottest is obtained from the "hot" N_2 profile (LH) is actually only due to the fact that the relative uncertainty on the temperatures increases with altitude.

(iv) The coldest of all possible thermal profiles is obtained by injecting maximal (saturated) methane in the "cold" pure N_2 (LC) profile. This profile (called OC) has an inversion temperature of 70.5°K, and CH_4 saturates at 1.5% at the 71.5°K cold trap.

All these constraints will be refined by fitting the ν_4 emission of CH_4, as discussed in Section 3. The extreme profiles obtained at this step of the analysis (OC and OH) are shown in Fig. 2 and their parameters summarized in Table I.

2.2. *The Troposphere*

The constraints found on the stratospheric abundances and profile are not easy to transpose to the troposphere, because the physical conditions prevailing at the methane cold trap are largely unknown. For example, due to a possible undersaturation of CH_4 in the stratosphere, the abundance of methane just above the cold trap can be much lower than the abundance just below. Thus, it is possible for the stratospheric profile to be represented by the hottest of all the profiles, and for the methane abundance just under the cold trap to be saturated at 3.4%, although such a value for the stratospheric methane is obviously not compatible with the hottest profile from the point of view of the ν_4 emission. Moreover, as will be shown below, the ν_4 emission of CH_4 does not provide any information on the troposphere. Therefore, extreme tropospheric temperatures can be found by considering only the radio-occultation data. Due to the arguments advanced by Toon *et al.* (1988), we do not use the possible lower value of the atmospheric temperature at the surface (93.6°K) as a further constraint.

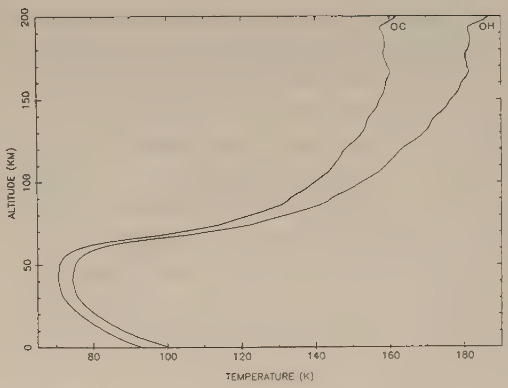

FIG. 2. The two extreme profiles compatible with the radio-occultation data only. OH is the hottest acceptable profile, OC the coldest.

As tropospheric pressures increase and approach 1 bar, departure from ideal gas becomes significant. To describe the behavior of the mixture of real gases, we use the first-order development of the Redlich–Kwong equation of state modified by Wilson (Reid *et al.* 1977; see Appendix).

In the absence of any other independent constraint on the profile, it is clear that the colder profiles are obtained in the cases without argon, and that methane introduced in uniform quantities tends to produce cold profiles. However, methane abundance may strongly increase as temperature increases with decreasing altitude, and as found earlier by Flasar (1983), the introduction of methane in large nonuniform quantities leads to strong temperature gradients in the low troposphere. Thus, the relationship between temperature and methane content is not simple, and it appears quite difficult to determine the lower limit of the thermal profile below the cold trap. If we use the "cold" pure N_2 profile (LC) with maximal stratospheric methane at 1.5% (case (iv) above), and assume a uniform CH_4 mole fraction of 1.5% down to the ground, and no argon, we obtain an atmospheric temperature of 93.1°K at the ground level, which should be close to the lowest possible value.

The warmest tropospheric temperatures are obtained if methane is introduced in saturated quantities (again, iteration is necessary to find profiles which are consistent with refractivity data and methane saturation). Actually, saturated methane profiles lead to superadiabatic profiles under 4 km. Such profiles are unstable against convection and therefore physically unacceptable. Thus, below 4 km, we iteratively calculate the percentage of saturation of CH_4 so that, with the corresponding temperature and CH_4 abundance, the lapse rate of the obtained profile exactly fits the adiabat. The same procedure was previously used by Flasar (1983) (with another equation of state). The major difference with Flasar's work is that we do not consider any contribution of CH_4 condensate to refractivity (and therefore the introduction of virtual temperatures is not necessary). There is evidence that methane clouds are present in the 10 to 30 km region (Hanel *et al.* 1981, Lindal *et al.* 1983, Toon *et al.* 1988), but it is difficult to take them into account because the condensate abundance is unknown and its refractivity uncertain. Toon *et al.* (1988) estimate the mass of methane in the cloud to be only a small fraction of the mass of methane in the vapor. If the Lorentz–Lorenz law is valid (Flasar 1983), the contribution of clouds to refractivity will be small. A final justification for neglecting the cloud contribution is provided by our purpose of finding the highest possible tropospheric temperatures: qualitatively, when condensate is present, less methane gas is needed to account for the observed refractivity, and since the gas is then saturated, the corresponding temperatures are lower than without condensate, as pointed out by Flasar (1983). In this respect, the adiabat which the lapse rate has to be compared to is the dry adiabat corresponding to the gas mixture considered (which is higher and thus less constraining than the wet one). We are in the physical situation where CH_4 is at each level (except below 4 km) at the saturation limit, but still without condensate, and the atmosphere is thus dry. Although this is not the most plausible situation, it cannot be excluded, and we must consider it for our purpose. The dry adiabat was calculated from the adopted equation of state. The results are the following:

If no Ar is present, CH_4 can reach a maximum 0.117 mole fraction near the surface, which, for a 95.2°K temperature, is about 83% saturated. If argon is included in maximum proportions (i.e., when the tropopause temperature is equal to 74.5°K), the maximum CH_4 mole fraction is 0.21, which, for a maximal 100.6°K temperature near the surface, is about 85% saturated. The atmospheric argon mole fraction at the surface level is then 0.17. Allowing for a possible 0.5°K temperature difference between the surface and the atmosphere just above it, the uncertainty on the surface temperature is about 5% ($T = 96.8 \pm 4.3$°K). The possibility of a high surface temperature has important consequences that will be discussed in Section 4.

3. FITTING OF THE METHANE ν_4 BAND

3.1. *The Procedure*

Further constraints on the stratospheric thermal profile are obtained by a direct comparison between synthetic spectra calculated in the spectral range of the ν_4 CH_4 band (1270–1350 cm^{-1}) with various occultation-derived temperature profiles, and an IRIS spectrum recorded within the equatorial region.

The procedure is as follows: Radio-occultation profiles are generated for a given N_2–Ar–CH_4 composition, starting from a given pure N_2 profile. Synthetic spectra are calculated with each profile and the corresponding CH_4 molar abundance, and compared with the observations. If the agreement is not satisfactory, synthetic spectra are recalculated for different methane mixing ratios until an acceptable fit of the observations is reached. (Agreement is considered acceptable when within a 3 σ error bar throughout the spectral region, where σ is the noise level on the observed spectrum.) A new radio-occultation profile is then recalculated with the CH_4 abundance corresponding to the best fit. The iterative procedure is pursued until convergence on the CH_4 mixing ratio is reached.

3.2. Observations

The selected spectrum is an average of 31 IRIS spectra recorded in the equatorial region of Titan (mean latitude: 5°N). The corresponding mean emission angle is 14° and the maximum projected field is 27° in planetary coordinates. The average distance from Titan is 2.2×10^5 km. Given the instrumental noise in the 1270–1350 cm^{-1} region, which is of about 0.08 erg cm^{-2} sec^{-1} sr^{-1}/cm^{-1} per individual spectrum (Hanel *et al.* 1982), the noise level σ in our averaged spectrum is about 0.014 erg cm^{-2} sec^{-1} sr^{-1}/cm^{-1}, and the signal-to-noise ratio is about 30.

3.3. Radiative Transfer

In order to test thermal profiles against observations, synthetic spectra are generated through a radiative transfer program which incorporates the temperature profile and the associated vertical distribution of methane.

The outgoing monochromatic radiance is calculated through the equation

$$I(\nu) = \int_{\mathrm{atm}} B(\nu, T) d[\exp(-\tau(\nu, z))], \quad (1)$$

where $B(\nu, T)$ is the source function at temperature T and wavenumber ν. τ, the monochromatic integrated opacity at altitude z, becomes large in the troposphere in the involved spectral range, so that the surface contribution can be neglected.

From this equation, the intensity emerging from Titan's multilayer atmosphere is calculated by means of a line-by-line radiative transfer program derived from a code initially designed by Scott (1974) and adapted to account for Titan's characteristics, such as the sphericity of the satellite's atmosphere, and the variation of gravity with altitude (more details are given in Coustenis *et al.* 1989). For direct comparison with the observations, the outgoing monochromatic radiance is convolved with the IRIS apparatus function (the Fourier transform of the Hamming function, corresponding to a resolution of 4.3 cm^{-1} (Hanel *et al.* 1981)).

The spectroscopic parameters are taken from the "GEISA" data bank (Husson *et al.* 1986). The methane band intensities are from Brown (1982). A Voigt lineshape is used for the CH_4 line profile at all atmospheric levels. Lorentz profiles are calculated as in Gautier *et al.* (1982).

3.4. Departure from Local Thermodynamical Equilibrium

The source function in the transfer equation is the Planck function so long as methane emission in the ν_4 band occurs in the conditions of local thermodynamical equilibrium (LTE). However, due to the strength of this band and the high mixing ratio of CH_4, significant absorption by CH_4 can occur up to altitudes where the ambient density is so low that CH_4 is not in LTE. It is therefore important to evaluate the altitude range where the LTE approximation is valid.

Unfortunately, data on vibrational deactivation of methane in nitrogen are scarce. Yardley *et al.* (1970) report a deactivation rate of the ν_4 of about $k = 67$ sec^{-1} $Torr^{-1}$ at 300°K. No experimental study of the temperature dependence was performed. Wang and Springer (1977) have measured the relaxation times in various methane–nitrogen mixtures with nitrogen mixing ratios ranging from 0 to 30%, at various temperatures. Extrapolation of the data to nitrogen-dominant mixtures leads to $k = 260$ sec^{-1} Torr^{-1} at 300°K, but is very uncertain. The temperature dependence observed varies strongly with the composition of the mixture, and cannot be extrapolated to high N_2 mixing ratios. Theory (Lambert 1977) predicts a (so-called Landau–Teller) $T^n \exp(-A/T^{1/3})$ dependence, with $n = -0.5$ if k is in Torr^{-1} sec^{-1}, and $n = 0.5$ if k is in cm^3 sec^{-1}. The A parameter depends on the frequency of the band, the reduced mass of the colliding partners, and a typical length characterizing the range of the interaction potential, and is therefore too complex to be evaluated theoretically. Still, the predicted temperature dependence is observed in most of the cases. Yuan *et al.* (1973) have performed measurements on the relaxation of ethylene by rare gases. For C_2H_4–Ne relaxation, one can derive $A = 35$. We adopt the same value for CH_4–N_2 relaxation. With this and Yardley *et al.*'s (1970) value, we obtain $k = 6 \times 10^{-16}$ cm^3 sec^{-1} at 180°K.

Adopting a band intensity of 125 cm^{-2} atm^{-1} at 296°K (Brown 1982), we found that the transition probability for a photon to be emitted in the ν_4 band of CH_4 is 2.2 sec^{-1}. The band is in LTE so long as this transition probability is small compared to the collisional deactivation probability $k \times N$, where N is the atmospheric concentration. We find that the two probabilities are equal for $N = 3.5 \times 10^{15}$ moles cm^{-3}, i.e., at 300 km (Lellouch and Hunten 1987). (If we adopt for k the value inferred from Wang and Springer (1977), we find that the LTE region extends 70 km higher.)

A rigorous modeling of the CH_4 emission would therefore need to include the progressive departure from LTE in the source function above about 200 km. For simplicity, we use the Planck function up to 300 km, and ignore the emission from above this altitude.

3.5. Contribution Functions

The intensity emitted by a planetary atmosphere is defined by the integral equation

$$I(\nu) = \int B_\nu(T(P))WF_\nu(P)d \ln P$$

where $B_\nu(T)$ is the Planck function for the temperature T at the pressure level P, while the weighting function $WF_\nu(P)$ describes, for a quasi-isothermal atmosphere, the atmospheric region from which the emission originates.

Since at 7 μm, $B_\nu(T)$ varies rapidly with temperature, it is more appropriate to consider the whole integrand, or the normalized contribution function CF defined by

$$CF = \frac{WF_\nu(P)B_\nu(T(P))}{I(\nu)}.$$

Typical contribution functions calculated for a mean thermal profile and a CH_4 stratospheric mole fraction of 1.8% are shown in Fig. 3. The upper curve results from the convolution of monochromatic functions with the IRIS apparatus function at 1304.3 cm^{-1}, in the center of the ν_4 band of CH_4. The lower curve is similarly calculated at 1292 cm^{-1}, in the wing of the band.

Figure 3 shows that the ν_4 emission originates from stratospheric levels located be-

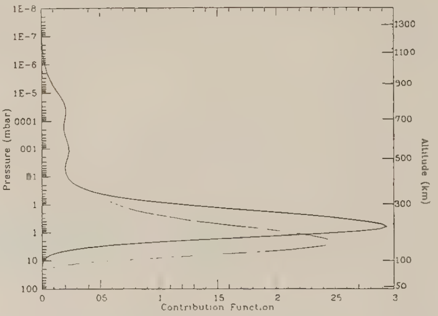

FIG. 3. Contribution functions in the ν_4 band of CH_4 for a CH_4 mole fraction of 1.8%, calculated at 1304.3 cm^{-1} (solid line) and 1291.8 cm^{-1} (dotted line) and convolved with the IRIS apparatus function.

tween pressure levels of 30 and 0.1 mbar (80 to 300 km). Information on the lower stratosphere may be extracted from spectral measurements in the wings of the ν_4 band, but no information is available on the troposphere. On the other hand, as the result of our considerations on the departure from LTE, the *CF* function is truncated at 300 km, which corresponds to a loss of about 15% of the emission.

Since information on the temperature profile from the radio-occultation experiment extends only up to 200 km, it is necessary to extrapolate the profiles between 200 and 300 km. We assume uniform temperature gradients above 200 km, and, because the observed gradient at 200 km is positive and decreasing with altitude, we limit the range of possible gradients between zero (isothermal extrapolation) and a value corresponding to a linear extrapolation of the smoothed profile between 150 and 200 km. Numerical tests and inspection of Fig. 3 show that fitting the data in the wings of the ν_4 band provides information on the CH_4 mole fraction while the appropriate thermal extrapolation can be determined from fitting the band center.

3.6. Constraints on the Stratospheric Profile and Constituent Abundances

3.6.1. The warmest possible profile and the lower limit of methane abundance. The hottest of all profiles derived from the occultation data only (profile OH, shown in Fig. 2) is not acceptable, because, for whatever CH_4 mixing ratio used, and even if an isothermal extrapolation is assumed, the corresponding emission is too strong in the center compared to the wings. The warmest possible profile compatible with the ν_4 emission (shown in Fig. 9) corresponds to 15% Ar, 84.5% N_2, and 0.5% CH_4. It is somewhat warmer than the Lindal "hot" pure N_2 profile (LH). Figure 4 shows the fit of the ν_4 emission obtained in this case. Higher values of Ar lead to a calculated contrast between the center and the wings of the ν_4 feature higher than is observed.

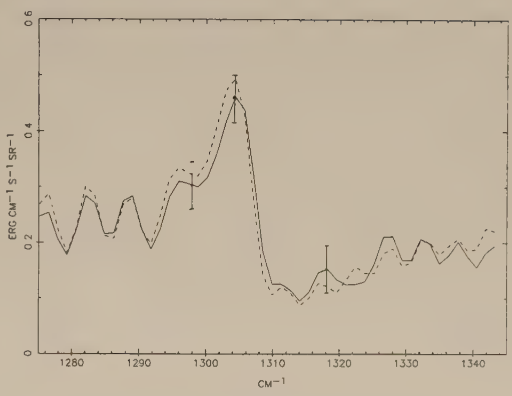

FIG. 4. Fit of the ν_4 band of CH_4 with the warmest acceptable thermal profile. The CH_4 mole fraction is 0.5%. Solid line: IRIS data (3σ error bars are indicated). Dashed line: model.

Thus, the lower limit of the CH_4 mole fraction in the Titan stratosphere appears to be 0.5%. If we assume that argon is not present in the atmosphere, the warmest profile is derived from the Lindal pure N_2 "hot" profile (LH) by introducing the amount of methane required to fit the ν_4 emission. The fit is shown in Fig. 5, and corresponds to a minimal CH_4 molar abundance of 1%.

3.6.2. The coldest profile and the maximal methane abundance. A thermal profile that is able to produce a spectrum which fits

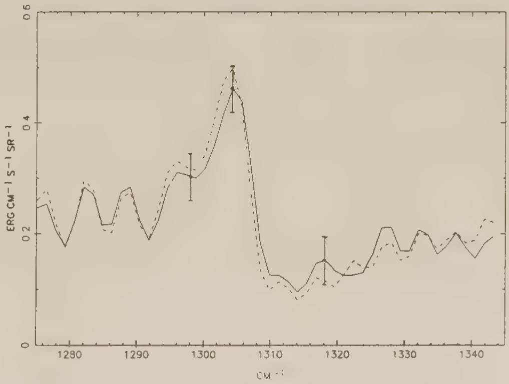

FIG. 5. Fit of the ν_4 band of CH_4 with the warmest possible thermal profile for a N_2–CH_4 atmosphere. The CH_4 mole fraction is 1%. Solid line: IRIS data (3σ error bars are indicated). Dashed line: model.

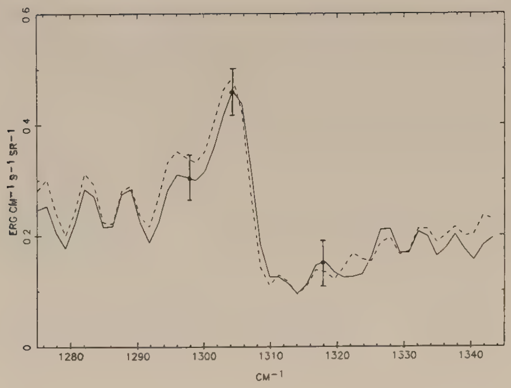

FIG. 6. Fit of the ν_4 band of CH_4 with the coldest acceptable thermal profile. The CH_4 mole fraction is 3.4%. Solid line: IRIS data (3σ error bars are indicated). Dashed line: model.

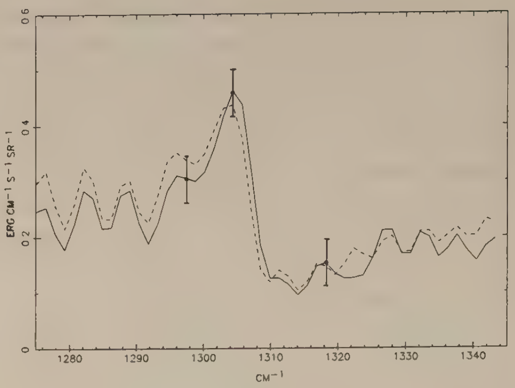

FIG. 8. Fit of the ν_4 band of CH_4 with the maximum mean molecular mass (29.36). The CH_4 mole fraction is 3.3%, and the Ar mole fraction is 21%. Solid line: IRIS data (3σ error bars are indicated). Dashed line: model.

the observed emission necessarily contains temperatures at least equal to the maximal brightness temperature in the band (namely 170.6°K). For this reason, the coldest of all profiles, as inferred from the occultation alone (OC), is much too cold: even if the maximum extrapolation is used, the synthetic spectrum is too cold by at least 10°K at the center of the band.

If argon is present, the maximum CH_4 mixing ratio is 3.4%. Starting from the "cold" pure N_2 profile (LC), the coldest profile is obtained by adding argon until the observed ν_4 emission can be fitted with 3.4% CH_4. Incidentally, the resulting profile is almost identical to the "nominal" pure N_2 profile (LN). The fit is shown in Fig. 6.

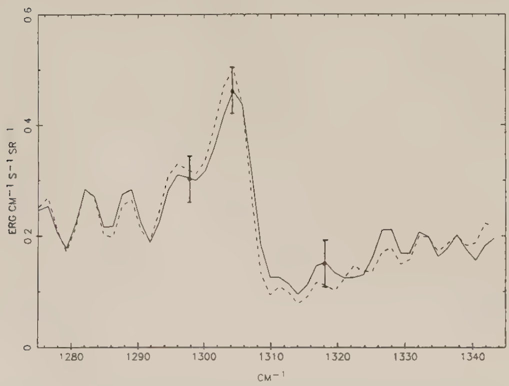

FIG. 7. Fit of the ν_4 band of CH_4 with the coldest possible thermal profile for a N_2–CH_4 atmosphere. The CH_4 mole fraction is 1.8%. Solid line: IRIS data (3σ error bars are identical). Dashed line: model.

If argon is absent, the maximum CH_4 mixing ratio saturates at 1.7% (and this value varies only slightly with profiles LN, LC, LH since they exhibit very close tropopause temperatures). In this case, the coldest profile compatible with the ν_4 emission is intermediate between LN and LH. The corresponding fit (for a stratospheric methane abundance of 1.7%) is shown in Fig. 7.

3.6.3. Maximum argon abundance. As discussed in Section 2, the maximum molecular mass (obtained by scaling the "cold" pure N_2 profile (LC) to a tropopause temperature of 74.5°K) compatible with the *Voyager* results is 29.36. The corresponding thermal profile is compatible with the ν_4 emission if the CH_4 abundance is 3.3% (Fig. 8). The mole fraction of argon then corresponding to $m = 29.36$ is 21% ($Ar/N_2 = 0.27$), which appears to be the maximal argon abundance in Titan's atmosphere.

3.6.4. Summary of the results on the stratosphere. The extreme profiles are shown in Fig. 9 from the ground up to 200 km. The comparison with Fig. 1 shows that:

—the uncertainty on the stratospheric temperature has been substantially reduced, although a significant part of it comes from the possible presence of argon, not considered by Lindal *et al.* (1983).

—the actual stratospheric profile is probably significantly warmer than the Lindal nominal one (LN).

Concerning the composition, it appears that:

—the argon mixing ratio relative to nitrogen is poorly constrained, between 0 and 0.27 (which corresponds to an argon mole fraction ranging from 0 to 21%).

—the stratospheric methane mole fractions is relatively well constrained, between 0.5 and 3.4%. If argon is absent, the range of possible stratospheric CH_4 mole fractions is 1.0–1.7%.

3.7. Titan's Equatorial Possible Profiles

The four profiles drawn in Fig. 9 were obtained by juxtaposition of the corresponding tropospheric and stratospheric extreme profiles. It must be recalled here that the tropospheric and stratospheric parts of a given profile were derived almost completely independently, in Sections 2.2 and 3.6, respectively. The main reason for this is that it is not possible to infer the abundance of CH_4 in the troposphere from the value measured in the stratosphere from the comparison with the IRIS spectra. As a consequence, the compositions in the tropospheric and stratospheric parts of the extreme profiles are different. In this respect, the extreme profiles are not necessarily possible as profiles, but, rather, they are "envelope" profiles, in the sense that they give the borders between which all possible profiles are lying. Not all the profiles contained between the limiting profiles are possible, but, reversely, any profile which at some level falls outside the limiting profiles is excluded. In the same sense, we have obtained the envelope profiles for the abundances of the major constituents. The Ar/N_2 ratio is bounded between 0 and 0.27. Figure 10 shows the extreme possible profiles for the CH_4 mixing ratio. However, there is no biunivocal correspondence between the profiles in Figs. 9 and 10.

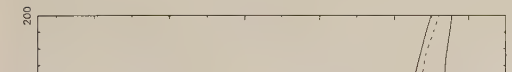

FIG. 9. The extreme possible thermal profiles of Titan's atmosphere between 0 and 200 km. Solid lines: the warmest and coolest profiles for a N_2–Ar–CH_4 atmosphere. Dashed lines: same for a N_2–CH_4 atmosphere.

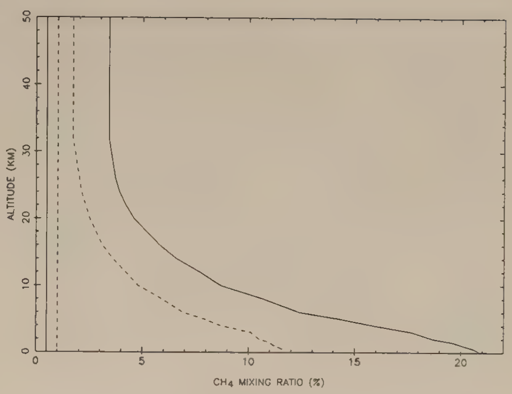

FIG. 10. The extreme possible profiles of methane abundance. Solid lines: minimal and maximal methane mixing ratios for a N_2–Ar–CH_4 atmosphere. Dashed lines: same for a N_2–CH_4 atmosphere.

In the framework of the *Cassini* mission, such a situation may be somewhat disturbing for Titan Probe entry and descent studies, which ideally require a set of extreme thermal profiles with their associated composition profiles (mainly for mass density and speed of sound calculations). Such a clear case cannot be reached, simply because, due to the uncertainties in the radio-occultation data, a given temperature profile can be obtained with various compositions. For a conservative approach, we think one should use each of the extreme temperature profiles with the whole range of composition allowed by Fig. 10, although a given thermal profile is not necessarily compatible with any composition. We also recall that our work refers to the equatorial profile of Titan at the date of the *Voyager* encounter, and that *Cassini* Probe studies should also consider the spatial and temporal variability of the thermal profile (Flasar, private communication, Lellouch and Hunten 1987).

With these caveats, we propose for practical use a ''nominal'' profile with an associated level-by-level composition, which is compatible with observations.

The choice of such a profile is to a large extent arbitrary. Our ''nominal'' profile lies roughly midway from the extreme argon-free profiles. Since definitely the presence of argon cannot be established, it includes no argon in its nominal composition, although the same temperatures could be obtained with various amounts of argon. The methane mole fraction is 8% at the ground and upward until saturation is reached, then follows the saturation up to the cold trap, where it is equal to 1.7%. Above the tropopause, methane is assumed—although this may be questionable—to be slightly undersaturated at 1.5% mole fraction. Casually, the profile fits that of Lindal *et al.* (1983) almost perfectly in the troposphere (71.1°K at the tropopause; 93.9°K at the surface), and, in order to fit the *Voyager* IRIS spectrum, is significantly warmer above, reaching 174°K at 200 km. Numerical values are given in Table II.

We emphasize that many other different solutions are equally possible. An example is given by the baseline profile of Coustenis *et al.* (1989), which was derived under the assumption that the stratospheric methane mole fraction is equal to the cold trap saturation value.

4. CONSEQUENCES ON TITAN'S POSSIBLE OCEAN

4.1. The Likely Presence of an Ocean

Atmospheric methane is irreversibly photolyzed, either directly in the mesosphere, or, catalytically, through acetylene photolysis, in the stratosphere (Yung *et al.* 1984). This photolysis is extremely efficient, and in the absence of a CH_4 reservoir at the surface of Titan, all the atmospheric CH_4 would be consumed in about 10 myr. An ocean could be such a reservoir.

The natural idea of a global pure methane ocean at the surface of Titan seems to be ruled out by previous analyses of the occultation data in terms of a N_2–CH_4 atmosphere (Eshleman *et al.* 1983, Flasar 1983). (Dynamical aspects related to Titan's high eccentricity suggest that an ocean on Titan, if it exists, must be nearly global (Sagan and Dermott 1982).) Considering that ethane is the main net product of methane photolysis, and should be in liquid phase at the surface, Lunine *et al.* (1983) have proposed that Titan is covered by an ocean consisting mainly of ethane, with some quantities of methane and dissolved nitrogen, at 94°K. Such an ocean would act as a reservoir of hydrocarbons and control the abundance of atmospheric CH_4. Its minimum depth is constrained by the quantity of ethane having fallen down to the surface since Titan's formation. Assuming a constant ethane flux over the age of the Solar System, equal to its photolytic rate of formation, 5.8×10^9 cm^{-2} sec^{-1} (Yung *et al.* 1984), the ocean would be at least ~700 m deep. In addition, it should contain a noticeable fraction of dissolved gases and solutes.

4.2. A Close Dependence between the Atmosphere and the Ocean

Within the reasonable hypothesis that the ocean and atmosphere are in thermodynamical equilibrium, the oceanic main composition can be evaluated as a function of the atmospheric composition and surface

TABLE II

NOMINAL PROFILE OF TITAN'S ATMOSPHERE

Altitude (km)	Number density (cm^{-3})	CH_4 mixing ratio	Pressure (bar)	Temperature (°K)
200.0	3.11×10^{16}	0.015	7.59×10^{-4}	174.0
198.0	3.30×10^{16}	0.015	7.98×10^{-4}	173.9
196.0	3.47×10^{16}	0.015	8.37×10^{-4}	173.8
194.0	3.70×10^{16}	0.015	8.77×10^{-4}	173.6
192.0	3.90×10^{16}	0.015	9.20×10^{-4}	173.4
190.0	4.09×10^{16}	0.015	9.64×10^{-4}	173.2
188.0	4.25×10^{16}	0.015	1.01×10^{-3}	173.0
186.0	4.48×10^{16}	0.015	1.06×10^{-3}	172.9
184.0	4.67×10^{16}	0.015	1.11×10^{-3}	172.7
182.0	4.93×10^{16}	0.015	1.16×10^{-3}	172.5
180.0	5.16×10^{16}	0.015	1.22×10^{-3}	172.4
178.0	5.45×10^{16}	0.015	1.28×10^{-3}	172.2
176.0	5.68×10^{16}	0.015	1.35×10^{-3}	172.0
174.0	5.97×10^{16}	0.015	1.41×10^{-3}	171.8
172.0	6.27×10^{16}	0.015	1.48×10^{-3}	171.6
170.0	6.56×10^{16}	0.015	1.55×10^{-3}	171.4
168.0	6.91×10^{16}	0.015	1.63×10^{-3}	171.2
166.0	7.20×10^{16}	0.015	1.71×10^{-3}	171.0
164.0	7.55×10^{16}	0.015	1.79×10^{-3}	170.8
162.0	7.98×10^{16}	0.015	1.88×10^{-3}	170.4
160.0	8.41×10^{16}	0.015	1.97×10^{-3}	169.9
158.0	8.86×10^{16}	0.015	2.07×10^{-3}	169.5
156.0	9.34×10^{16}	0.015	2.17×10^{-3}	169.0
154.0	9.83×10^{16}	0.015	2.29×10^{-3}	168.5
152.0	1.04×10^{17}	0.015	2.40×10^{-3}	167.9
150.0	1.09×10^{17}	0.015	2.52×10^{-3}	167.4
148.0	1.15×10^{17}	0.015	2.65×10^{-3}	166.7
146.0	1.22×10^{17}	0.015	2.78×10^{-3}	166.0
144.0	1.28×10^{17}	0.015	2.93×10^{-3}	165.3
142.0	1.36×10^{17}	0.015	3.08×10^{-3}	164.5
140.0	1.44×10^{17}	0.015	3.24×10^{-3}	163.7
138.0	1.52×10^{17}	0.015	3.41×10^{-3}	163.0
136.0	1.61×10^{17}	0.015	3.59×10^{-3}	162.4
134.0	1.69×10^{17}	0.015	3.78×10^{-3}	161.8
132.0	1.79×10^{17}	0.015	3.90×10^{-3}	161.2
130.0	1.89×10^{17}	0.015	4.19×10^{-3}	160.5
128.0	2.00×10^{17}	0.015	4.42×10^{-3}	159.6
126.0	2.13×10^{17}	0.015	4.66×10^{-3}	158.6
124.0	2.26×10^{17}	0.015	4.91×10^{-3}	157.5
122.0	2.41×10^{17}	0.015	5.19×10^{-3}	156.3
120.0	2.56×10^{17}	0.015	5.48×10^{-3}	155.3
118.0	2.72×10^{17}	0.015	5.78×10^{-3}	154.3
116.0	2.88×10^{17}	0.015	6.10×10^{-3}	153.4
114.0	3.06×10^{17}	0.015	6.45×10^{-3}	152.6
112.0	3.26×10^{17}	0.015	6.82×10^{-3}	151.9
110.0	3.46×10^{17}	0.015	7.22×10^{-3}	151.0
108.0	3.68×10^{17}	0.015	7.63×10^{-3}	150.1
106.0	3.92×10^{17}	0.015	8.08×10^{-3}	149.0
104.0	4.19×10^{17}	0.015	8.56×10^{-3}	147.8
102.0	4.48×10^{17}	0.015	9.06×10^{-3}	146.5
100.0	4.80×10^{17}	0.015	9.61×10^{-3}	145.1
98.0	5.14×10^{17}	0.015	1.02×10^{-2}	143.7
96.0	5.51×10^{17}	0.015	1.08×10^{-2}	142.1
94.0	5.92×10^{17}	0.015	1.15×10^{-2}	140.6
92.0	6.38×10^{17}	0.015	1.22×10^{-2}	139.1
90.0	6.86×10^{17}	0.015	1.30×10^{-2}	137.6
88.0	7.36×10^{17}	0.015	1.38×10^{-2}	135.8
86.0	7.95×10^{17}	0.015	1.47×10^{-2}	133.8
84.0	8.65×10^{17}	0.015	1.57×10^{-2}	131.5
82.0	9.45×10^{17}	0.015	1.68×10^{-2}	128.8
80.0	1.04×10^{18}	0.015	1.80×10^{-2}	125.8
78.0	1.14×10^{18}	0.015	1.93×10^{-2}	122.7
76.0	1.26×10^{18}	0.015	2.07×10^{-2}	119.7
74.0	1.39×10^{18}	0.015	2.23×10^{-2}	116.6
72.0	1.56×10^{18}	0.015	2.40×10^{-2}	111.9
70.0	1.78×10^{18}	0.015	2.60×10^{-2}	106.1
68.0	2.04×10^{18}	0.015	2.83×10^{-2}	100.5
66.0	2.43×10^{18}	0.015	3.10×10^{-2}	92.6
64.0	2.89×10^{18}	0.015	3.42×10^{-2}	85.9
62.0	3.40×10^{18}	0.015	3.79×10^{-2}	80.9
60.0	3.96×10^{18}	0.015	4.23×10^{-2}	77.6
58.0	4.57×10^{18}	0.015	4.75×10^{-2}	75.4
56.0	5.25×10^{18}	0.015	5.34×10^{-2}	73.8
54.0	6.00×10^{18}	0.015	6.01×10^{-2}	72.8
52.0	6.83×10^{18}	0.015	6.79×10^{-2}	72.2
50.0	7.77×10^{18}	0.015	7.67×10^{-2}	71.7
48.0	8.83×10^{18}	0.015	8.67×10^{-2}	71.5
46.0	1.00×10^{19}	0.015	9.81×10^{-2}	71.4
44.0	1.14×10^{19}	0.015	0.111	71.2
42.0	1.29×10^{19}	0.015	0.126	71.1
40.0	1.46×10^{19}	0.015	0.142	71.1
38.0	1.66×10^{19}	0.015	0.161	71.2
36.0	1.87×10^{19}	0.015	0.183	71.4
34.0	2.12×10^{19}	0.015	0.207	71.5
32.0	2.39×10^{19}	0.016	0.235	71.8
30.0	2.69×10^{19}	0.017	0.265	72.3
28.0	3.02×10^{19}	0.017	0.300	73.1
26.0	3.38×10^{19}	0.018	0.340	73.9
24.0	3.78×10^{19}	0.020	0.383	74.7
22.0	4.21×10^{19}	0.021	0.432	75.7
20.0	4.68×10^{19}	0.023	0.487	76.7
18.0	5.19×10^{19}	0.026	0.547	78.0
16.0	5.75×10^{19}	0.029	0.614	79.2
14.0	6.34×10^{19}	0.034	0.688	80.6
12.0	6.97×10^{19}	0.040	0.770	82.1
10.0	7.66×10^{19}	0.045	0.859	83.6
8.0	8.36×10^{19}	0.055	0.957	85.5
6.0	9.11×10^{19}	0.065	1.06	87.3
5.0	9.48×10^{19}	0.074	1.12	88.5
4.0	9.88×10^{19}	0.080	1.18	89.5
3.0	1.03×10^{20}	0.080	1.24	90.5
2.0	1.07×10^{20}	0.080	1.30	91.5
1.5	1.09×10^{20}	0.080	1.34	92.1
1.0	1.11×10^{20}	0.080	1.37	92.7
0.5	1.13×10^{20}	0.080	1.40	93.3
0.0	1.15×10^{20}	0.080	1.44	93.9

temperature. Assuming a CH_4 mole fraction in the low atmosphere of 3%, Lunine *et al.*'s (1983) model ocean is made of 70% C_2H_6, 20% CH_4, and 5% N_2. Refined calculations on phase equilibria in the N_2–CH_4–C_2H_6 system by Lunine and Stevenson (1985) and Thompson (1985) defined a range of possible oceanic compositions. These estimations, however, which apply mostly at a present ocean temperature of 94°K, do not take into account the possible presence of argon, and also ignore the likely presence of other solutes in the ocean.

Recent modeling of Titan's aerosol formation and evolution, using a microphysical approach (Frère *et al.* 1988), indicates that there may be a permanent rainfall down to the surface of aerosol droplets with mean diameters up to a few hundred microns. This is in agreement with the work by Toon *et al.* (1988), who from a reanalysis of the *Voyager* IRIS data between 150 and 600 cm^{-1} with a multiple scattering radiative transfer model, suggest the existence of a methane rain on Titan, with cloud particles probably larger than 50 μm. In the model of Frère *et al.* (1988), these aerosols would be formed by the condensation of light atmospheric compounds, induced by submicron particles formed in high atmospheric regions by photopolymerization processes of C_2H_2, C_2H_4, and HCN. Near the surface of Titan, the particles consist of a core with a mean diameter of several tens of microns, mainly composed of nitriles and acetylene and covered, successively, by a C_3H_8–C_2H_6–CH_4 envelope. In the droplets, most of the organics are highly enriched relative to the atmosphere.

This rainfall continuously and irreversibly feeds the low troposphere and finally the ocean with ethane and other organics. Most of the organic compounds are solid at the temperature of the surface, with the noticeable exception of propane, which is liquid at 94°K and miscible in very large proportions in methane–ethane mixtures. Assuming that the downward flux of propane, like that of ethane, has been constant throughout Titan's history and is equal to 1.4×10^8 cm^{-2} sec^{-1} (Yung *et al.* 1984), then the mole fraction of propane in the ocean is simply equal to that of ethane multiplied by the ratio of their fluxes (0.024). The solid organic compounds dissolve partly or totally in the ocean. Thermodynamical modeling of the dissolution at 94°K has been recently carried out, first for a few light organics in a C_2H_6–CH_4 mixture (Raulin 1985), and then by considering a C_2H_6–CH_4–N_2 solvent, and a larger variety of solutes (Raulin 1987). The results suggest that Titan's ocean could be very rich in organic solutes, with concentrations in the range 10^{-6} to 1 mole liter^{-1}, depending on their chemical nature. With the exception of alkanes and cycloalkanes, very soluble in such a solvent, saturation could be reached for most of the other solutes. This is the case, in particular, of acetylene and also of nitriles, even more polar than alcynes and thus less soluble in this apolar solvent.

Two main consequences for the properties of the ocean can be expected from the uncertainty on the tropospheric profile. First, the large possible range of atmospheric methane allows for a wide range of oceanic composition. Second, the solubility of the minor compounds in the ocean is strongly dependent on the nature of the solvent (i.e., the CH_4 content) and of its temperature, which is closely related to the atmospheric temperature near the surface. In the following, we examine these effects quantitatively, by studying a C_2H_6–CH_4–N_2–Ar system, in the 92.5–101°K temperature range.

4.3. Consequences for the Ocean Composition

The main composition of the ocean has been determined as a function of that of the atmosphere at the two extreme possible temperatures (92.5 and 101°K). We have considered the case of an argon-free atmosphere for both temperatures, and the case of an atmosphere containing 17% argon at 101°K. Although the case of an argon-free atmosphere at 101°K is not realistic (as shown in Section 2, the maximum tropospheric temperature is 95.2°K if no argon is present), the objective of considering it is to study the influence of the possible presence of argon on the main composition of the ocean and the solubility of minor components. Since these two quantities exhibit a strong temperature dependence, the influ-

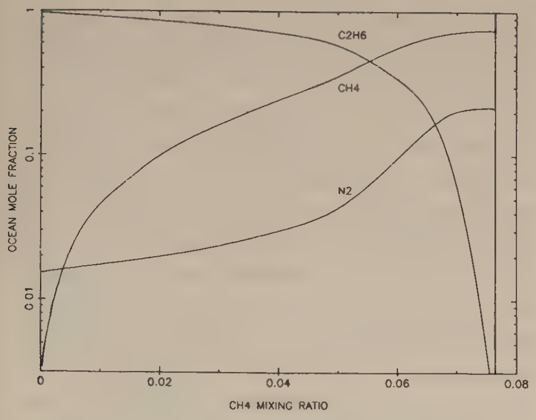

FIG. 11. The main composition of the ocean at T = 92.5°K as a function of the atmospheric methane mole fraction. The atmospheric argon mole fraction is 0. The vertical line shows the maximum methane mixing ratio compatible with thermodynamical equilibrium.

ence of argon can be best studied by comparing the results obtained at a given temperature, with and without argon. In addition to the main oceanic components already mentioned (CH_4, C_2H_6, N_2, and possibly Ar), we include the presence of propane, with a constant mixing ratio of 0.024 relative to ethane. Since the argon mole fraction is fixed (0 or 0.17), the main atmospheric composition can be expressed as a function of one parameter only, namely the CH_4 mole fraction, $f(CH_4)$. Figures 11 and 12 display the main composition of the ocean versus $f(CH_4)$, at 92.5 and 101°K, respectively. Details on the equations used in the calculations are given in the Appendix.

At 92.5°K, if the atmosphere and the ocean are in thermodynamical equilibrium, the atmospheric methane mole fraction at the surface cannot exceed 7.7%. In this case, the maximum mole fraction of nitrogen dissolved in the methane ocean is 0.24. However, such an extreme, ethane-free, composition is not realistic, since the methane photolysis during 4.6 byr implies a substantial quantity of ethane. This also implies that a given atmospheric composition corresponds not only to a certain ocean composition, but also to a certain ocean depth, which can be estimated from the ethane flux and the composition and molar volume of the ocean. For instance, a 1.5% constant mole fraction of methane in the troposphere, as discussed in Section 2, corresponds to an ocean made of 7.3% CH_4, 88.8% C_2H_6, 2.1% C_3H_8, and 1.8% dissolved N_2 and 700 m deep.

At 101°K, the maximum atmospheric methane mixing ratio compatible with thermodynamical equilibrium is markedly enhanced: 23.2% in an argon-free atmosphere, and 22.2% in an atmosphere containing 17% argon. For a given oceanic methane mole fraction, the concentration of dissolved nitrogen decreases when the temperature increases. However, since N_2 is more soluble in methane than in ethane, the large increase in the allowed oceanic methane mole fraction at 101°K induces a large increase in the mole fraction of allowed dissolved nitrogen. At 101°K, in an almost pure methane ocean, it is more than 8% in the absence of argon, and 6.7% if the atmosphere contains 17% argon. In the last case, the ocean can dissolve up to 5.7% argon. As shown in Section 2, at the highest atmospheric temperature (100.6°K), the composition of the atmosphere near the surface is 62% nitrogen, 21% methane, and

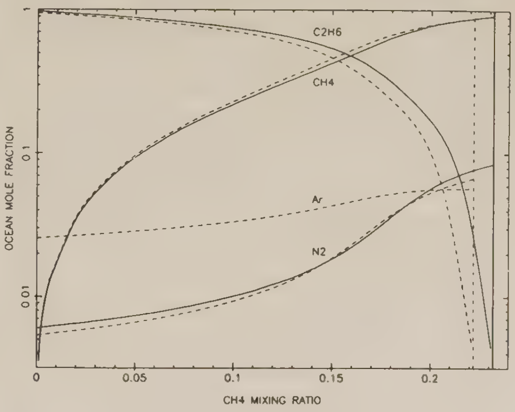

FIG. 12. The main composition of the ocean at T = 101°K as a function of the atmospheric methane mole fraction. The atmospheric argon mole fraction is 0 (solid curves) or 0.17 (dashed curves). The vertical lines show the maximum methane mixing ratios compatible with thermodynamical equilibrium.

17% argon. Such an atmosphere is compatible with an ocean mainly composed of 83.4% CH_4, 5% C_2H_6, 6% N_2, and 5.6% Ar. The ocean would be about 9 km deep.

We have also estimated the solubility in the ocean of the two minor noncondensable constituents detected in Titan's atmosphere, CO and H_2. As already observed for Ar and N_2, CO and H_2 are markedly more soluble in methane than in ethane; for a given solvent, their solubility decreases as the temperature increases. With a mixing ratio of 6×10^{-5} in the near-surface troposphere, the mole fraction of dissolved CO at 92.5°K is about 3×10^{-6} in an ethane-rich ocean and 2×10^{-5} in a methane-rich ocean. At 101°K, these values drop to 10^{-6} and 10^{-5}, respectively. Within the allowed atmospheric conditions described in Section 2, the oceanic mole fraction of CO would be about 3×10^{-6} at 92.5°K and 10^{-5} at 101°K. Taking into account the corresponding ocean depths, such concentrations would correspond to about 5×10^{15} and 2×10^{17} dissolved moles of CO, at 92.5 and 101°K, respectively. The last value is 10 times higher than the total amount of atmospheric CO. Thus a warm ocean, because of its large depth, might be a very efficient CO reservoir.

The solubility of H_2 is not very temperature dependent. For a H_2 atmospheric mixing ratio of 0.002 (Samuelson *et al.* 1981), it ranges between about 10^{-6} (ethane-rich ocean) and 3×10^{-6} (methane-rich ocean).

Calculation of the solubility of various plausible solid solutes (carbon dioxide, unsaturated hydrocarbons, and nitriles) in this model ocean (Dubouloz *et al.* 1989) confirms that, as previously observed, the saturation concentration decreases when the CH_4 oceanic mole fraction increases. The solubilities are not significantly modified by the presence of argon. On the other hand, for a given oceanic main composition, solubilities are strongly enhanced by an increase in temperature (by a factor of 4 between 92.5 and 101°K for most of the solutes). However, since such an increase in temperature also increases the allowed oceanic methane mole fraction, its global effect on the range of concentration of minor solid solutes may be small. For example, the solubility of acetylene in an ethane-rich ocean at 92.5°K is 4×10^{-4} (about 0.01 mole liter^{-1}). A similar value of 3×10^{-4} holds for a methane-rich ocean at 101°K. With the nitriles, the increase of solubility with temperature is even too low to compensate for the decrease due to methane enrichment. The solubility of HCN, for example, is about 9×10^{-6} in the ethane ocean at 92.5°K, and a factor of about 4 lower in the methane ocean at 101°K. Finally, it must be pointed out that, even at the highest temperature, the solubility of the minor compounds is generally not large enough to allow for their total dissolution in Titan's ocean, even though a high temperature may correspond to a deeper (because ethane-poor) ocean. Thus, for most of the minor compounds, the saturation could be reached. The excess of solids, probably denser than the oceanic liquid (Raulin 1985, 1987), would form thick organic layers at the bottom of the ocean, efficiently buffering their concentration.

5. CONCLUSION

We have simultaneously reanalyzed the *Voyager 1* radio-occultation and IRIS 7.7-μm data of the Titan equatorial region to infer constraints on the temperature profile and the main gaseous composition between 0 and 200 km, and derived consequences on some properties (main composition, depth, and solubility of minor species) of Titan's possible ocean. The bulk of our results can be summarized as follows:

—the atmospheric Ar/N_2 ratio can be between 0 and 0.27. We emphasize that the entire set of data is compatible with no argon in the atmosphere.

—the stratosphere methane mole fraction is between 0.5 and 3.4% (1.0–1.7% if the atmosphere is argon free). In the troposphere, the maximum CH_4 mole fraction is

21% at the surface (12% if no argon is present).

—the uncertainty on the stratospheric temperature profile is about ±2°K at the tropopause and ±4°K between 150 and 200 km. In the troposphere, the uncertainty on the temperature is primarily due to composition uncertainties, and becomes very small if argon is absent. The surface temperature is between 92.5 and 101°K (95.7°K if argon is absent). The actual temperature profile is probably somewhat warmer than the profile proposed by Lindal *et al.* (1983), especially in the stratosphere.

—the possible ocean can be almost pure ethane and relatively shallow (700 m deep) at 92.5°K, almost pure methane and 10 km deep at 101°K, or anything between. Nitrogen can be dissolved in the ocean with a mole fraction ranging from 2 to 6%. The ocean, if warm, could be an efficient CO reservoir. Finally, for most of the solid solutes, saturation could be reached in any possible ocean.

APPENDIX

A. Equation of State of the Atmosphere

To describe the behavior of the atmosphere, which is a mixture of three real gases, we use the first-order development of the Redlich–Kwong equation modified by Wilson (Reid *et al.* 1977),

$$P = NkT[1 + Nb(1 - \Omega F(T))],$$

where

$$b = \sum_{i=1}^{3} b_i x_i$$

$$b_i = 0.08664 RT_{c_i}/P_{c_i}$$

$$F(T) = \sum_{i=1}^{3} F_i x_i$$

$$F_i = 1 + (1.57 + 1.62\omega_i)(T_{c_i}/T - 1)$$

$$\Omega = 4.933962,$$

where the i index refers to the three molecules N_2, CH_4, and Ar. T_{c_i} and P_{c_i} are the critical temperature (in °K) and pressure (in Pa) of component i. ω_i is the acentric factor and x_i the mole fraction. The values used were

$$N_2 : T_c = 126.2°\mathrm{K}, \ P_c = 33.5 \text{ atm}, \quad \omega = 0.04$$

$$CH_4 : T_c = 190.6°\mathrm{K}, \ P_c = 45.4 \text{ atm}, \quad \omega = 0.008$$

$$\mathrm{Ar} : T_c = 150.8°\mathrm{K}, \ P_c = 48.1 \text{ atm}, \quad \omega = -0.004.$$

The adiabatic lapse rate can be expressed as

$$\nabla T_{ad} = -\frac{gm}{C_p}\frac{T}{V}\frac{\partial V}{\partial T}\bigg|_P,$$

where, for the considered equation of state,

$$C_p = C_p^0 + 2\Omega bP(1.57T_c + 1.62\overline{\omega T})/T^2$$

$$\frac{T}{V}\frac{\partial V}{\partial T}\bigg|_P = 1 - Nb\left[1 - \Omega\left\{1 + 1.57\left(2\frac{T_c}{T} - 1\right) + 1.62\omega\left(2\frac{\overline{\omega T}}{T\omega} - 1\right)\right\}\right],$$

where C_p^0 is the molar specific heat of the ideal mixture of gases and can be expanded in powers of T (Reid *et al.* 1977), and

$$T_c = \sum_{i=1}^{3} T_{c_i} x_i$$

$$\omega = \sum_{i=1}^{3} \omega_i x_i$$

$$\overline{\omega T} = \sum_{i=1}^{3} \omega_i T_{c_i} x_i .$$

B. Saturation Law of Methane

At the temperatures of the lower atmosphere of Titan, methane gas can coexist with both condensed phases. For the vapor–liquid equilibrium, which occurs at $T \geq T_f$ (triple point, 90.7°K), we use the Thek–Stiel equation, which reproduces experimental data to an accuracy of at least

3%. The vapor pressure for the vapor–liquid equilibrium P_{gl} is given by

$$\ln(P_{gl}/P_c) = A[1.14893 - T_r^{-1} - 0.11719T_r - 0.03174T_r^2 - 0.375 \ln T_r] + B[(T_r^a - 1)/a + 0.04(T_r^{-1} - 1)],$$

where

$$T_r = T/T_c$$

$$A = H_{vb}/[RT_c(1 - T_{br})^{0.375}]$$

$$T_{br} = T_b/T_c$$

$$B = 1.042a_c - 0.46284A$$

$$a_c = (0.315\psi_b + \ln P_c)/(0.0838\psi_b - \ln T_{br})$$

$$\psi_b = -35 + 36/T_{br} + 42 \ln T_{br} - T_{br}^6$$

$$a = 5.2691 + 2.0753A - 3.1738h$$

$$h = T_{br} \ln P_c/(1 - T_{br}).$$

H_{vb} is the vaporization enthalpy at normal pressure, and can be expressed as

$$H_{vb} = RT_b(0.4343P_c - 0.68859 + 0.89584T_{br})/(0.37691 - 0.37306T_{br} + 0.14878T_{br}^{-2}/P_c),$$

where T_b is the normal boiling temperature (111.7°K). In the expressions of h and H_{vb}, the critical pressure P_c must be in atmospheres.

For the vapor–solid equilibrium, we have assumed that the fusion enthalpy H_f is independent of temperature. The vapor pressure P_{gs} for this equilibrium is given at $T \leq$ 90.7°K by

$$P_{gs} = P_{gs} \exp[H_f/R(T_f^{-1} - T^{-1})]$$

and we use $H_f = 18$ J/g, which is very different from the experimental value, 56 J/g (Reid *et al.* 1977), but allows a better fit of the vapor–solid equilibrium data.

C. Composition of the Ocean

C.1. Main composition. At temperature T, for each atmospheric constituent k in equilibrium with the liquid phase, the mole fraction in the ocean, X_k, is related to that in the atmosphere, f_k, assuming fugacities equal to 1, by the relation

$$Y_kX_k = f_kP/P_k, \tag{2}$$

where

P = total atmosphere surface pressure,
P_k = vapor pressure of pure constituent k at temperature T,
Y_k = activity coefficient of k in the liquid phase.

Values of P_k have been determined by interpolating or extrapolating published experimental data, or by using the Harlacher equation (Reid *et al.* 1977, 1987). Activity coefficients have been calculated from the "Regular Solution" theory:

$$RT \ln Y_k = \sum_i \sum_j (A_{ik} - A_{ij}/2)Q_iQ_j \tag{3}$$

with

$$A_{ij} = (\delta_i - \delta_j)^2 + 2l_{ij}\delta_i\delta_j \tag{4}$$

$$Q_i = X_iV_i \Big/ \Big(\sum_i X_iV_i + V_e\Big), \tag{5}$$

where, for each oceanic constituent i (i = CH_4, C_2H_6, C_3H_8, N_2, and Ar),

V_i = molar liquid volume,
δ_i = solubility parameter,
Q_i = volumic fraction,
l_{ij} is an empirical parameter of interaction between constituents i and j. V_e is the excess volume of the liquid mixture.

V_i and δ_i have been calculated at T using correlation tables, knowing the critical constants and the acentric factor of constituent i (Reid *et al.* 1987, Raulin 1985, 1987). l_{ij} values have been taken from the same sources (Table A1). V_e has been estimated, as a function of $X(CH_4)$, by neglecting the contribution of the other constituents, from C_2H_6–CH_4 data (Rodosevich and Miller 1973):

$$V_e = 3.05[0.5 - X(CH_4)]^{2.16} - 0.68 \text{ cm}^3 \text{ mole}^{-1}. \tag{6}$$

C.2. Other gas phase constituents: CO and H_2. For estimating the concentration of

TABLE A1

VALUES OF THERMODYNAMICAL PARAMETERS USED IN THE CALCULATIONS RELATED TO THE ATMOSPHERE/OCEAN EQUILIBRIUM AND TO THE ORGANIC SOLUBILITIES

T (°K)	$P_k{}^a$ (atm)		ω^b	$\delta_k{}^c$ (cal cm^{-3})$^{1/2}$		$V_k{}^c$ (cm^{-3})		$l_{ij}{}^d$				
	92.5	101		92.5	101	92.5	101	CH_4	C_2H_6	N_2	Ar	CO
CH_4	0.146	0.378	.008	7.23	7.04	35.8	36.8	—	.01	−.02	.02	0
C_2H_6	2×10^{-5}	1.4×10^{-4}	.1	9.07	8.95	46.8	47.5	.01	—	.01	.012	0
N_2	4.38	8.22	.04	5.3	4.96	38.7	41.4	−.02	.01	—	0	0
Ar	1.69	3.4	.001	6.8	6.48	29.2	30.4	.02	.012	0	—	0
CO	2.95	5.78	.066	5.72	5.37	38.3	40.6	0	0	0	0	—

[a] Determined by interpolating the Boublik *et al.* (1984) data (for CH_4 and Ar), using the Harlacher equation (Reid *et al.* 1977).

[b] Values from Reid *et al.* (1977, 1987).

[c] Calculated from the Lyckman *et al.* correlation tables (Raulin 1987).

[d] Taken from the literature (see references in Raulin 1987); if not available, assumed to be 0.

CO in the ocean, Eqs. (1)–(5) have been used (see also Table A1). For H_2, Henry's law was used,

$$X(H_2) = f(H_2)P/H,$$

where H is Henry's constant of H_2 related to the oceanic mixture, estimated from

$$\ln H = \sum_i X_i \ln H_i.$$

H_i is Henry's constant of H_2 in pure liquid, estimated from experimental published data (Orentlicher and Prausnitz 1964).

C.3. Solubility of solid solutes. The mole fraction X_s of a solid solute in a saturated solution of C_2H_6–CH_4–N_2–Ar in equilibrium with Titan's atmosphere at temperature T has been calculated by the method of Preston and Prausnitz (1970).

The activity of the solute is given by

$$\ln(Y_s X_s) = (1 - T_f/T)\Delta H_f/(RT_f) + \Sigma(1 - T_{tr}/T)\Delta H_{tr}/(RT_{tr}),$$

where ΔH_f and ΔH_{tr} are the enthalpies of fusion and of phase transitions, and T_f and T_{tr} the corresponding temperatures.

The activity coefficient Y_s has been determined from Eqs. (1)–(5). The solubility parameter and molar liquid volume have been estimated at different temperatures by the method described above. Values of enthalpies T_f and T_{tr} have been taken from the literature, or estimated by an analog method, as previously described (Raulin 1987).

ACKNOWLEDGMENTS

We thank C. McKay and R. Courtin for their interesting comments on the manuscript. Parts of this study have been supported by the Centre National d'Etudes Spatiales (Grants 86/CNES/1245 and 87/CNES/1247).

REFERENCES

APPLEBY, J. F. 1986. Radiative–convective equilibrium models of Uranus and Neptune. *Icarus* **65,** 383–405.

BOUBLIK, T., V. FRIED, AND E. HALA 1984. The vapour pressure of pure substances. In *Physical Sciences Data,* Vol. 17. Elsevier, Amsterdam.

BROADFOOT, A. L., B. R. SANDEL, D. E. SHEMANSKY, J. B. HOLBERG, G. R. SMITH, D. F. STROBEL, J. C. MCCONNELL, S. KUMAR, D. M. HUNTEN, S. K. ATREYA, T. M. DONAHUE, H. W. MOOS, J. L. BERTAUX, J. E. BLAMONT, R. B. POMPHREY, AND S. LINICK 1981. Extreme ultraviolet observations from *Voyager 1* encounter with Saturn. *Science* **212,** 206–211.

BROWN, L. R. 1982. Experimental line strengths for the ν_4 and ν_2 bands of methane in the 7 μm region. *Bull. Amer. Astron. Soc.* **17,** 734.

Courtin, R., D. Gautier, and A. Lacombe 1979. Indications of supersaturated stratospheric methane on Neptune from its atmospheric thermal profile. *Icarus* **37,** 236–248.

Coustenis, A., B. Bezard, and D. Gautier 1989. Titan's atmosphere from *Voyager* infrared observations. I. The gas composition of Titan's equatorial region. *Icarus,* in press.

de Bergh, C., B. L. Lutz, T. Owen, and J. Chauville 1988. Monodeuterated methane in the outer solar system. III. Its abundance on Titan. *Astrophys. J.* **329,** 951–955.

Dubouloz, N., F. Raulin, E. Lellouch, and D. Gautier 1989. Titan's hypothesized ocean properties: The influence of surface temperature and atmospheric composition uncertainties. Submitted for publication.

Eshleman, V. R., G. F. Lindal, and G. L. Tyler 1983. Is Titan wet or dry? *Science* **221,** 53–54.

Fink, U., and H. P. Larson 1979. The infrared spectrum of Uranus, Neptune, and Titan from 0.8 to 2.5 microns. *Astrophys. J.* **233,** 1021–1040.

Flasar, F. M. 1983. Oceans on Titan? *Science* **221,** 55–57.

Frère, C., F. Raulin, G. Israel, and M. Cabane 1989. Microphysical modelling of Titan's aerosols: Application to the *in situ* analysis. *Adv. Space Res.,* in press.

Friedson, A. J., and Y. L. Yung 1984. The thermosphere of Titan. *J. Geophys. Res. A1* **89,** 85–90.

Gautier, D. 1985. The composition of the Titan atmosphere. In *The Atmospheres of Saturn and Titan.* Alpbach, Austria, 16–19 September 1985 (ESA-241).

Gautier, D., B. Bezard, A. Marten, J. P. Baluteau, N. Scott, A. Chedin, V. Kunde, and R. Hanel 1982. The C/H ratio in Jupiter from the *Voyager* infrared investigation. *Astrophys. J.* **257,** 901–912.

Hanel, R., B. Conrath, F. M. Flasar, V. Kunde, W. Maguire, J. Pearl, J. Pirraglia, R. Samuelson, L. Herath, M. Allison, D. Cruikshank, D. Gautier, P. Gierasch, L. Horn, R. Koppany, and C. Ponnamperuma 1981. Infrared observations of the Saturnian system from *Voyager. Science* **212,** 192–200.

Hanel, R. A., J. C. Pearl, and L. A. Mayo 1982. *Voyager Infrared Interferometer Spectrometer and Radiometer (IRIS): Documentation for Reduced Data Records (RDR) for the Saturnian System,* NASA Special Publication X-693-82-30. NASA, GSFC, Greenbelt, MD 20771.

Houghton, J. T. 1984. Tropospheric stratospheric exchange of trace constituents: The water vapor puzzle. In *Dynamics of the Middle Atmosphere* (Holton and Matsumo, Eds.), Terra Scientific, Tokyo.

Hunten, D. M., M. G. Tomasko, F. M., Flasar, R. E. Samuelson, D. F. Strobel, and D. J. Stevenson 1984. Titan. In *Saturn* (T. Gehrels and M. S. Matthews, Eds.), pp. 671–759. Univ. of Arizona Press, Tucson.

Husson, N., A. Chedin, N. A. Scott, D. Bailly, G. Graner, N. Lacome, A. Levy, C. Rossetti, G. Tarrago, C. Camy-Peyret, L. M. Flaud, A. Bauer, J. M. Colmont, N. Monnanteuil, J. C. Hilico, G. Pierre, M. Loete, J. P. Champion, L. S. Rothman, L. R. Brown, G. Orton, P. Varanasi, C. P. Rinsland, M. A. H. Smith, and A. Goldman 1986. The GEISA spectroscopic line parameters data bank in 1984. *Ann. Geophys.* **4,** 185–190.

Lambert, J. D. 1977. *Vibrational and Rotational Relaxation in Gases.* Clarendon, Oxford.

Lellouch, E., W. B. Hubbard, B. Sicardy, F. Vilas, and P. Bouchet, 1986. Occultation determination of Neptune's oblateness and stratospheric methane mixing ratio. *Nature (London)* **324,** 227–231.

Lellouch, E., and D. M. Hunten 1987. *Titan Atmosphere Engineering Model.* E.S.A. Space Science Department Internal Publication, ESLAB 87-199.

Lindal, G. F., G. E. Wood, H. B. Hotz, D. N. Sweetnam, V. R. Eshleman, and G. L. Tyler 1983. The atmosphere of Titan: An analysis of the *Voyager 1* radio-occultation measurements. *Icarus* **53,** 348–363.

Lunine, J. I., and D. J. Stevenson 1985. Evolution of Titan's coupled ocean–atmosphere system and interaction of ocean with bedrock. In *Ices in the Solar System* (J. Klinger *et al.,* Eds.), pp. 741–757. Reidel, Dordrecht.

Lunine, J. I., D. J. Stevenson, and Y. L. Yung 1983. Ethane ocean on Titan. *Science* **222,** 1229–1230.

Orentlicher, M., and J. M. Prausnitz 1964. Thermodynamics of hydrogen solubility in cryogenic solvents at high pressure. *Chem. Eng. Sci.* **19,** 775–782.

Owen, T. 1982. The atmosphere of Titan. *J. Mol. Evol.* **18,** 150–156.

Preston, G. T., and J. M. Prausnitz 1970. Thermodynamics of solid solubility in cryogenic solvents. *Ind. Eng. Chem. Process Des. Dev.* **9**(2), 264–271.

Raulin, F. 1985. Chimie organique dans Titan: Expériences de laboratoire et spéculations. In *The Atmospheres of Saturn and Titan.* Alpbach, Austria, 16–19 September 1985 (ESA-241).

Raulin, F. 1987. Organic chemistry in the oceans of Titan. *Adv. Space Res.* **7**(5), 71–81.

Reid, R. C., J. M. Prausnitz, and B. Poling 1987. *The Properties of Gases and Liquids,* 4th ed. McGraw–Hill, New York.

Reid, R. C., J. M. Prausnitz, and T. Sherwood 1977. *The Properties of Gases and Liquids,* 3rd ed. McGraw–Hill, New York.

Rodosevich, J. B., and R. C. Miller 1973. Experimental liquid mixture densities for testing and improving correlations for liquefied natural gas. *AIChE* **19**(4), 729–735.

Sagan, C., and S. F. Dermott 1982. The tide in the seas of Titan. *Nature (London)* **300,** 731–733.

Samuelson, R. E., R. A. Hanel, V. G. Kunde, and W. C. Maguire 1981. Mean molecular weight and hydrogen abundance of Titan's atmosphere. *Nature (London)* **292,** 688–693.

Scott, N. A. 1974. A direct method of computation of the transmission function of an inhomogeneous gaseous medium. I. Description of the method. *J. Quant. Spectrosc. Radiat. Transfer* **14,** 691–704.

Smith, G. R., D. F. Strobel, A. L. Broadfoot, B. R. Sandel, D. E. Shemansky, and J. B. Holberg 1982. Titan's upper atmosphere: Composition and temperature from the EUV solar occultation results. *J. Geophys. Res. A3* **87,** 1351–1359.

Thompson, W. R. 1985. Phase equilibria in N_2–hydrocarbon systems: Application to Titan. In *The Atmospheres of Saturn and Titan.* Alpbach, Austria, 16–19 September 1985 (ESA-241).

Toon, O. B., C. P. McKay, R. Courtin, and T. P. Ackerman 1988. Methane rain on Titan. *Icarus* **75,** 255–284.

Wang, J. C. F., and G. S. Springer 1977. Vibrational relaxation times in CH_4–N_2 and C_2H_4–N_2 mixtures. *Prog. Astronaut. Aeronaut.* **51,** 849–858.

Yardley, J. T., M. N. Fertig, and C. B. Moore, 1970. Vibrational deactivation in methane mixtures. *J. Chem. Phys.* **52,** 1450–1453.

Yuan, R. C. L., J. M. Preses, G. W. Flynn, and A. M. Ronn 1973. V–V and V–T/R energy transfer studies of C_2H_4 by infrared double resonance. *J. Chem. Phys.* **59,** 6128–6135.

Yung, Y. L., M. Allen, and J. P. Pinto 1984. Photochemistry of the atmosphere of Titan: Comparison between model and observations. *Astrophys. J. Suppl. Ser.* **55,** 465–506.

ICARUS 79, 350–361 (1989)

Solid Organic Residues Produced by Irradiation of Hydrocarbon-Containing H_2O and H_2O/NH_3 Ices: Infrared Spectroscopy and Astronomical Implications

B. N. KHARE, W. R. THOMPSON, B. G. J. P. T. MURRAY,[1] C. F. CHYBA, AND C. SAGAN

Laboratory for Planetary Studies, Cornell University, Ithaca, New York 14853

AND

E. T. ARAKAWA

Oak Ridge National Laboratory, Oak Ridge, Tennessee 37831

Received April 11, 1988; revised October 27, 1988

Methane clathrate ($CH_4 \cdot nH_2O$)—expected in cometary nuclei, in outer Solar System satellites, and perhaps in interstellar grains—as well as ices prepared from other combinations of CH_4, C_2H_6, or C_2H_2 with H_2O (and sometimes with NH_3) were irradiated at 77°K by plasma discharge. CH_4 clathrate and other H_2O/hydrocarbon ices color and darken noticeably after a dose $\sim 10^8$ to $\sim 10^9$ erg cm^{-2} over a period of 1–10 hr. Upon evaporation of the now yellowish to tan irradiated ices, a colored solid film adheres to the walls of the reaction vessel at room temperature. Transmission measurements of these organic films were made from 2.5 to 50 μm wavelength. The residue left after $CH_4 \cdot nH_2O$ irradiation exhibits IR bands which we tabulate and identify with alkane, aldehyde, alcohol, and perhaps alkene and substituted aromatic functional groups. Aldehydes are especially well indicated, and may be related to recent claims of polyoxymethylene $(H_2CO)_n$ in the coma of Comet Halley. Spectra presented here are compared with previous studies of UV or proton-irradiated, nonenclathrated hydrocarbon-containing ices and may be useful for interpreting infrared features found in the spectra of comets and interstellar grains. © 1989 Academic Press, Inc.

INTRODUCTION

Recent observations show that some cometary nuclei are dark and/or red (Degewij and Tedesco 1982, Cruikshank *et al.* 1985, Hartmann *et al.* 1987), a conclusion confirmed by Giotto spacecraft observations deep within the coma of Comet Halley (Sagdeev *et al.* 1986, Keller *et al.* 1986). The icy conglomerate model (Whipple 1950, 1951) and the spectroscopic detection of CHO, CO, CN, HCN, CH_3CN, NH, NH_2, C_2, and C_3, among other products, in the coma indicates the presence of other volatiles besides H_2O. Combinations of simple hydrocarbon and H_2O ices including clathrates (Delsemme and Swings 1952, Delsemme 1976) are likely constituents. CH_4 clathrate ($CH_4 \cdot 5.75H_2O$ in saturated form) retains CH_4 at temperatures much higher than those at which pure CH_4 could be accreted, or subsequently retained against evaporation. It is therefore expected to be a major repository of CH_4 in cometary ices, and in icy satellites in the outer Solar System (Lewis 1971, 1972). Equilibration of CO to CH_4 and retention of

---

[1] Present address: Thinking Machines Corporation, Cambridge, MA.

0019-1035/89 $3.00
Copyright © 1989 by Academic Press, Inc.
All rights of reproduction in any form reserved.

H_2O and CH_4 in the early Solar System appear to be favored, and methane clathrate is expected in the outer regions of the Saturn system and at greater heliocentric distances (cf. Prinn and Fegley 1981, Stevenson 1987, Lunine and Stevenson 1985a, Thompson *et al.* 1987a, and discussion and references given there). Methane has been found mass spectrometrically in the coma of Comet Halley at a gas production rate 0.02 that of water vapor (Allen *et al.* 1987), strengthening the case for some form of methane in the cometary nucleus. This rate implies that CH_4 constitutes at least 10% of the volatile C inventory, since the CO gas production rate is ≤ 0.2 that of H_2O. However, prolonged exposure to cosmic rays while in the Oort cloud should chemically modify cometary surfaces to a depth of several to tens of meters in 4.5×10^9 years (Shul'man 1972, Whipple 1977, Draganic *et al.* 1984, Ryan and Draganic 1986). In addition, preaccretion irradiation of ice-rich interstellar grains, which later aggregate into the cometary nucleus, may also result in significant chemical modification from UV (Greenberg 1982, Greenberg and Grim 1986) or low-energy cosmic ray processing. In the latter case, Strazzulla *et al.* (1983) have argued that low-energy cosmic rays should entirely polymerize C-containing ices on time scales less than dust cloud lifetimes. Finally, during the first $\sim 10^6$ to 10^7 years of a comet's lifetime, cometary ices would be irradiated by decaying radionuclides, now extinct, which had been incorporated into the comet during its formation (Draganic *et al.* 1984). Thus, CH_4 clathrate and other hydrocarbon-containing ices in the outer mantles of comets will be substantially processed long before entering the inner Solar System.

In the present investigation, we examine the infrared spectrum of the colored, involatile organic residue (which we call ice tholin) left behind after evaporation of the volatile component of (in this paper, moderately) irradiated clathrate or ice mixtures. The solid organic residue formed by charged particles from laboratory mixtures of H_2O (or $H_2O + NH_3$) with simple hydrocarbons may chemically resemble the involatile components formed in the outer layers of comets and satellites during long-term exposure to radiation, or incorporated into comets after preaccretion UV and cosmic ray, or postaccretion radionuclide processing. These products will be released during evaporation of the bulk unprocessed ice when the comet enters the inner Solar System, and may therefore provide a substantial component of the involatile solids ejected from the cometary surface, which are known from Vega and Giotto mass spectrometric results to be rich in organics (Kissel *et al.* 1986a, 1986b, Balsinger *et al.* 1986, Korth *et al.* 1986). They may also be responsible, as a refractory lag deposit, for the color and low albedo of the nuclei of periodic comets (e.g., Johnson *et al.* 1987). The visible spectra and product yields of irradiated ices and the application of these findings to outer Solar System satellites and Pluto are discussed elsewhere (Thompson *et al.* 1987a). Previous work on infrared spectra of irradiated ices is discussed below.

EXPERIMENTAL

Except for preliminary announcements of these results (Sagan *et al.* 1984a, 1986, Murray *et al.* 1985, Khare *et al.* 1985), no previous laboratory work on irradiated methane clathrates is apparent in the literature, although there have been extensive studies, beginning with Berger (1961), on irradiation of pure or mixed ices, which are sampled below.

The production of CH_4–H_2O clathrate was best accomplished by crushing H_2O ice with a steel ball in a commercial paint shaker at 195°K under 30–140 bars of CH_4 gas for 1 to 3 days. Unenclathrated CH_4 was removed by sustained pumping at $P < 10^{-3}$ mbar and $T = 77°K$. The $CH_4 : H_2O$ ratio was checked directly by evaporating a sample of the clathrate and measuring the CH_4 gas released manometrically. Since the equilibrium vapor pressure of CH_4 gas over the pure condensate is 11.8 mbars at 77°K (Brown and Ziegler 1979), much lower measured values of CH_4 partial pressure directly indicate the presence of the clathrate. Results were repeatable in successive experiments. The identity of the methane gas released from the clathrate was confirmed by infrared spectroscopy. That clathrates rather than simple ice mixtures are produced by a similar procedure has been demonstrated via neutron and X-ray diffraction studies (Davidson *et al.* 1984). $CH_4:H_2O$ ratios ~1:20 are typical in our experiments. Partial clathrates produced at 77°K by direct cocondensation, or by exposure of H_2O frost to liquid CH_4, retained much less CH_4 (~1:200). These occupancy ratios are consistent with the disequilibrium values of a few percent calculated by Lunine and Stevenson (1985); structurally, the overall ratio probably results from H_2O ice grains with a thin veneer of CH_4 clathrate of much higher occupancy (Lunine and Stevenson 1985). Physically trapped (occluded) CH_4 cannot be present in significant quantities, because it would not freeze at 195°K in the crushing method, and cannot penetrate the already-formed H_2O frost in at least one of the direct condensation methods—all of which, however, produced approximately the same $CH_4:H_2O$ ratio. For all occupancy ratios studied, chromophores and new infrared-active organic molecules were produced under irradiation. In other experiments, mixed ices of less volatile gases ($C_2H_6 + H_2O$, $C_2H_6 + NH_3 + H_2O$, and $C_2H_2 + H_2O$) were generally produced by cocondensation of frosts from a gas mixture of the desired composition. These frosts differ from the glassy matrix of molecules which characterizes films frozen on cold fingers at 10–20°K, such as have been utilized in interstellar simulations (e.g., Greenberg 1982), and for which clathrates are not expected.

All frosts discussed here were condensed and irradiated inside irradiation ampules at 77°K, as shown in Fig. 1. A high-frequency corona discharge was sustained above the ice surface at a flux ~10^5–10^6 ergs cm^{-2} sec^{-1} by typically using one or more tesla coils in complementary duty cycles. The discharge is characterized (cf. Bell 1974) by a roughly Maxwellian distribution of electron energy, with mean energy of a few electron volts; the high-energy tail is responsible for most of the processing of the ice. As long as the incident charged particles are considerably more energetic than the bond energies of the target, the resulting chemistry is unlikely to depend sensitively on the incident energy (see Thompson *et al.* 1987b). Both the thickness of the clathrate layer on the ice crystals and the penetration depth of the plasma electrons are small: residues produced here result from irradiation of a thin, clathrate-rich layer even though the overall ratio was ~1:200 $CH_4:H_2O$.

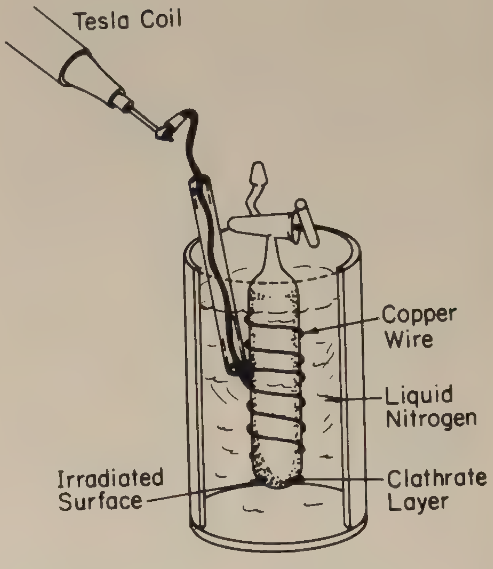

FIG. 1. Experimental configuration for corona discharge irradiation of CH_4 clathrates or mixed hydrocarbon-containing ices. Independent calibration by calorimetry and by ethylene frost dosimetry indicates an effective flux ~5×10^4 ergs cm^{-2} sec^{-1} delivered by the plasma to the inner surface of the irradiation ampule.

Electron and ion bombardment mimics (cf. Thompson *et al.* 1987a) the solar wind irradiation of comets and cometary grains in the inner Solar System, and (although at much lower particle energies) trapped magnetospheric particle irradiation of satellite surfaces; the cosmic ray irradiation of cometary ice in the Oort cloud as well as of satellite subsurface ice; and the preaccretion cosmic ray and postaccretion radionuclide irradiation of cometary ices. Independent measurements from calorimetry and from ethylene frost dosimetry (Thompson *et al.* 1987a) imply an effective flux $\sim 5 \times 10^4$ ergs cm^{-2} sec^{-1} delivered by the plasma to the inner surface of the irradiation ampule. Irradiation was maintained from 10 hr to 1 week. The ampule was then allowed to equilibrate to room temperature, the ice was evaporated, and residual H_2O and CH_4 (or other precursor hydrocarbons) were pumped away under high vacuum at room temperature. Transmission measurements of pressed pellets of the involatile organic residue (not the irradiated ices) dispersed in a CsI matrix were made on a PE Model 621 infrared spectrometer. [Spectra of the same residues after devolatilization under vacuum at 150°C are presented by Thompson *et al.* (1987a).]

This experimental procedure provides a simulation of particular relevance to cometary spectra (Chyba and Sagan 1987a,b). As a comet approaches perihelion, icy grains with incorporated refractory residue are ejected from its surface or jetted from its interior, and the ice sublimes. The refractory residue, probably stable to 500–1000°K (Sagan *et al.* 1984b) remains largely in solid form, and heated by sunlight emits in the infrared. Partial evaporation may contribute to gas phase fluorescence. (The infrared comparison of laboratory and astronomical spectra is discussed further below.)

RESULTS

CH_4 clathrate and all other water/hydrocarbon ices we have examined show coloration, progressive darkening, and the formation of involatile organic products upon continuing irradiation. These results are consistent with many others in the literature, but this is the first such finding for low-energy electron bombardment or for demonstrated clathrates. Two categories of control experiments were performed: (1) Methane clathrate, subjected to identical experimental protocols but not irradiated, shows no reddening, no darkening, and no involatile residue. (2) The same is true of irradiated fine-grained pure water frosts, except that they typically appear blue-white relative to a $BaSO_4$ standard before irradiation and evolve a flatter spectrum under irradiation—perhaps because of sintering.

In experimental runs, spectral reddening at optical frequencies, noticeable visually and by reflection spectroscopy, typically appears within a few hours after the start of irradiation. A well-developed color, indicating the synthesis of involatile residue, is generally seen after the deposition of $\sim 10^8$ ergs cm^{-2} per μm of ice thickness. A similar product would therefore be expected to be distributed through the near-surface layers of comets and satellites containing such ices, since the total galactic cosmic ray dose accumulated over 4.5×10^9 years is $\sim 2 \times 10^8$ ergs cm^{-2} per μm thickness through the upper 20 cm of cometary ice; during this period, an estimated 34% of the molecules at the surface, 30% of the molecules at 1 m, and 17% at 2 m would be processed (Whipple 1977, see also Moore *et al.* 1983, Thompson *et al.* 1987a).

Residues were produced by irradiation of CH_4 clathrate and the ices cocondensed from gas phase $C_2H_6 + H_2O$, $C_2H_6 + H_2O + NH_3$, and $C_2H_2 + H_2O$. The relative proportions of precursor gases were 1:3, 1:1:1, and 1:3, respectively. Residues other than from CH_4 clathrate were produced over periods ~ 100 hr at lower fluxes, $\sim 10^4$ ergs cm^{-2} sec^{-1}. The initial products of CH_4 clathrate and $C_2H_6 + H_2O$ irradiation are each a light yellow, while the color is a more pronounced yellow for $C_2H_6 + H_2O + NH_3$ (cf. Greenberg *et al.* 1983) and

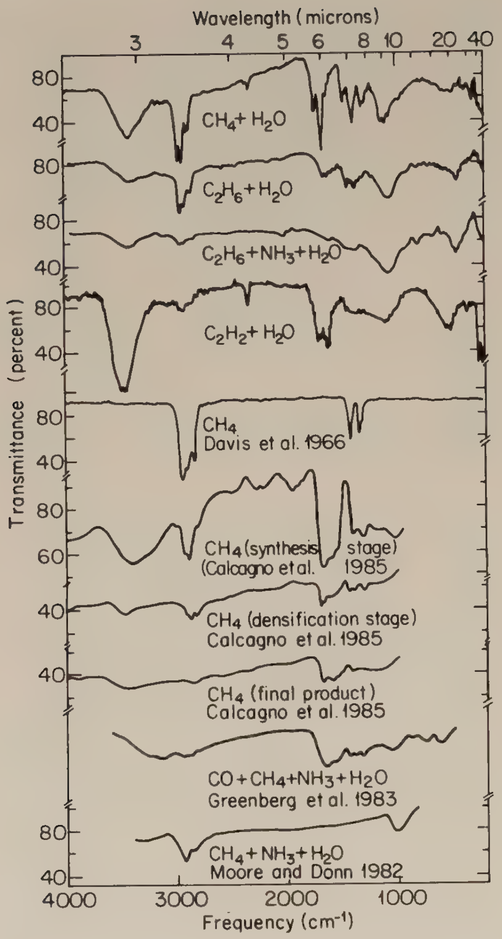

FIG. 2. A comparison of our irradiated $CH_4 + H_2O$ low-occupancy clathrate ($CH_4/H_2O \sim 1:200$) residue spectra with spectra of residue produced by 1.5-MeV proton irradiation of CH_4 ice (Calcagno *et al.* 1985) indicates some common hydrocarbon functional groups (see text). A high dose (CH_4 "final" spectrum) produces broad structureless bands attributed to further chemical processing and polymerization. Also shown is an early spectrum (Davis *et al.* 1966) of the residue of ^{60}CO γ-irradiation of pure CH_4 ice. Our IR spectra of $CH_4 + H_2O$ and $C_2H_6 + NH_3 + H_2O$ ice residues are also compared to residues of $CO + CH_4 + NH_3 + H_2O$ produced by UV irradiation (Greenberg *et al.* 1983) and $CH_4 + NH_3 + H_2O$ produced by proton irradiation (Moore and Donn 1982). The presence of bands near 3.4, 6, 7.3, 9.5 μm, etc., indicate formation of $-CH_3$, $-CH_2-$, $-CH_2-CHO$, $C-CH_3$, $-CHO$, and C–O functional groups. Radiation doses for the first four spectra starting from the top are all $\sim 10^{10}$ ergs cm^{-2}; Davis *et al.*, $\sim 10^9$–10^{10} ergs g^{-1}; Calcagno *et al.*, $\sim 5 \times 10^{10}$ (upper), 8×10^{10} (middle), and 2×10^{11} (lower) ergs cm^{-2}; Greenberg *et al.*, $\sim 5 \times 10^7$ ergs cm^{-2}; and Moore and Donn, $\sim 10^9$ ergs cm^{-2}. Spectra

tan for $C_2H_2 + H_2O$. When the $C_2H_2 + H_2O$ reside (with ices removed) is further irradiated to ~10 times the initial dose ($\sim 10^{11}$–10^{12} ergs cm^{-2}), the color evolves to a distinct brown. Progressive deepening of color to darker, more subdued hues also occurs for methane clathrate. These changes are caused, of course, by progressive changes in the organic chemistry of the ice residues; the asymptotic state after prolonged irradiation may be a black sample rich in polycyclic aromatics and elemental carbon (cf. Khare *et al.* 1987). Visible frequency spectra of the residues, and the reflection spectrum of 200 : 1 $CH_4 + H_2O$ clathrates are displayed in Thompson *et al.* (1987a).

The infrared transmission spectra of four ice tholin residues are shown in Fig. 2, where they are compared with previous work on ^{60}Co γ-irradiation of pure methane ice with a dose in the range 4×10^8 to 1.5×10^{10} ergs g^{-1} (Davis *et al.* 1966); 1.5-MeV proton bombardment of pure methane ice at doses of $\sim 5 \times 10^{10}$ (upper), 8×10^{10} (middle), and 2×10^{11} (lower) ergs cm^{-2} (Calcagno *et al.* 1985); and on UV (Greenberg *et al.* 1983) and proton (Moore and Donn 1982) irradiation of mixed $CH_4 + NH_3 + H_2O$ ices at doses, respectively, of $\simeq 5 \times 10^{-7}$ erg cm^{-2} and 2.7×10^{-11} erg g^{-1}.

Our spectra of the $CH_4 + H_2O$ and $C_2H_6 + H_2O$ products show many well-defined spectral bands.[2] Maximum probable error is ± 5 cm^{-1}, and greater accuracy was obtained at slow scan rates. Table I lists the

---

[2] Since these spectra are obtained in air, we might be concerned that some of the features (e.g., in the 2.8–4.0 μm region) are due to postexperimental oxidation or hydration. However, in the production of organic tholin films by corona discharge through a 90% N_2/10% CH_4 mixture in an IR cell and subsequent exposure to air no change in IR spectra was detectable (Khare *et al.* 1984b), a result probably applicable to the organic residues discussed in the present study, especially since H_2O is here the principal precursor material.

---

of residues which have been devolatilized by exposure to sustained high vacuum at 150°C are presented in Thompson *et al.* (1987a).

TABLE I

ANALYSIS OF IR ABSORPTION BANDS IN THE SPECTRUM OF INVOLATILE RESIDUE LEFT AFTER EVAPORATION OF IRRADIATED CH_4 + H_2O ICE[a]

Wavelength, μm (Frequency, cm^{-1})	Intensity[b]	Vibrational classification	Chemical functional groups
2.92 (3425)	M	O–H stretching	Alcohol
3.38 (2955)	S	C–H stretching	Alkanes $-CH_3$, $-CH_2-$
3.42 (2927)	S		
3.48 (2870)	M		
3.50 (2856)	M	C–H stretching	Aldehydes –CHO
5.82 (1718)	M	C=O stretching	Aldehyde or ketones
6.07 (1648)	S	C=C or C=O stretching	Alkene, aldehydes, or ketones
6.27 (1596)	M	C=C stretching	Conjugated alkene or aromatic
6.90 (1450)	M	$-CH_2-$, $-CH_3$ scissoring	Alkanes
7.30 (1370)	M	C–H bending	Aldehyde or alkanes
7.81 (1280)	W	O–H or C–H bending	Alcohol or aldehyde
8.98 (1114)	M	C–O, C–C stretching	Alcohol, alkanes, aldehyde
9.38 (1066)	M		
9.66 (1035)	M		
10.47 (955)	ShM		
11.14 (898)	M		
13.64 (733)	W	C–H rocking	Alkene, aromatic, aldehyde
18.12 (552)	W		
19.84 (504)	W		
22.62 (442)	W		
29.33 (341)	W		
38.61 (259)	W		

Note. Spectral features of the residue which has been further devolatilized under vacuum at 425°K (Thompson *et al.* 1987a) are similar except for diminution of the 2.92-μm O–H feature and of weak bands at 3.48–3.50 and 6.27 μm.

[a] Analysis is based on the Colthup compilation of characteristic IR functional groups (Colthup 1950).

[b] Intensity code: S = strong, M = medium, W = weak, Sh = shoulder.

IR bands in the CH_4 + H_2O residue, indicating the presence of carbonyl, hydroxyl (alcohol), alkane, aldehyde, and perhaps alkene and aromatic (substituted benzene) groups. Since all precursor ices have been evaporated, these spectral features apply only to the product organic film. The complexity of these residue spectra limits further IR analysis. The aliphatic aldehyde group $-CH_2-CHO$ in the residue is strongly indicated by the presence of the bands at 3.50 (M), 6.07 (S), 7.30 (M), 9.38 (M), and 10.47 (ShM) μm, which agree well in wavelength and relative intensity with catalogued bands for aliphatic aldehydes (Colthup 1950); features at 6.90 (M), 10.47 (ShM), and 13.64 (W) μm are suggestive of $(CH_2)_4$ functional groups (Bellamy 1958).

Residues from CH_4 clathrate and mixed C_2H_6 + H_2O + NH_3 ices are compared with other organic residues derived from photolysis or proton irradiation of CH_4 ice or mixed CH_4 + H_2O + NH_3 ice in Fig. 2. While there are important differences in detail, depending on starting materials, radiation dose, and perhaps radiation source and sample temperature, there are many similarities due to common or similar functional groups. The residue obtained from depositing $\sim 10^{10}$ ergs cm^{-2} by coronal discharge on CH_4 + H_2O ice exhibits bands similar to those found in the initial residue obtained when $\sim 10^{10}$ ergs cm^{-2} are incident on pure CH_4 ice using 1.5-MeV protons (Calcagno *et al.* 1985). Our band at 2.9 μm corresponds to the 2.9-μm band of Calcagno *et* *al.* and is due to organic O–H stretching vibrations in both residues. While for CH_4 + H_2O ice tholin, OH is an expected functional group in the residue, features attributable to OH in the CH_4 ice residue of Calcagno *et al.* must, of course, be experimental artifacts due to ambient H_2O or O_2. Upon prolonged heating of the CH_4 + H_2O and other residues at 150°C under high vacuum, the OH band greatly diminishes in prominence. We conclude this is due to the loss of one or more moderately volatile organic components, since the band position is inconsistent with that of adsorbed H_2O. The band structure at 3.4 μm is present in many of the spectra and is due to the symmetric and asymmetric stretching vibrations in methyl ($-CH_3$) and methylene ($-CH_2$) groups. The sharp peaks for CH_4–H_2O ice tholin at 5.82 μm and 6.07 μm are attributed to C=O and C=C, while Calcagno *et al.*'s CH_4 ice residue shows a broad feature at 5.8 to 6.1 μm that is attributed to C=C with perhaps some contribution from C=O due to carboxylic acids or ketones. The band near 7 μm is also seen in both residues and is due to CH_2 and CH_3 groups.

The residue of γ-irradiation of CH_4 ice (Davis *et al.* 1966) shows features at 3.38, 3.42, and 3.49 μm that roughly correspond to the 3.4-μm features in the other spectra shown; however, here the ≃6-μm features are absent, while absorptions are present at 6.86 and 7.28 μm, attributed by Davis *et al.* to $-CH_3$ and $-CH_2-$. Similarly, we find that our CH_4 + H_2O and C_2H_6 + NH_3 + H_2O irradiated ice residues have functional groups that are also present in the residues from UV photolysis of a CO + CH_4 + NH_3 + H_2O ice (Greenberg *et al.* 1983) and from proton irradiation of a 4 : 5 : 2 CH_4 + NH_3 + H_2O ice (Moore and Donn 1982) at doses, respectively, of $\simeq 5 \times 10^7$ ergs cm^{-2} and $\sim 10^9$ ergs cm^{-2} (Moore 1981).

Our spectra exhibit considerably richer detail than the earlier spectra shown. The broadening and loss of structure with increasing dose in the three Calcagno *et al.* spectra (Fig. 2) are indicative of further chemical processing and polymerization at high irradiation doses. Irradiation products of NH_3-containing ices show no features (such as the 4.6-μm nitrile or isocyanide bands) unambiguously attributed to nitrogenous functional groups. The differences between the second and third spectra in Fig. 2 seem due entirely to the presence or absence of 33% NH_3 in the initial mixture; NH_3 seems somehow to contribute to the production of a flatter spectrum.

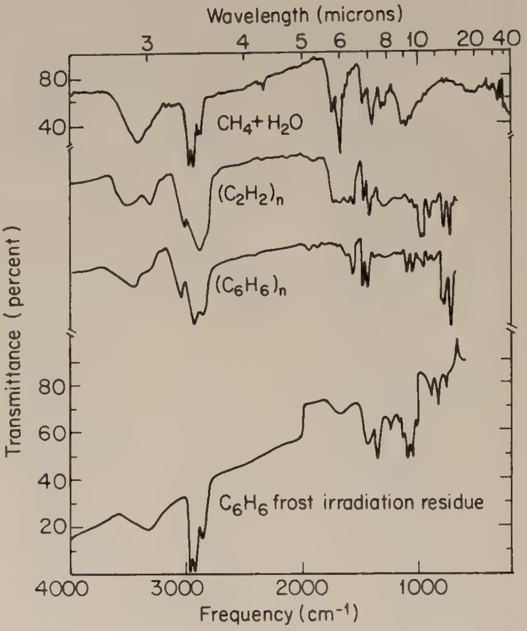

FIG. 3. A comparison of our irradiated CH_4 + H_2O low-occupancy clathrate (CH_4/H_2O ~ 1:200) with samples of radiation-produced polyacetylene and polybenzene (Lind 1961), and residue obtained from C_6H_6 frost bombarded at 77°K with a 100-keV proton beam (5×10^{15} p^+ cm^{-2}) (Strazzulla *et al.* 1984).

In Fig. 3 is a comparison between our spectra of the organic residues of irradiated $CH_4 : H_2O$ low-occupancy clathrate, with spectra of (poorly characterized) polyacetylene and polybenzene (both from Lind 1961) and of proton-irradiated benzene (Strazzulla *et al.* 1985). The strong alkene, alkyne, and aromatic C–H features at 12 to 16 μm in $(C_2H_2)_n$ and $(C_6H_6)_n$ are missing in the clathrate residue. The 2.70- to 2.85-μm features in the $(C_2H_2)_n$ and $(C_6H_6)_n$ polymers, but not in the clathrate residue, are probably due to O–H stretching transitions in adsorbed water; this conclusion is supported by the presence in the clathrate residue of features near 7.3 and 9 μm (attributed to alcohols or aldehydes) which are absent from the $(C_2H_2)_n$ and $(C_6H_6)_n$ spectra. Nevertheless, the overall similarities among the spectra of Fig. 3 suggest the important possibility that complex organics of quite different origins may have similar spectra, especially when irradiation dose is an unconstrained free parameter.

COMPARISON OF LABORATORY AND ASTRONOMICAL SPECTRA

Accuracies in measuring laboratory band "centers" depend on band shape and width; at the shorter IR wavelengths between 2.5 and 25 μm they are typically at least ±0.01 μm, and at the longer wavelengths to 50 μm, they are typically at least ±0.5 μm. IR features of the residue from CH_4 clathrate near 2.92 (M), 3.42 (S), 6.27 (M), and 6.90 (M) μm seem in fair agreement with dust absorption bands found in IR galactic sources (cf. Sagan and Khare 1979, Strazzulla *et al.* 1984). The laboratory C–H stretching features at 3.38 (S), 3.42 (S), 3.48 (M), and 3.50 (M) μm seem to match observations (Wickramasinghe and Allen 1980, Butchard *et al.* 1986) of the galactic infrared source IRS 7 (features at 3.38, 3.41, and 3.48 μm)—that Hoyle and Wickramasinghe (1986) believe are due to interstellar bacteria, a less plausible hypothesis (cf. Chyba and Sagan 1987c). The view that UV-irradiated interstellar ices produce organic molecules that account for the unidentified interstellar IR bands has been championed by Greenberg (cf. Greenberg *et al.* 1983 and Fig. 2; cf. also Sagan and Khare 1979). The agreements between laboratory and interstellar spectra are certainly not one-to-one, however; e.g., the prominent 9- to 10-μm feature in most of the spectra of Fig. 2 is not apparent in the usual list of "unidentified" interstellar emission features (cf. Russell *et al.* 1977).

The spectra of these residues are dominated by transitions from the vibrational ground state without rotational structure, and thus are insensitive to the differences in pressure and temperature between the laboratory and the astronomical environment. We distinguish these solids—which persist at both low and high (e.g., cometary dust) temperatures—from simple ices and clathrates (such as our starting materials), volatile organic products, and trapped radicals, all of which also contribute spectral features to interstellar grains (Greenberg *et al.* 1983).

There are virtually no infrared spectra at $\lambda > 3$ μm now available for icy bodies in the outer Solar System, but the infrared analysis of complex organic molecules in comets has recently been initiated after the close approach of Comets Halley and Wilson. Spacecraft (Combes *et al.* 1986, Encrenaz *et al.* 1987) and ground-based (Baas *et al.* 1986, Danks *et al.* 1986, Knacke *et al.* 1986, Wickramasinghe and Allen 1986) observations of P/Halley reveal a triple-peaked emission feature near 3.4 μm, characteristic of C–H stretching in hydrocarbons. The strongest emission feature is near 3.36 (Baas *et al.* 1986) or 3.37 μm (Danks *et al.* 1986), close to the strong doublet in our laboratory spectra at 3.38 (±0.01) and 3.42 (±0.01) μm (Table I and Fig. 2). Observations of Comet Wilson show a very similar emission feature at 3.4 μm (Allen and Wickramasinghe 1987, Brooke *et al.* 1987). While some contribution from gas phase fluorescence of as yet unidentified hydrocarbons is expected (Croviser and Encrenaz 1983, Combes *et al.* 1986), small organic grains have been detected directly in the comae of P/Halley by mass spectrometers aboard both the Vega (Kissel *et al.* 1986a) and Giotto (Kissel *et al.* 1986b) spacecraft.

Using the infrared spectrum of the 425°K-devolatilized organic residue from irradiated low-occupancy methane clathrate as shown in Thompson *et al.* (1987a) and tabulated in Table I of the present paper (see table note), Chyba and Sagan (1987b, 1989) have matched the observed 3.4-μm emission feature in P/Halley with a model consistent with observations in the comet's coma and without predicting longer wavelength features where none is observed. This agreement is of additional interest because of the identification of irradiated low-occupancy methane clathrate residue IR features with aldehydes (above, Table I and Sagan *et al.* 1986), while the formaldehyde polymer polyoxymethylene $(H_2CO)_n$ has been tentatively identified by the *Giotto* mass spectrometer in the coma of Comet Halley (Huebner 1987, Huebner *et al.* 1987). (We note that this is not the only possible formaldehyde polymer.) Modeling with infrared spectra of other candidate irradiated cometary ices (cf. Fig. 2) is being undertaken. By no means do all organic solids show a 3.4-μm feature; e.g., the complex hydrocarbon ($[C/H] \simeq 0.7$) formed by plasma irradiation of a 3% CH_4/25% He/ 72% H_2 gas mixture at submillibar pressures shows extensive absorption at $\lambda > 6$ μm, but no IR features at shorter wavelengths (Khare *et al.* 1987).

The foregoing results and those of Thompson *et al.* (1987a) represent a first look at the experimental problem. We are now proceeding to a better-quantified exploration of the composition/dose parameter space. With a more complete set of experimental results in hand, it seems likely that IR spectroscopy will be a useful diagnostic tool in future studies of the organic chemistry of irradiated ices in cometary nuclei, in the satellites in the outer Solar System and Pluto, and in the interstellar medium. Future spacecraft encountering these locales should be equipped for infrared spectroscopy of appropriate wavelength, resolution, and sensitivity.

ACKNOWLEDGMENTS

We are grateful to L. Allamandola and two anonymous referees for helpful discussion. This research was supported in part by NASA Grants NGR 33-010-220 and NGR 33-010-101, and by the Office of Health and Environmental Research, U.S. Department of Energy, under Contract DE-AC05-840R21400 with Martin Marietta Energy Systems, Inc.

REFERENCES

Allen, D. A., and D. T. Wickramasinghe 1987. Discovery of organic grains in Comet Wilson. *Nature (London)* **329,** 615–616.

Allen, M., M. Delitsky, W. Huntress, Y. Yung, W. H. Ip, R. Schwenn, H. Rosenbauer, E. Shelley, H. Balsiger, and J. Geiss 1987. Evidence for methane and ammonia in the coma of Comet P/Halley. *Astron. Astrophys.* **187,** 502–512.

Baas, F., T. R. Geballe, and D. M. Walther 1986. Spectroscopy of the 3.4 micron emission feature in Comet Halley. *Astrophys. J.* **311,** L97–L101.

Balsinger, H., K. Altwegg, F. Buhler, J. Geiss, A. G. Ghielmetti, B. E. Goldstein, R. Goldstein, W. T. Huntress, W. H. Ip, A. J. Lazarus, A. Meier, M. Neugebauer, U. Rettenmund, H. Rosenbauer, R. Schwenn, R. D. Sharp, E. G. Shelley, E. Ungstrup, and D. T. Young 1986. Ion composition and dynamics at Comet Halley. *Nature (London)* **321,** 330–336.

Bell, A. T. 1974. Fundamentals of plasma chemistry. In *Techniques and Applications of Plasma Chemistry* (J. R. Hollahan and A. T. Bell, Eds.), pp. 1–56. Wiley, New York.

Bellamy, L. J. 1958. *The Infrared Spectra of Complex Molecules.* Wiley, New York.

Berger, R. 1961. The proton irradiation of methane, ammonia, and water at 77°K. *Proc. Natl. Acad. Sci. U.S.A.* **47,** 1434–1436.

Brooke, T. Y., R. F. Knacke, T. C. Owen, and A. T. Tokunaga 1987. Detection of infrared emission features in Comet Wilson. *Bull. Amer. Astron. Soc.* **19,** 893.

Brown, G. N., Jr., and W. T. Ziegler 1979. Vapor pressure and heats of vaporization and sublimation of liquids and solids of interest in cryogenics below 1 atm pressure. *Adv. Cryogen. Eng.* **25,** 662–670.

Butchard, I., A. D. McFadzean, D. C. B. Whittet, T. R. Geballe, and J. M. Greenberg 1986. Three micron spectroscopy of the galactic centre source IRS7. *Astron. Astrophys.* **154,** L5–L7.

Calcagno, L., G. Foti, L. Torrisi, and G. Strazzulla 1985. Fluffy layers obtained by ion bombardment of frozen methane: Experiments and applications to Saturnian and Uranian satellites. *Icarus* **63,** 31–38.

Chyba, C., and C. Sagan 1987a. Infrared emission from organic grains in Halley's comet. In *Proceedings of the International Workshop on Laboratory Simulation of Organic Cometary Material* (J. Kissel and G. Strazzula, Eds.), pp. 50–57. Univ. of Catania, Sicily; Cornell CRSR Preprint No. 877.

Chyba, C., and C. Sagan 1987b. Infrared emission by organic grains in the coma of Comet Halley. *Nature (London)* **330,** 350–353.

Chyba, C., and C. Sagan 1987c. Cometary organics but no evidence for bacteria. *Nature (London)* **329,** 208.

CHYBA, C., AND C. SAGAN 1989. The heliocentric evolution of infrared cometary spectra: Results from an organic grain model. *Icarus,* in press.

COLTHUP, N. B. 1950. Spectra-structure correlations in the infrared region. *J. Opt. Soc. Amer.* **40,** 397–400.

COMBES, M., V. I. MOROZ, J. F. CRIFO, J. M. LAMARRE, J. CHARRA, N. F. SANKO, A. SOUFFLOT, J. P. BIBRING, S. CAZES, N. CORON, J. CROVISIER, C. EMERICH, T. ENCRENAZ, R. GISPERT, A. V. GRIGORYEV, G. GUYOT, V. A. KRASNOPOLSKY, YU. V. NIKOLSKY, AND F. ROCARD 1986. Infrared sounding of Comet Halley from Vega 1. *Nature* (*London*) **321,** 266–268.

CROVISIER, J., AND T. ENCRENAZ 1983. Infrared fluorescence of molecules in comets: The general synthetic spectrum. *Astron. Astrophys.* **126,** 170–182.

CRUIKSHANK, D. P., W. K. HARTMANN, AND D. J. THOLEN 1985. Colour, albedo and nucleus size of Halley's comet. *Nature* (*London*) **315,** 122–124.

DANKS, A., T. ENCRENAZ, P. BOUCHET, T. LE BERTRE, A. CHALABAEV, AND N. EPCHTEIN 1986. Observation of an emission feature at 3.4 μ in the spectrum of Comet Halley. In *20th ESLAB Symposium on the Exploration of Halley's Comet,* Vol. 3 (ESA SP-200), pp. 103–106.

DAVIDSON, D. W., Y. P. HANDA, C. I. RATCLIFFE, J. S. TSE, AND B. M. POWELL 1984. The ability of small molecules to form clathrate hydrates of structure II. *Nature* (*London*) **311,** 142–143.

DAVIS, D. R., W. F. LIBBY, AND W. G. MEINSCHEIN 1966. Chemistry of positive ions. VI. Positive-ion chemistry in solid methane. *J. Chem. Phys.* **45,** 4481–4492.

DEGEWIJ, J., AND E. F. TEDESCO 1982. Do comets evolve into asteroids? Evidence from physical studies. In *Comets* (L. L. Wilkening, Ed.), pp. 665–695. Univ. of Arizona Press, Tucson.

DELSEMME, A. H. 1976. Chemical nature of the cometary snows. *Mem. Soc. R. Sci. Liege* **9,** 135–145.

DELSEMME, A. H., AND P. SWINGS 1952. Hydrates de gaz dans les noyaux cometaires et les grains interstellaires. *Ann. Astrophys.* **15,** 1–6.

DRAGANIC, I. G., Z. D. DRAGANIC, AND S. VUJOSEVIC 1984. Some radiation-chemical aspects of chemistry in cometary nuclei. *Icarus* **60,** 464–475.

ENCRENAZ, TH., J. CROVISIER, M. COMBES, V. I. MOROZ, AND A. GRIGORIEV 1987. Observation of the spectra of P/Halley between 6 and 12 microns from the IKS-Vega experiment. *Bull. Amer. Astron. Soc.* **19,** 879.

GREENBERG, J. M. 1982. What are comets made of? A model based on interstellar dust. In *Comets* (L. L. Wilkening, Ed.), pp. 131–163. Univ. of Arizona Press, Tucson.

GREENBERG, J. M., AND R. GRIM 1986. The origin and evolution of comet nuclei and Comet Halley results. In *20th ESLAB Symposium on the Exploration of Halley's Comet,* Vol. 2 (ESA SP-250), pp. 255–263.

GREENBERG, J. M., C. E. P. M. VAN DE BULT, AND L. J. ALLAMANDOLA 1983. Ices in space. *J. Phys. Chem.* **87,** 4243–4260.

HARTMANN, W. K., D. J. THOLAN, AND D. P. CRUIKSHANK 1987. The relationship of active comets, "extinct" comets, and dark asteroids. *Icarus* **69,** 33–50.

HOYLE, F., AND N. C. WICKRAMASINGHE 1986. On the nature of the interstellar grains. *Q. J. R. Astron. Soc.* **27,** 21–37.

HUEBNER, W. F. 1987. First polymer in space identified in Comet Halley. *Science* **237,** 628–630.

HUEBNER, W. F., D. C. BOICE, AND C. M. SHARP 1987. Polyoxymethylene in Comet Halley. *Astrophys. J.* **320,** L149–L152.

JOHNSON, R. E., J. F. COOPER, L. J. LANZEROTTI, AND G. STRAZZULLA 1987. Radiation formation of a non-volatile comet crust. *Astron. Astrophys.* **187,** 889–892.

KELLER, H. U., C, ARPIGNY, C. BARBIERI, R. M. BONNET, S. CAZES, M. CORADINI, C. B. COSMOVICI, W. A. DELAMERE, W. F. HUEBNER, D. W. HUGHES, C. JAMAR, D. MALAISE, H. J. REITSEMA, H. U. SCHMIDT, W. K. H. SCHMIDT, P. SEIGE, F. L. WHIPPLE, AND K. WILHELM 1986. First Halley multicolour camera imaging results from Giotto. *Nature* (*London*) **321,** 320–326.

KHARE, B. N., B. G. J. P. T. MURRAY, C. SAGAN, AND W. R. THOMPSON 1985. Are there diagnostic spectral features of irradiated cometary ices? *Astrochemistry,* IAU Symposium No. 120, Goa, India (M. S. Vardya and S. P. Tarafoder, Eds.). Reidel, Dordrecht.

KHARE, B. N., C. SAGAN, E. T. ARAKAWA, F. SUITS, T. CALLCOTT, AND M. WILLIAMS 1984a. Optical constants of organic tholins produced in a simulated Titanian atmosphere: From soft X-rays to microwave frequencies. *Icarus* **60,** 127–137.

KHARE, B. N., W. R. THOMPSON, C. SAGAN, M. L. COOKE, J. DIMAURO, B. G. J. P. T. MURRAY, AND E. T. ARAKAWA 1984b. Time-evolution of infrared absorption features in an oxygen-free Titan organic synthesis experiment. *Bull. Amer. Astron. Soc.* **16,** 664–665.

KHARE, B. N., C. SAGAN, W. R. THOMPSON, E. T. ARAKAWA, AND P. VOTAW 1987. Solid hydrocarbon aerosols produced in simulated Uranian and Neptunian stratospheres. *J. Geophys. Res.* **92,** 15,067–15,081.

KISSEL, J., R. Z. SAGDEEV, J. L. BERTAUX, V. N. ANGAROV, J. AUDOUZE, J. E. BLAMONT, K. BUCHLER, E. N. EVLANOV, H. FECHTIG, M. N. FOMENKOVA, H. VON HOERNER, N. A. INOGAMOV, V. N. KHROMOV, W. KNABE, F. R. KRUEGER, Y. LANGEVIN, V. B. LEONAS, A. C. LEVASSEUR-REGOURD, G. G. MANAGADZE, S. N. PODKOLZIN, V. D. SHAPIRO, S. R. TABALDYEV, AND B. V. ZUBKOV 1986a. Composition of Comet Halley dust particles from Vega observations. *Nature* (*London*) **321,** 280–282.

Kissel, J., D. E. Brownlee, K. Buchler, B. C. Clark, H. Fechtig, E. Grun, K. Hornung, E. G. Igenbergs, E. K. Jessberger, F. R. Krueger, H. Kuczera, J. A. M. McDonnell, G. M. Morfill, J. Rahe, G. H. Schwehm, Z. Sekanina, N. G. Utterback, H. J. Volk, and H. A. Zook 1986b. Composition of Comet Halley dust particles from Giotto observations. *Nature* (*London*) **321,** 336–337.

Knacke, R. F., T. Y. Brooke, and R. R. Joyce 1986. Observations of 3.2–3.6 micron emission features in Comet Halley. *Astrophys. J.* **310,** L49–L53.

Korth, A., A. K. Richter, A. Loidl, K. A. Anderson, C. W. Carlson, D. W. Curtis, R. P. Lin, H. Reme, J. A. Sauvaud, C. d'Uston, F. Cotin, A. Cros, and A. Mendis 1986. Mass spectra of heavy ions near Comet Halley. *Nature* (*London*) **321,** 335.

Lewis, J. S. 1971. Satellites of outer planets: Their physical and chemical nature. *Icarus* **15,** 174–185.

Lewis, J. S. 1972. Low temperature condensation from the solar nebula. *Icarus* **16,** 241–252.

Lind, S. C. 1961. *Radiation Chemistry of Gases*, p. 172. Reinhold, New York.

Lunine, J. I., and D. J. Stevenson 1985. Thermodynamics of clathrate hydrate at low and high pressures with application to the other Solar System. *Astrophys. J. Suppl. Ser.* **58,** 493–531.

Moore, M. 1981. *Studies of Proton Irradiated Cometary-type Ice Mixtures*. Ph.D. thesis, University of Maryland at Baltimore.

Moore, M. H., and B. Donn 1982. The infrared spectrum of a laboratory-synthesized residue: Implications for the 3.4 micron interstellar absorption feature. *Astrophys. J.* **257,** L47–L50.

Moore, M. H., B. Donn, R. Khanna, and M. F. A'Hearn 1983. Studies of proton-irradiated cometary-type ice mixtures. *Icarus* **54,** 388–405.

Murray, B. G. J. P. T., B. N. Khare, W. R. Thompson, L. Flynn, and C. Sagan 1985. Ices in the outer Solar System: Spectra of irradiation products. *Bull. Amer. Astron. Soc.* **17,** 723.

Prinn, R. G., and B. Fegley, Jr. 1981. Kinetic inhibition of CO and N_2 reduction in circumplanetary nebulae: Implications for satellite composition. *Astrophys. J.* **249,** 308–317.

Russell, R. W., B. T. Soifer, and S. P. Wilner 1977. The 4 to 8 micron spectrum of NGC 7027. *Astrophys. J.* **217,** L149–L153.

Ryan, M. P., and I. G. Draganic 1986. An estimate of the contribution of high energy cosmic-ray protons to the absorbed dose inventory of a cometary nucleus. *Astrophys. Space Sci.* **125,** 49–67.

Sagan, C., and B. N. Khare 1979. Tholins: Organic chemistry of interstellar grains and gas. *Nature* (*London*) **277,** 102–107.

Sagan, C., W. R. Thompson, B.N. Khare, B. G. J. P. T. Murray, and S. W. Squyres 1984a. Coloration and darkening of CH_4 hydrate and other ices upon charged-particle irradiation. *Bull. Amer. Astron. Soc.* **16,** 668.

Sagan, C., B. N. Khare, and J. S. Lewis 1984b. Organic matter in the Saturn system. In *Saturn* (T. Gehrels and M. S. Matthews, Eds.), pp. 788–807. Univ. of Arizona Press, Tucson.

Sagan, C., W. R. Thompson, B. N. Khare, and B. G. J. P. T. Murray 1986. Radiation darkening of CH_4 clathrate: Implications for the Uranian satellites. *Bull. Amer. Astron. Soc.* **18,** 785.

Sagdeev, R. Z., F. Szabo, G. A. Avanesov, P. Cruvellier, L. Szabo, K. Szego, A. Abergel, A. Balazs, I. V. Barinov, J. L. Bertaux, J. Blamont, M. Detaille, E. Demarelis, G. N. Dul'nev, G. Endroczy, M. Gardos, M. Kanyo, V. I. Kostenko, V. A. Krasikov, T. Nguyen-Trong, Z. Nyitrai, I. Reny, P. Rusznyak, V. A. Shamis, B. Smith, K. G. Sikhanov, F. Szabo, S. Szalai, V. I. Tarnopolsky, I. Toth, G. Tsukanova, B. I. Valnicek, L. Varhalmi, Yu K. Zaiko, S. I. Zatsepin, Ya L. Ziman, M. Zsenei, and B. S. Zhukov 1986. Television observations of Comet Halley from Vega spacecraft. *Nature* (*London*) **321,** 262–266.

Shul'man, L. M. 1972. The evolution of cometary nuclei. In *The Motion Evolution of Orbits and Origin of Comets, Proc. IAU Symposium No. 45* (G. A. Chebotarev, E. I. Kazimirchak-Polonskaya, and B. G. Marsden, Eds.), pp. 265–270. Reidel, Dordrecht.

Stevenson, D. J. 1987. Chemical processing of the solar nebula by leaky protoplanets (where did all the CO go?). Paper presented at the *NASA Conference on the Origin and Evolution of Planetary and Satellite Atmospheres, Tucson, AZ.*

Strazzulla, G., L. Calcagno, and G. Foti 1983. Polymerization induced on interstellar grains by low-energy cosmic rays. *Mon. Not. R. Astron. Soc.* **204,** 59P–62P.

Strazzulla, G., L. Calcagno, and G. Foti 1984. Build up of carbonaceous material by fast protons on Pluto and Triton. *Astron. Astrophys.* **140,** 441–444.

Strazzulla, G., L. Calcagno, and G. Foti 1985. Dark material produced by fast protons on frozen methane. II. Astrophysical application. *Nuovo Cimento 8C* **5,** 63–75.

Strazzulla, G., R. S. Cataliotti, L. Calcagno, and G. Foti 1984. The IR spectrum of laboratory synthesized polymeric residues. *Astron. Astrophys.* **133,** 77–79.

Thompson, W. R., B. G. J. P. T. Murray, B. N. Khare, and C. Sagan 1987a. Coloration and darkening of methane clathrate and other ices by charged particle irradiation: Applications to the outer Solar System. *J. Geophys. Res.* **92,** 14,933–14,947.

Thompson, W. R., T. Henry, B. N. Khare, L. Flynn, J. Schwartz, and C. Sagan 1987b. Light hydrocarbons from plasma discharge in H_2–He–CH_4: First results and Uranian auroral chemistry. *J. Geophys. Res.* **92,** 15,083–15,092.

Whipple, F. L. 1950. A comet model. I. The acceleration of Comet Encke. *Astrophys. J.* **111,** 375–394.

Whipple, F. L. 1951. A comet model. II. Physical relations for comets and meteors. *Astrophys. J.* **113,** 464–474.

Whipple, F. L. 1977. The constitution of cometary nuclei. In *Comets, Asteroids, Meteorites* (A. H. Delsemme, Ed.), pp. 25–35. Univ. of Toledo Press, Toledo, OH.

Wickramasinghe, D. T., and D. A. Allen 1980. The 3.4 μm interstellar absorption feature. *Nature* (*London*) **287,** 518–519.

Wickramasinghe, D. T., and D. A. Allen 1986. Discovery of organic grains in Comet Halley. *Nature* (*London*) **323,** 44–46.

ICARUS 79, 362–381 (1989)

The Heliocentric Evolution of Cometary Infrared Spectra: Results from an Organic Grain Model

CHRISTOPHER F. CHYBA AND CARL SAGAN

Laboratory for Planetary Studies, Cornell University, Ithaca, New York 14853-6801

AND

MICHAEL J. MUMMA

Planetary Systems Branch, NASA-Goddard Space Flight Center, Code 693, Greenbelt, Maryland 20771

Received February 16, 1988; revised November 30, 1988

Observations of Comets Halley and Wilson reveal an emission feature peaking near 3.4 μm, characteristic of C–H stretching in hydrocarbons. We have previously (Chyba and Sagan 1987a, *Nature* (*London*) 330, 350–353) fit this feature with a simple two-component thermal emission model for dust in the cometary coma (one component corresponding to large, cool, optically thick particles, the other due to smaller, hotter, organic grains) by employing laboratory spectra of the organic residue produced by the irradiation of carbon-bearing ices. This procedure yields optical depths in agreement with limits from spacecraft data. One remarkable result of such modeling is that at ~1 AU emission features at wavelengths longer than 3.4 μm are largely overwhelmed (or "diluted") by continuum emission. The large particle optical depth is ~10^2 times that of the emitting organics, so that, relative to the continuum, only near the continuum minimum can the emitting organics make a significant contribution. At ~1 AU, the 3.4-μm feature is the sole feature near that minimum, lying at the intersection of the curves for particle thermal emission and scattered sunlight. Thus, since as a comet moves away from perihelion the intersection of the scattered solar spectrum and the comet's thermal emission spectrum will move to longer wavelengths, we predicted (Chyba and Sagan 1987a) that the 3.4-μm feature is diluted while those at longer wavelengths are progressively revealed—so long as the comet retains its coma. We now quantitatively develop this model and find agreement with observational data for Comet Halley for certain plausible values of optical constants. Thus the observed heliocentric evolution of the 3.4-μm feature provides information on the composition, and perhaps structure, of the organic grains in Comet Halley. In addition, we argue that the heliocentric evolution of organic features will differ in the cases of thermal emission from small grains and gas-phase fluorescence. Therefore observations of cometary spectral evolution can in principle distinguish between solid or gas-phase origins for these features. © 1989 Academic Press, Inc.

I. THE NEAR-INFRARED SPECTRA OF COMETS HALLEY AND WILSON

Observations of the infrared spectrum of Comet Halley both by spacecraft (Combes *et al.* 1988) and ground-based telescopes (Baas *et al.* 1986, Danks *et al.* 1986, Knacke *et al.* 1986, Wickramasinghe and Allen 1986, Tokunaga *et al.* 1987) reveal an emission feature centered at about 3.36 μm, characteristic of C–H stretching in hydrocarbons. This feature has been interpreted as thermal emission from organic grains in the Halley coma (Wickramasinghe and Allen 1986, Chyba and Sagan 1987a, 1988a), although some contribution to the 3.4-μm feature by gaseous emission is expected

0019-1035/89 $3.00
Copyright © 1989 by Academic Press, Inc.
All rights of reproduction in any form reserved.

(Crovisier and Encrenaz 1983, Combes *et al.* 1988). However, Drapatz *et al.* (1987) observed the ~3.2–3.4 μm region of the Halley spectrum at high resolution ($\lambda/\Delta\lambda \sim 1.1 \times 10^4$) and found no prominent line structure typical of gas-phase emission. Moreover, mass spectrometric observations by spacecraft flying through the coma directly demonstrate the presence of organic-rich grains (Kissel and Krueger 1987, Clark *et al.* 1987), although there remains ample room for debate on the detailed composition.

Observations of Comet Wilson (Allen and Wickramasinghe 1987, Brooke *et al.* 1987) also reveal a 3.4-μm emission band which closely resembles the Comet Halley feature for approximately the same heliocentric distance. Again, high resolution ($\lambda/\Delta\lambda \sim 3.3 \times 10^4$) observations in the 3.2–3.3 μm region reveal no prominent line structure in Comet Wilson, although a possible (3σ) detection of methane has been reported (Larson *et al.* 1989). It is remarkable that dynamically old (Halley) and new (Wilson) comets should display such a nearly identical emission feature, a similarity which strengthens the case (Greenberg and Grim 1986, Chyba and Sagan 1987a, 1988a,b, Brooke *et al.* 1987, Johnson *et al.* 1987) for the primordial, although not necessarily the interstellar, origin of cometary organics.

Any proposed identifications of the molecules responsible for the 3.4-μm feature must take into account the absence of organic emission features in cometary infrared spectra at longer wavelengths. The peak position of the 3.4-μm feature itself is indicative of alkanes ($-CH_3$, $-CH_2-$), while substructure indicates the presence of other organics [e.g., aldehydes ($-CHO$) emit near 3.5 μm]; naively one might expect the presence of these or other plausible classes of organic molecules to result in observable spectral features in the 4.5–8 μm region. For example, alkanes exhibit prominent deformation bands in the 6.8–8 μm region; alkenes and aromatics exhibit (C=C) bands in the 6–7 μm region; and ketones and aldehydes have a carbonyl (C=O) feature near 5.8 μm. Such features are typically present in the transmission spectra of the organic residue of irradiated candidate cometary ices (Thompson *et al.* 1987, Khare *et al.* 1989), for example, in that of the residue of irradiated methane ice clathrate (Fig. 1). Organic solids produced by irradiating N_2/CH_4 gas mixtures exhibit a prominent nitrile or isocyanide (C≡N) feature at 4.6 μm (Khare *et al.* 1984). Yet observations of both Comet Halley (Combes *et al.* 1988, Bregman *et al.* 1987) and Comet Wilson (Lynch *et al.* 1988) in the 5–13 μm range have shown such features to be absent at the ≳2% level.

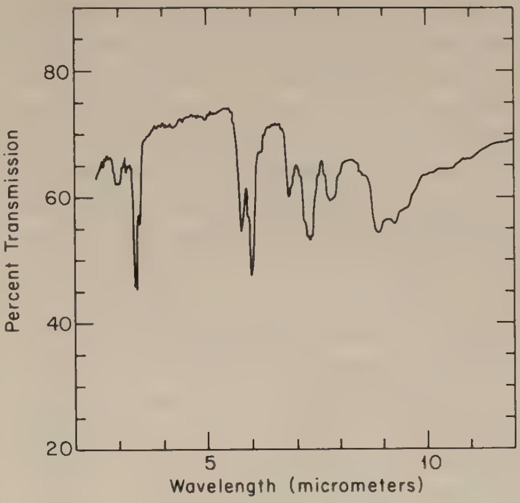

FIG. 1. The 2–12 μm transmission spectrum of the organic residue of irradiated methane hydrate clathrate. See Thompson *et al.* (1987) and Khare *et al.* (1989) for the transmission spectrum of this and other irradiation-produced residues presented on a scale linear in wavenumber.

In a recent model (Chyba and Sagan 1987a,b) for infrared emission by organic grains in the Halley coma, we have explained the absence of these longer wavelength bands as due to the dilution of spectral features by the continuum when such features do not lie near the intersection of the scattered solar and thermal emission curves of the dust in the cometary coma. At the heliocentric distances of the 5 to 13-μm observations [~1.3 and ~1.2 AU for Comets Halley (Bregman *et al.* 1987) and Wilson (H. Campins, personal communication), respectively], the 3.4-μm band is the sole feature near the minimum in the continuum. Our model quantitatively demonstrates that it is the only organic feature likely to be observable at these distances. Therefore spectroscopic attempts to rule out certain organic functional groups or polycyclic aromatic hydrocarbons in Comets Wilson or Halley (Bregman *et al.* 1987) appear premature. The presence of absorption features in laboratory transmission spectra does not necessarily require them to be observable in cometary emission, even if the corresponding molecular functional groups are present in substantial abundance.

However, with changing heliocentric distance, the intersection of the scattered solar and thermal emission flux will sweep through the infrared spectrum. Thus, for a comet moving away from perihelion, Chyba and Sagan (1987a) predicted that the contrast between the 3.4-μm feature and the continuum would be gradually suppressed, and spectral features at longer wavelengths progressively revealed, as this intersection moves toward longer wavelengths. In this paper, we present quantitative results of a model for the heliocentric evolution of the Comet Halley infrared spectrum. We expect any comet that displays organic emission features in the infrared to exhibit an analogous evolution with heliocentric distance, although the details of such evolution will vary according to the nature of a given comet's organics (see below). Such spectral evolution should be testable by Earth-based observations and, especially, by future comet rendezvous missions.

II. EMISSION BY ORGANIC GRAINS IN THE COMA OF COMET HALLEY

A variety of plausible cometary materials exhibit C–H stretching features near 3.4 μm, including the organic residue of candidate cometary ices irradiated by charged particles. Higher resolution spectroscopic observations will be required in the future to understand the nature of the organic material responsible for cometary emission. For now, tentative identifications must rest on additional evidence, including a plausible account of the origins of the organic material, a plausible model for the infrared emission of this material, and a demonstration that this conjunction of material and model not only matches the 3–4 μm spectrum, but also does not yield additional emission features where none is observed (Chyba and Sagan 1987b).

We have embarked on an experimental survey of diagnostic spectral features for the organics produced by irradiation of a variety of hydrocarbon and ammonia-bearing ices (Thompson *et al.* 1987, Khare *et al.* 1988), and are beginning an examination of other (e.g., CO and CO_2) ices as well. We have argued that the laboratory synthesis of the organic residue well simulates certain types of pre- and post-accretion radiation processing experienced by cometary ices. As an example of one such organic remnant, we have considered the residue, after evaporation of the ices, of irradiated low-occupancy methane hydrate clathrate (Chyba and Sagan 1987a, 1988a). There is evidence from the Giotto ion mass spectrometer for methane in the Halley coma with a production rate ~2% that of water (Allen *et al.* 1987), and in cometary ices, clathrates are thermodynamically favored (Delsemme 1976). A possible 3σ spectroscopic detection of CH_4 in Comet Wilson has been reported (Larson *et al.* 1988), equivalent to $[CH_4]/[H_2O] \sim 0.04$. However, by no means do we insist on methane clathrate as the only plausible candidate ice yielding radiation-processed organics. Rather, a comparison of experimentally determined spectra with observed cometary emission features may allow certain otherwise plausible ices to be excluded as candidates for the origins of cometary organics (Khare *et al.* 1988).

In addition to the variety of plausible C- and N-rich ices which may contribute to irradiation-produced cometary organics, there is also a range of radiation environments which must be considered (Chyba and Sagan 1988c). We have argued (Chyba and Sagan 1987a, 1988c) that while some of the emitting organic dust in the Halley coma will be due to fragments of the observed low albedo crust, most is probably jetted from the cometary interior, with organics thus due mainly to processing by radionuclides (Draganić *et al.* 1984) and preaccretion irradiation. Strazzulla *et al.* (1983) have shown that low-energy cosmic rays should totally polymerize C-containing ices in interstellar grains on timescales less than dust cloud lifetimes. Ultraviolet irradiation in the interstellar medium may also play an important role (Greenberg and Grim 1986).

Deriving a simple two-component model for emission from dust in the Halley coma (Chyba and Sagan 1987a), we used the laboratory-determined transmission spectrum (Thompson *et al.* 1987) of the organic residue of irradiated methane hydrate clathrate to fit the Halley spectrum in the 3–4 μm range, as observed by Wickramasinghe and Allen (1986) for 31 March 1986 (heliocentric distance $R = 1.16$ AU, geocentric distance $\Delta = 0.549$ AU; all heliocentric and geocentric distances cited in this paper are from the ephemeris of Yeomans (1986)). This model fits the 3.4-μm feature, provides optical depths in good agreement with those determined by spacecraft observations, and accounts for the absence of features at longer infrared wavelengths, despite their presence in the transmission spectrum of the organic residue.

Our model predicted an observed infrared flux given by

$$F_\lambda = C_\lambda + \Omega\tau'_\lambda B_\lambda(T_r) + \Omega\tau B_\lambda(T_c), \quad (1)$$

where C_λ was the scattered solar flux, Ω the telescope solid angle, τ the optical depth of the blackbody continuum emitters (at temperature T_c), $\tau'_\lambda = \beta(a/\lambda)\ln(t_\lambda^{-1})$ the optical depth of the submicron (radius $a \sim 0.1$ μm) organic emitters (temperature T_r), and t_λ the transmissivity of the laboratory sample (given by Fig. 1, with maximum transmissivity set equal to 100%). β and τ were free parameters varied to provide a best (χ^2) fit to the data. β and τ have clear physical interpretations and are tightly constrained by spacecraft and ground-based data, as discussed below.

Several minor improvements have since been made to the model summarized by Eq. (1). For purposes of comparison with the Wickramasinghe and Allen observations of 31 March 1986, Chyba and Sagan (1987a) took the scattered solar flux C_λ to be given directly by the flux measured that night in two wavelength windows between 1.5 and 2.5 μm. This procedure slightly overestimates the solar contribution to F_λ, as there is also a minor contribution to the flux measured at these short wavelengths by the final two B_λ terms in Eq. (1). We therefore now adopt the following procedure: For each value of β and τ examined in the χ^2 minimization, we subtract from C_λ at 0.1 μm intervals over the 1.5–2.5 μm range the two small B_λ contributions. We then perform a linear regression [$\log(F_\lambda)$ vs $\log(\lambda)$] to obtain the scattered solar curve (i.e., with the B_λ contributions removed) for this choice of β and τ. This avoids a double counting of the B_λ contributions at short wavelengths and also results in a better fit to observations in the 3 μm region (Fig. 2). No attempt is made to model a possible band at 3.05 μm, which may be due to O–H absorption (Combes *et al.* 1988). Thus, we now write

$$F_\lambda = S_\lambda + \Omega\tau_\lambda B_\lambda(T_r) + \Omega\tau B_\lambda(T_c), \quad (2)$$

where S_λ, the scattered solar continuum, is given at any λ via the above regression. We also now set $\tau_\lambda = \gamma(2\pi a/\lambda)\ln(t_\lambda^{-1})$, where γ differs from the previously employed β by a factor 2π, so that the usual $2\pi a/\lambda$ Mie theory dependence is explicitly displayed. In addition, we have recognized a multiplicative error in the values of β and τ'_λ reported

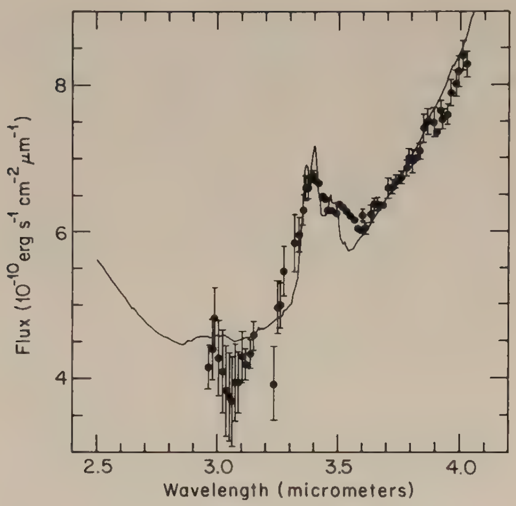

FIG. 2. Our best fit (continuous curve) to the 3–4 μm 31 March 1986 spectrum of Comet Halley (Wickramasinghe and Allen 1986), using a temperature T_r = 450°K appropriate to Titan tholin optical constants, and the spectrum of Fig. 1. The 3.4-μm feature lies almost at the minimum of the scattered solar flux (declining from the left) and blackbody thermal emission (rising to the right). The best fit for T_r = 560°K, appropriate to glassy carbon optical constants, is nearly identical to that shown here. A possible 3.05-μm feature is not modeled.

in Chyba and Sagan (1987a). The values cited there should instead have read $\beta = 3.7 \times 10^{-4}$ and $\tau'_\lambda = 3.6 \times 10^{-6}$ (giving $\tau'_\lambda/\tau = 2.6 \times 10^{-2}$ at $\lambda = 3.4$ μm); these changes do not affect other reported results in any way.

Equation (2) requires a choice of temperatures T_c and T_r. T_c may be determined empirically from observations of continuum emission in the Halley coma. Wickramasinghe and Allen (1986) find that the Halley spectrum in the 3–4 μm range (exclusive of the emission feature at 3.4 μm, and a possible O–H absorption feature at 3.05 μm) is best fit by $T_c = 350 \pm 10$°K. This temperature is ~25% hotter than the temperature of a blackbody at that heliocentric distance, presumably due to the presence of submicron grains in the coma. The temperature T_r of the submicron organic emitters, as a function of heliocentric distance and grain size, may be found via Mie theory calculations using the optical constants of laboratory-produced organic residue or other candidate materials. Hanner (1986) and Lamy and Perrin (1988) have performed such calculations for an organic residue ("Titan tholin") produced by sparking 10% CH_4 in a nitrogen atmosphere (Khare *et al.* 1984). [We stress that Titan tholin is an unlikely material for cometary grains; it was selected by these authors because it is an organic irradiation residue the optical constants of which are well-characterized (Khare *et al.* 1984).] Taking a typical particle size for presumed spherical emitting organic grains in the Halley coma to be ~0.1 μm then gives T_r = 450°K at 1.16 AU. By contrast, Mie calculations for 0.1-μm glassy carbon grains (Hanner 1983) yield T_r = 560°K at 1.16 AU. T_r = 560°K is also close to the temperature given by Mie calculations for biologically derived organic grains of radius 0.1 μm (Wallis *et al.* 1987). If cometary grains are highly porous and nonspherical these temperatures would be higher, and particles as large as tens of microns in size might be much hotter than expected for a blackbody (Greenberg and Zhao 1989).

III. COMPARISON WITH SPACECRAFT RESULTS

Given choices for T_c and T_r, we vary τ and γ in Eq. (2) to minimize χ^2; our best fit to the 31 March 1986 observations is shown in Fig. 2. The resulting values of τ and τ_λ may then be compared with spacecraft-determined filling factors for the Halley coma. For T_r = 560°K (glassy carbon), we find $\tau = 1.5 \times 10^{-4}$ and $\gamma = 2.4 \times 10^{-5}$, giving $\tau_\lambda = 1.5 \times 10^{-6}$ at $\lambda = 3.36$ μm, or $\tau_\lambda/\tau = 1.0 \times 10^{-2}$. τ_λ is sensitive to the choice of T_r; at a temperature appropriate for Titan tholin, T_r = 450°K, we find $\tau = 1.5 \times 10^{-4}$ and $\gamma = 1.5 \times 10^{-4}$, giving $\tau_\lambda = 9.1 \times 10^{-6}$ and $\tau_\lambda/\tau = 6.1 \times 10^{-2}$. It must be emphasized that neither the optical constants for glassy carbon nor those of Titan tholin are necessarily appropriate for the organic residue of an irradiated carbon-bearing ice, so these temperatures and τ_λ/τ ratios should be thought of only as indicators of a plausible range of values. In particular, irradiated ice residues typically show a strong absorption in the 3.4 μm region (Khare *et al.* 1988), which Titan tholin and glassy carbon do not. To our knowledge, measurements of the optical constants of an ice residue over a wavelength range sufficient to allow Mie theory calculations have never been performed. Such measurements (which, for ice residues, pose difficult experimental problems) are of considerable importance, and are being pursued by our group.

Chyba and Sagan (1987a) compared τ to the geometrical filling factor $A_{WA} = 1.9 \times 10^{-4}$ for the dust in the field of view of the Wickramasinghe and Allen (1986) aperture. A_{WA} is calculated by integrating over the telescope aperture the dust fluence as a function of mass and nucleocentric distance determined by the spacecraft Giotto (McDonnell *et al.* 1986, 1987), convolved with a model for the density–radius relationship for Halley dust (Divine *et al.* 1986), correcting for heliocentric distance. The interim assessment of the Halley dust distribution (McDonnell *et al.* 1986) used for this calculation by Chyba and Sagan has since been finalized in a slightly different form (McDonnell *et al.* 1987), so that A_{WA} must now be reassessed. The current best values for the Giotto-observed dust fluence indicate a mass distribution index $\alpha \approx -0.85$ [where the number of particles having mass greater than m is given by $N(>m) \propto m^{\alpha}$] for $m < 10^{-8}$ kg, above which the exponent changes to $\alpha \approx -0.54$. McDonnell *et al.* consider two upper limits to which the mass integration may be extended, 10^{-3} and 1 kg. The first of these corresponds to the upper limit needed to give a total mass sufficient to account for the observed deceleration of the Giotto spacecraft. The second is chosen to yield a dust/gas ratio of 1 : 1; it is not an observation-based quantity, although larger dust particles than those encountered by Giotto may well exist in the Halley coma. Depending on which choice is made, one finds $A_{WA} = 9.4 \times 10^{-5}$ (for 10^{-3} kg) or $A_{WA} = 1.5 \times 10^{-4}$ (for 1 kg.). As cometary dust emission is known to be highly time-variable [emission from Halley has been observed to deviate from an overall R^{-4} law for infrared flux by as much as a factor of 7 over a few days (Gehrz and Ney 1986), and there were 2 weeks between the Giotto flyby and the Wickramasinghe and Allen observations], the agreement between A_{WA} and the optical depth τ required by our model is excellent.

It is more difficult to compare quantitatively the optical depth τ_λ found for the emitting organic grains with the spacecraft results. Submicron grains in the Halley coma certainly contribute to the 3.4-μm feature, but much larger particles might also contribute if the grains are sufficiently fluffy (Greenberg and Zhao 1989). The Giotto-determined dust distribution can be integrated to find the percentage of the coma filling factor due to grains smaller than a certain radius. Using the latest (McDonnell *et al.* 1987) results for the distribution observed along the Giotto trajectory, one finds that dust particles with radii ≤ 1 μm contribute between 2.8 and 4.4% of the total filling factor, depending upon whether the integration is continued to 1 or 10^{-3} kg, respectively. Similarly, grains with radii ≤ 10 μm contribute between 25 and 40% of the total filling factor. More recently, however, Perry *et al.* (1988) have re-examined the Giotto data, in light of discrepancies between the spacecraft results and ground-based observations made shortly before encounter. Taking into account the dependence of grain outflow velocity on size, they conclude that the change in the value of the exponent α at 10^{-8} kg may have been an artifact of variations in the level of dust production at the nucleus. They therefore recommend that modeling of the Halley coma should not include the large mass excess actually observed by Giotto, but rather that the small-particle exponent ($\alpha \approx -0.85$) should be extended through the larger sizes. If this recommendation is followed, one finds that submicron grains contribute ~6% of the filling factor, while grains ≤ 10 μm contribute ~50%. These results are independent of whether the integration range extends to 10^{-3} or 1 kg, as the large negative exponent α in this case guarantees that particles larger than 1 g contribute almost negligibly to the coma filling factor. Finally, it should be noted that these results make use of the Divine *et al.* (1986) density–radius distribution, which assumes that the smallest coma particles have densities approaching 3 g/cm^3, with density dropping with increasing size up to a large-particle limit of 0.8 g/cm^3. To test the sensitivity of the above results to alternate density–radius models, we have convolved the Giotto-measured mass fluence with a dust particle density 0.8 g/cm^3, taken to be independent of particle size. We find that the resulting filling factors differ little from those cited above.

The range of optical depths τ_λ found above for the emitting organic grains, $\tau_\lambda/\tau = 0.01$–0.06, may be compared with upper bounds placed on this ratio by the fraction A_f of the total coma filling factor determind from Giotto data for dust grains with radii less than 1 and 10 μm, viz., A_f (≤ 1 μm) = 0.03–0.06 and A_f (≤ 10 μm) = 0.25–0.5. Only some portion of A_f is due to organic grains, but this component appears large: Some 84% of Halley's dust contains carbon (Jessberger *et al.* 1988), and Kissel and Krueger (1987) have interpreted Vega mass spectrometer data to mean that most Halley dust consists of a chondritic core coated with an organic mantle.

τ_λ and A_f cannot be directly compared, however. In general, the absorption optical depth of the organic emitters at a wavelength λ is given by

$$\tau_\lambda = \int \tau(\lambda, a) da, \quad (3)$$

with

$$\tau(\lambda, a) = \int n(a) \pi a^2 Q_{\text{abs}}(\lambda, a) dl, \quad (4)$$

where $n(a)$ is the number density for particles of radius a, and $Q_{\text{abs}}(\lambda, a)$ is the dimensionless absorption efficiency factor for these particles at wavelength λ. The integral in Eq. (4) is taken along the line of sight through the coma. For optically thick grains, $Q_{\text{abs}}(\lambda, a) \approx 1$, so that the optical depth is just the geometrical filling factor. Thus τ can be compared directly to A_{WA}, as was done above. For grains with $a \lesssim \lambda$, however, Q_{abs} may be either greater or less than 1, typically becoming very small for $a \ll \lambda$. To compare τ_λ with the Giotto-determined filling factors A_f, we need Q_{abs} at $\lambda = 3.4$ μm throughout the range of interest in a. Most simply, τ_λ could be approximated by the expression $\tau_\lambda/\tau \approx \overline{Q}_{\text{abs}} A_f$, where $\overline{Q}_{\text{abs}}$ is some "typical" value of Q_{abs} for the emitting organic grains over the appropriate range of grain radii.

Q_{abs} may be calculated from Mie theory if the optical constants (complex refractive index $n_c = m - ik$, where m is the real and k the imaginary part of the refractive index) are given. Although such constants are not known for ice residues at 3.4 μm, we can delineate a plausible range of values by considering m and k for Titan tholin and glassy carbon. At $\lambda = 3.4$ μm, n_c for Titan tholin (interpolated from Khare *et al.* 1984) is given by $m = 1.65$ and $k = 0.041$; glassy carbon at this wavelength (interpolated from Edoh 1983) has $m = 2.93$ and $k = 1.01$. Wickramasinge (1973) has compiled Mie theory results for extinction and scattering efficiencies, Q_{ext} and Q_{sca}, over a wide variety of m and k values. Employing the relation $Q_{\text{abs}} = Q_{\text{ext}} - Q_{\text{sca}}$, we use his tables for $m = 1.7$ and $k = 0.05$, and $m = 3.0$ and $k = 1.0$, to approximate the efficiency factors for Titan tholin and glassy carbon, respectively, over a range of values for $x \equiv 2\pi a/\lambda$. At $\lambda = 3.4$ μm, these x-values correspond to particles of definite radii a. Our results are summarized in Table I. We see that Q_{abs} for glassy carbon is typically >1 for particles with radii in the range ~0.3–3 μm, wherease Q_{abs} for Titan tholin ~0.1–1 over the same range of a. We can thus conclude that the values $\tau_\lambda/\tau \sim 10^{-2}$ required by our model are consistent with the spacecraft-determined values $A_f \sim 0.03$–0.5, at least given the large range of uncertainty in A_f

TABLE I

APPROXIMATE EFFICIENCY FACTORS FOR TITAN THOLIN AND GLASSY CARBON AT 3.4 μm

Particle radius a(μm)	$x = 2\pi a/\lambda$[a]	Q_{abs}, Titan tholin[b]	Q_{abs}, glassy carbon[c]
0.1	0.2	0.009	0.1
0.25	0.5	0.05	0.5
0.5	0.9	0.1	1.7
1.0	1.9	0.4	1.5
2.0	3.7	0.8	1.2
2.7	5.0	0.9	1.1

[a] x evaluated at $\lambda = 3.4$ μm.

[b] At 3.4 μm, Titan tholin has $n_c = 1.65 - 0.041i$ (Khare *et al.* 1984); Wickramasinghe (1973) lists $n_c = 1.7 - 0.05i$.

[c] At 3.4 μm, glassy carbon has $n_c = 2.93 - 1.01i$ (Edoh 1983); Wickramasinghe (1973) lists $n_c = 3.0 - 1.0i$.

and Q_{abs}. Agreement is more easily obtained with glassy carbon optical constants than with those appropriate for Titan tholin. Optical constants for an actual ice residue over the crucial wavelength range, as well as a better knowledge of the fluffiness of cometary grains, are critical to performing this calculation more definitively.

IV. HELIOCENTRIC EVOLUTION OF COMETARY EMISSION FEATURES

Green *et al.* (1986) have shown that the Halley continuum spectrum over the range 1–20 μm as a function of heliocentric distance R (measured in AU) is well fit by a combination of scattered sunlight and blackbody emission at a temperature

$$T_c = 329R^{-0.53}, \tag{5}$$

a relation derived from observations of a number of comets. This value of T_c is ~15% lower than that found both by Wickramasinghe and Allen (1986) for the 3–4 μm region, and by Bregman *et al.* (1987) for the range 5–13 μm. This discrepancy may be explained as due to the different wavelength ranges being fit: as increasingly longer wavelengths are considered, the contribution due to small, hot grains in the coma becomes less and less significant. Indeed, Tokunaga *et al.* (1988) have also recently determined a relation similar to Eq. (5) for Comet Halley, finding that color temperatures defined by the flux ratio 4.8 μm/7.8 μm are ~15% higher than those derived for 7.8 μm/12.5 μm data, which are in turn ~15% hotter than equilibrium blackbody temperatures. Thus the continuum over the range 2–12 μm is expected to be best fit by a temperature higher than that given by Eq. (5). Indeed, our own numerical investigations show that our model cannot fit the Wickramasinghe and Allen observations well for temperatures outside the range 350 ± 10°K. Therefore, for consistency with the results of Wickramasinghe and Allen and Bregman *et al.*, we take the temperature of the continuum emitters at 3–4 μm to be given by

$$T_c = 350(R/1.16)^{-0.53}. \tag{6}$$

The exponent is close to that (−0.50) expected for a gray body in thermodynamic equilibrium.

Thus it is possible to model Halley emission over the range 2–12 μm using the model given by Eq. (2). The continuum optical depth $\tau \sim 10^2$ times the optical depth due to the emitting organics (τ_λ), so that only near the minimum in the continuum radiation can an organic emission feature achieve good visibility relative to the continuum. At 1 AU, the 3.4-μm feature is the sole feature near that minimum, lying near the intersection of the scattered solar and 350°K blackbody curves. However, as the comet moves away from perihelion, the intersection of the scattered solar spectrum and the comet's thermal emission spectrum will move to longer wavelengths. Thus, relative to the continuum, we expect the 3.4-μm feature to be diluted and those at longer wavelengths progressively revealed, as the minimum in continuum emission sweeps through the infrared spectrum toward longer wavelengths.

Of course, this evolution is only relevant at those heliocentric distances R at which the comet retains its coma. Water ice is expected to vaporize in the solar radiation field for $R \lesssim 3$ AU (Delsemme 1982) and, indeed, it is at this distance that comets typically develop an obvious, extended coma.

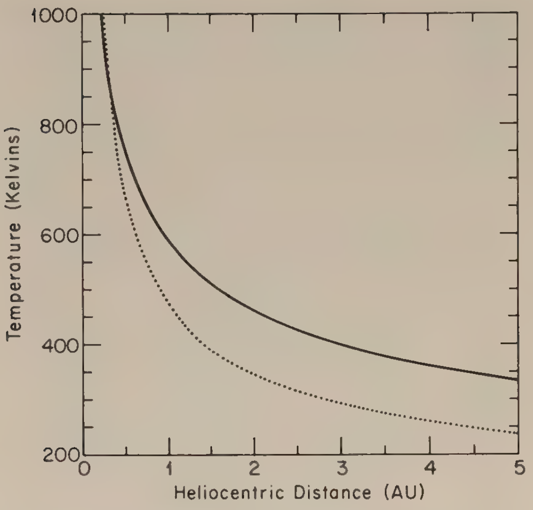

FIG. 3. The temperature of 0.1-μm grains as a function of heliocentric distance for glassy carbon (solid line) and Titan tholin (dotted line) optical constants. Titan tholin results are from Lamy and Perrin (1988) and Hanner (1986). Glassy carbon results are given by Hanner (1983) for $R < 2$ AU, and are extremely well fit by the relation $\log T = 2.77 - 0.355 \log R$. This relation is then used to extrapolate out to 5 AU.

However, some comets develop comae at larger distances. Comet Bowell 1980b exhibited an extended dust coma (but no detectable gaseous emission spectrum) for R as large as 7.2 AU (Cochran and McCall 1980). In the case of Comet Halley, there is evidence for a gaseous coma beginning at $R \sim 6$ AU (Green and Morris 1987), and for a coma of dust grains within $R = 5.4$ AU (Hanner 1986).

Using the values of the parameters found in Eq. (2) to provide the best fit to the 3 to 4-μm emission of Comet Halley at 1.16 AU, we can predict the spectrum of the comet at all wavelengths in the range 2–12 μm as a function of heliocentric distance R. We simply evaluate the flux given by Eq. (2), with T_c given by Eq. (6) and T_r taken to be the temperature of 0.1-μm spherical grains found by Mie theory for either glassy carbon (Hanner 1983) or Titan tholin (Hanner 1986, Lamy and Perrin 1988) optical constants at the appropriate R. The temperature of these grains as a function of R is shown in Fig. 3. In addition, it is known that dust production by Comet Halley exhibited an approximate R^{-2} dependence on heliocentric distance (Gehrz and Ney 1986). Thus the two B_λ terms in Eq. (2) are further reduced by this amount. S_λ falls off as R^{-4}, one R^{-2} factor due to reduced dust production, and one due simply to the decreasing angle subtended by each dust particle as a function of increasing R. Note that our model describes the spectral evolution of organic features only; it does not, for example, include emission due to silicates [observed in both Comets Halley (Bregman *et al.* 1987) and Wilson (Lynch *et al.* 1988)] or carbonates [tentatively identified in Comet Halley (Bregman *et al.* 1987)]. Nor does our model include a possible O–H absorption feature near 3.05 μm, as suggested by Combes *et al.* (1988).

Our results are displayed in Figs. 4 and 5. In each we present parallel results for both glassy carbon and Titan tholin optical constants, over the spectral range 2.5–12 μm. Beginning at ~8 μm, however, silicate emission should begin substantially to alter the results predicted here (see below), and beyond ~10 μm the assumption of constant T_c will begin to fail.

Figure 4 shows the predicted spectrum of Comet Halley for six different representative heliocentric distances. (Halley's perihelion distance was 0.59 AU; we have however extended our calculations to 0.3 AU, in anticipation of observations of comets with perihelion distances within several tenths of an AU of the Sun. Our 0.3-AU spectra may serve as predictions for such comets only if their 3.4 μm spectrum near 1 AU resembles that of Comet Halley, however, and if there is no significant thermal or radiation processing of the grains preferentially at small R.) The decrease in overall flux from the comet due to decreased dust production is evident. No account is taken of changing geocentric distance in calculating the overall magnitude of the flux. Thus, the magnitude of the flux in Fig. 4 changes in the manner that would be observed by a co-orbiting spacecraft that maintained a fixed distance from the cometary nucleus.

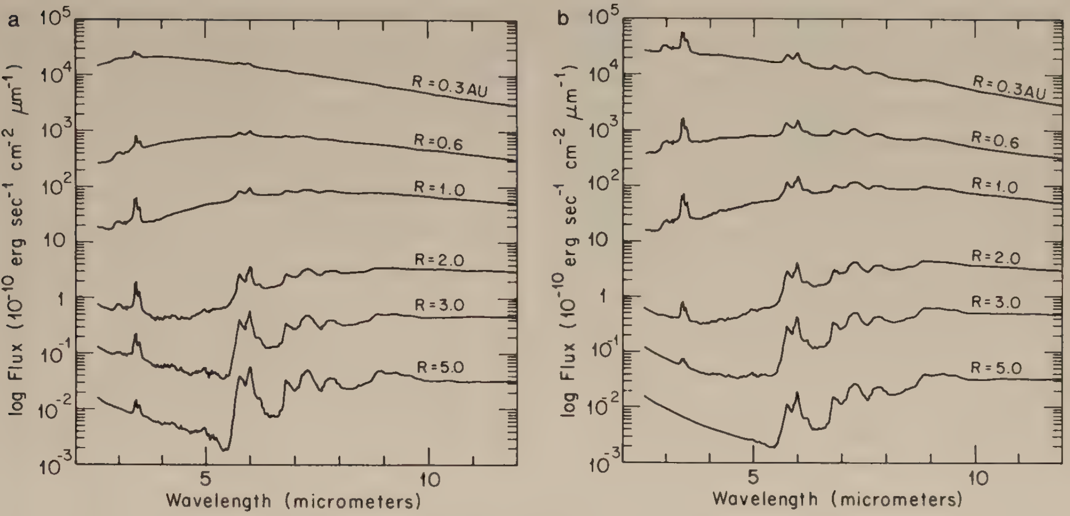

FIG. 4. (a) The 2–12 μm spectrum of Comet Halley predicted by our model for T_r given by glassy carbon optical constants (solid line in Fig. 3) at six different heliocentric distances. Emission features have been exaggerated by a factor of 10 for clarity. The prominence given to successive organic emission features by the minimum in the continuum spectrum as the comet moves to larger heliocentric distances is evident. (b) The same as (a) but for T_r given by Titan tholin optical constants (dotted line in Fig. 3).

As seen in Fig. 4, as the continuum minimum sweeps to longer wavelengths, the ~6-μm feature (present at the level of the 3.4-μm feature in the transmission spectrum of Fig. 1, but greatly suppressed in emission relative to the continuum at ~1 AU) becomes progressively enhanced. We have exaggerated the strength of the emission features in Fig. 4 by a factor of 10, in order to make this evolution more apparent. Note the evolution of the continuum underlying the 3.4-μm feature from thermal emission to scattered solar continuum as the comet moves from R = 0.3 to 2.0 AU. Such an evolution has been observed by Knacke *et al.* (1986) in ground-based observations for Comet Halley moving between R = 1.08 and 1.54 AU. The movement of the continuum minimum toward longer wavelengths with increasing R found in Fig. 4 is in quantitative agreement with continuum measurements for Comet Halley made by Tokunaga *et al.* (1986) over the heliocentric range 0.9–2.8 AU.

In Fig. 5, we divide out the continuum from the predicted cometary emission spectra in order to make evident the evolving strengths of the features relative to the continuum. No exaggeration of emission features is made here. There are important similarities and contrasts between the heliocentric evolution predicted by glassy carbon (solid line) and Titan tholin (dotted line) optical constants. In both cases, the strength of the 3.4-μm feature increases from a low level at 0.3 AU out to a maximum between 1 and 2 AU, then becomes nearly negligible by the time the comet is 5 AU from the Sun. (Of course, the cometary coma may have already disappeared by this heliocentric distance.) Simultaneously, the features at ~6 μm grow from only a few percent above continuum at ~0.3 AU to ~100% over continuum at 5 AU. For best visibility relative to the continuum, observations of the 6-μm or longer wavelength features should evidently be conducted at heliocentric distances greater than 2 AU.

Finally, we note that the 3.4-μm feature increases in strength between 1 and 2 AU in the case of glassy carbon optical constants, whereas it decreases in strength over the same range of distances for Titan tholin optical constants. This is immediately explicable in terms of the differing heliocentric temperature dependence for these materials as displayed in Fig. 3. Glassy carbon, with a much larger imaginary refractive index, is more highly absorbing than Titan tholin, so that grains of this material reach higher temperatures. The resulting differences in spectral feature heliocentric evolution provide an observational diagnostic of cometary organic composition, as will be addressed in the following section.

V. COMPARISON WITH AIRBORNE AND GROUND-BASED OBSERVATIONS

Observations of Comet Halley in the 5–13 μm range (Bregman *et al.* 1987) at helio-

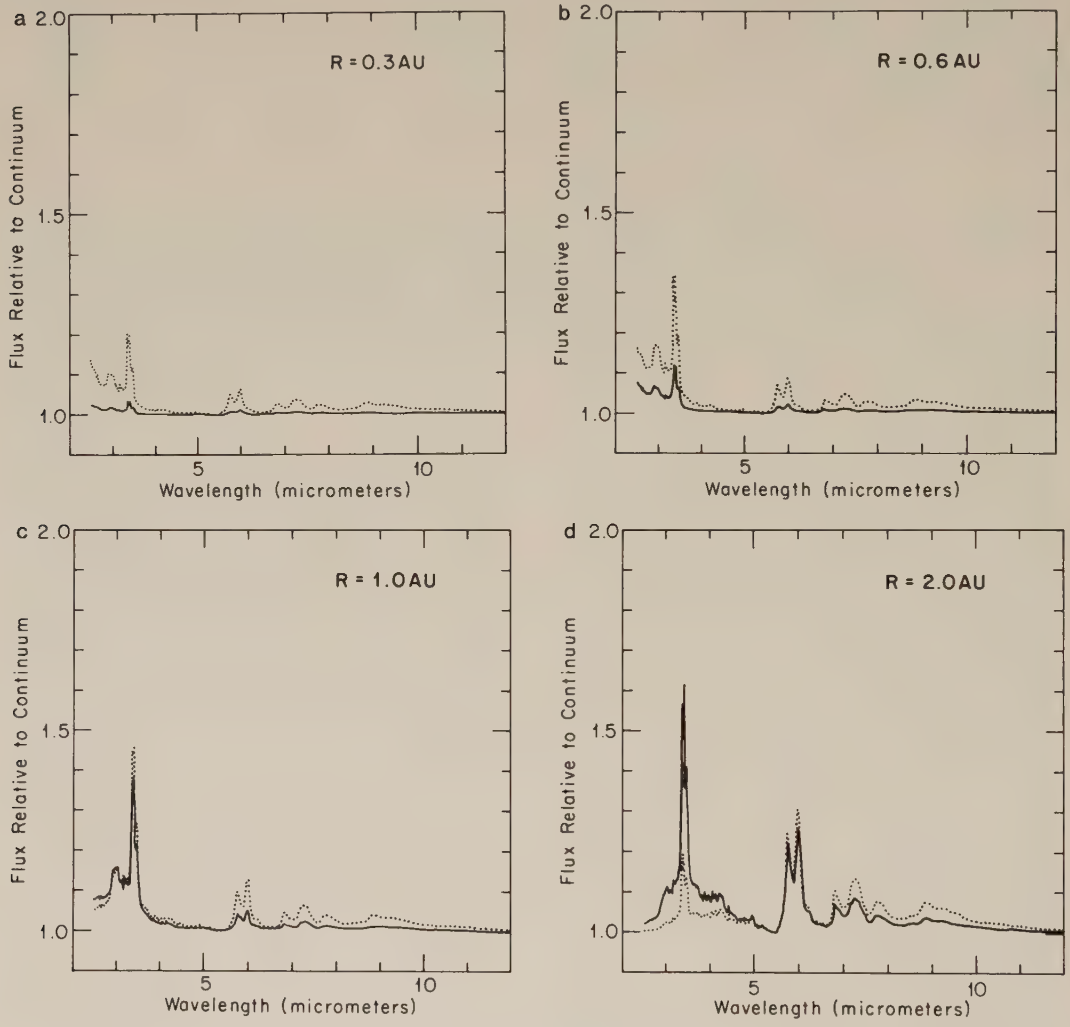

FIG. 5. (a) The 2–12 μm spectrum of Comet Halley predicted by our model at heliocentric distance $R = 0.3$ AU, after dividing out the continuum. The solid line depicts a model in which the 0.1-μm emitting organics are assigned a temperature T_r appropriate to glassy carbon optical constants. The dotted line assumes a T_r appropriate to Titan tholin optical constants (see Fig. 3). (b) The same as (a) for the case $R = 0.6$ AU. (c) The case $R = 1.0$ AU. (d) The case $R = 2.0$ AU. (e) The case $R = 3.0$ AU. (f) The case $R = 5.0$ AU. Note the great suppression of the 6-μm feature (compared to its strength in the transmission spectrum shown in Fig. 1) within $R \sim 2$ AU, and the peaking of the 3.4-μm feature in the 1–2 AU range.

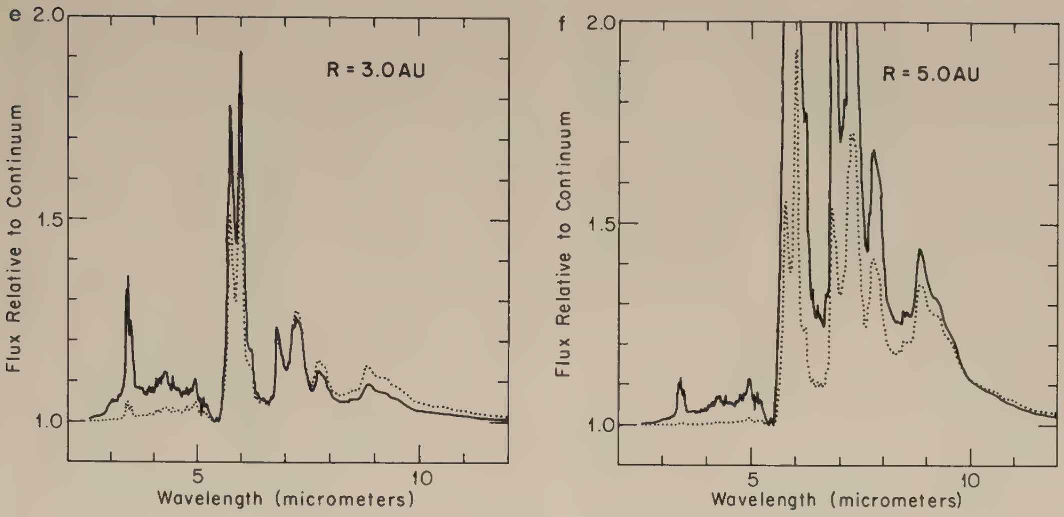

FIG. 5—*Continued, cases (e) and (f).*

centric distance $R \sim 1.3$ AU show a band rising to ~40% above continuum near 9 μm and to ~80% above continuum near 10 μm. This feature is usually attributed to Si–O stretching in small siliceous grains. Figure 5 shows that organic features predicted by our model in the vicinity of 9 μm from 0.3 to 2 AU rise to no more than ~10% above continuum, so Si emission is expected to swamp these features at these heliocentric distances. However, the 10-μm feature in comets typically disappears at larger heliocentric distances (Hanner 1986). At sufficiently large heliocentric distances (e.g., $R \gtrsim 3$ AU) it is therefore possible that organic spectral features near 9 μm could become visible (Figs. 5e, 5f).

Hanner (1986) and Lamy and Perrin (1988) have suggested that the Si feature may not be visible at large heliocentric distances because it is embedded in more volatile material which begins to evaporate only close to the Sun. Especially from the point of view of a Greenberg (1982) core–mantle interstellar grain model for cometary dust, it is interesting to speculate that the silicate material is embedded in a more volatile organic matrix. The correlation, if any, between the 3.4-μm feature and silicate emission in comets is unclear, however. For example, Comets West and IRAS-Araki-Alcock showed Si features in the absence of 3.4-μm features (Tokunaga and Brooke 1988). In addition, while Comets Halley and Wilson showed quite similar 3.4-μm organic features, their Si features differed significantly: Halley had an 11.3-μm feature which Wilson lacked, whereas Wilson displayed a 12.3-μm feature absent in the Halley spectrum (Lynch *et al.* 1988, Campins and Ryan 1988). Moreover, preliminary results for the PIA experiment in Giotto (Clark *et al.* 1987) indicate that ~30% of the "CHON" dust particles encountered by the Giotto spacecraft were, to the limits of detectability, purely organic in composition, rather than organics enclosing a silicate core. In addition, the similarity between the core–mantle interstellar dust model and interplanetary dust particles (IDPs or "Brownlee particles") of possible cometary origin is at best ambiguous. The only "ground truth" we have for cometary dust is the cometary fraction of the IDPs collected by high altitude aircraft in the Earth's stratosphere. But Walker (1988) has concluded that "nothing resembling the Greenberg model has been seen in the study of several hundred IDPs. We therefore doubt that it is a valid picture for typical cometary particles. . . . Some interstellar material is present but the volume fraction is small. . . .'' (See also Brownlee 1988).

The results of our model presented in Figs. 4–5 assume a greatly idealized regularity in the parameters necessary to predict cometary emission spectra. As previously noted, Comet Halley is in fact known to be highly time variable, both deviating from a simple R^{-4} law for infrared flux by as much as a factor of 7 over a few days (Gehrz and Ney 1986), and showing great variability of emission features relative to continuum on successive nights' observations. Similarly, Weaver *et al.* (1987) observed a 40% variation in Halley water molecule production over a space of only 2 hr on 24 March 1986. Thus heliocentric evolution of organic spectral features may well be indiscernible due to stochastic cometary variability, at least in the absence of sufficiently comprehensive observational statistics.

Given this variability, as well as the many uncertainties in our model, it is evident that one can at best make general predictions on the basis of Figs. 4 and 5. Uncertainties in the model include, among others, that the τ_λ/τ ratio appropriate for fitting the 3.4-μm feature on the date of Wickramasinghe and Allen's 31 March 1986 observation cannot be exactly appropriate for other dates; the strength of the 6-μm feature relative to that at 3.4 μm in the transmission spectrum used in the model is expected to vary with radiation dose; CH_4 hydrate clathrate is certainly not the only C- or N-containing ice initially present in a comet; the temperatures 450 and 560°K calculated from optical constants for a gas-phase N-rich product or glassy carbon can only be an approximation to the temperature appropriate to an ice residue; and, finally, the simple two-component model used here is obviously crude. We hope to address some of these dependencies in further experimental work (see also Khare *et al.* (1988) for an initial exploration of some of the relevant parameters).

Nevertheless, it is instructive to compare quantitatively the predictions of our model with actual observations of the heliocentric evolution of the 3.4-μm feature in Comet Halley. In Table II, we summarize the observations made of this feature for heliocentric distances between 1.08 and 1.96 AU. Column 3 of Table II lists the ratios $F_\lambda^{em}/F_\lambda^{cont}$ of the peak flux F_λ^{em} of the emission feature to the continuum flux F_λ^{cont}. These results are to be compared with the model predictions listed in columns 4–6. Quantifying the error associated with $F_\lambda^{em}/F_\lambda^{cont}$ in column 3 is difficult, as a determination of this ratio requires fitting an underlying continuum to the observed emission feature and a typically small number of neighboring points. However, we estimate typical uncertainties in our determinations of the ratios given in column 3 to be ±0.1.

The observed flux ratios given in column 3 make the extent of time variability in cometary emission clear. The preperihelion observation of Danks *et al.* (1986) made at $R = 1.11$ AU found the 3.4-μm feature at only the 1σ level. Observations by Wickramasinghe and Allen (1986) on 31 March and 1 April 1986 show a jump in $F_\lambda^{em}/F_\lambda^{cont}$ of ~35% between the 2 nights. Since T_c and T_r in Eq. (2) are virtually unchanged as a comet moves from $R = 1.16$ to $R = 1.18$ AU, this jump must be due to a change in the ratio τ_λ/τ. From Eq. (2), we have $F_\lambda^{em} = S_\lambda + \Omega\tau_\lambda B_\lambda(T_r) + \Omega\tau B_\lambda(T_c)$ and $F_\lambda^{cont} = S_\lambda + \Omega\tau B_\lambda(T_c)$, so that

$$F_\lambda^{em}/F_\lambda^{cont} - 1 = (\tau_\lambda/\tau)A_\lambda, \qquad (7)$$

where

$$A_\lambda \equiv B_\lambda(T_r)/[(S_\lambda/\Omega\tau) + B_\lambda(T_r)]. \qquad (8)$$

[We note that Eqs. (7) and (8), provided S_λ is known, serve to check the consistency of the result τ_λ/τ found by varying χ^2 in Eq. (2).] Since $S_\lambda \propto \tau$, A_λ in Eq. (8) is independent of τ, depending only on T_c and T_r; A_λ for the dates 31 March and 1 April 1986 is thus approximately constant. Dividing both sides of Eq. (7) for 1 April by Eq. (7) for 31 March, we note that A_λ cancels out and we

TABLE II

Comparison between Model and Observed Flux Ratios at $\lambda = 3.4\ \mu\text{m}$[a]

Observation date	Heliocentric distance R(AU)[b]	Observed flux ratio ($F_\lambda^{em}/F_\lambda^{cont}$)	Predicted flux ratio ($F_\lambda^{em}/F_\lambda^{cont}$)		
			Grains for which T = 900°K at 1.16 AU	Glassy carbon optical constants	Titan tholin optical constants
25 December 1985[c]	1.11	~0[h]	1.5	1.5	1.5
26 March 1986[d]	1.08	1.4	1.5	1.4	1.5
27 March 1986[d]	1.10	1.6	1.5	1.5	1.5
28 March 1986[c]	1.12	1.4	1.6	1.5	1.5
29 March 1986[d]	1.13	1.4	1.6	1.5	1.5
30 March 1986[e]	1.15	1.4	1.6	1.5	1.5
31 March 1986[e]	1.16	1.4	1.6	1.5	1.5
1 April 1986[e]	1.18	1.9	1.6	1.5	1.5
25 April 1986[d,f]	1.54	1.7	1.9	1.7	1.3
19–20 May 1986[g]	1.90	2.2	2.0	1.6	1.2
24 May 1986[f]	1.96	~2[i]	2.0	1.6	1.2

[a] It is shown in Section V that discrepancies between model predictions in columns 4 and 5 and observations lie within the stochastic variability of $F_\lambda^{em}/F_\lambda^{cont}$ observed for Comet Halley.

[b] Ephemeris from Yeomans (1986).

[c] Danks *et al.* (1986).

[d] Knacke *et al.* (1986).

[e] Wickramasinghe and Allen (1986).

[f] Baas *et al.* (1986).

[g] Tokunaga *et al.* (1987).

[h] Feature observed at the 1σ level.

[i] $F_\lambda^{em}/F_\lambda^{cont}$ is difficult to quantify, as the placement of the continuum baseline cannot be made with confidence.

find that the change in $F_\lambda^{em}/F_\lambda^{cont}$ between the two obsevations by the factor $1.9/1.4 \approx 1.4$ requires that τ_λ/τ change by a factor $(1.9 - 1)/(1.4 - 1) \approx 2.3$. Thus we discover that the optical depth of the emitting organic grains may change stochastically relative to the continuum optical depth by a factor of a least 2.3 on timescales of 1 day. Such a sudden increase in τ_λ/τ requires either a sudden increase in the number or the absorption coefficient of the organic grains in the coma; either result seems to imply significant nuclear heterogeneity. Such an outburst of small organic grains implies a change in the exponent α of the Halley dust distribution. This result should therefore also caution cometary modelers against drawing strong conclusions on the basis of the dust mass distribution measured by the Giotto or Vega spacecraft, as these may also be highly time-variable.

We remark that the evident outburst of emitting organic particles on 1 April 1986 coincided with an unusually strong CN-shell expansion at that date (Schlosser *et al.* 1986). This coincidence lends support to the hypothesis of A'Hearn *et al.* (1986) that CN jets in Comet Halley form as the CN dissociates directly from submicron organic dust particles in the coma (see also Lamy and Perrin 1988). In addition to CN jets, Halley exhibited OH outbursts between 24 and 29 March 1986, and 30 March and 4 April 1986 (Silva and Mirabel 1988). These outbursts also coincide with evident outbursts of emitting organics seen in Table II.

The greatest discrepancies between our model results and observations are for 25

December 1985, and for the period from 25 April to 24 May 1986. The lack of an observed 3.4-μm feature on 25 December is a further warning that comparisons between model predictions and observations for Comet Halley infrared emission cannot be expected to be exact when only a small number of observations are available for this highly time-variable object. We know from the dates 31 March and 1 April 1986 that variations in $F_\lambda^{\rm em}/F_\lambda^{\rm cont}$ of a factor ~1.4 occur unpredictably; the observed flux ratio for 25 April is just consistent with the model predictions for Titan tholin (column 6) to within this factor. Model predictions for glassy carbon (column 5) are in perfect agreement with observations on this date. The 19–20 May observations, however, appear to require an increase in $F_\lambda^{\rm em}/F_\lambda^{\rm cont}$ over that predicted by our model by a factor ~1.4 in the case of glassy carbon, and ~1.8 in the case of Titan tholin. In light of the time-variability exhibited by Halley, it is clear that, at least in the case of glassy carbon, changes of this magnitude (equal to that observed between 31 March and 1 April) in $F_\lambda^{\rm em}/F_\lambda^{\rm cont}$ are entirely possible. Thus we conclude that both the general evolutionary trend and quantitative values predicted by our model for glassy carbon optical constants are consistent with observations. Model predictions for Titan tholin optical constants, however, are more evidently discrepant with observations in both qualitative and quantitative respects. Thus the observed heliocentric evolution of the 3.4-μm feature provides information on the optical constants, and by extension the nature of the organic material, in Comet Halley.

Although the predictions shown in column 5 of Table II for our model with glassy carbon optical constants are consistent to within observed stochastic variability with the observational results listed in column 3, the match is far from perfect. In particular, $F_\lambda^{\rm em}/F_\lambda^{\rm cont}$ for glassy carbon optical constants peaks at ~1.5 AU, whereas the observed $F_\lambda^{\rm em}/F_\lambda^{\rm cont}$ for Comet Halley appears to continually rise to ~1.9 AU. Glassy carbon optical constants provide a closer fit to these observations than do those of Titan tholin because of the higher temperatures reached by the former. An obvious question, then, is what temperature emitting organic grains must attain at 1.16 AU in order to reach a peak $F_\lambda^{\rm em}/F_\lambda^{\rm cont} \sim 2$ at ~1.9 AU. Numerical experiments show that, for particles whose temperature falls off with heliocentric distance as a blackbody, $T_{\rm r} \sim 900$°K at 1.16 AU best matches the observational data. Results for a model with these temperatures are shown in column 4 of Table II. $T_{\rm r} \sim 900$°K gives $\tau_\lambda/\tau \sim 5.8 \times 10^{-4}$ for a χ^2 minimum fit to the 3.4-μm feature at 1.16 AU.

In fact, $T_{\rm r} \sim 900$°K is probably an overestimate of the temperature required at 1.16 AU to match the data of column 3. For submicron particles, temperature is expected to fall off with heliocentric distance more slowly than for a blackbody, because the long wavelength emissivity of small particles relative to that of a blackbody decreases with decreasing particle temperature (Greenberg 1971). Thus the temperature of submicron grains is expected to fall off as

$$T_{\rm r} = T_{\rm r}(R = 1.16\ {\rm AU})(R/1.16\ {\rm AU})^{-\xi}, \quad (9)$$

where $\xi < 0.5$ (Greenberg and Zhao 1989). Dumont and Levesseur-Regourd (1988) find ξ ~0.33 from IRAS data on zodiacal dust; if this choice of ξ were appropriate for Comet Halley submicron emitting organics (Greenberg and Zhao 1989), $T_{\rm r}(R = 1.16\ {\rm AU}) \sim 825$°K would fit the observational results listed in column 3. Such temperatures, higher than those expected for 0.1-μm glassy carbon spheres, may be due in part to a fluffy or fractal grain structure to comet dust (Meakin and Donn 1988). In such particles, flash heating of individual fractal elements by UV photon absorption may lead to temperatures well above those expected for a blackbody. We defer further discussion of these effects to a future publication.

VI. THERMAL EMISSION FROM GRAINS VS. GAS-PHASE FLUORESCENCE

It was first suggested by one of us (M.J.M.) at the workshop *Infrared Observations of Comets Halley and Wilson and Properties of the Grains* (M. Hanner, Ed. 1988) that the heliocentric evolution of organic spectral features will differ in the cases of thermal emission from small grains and gas-phase fluorescence. The observed intensity of a cometary emission feature will be proportional to the total number N of emitters present in that part of the coma subtended by the telescope aperture. N is in turn dependent upon the lifetime of the emitters. Using Mie theory, Wallis *et al.* (1987) have calculated lifetimes for biologically derived organic grains of radius ~0.1 μm. Assuming the range of bond energies of terrestrial Type II kerogen to be appropriate for cometary organics, they find that, at 1 AU, the grains experience almost no evaporation within a cometary coma of radius 5×10^4 km, the "nominal" size (McDonnell *et al.* 1987) of the Halley dust coma. [At these heliocentric distances, 0.1-μm grain lifetimes are well in excess of 10^6–10^7 sec; with an outflow velocity ~350 m/sec (McDonnell *et al.* 1987), such a grain will travel ~10^6 km prior to evaporation.] Organic molecular bonds with activation energies $\lesssim$50 kcal/mole will be disrupted on shorter time scales, but $\lesssim$5% of the bonds in kerogen have strengths below this level. Significant evaporation of 0.1-μm grains on time scales ~10^4 sec will begin only for heliocentric distances <0.64 AU or at grain temperatures >680°K (Wallis *et al.* 1987). Similarly, Combi (1987) has concluded that grain lifetimes are as short as ~10^5 sec only for grains that are very small (~10^{-3} μm, ~10^{-21} g).

These results are in rough agreement with thermogravimetric analyses of the involatile organic residue produced by electron, spark, or UV irradiation of cosmically abundant gases; typical results indicate that the residues are 50% stable at temperatures ranging from ~600 to 1200°K (Sagan and Khare 1979, Sagan *et al.* 1984). Since ground-based observations of Comet Halley at heliocentric distances ~1–2 AU typically subtend ~10^3–10^4 km across the coma, particle evaporation is evidently of little importance in evaluating N in the case where organic spectral features are due to thermal emission from grains. Of course, those most volatile organics which do evaporate should themselves contribute to gas-phase fluorescence.

If the organic spectral features are due primarily to fluorescence, however, limits on molecular lifetimes due to dissociation by solar ultraviolet light are of great significance. For example, at 1 AU, unshielded CH_4 and NH_3 lifetimes against UV dissociation are ~10^5 and ~10^4 sec, respectively (see Allen *et al.* 1987). CH_4 would contribute prominently to fluorescence near 3.3 μm, and NH_3 near 6 μm (Crovisier and Encrenaz 1983). With a typical gas outflow velocity from the nucleus ~1 km/sec (Allen *et al.* 1987), CH_4 and NH_3 molecules should experience significant UV dissociation within a 5×10^4 km dust coma radius. Ground-based observations conducted with aperture sizes large enough to include this molecular dissociation, but small enough to exclude significant organic grain evaporation, are in principle capable of determining which mechanism, grain thermal emission or gas-phase fluorescence, is primarily responsible for the observed cometary organic spectral features. In the simplest approximation, the lifetimes of gas-phase fluorescing molecules will increase as the square of the heliocentric distance R, whereas the lifetimes of thermally emitting organic grains ("infinite" for the purposes of these observations) will remain unchanged. Thus the band strengths predicted by these two mechanisms for the 3.4-μm emission feature differ by a factor R^2 in their heliocentric evolution. To observe this evolution, a sequence of observations over a range of heliocentric distances, with appropriately chosen aperture sizes, would be required.

Of course, the situation is in practice much more complex. For example, the fluorescing of daughter products of dissociated parent molecules (among other complications) must be taken into account. We hope to explore the details of such a more precise treatment elsewhere. In addition, lifetimes of evaporating grains depend both on grain size and on the binding energy of the relevant organics. For example, Lamy and Perrin (1988), choosing a uniform bond energy of 34.5 kcal/mole, find that 0.2-μm grains have lifetimes at 1 AU of $\sim 2 \times 10^5$ sec, traveling $\sim 7 \times 10^4$ km before being completely destroyed. If grain lifetimes are indeed on the order of molecular UV-dissociation lifetimes, heliocentric spectral evolution will not allow a choice between gas-phase fluorescence and solid particle thermal emission. However, given independent reasons to accept the thermal emission model, such evolution would put constraints on grain evaporation lifetimes, and hence, on the nature of the organic bonds present. Finally, it must again be noted that the stochastic variability of a comet's dust emission, if as great as that exhibited by Comet Halley, might well overwhelm the differences between fluorescent and thermal emission described here.

VII. DISCUSSION AND FUTURE OBSERVATIONS

In spite of the many uncertainties discussed above, certain broad conclusions can be drawn. We have demonstrated quantitatively that in the vicinity of 1 AU, spectral features in the 5–8 μm range should be overwhelmed by the continuum while the 3.4-μm feature should be apparent, whereas between 1.5 and 3 AU this relationship will reverse. Thus, for best visibility relative to the continuum, observations which hope to identify organic spectral features beyond 4 μm are preferably conducted at these larger heliocentric distances, placing a premium on early spectral observations of comets as soon as their comae develop (subject, of course, to signal-to-noise limitations). Observations within $\sim$2 AU potentially face the dilemma of yielding an uninterpretable null result: no spectral features may indicate a true paucity of molecules with emission features at these wavelengths, or the absence of such features may simply be a result of poor visibility relative to the continuum, the effect described here. The absence of organic spectral features at greater heliocentric distances, however, would begin significantly to constrain the organic composition of the comet in question. In the context of our model, such results would constrain the composition of the ices that are precursors to the organic grains (Khare *et al.* 1988).

Future comet rendezvous missions will be ideally placed to test the predictions of our model. Airborne and ground-based observations are also clearly of great importance. For example, spectral observations in the 5–8 μm range of a cometary coma as the comet moves from 1 to 3 AU would be especially valuable. In addition, observations of a comet approaching perihelion within several tenths of an AU of the Sun could serve to check the near-Sun evolution of the 3.4-μm feature predicted here.

Note added in proof. Danks *et al.* (1987, *Astron. Astrophys.* **184,** 329–332) present the observations described by Danks *et al.* (1986) in refereed form. However, the December observing date and corresponding heliocentric and geocentric distances listed in Danks *et al.* (1987) are in error, whereas those given in Danks *et al.* (1986) remain correct (A. Danks, personal communication). We therefore use the results of Danks *et al.* (1986) in this paper.

ACKNOWLEDGMENTS

We thank Alan Tokunaga, Humberto Campins, J. Mayo Greenberg, W. Reid Thompson, Bob Gehrz, Roger Knacke, Tony Danks, Tim Brooke, Lou Allamandola, Steven Beckwith, and Fred Jaquin for helpful discussions and criticism, and, in some cases, prepublication versions of recent results. This work was supported by NASA Grants NGR 33-010-220 and NGR 33-010-101.

REFERENCES

A'Hearn, M. F., S. Hoban, P. V. Birch, C. Bowers, R. Martin, and D. A. Klingesmith 1986.

Cyanogen jets in Comet Halley. *Nature* (*London*) **324,** 649–651.

Allen, D. A., and D. T. Wickramasinghe 1987. Discovery of organic grains in Comet Wilson. *Nature* (*London*) **329,** 615–616.

Allen, M., M. Delitsky, W. Huntress, Y. Yung, W.-H. Ip, R. Schwenn, H. Rosenbauer, E. Shelley, H. Balsiger, and J. Geiss 1987. Evidence for methane and ammonia in the coma of Comet P/Halley. *Astron. Astrophys.* **187,** 502–512.

Baas, F., T. R. Geballe, and D. M. Walther 1986. Spectroscopy of the 3.4 micron emission feature in Comet Halley. *Astrophys. J.* **311,** L97–L101.

Bregman, J. D., H. Campins, F. C. Witteborn, D. H. Wooden, D. M. Rank, L. J. Allamandola, M. Cohen, and A. G. G. M. Tielens 1987. Airborne and groundbased spectrophotometry of Comet P/Halley from 5–13 micrometers. *Astron. Astrophys.* **187,** 616–620.

Brooke, T. Y., R. F. Knacke, T. C. Owen, and A. T. Tokunaga 1987. Detection of infrared emission features in Comet Wilson. *Bull. Amer. Astron. Soc.* **19,** 893.

Brownlee, D. E. 1988. A comparison of Halley dust with meteorites, interplanetary dust and interstellar grains. In *Infrared Observations of Comets Halley and Wilson and Properties of the Grains,* NASA Conference Publication 3004 (M. S. Hanner, Ed.), pp. 66–67.

Campins, H., and E. V. Ryan 1988. The identification of crystalline olivine in cometary silicates. *Astrophys. J.*, in press.

Chyba, C., and C. Sagan 1987a. Infrared emission by organic grains in the coma of Comet Halley. *Nature* (*London*) **330,** 350–353.

Chyba, C., and C. Sagan 1987b. Cometary organics but no evidence for bacteria. *Nature* (*London*) **329,** 208.

Chyba, C., and C. Sagan 1988a. A two-component model for thermal emission from organic grains in Comet Halley. In *Infrared Observations of Comets Halley and Wilson and Properties of the Grains,* NASA Conference Publication 3004 (M. S. Hanner, Ed.), pp. 83–84.

Chyba, C., and C. Sagan 1988b. Cometary organic matter still a contentious issue. *Nature* (*London*) **332,** 592.

Chyba, C., and C. Sagan 1988c. The pre- and post-accretion irradiation history of cometary ices. In *Interstellar Dust: IAU Symposium 135,* NASA Conference Publication, in press.

Clark, B. C., L. Mason, and J. Kissel 1987. Systematics of the "CHON" and other light element particle populations in Comet P/Halley. *Astron. Astrophys.* **187,** 779–784.

Cochran, A. L., and M. L. McCall 1980. Spectrophotometric observations of Comet Bowell (1980b). *Publ. Astron. Soc. Pacific* **92,** 854–857.

Combes, M., V. I. Moroz, J. Crovisier, T. Encrenaz, J. P. Bibring, A. V. Grigoriev, N. F. Sanko, N. Coron, J. F. Crifo, R. Gispert, D. Bockelée-Morvan, Yu. V. Nikolsky, V. A. Krasnopolsky, T. Owen, C. Emerich, J. M. Lamarre, and F. Rocard 1988. The 2.5–12 μm spectrum of Comet Halley from the IKS-Vega experiment. *Icarus* **76,** 404–436.

Combi, M. R. 1987. Sources of cometary radicals and their jets: Gases or grains. *Icarus* **71,** 178–191.

Crovisier, J., and Encrenaz, Th. 1983. Infrared fluorescence of molecules in comets: The general synthetic spectrum. *Astron. Astrophys.* **126,** 170–182.

Danks, A., Th. Encrenaz, P. Bouchet, T. Le Bertre, A. Chalabaev, and N. Epchtein 1986. Observation of an emission feature at 3.4-μ in the spectrum of Comet Halley. In *20th Eslab Symposium on the Exploration of Halley's comet,* Vol. 3 (ESA SP-250), pp. 103–106.

Delsemme, A. H. 1976. Chemical nature of the cometary snows. *Mem. Soc. R. Sci. Liège* **9,** 135–145.

Delsemme, A. H. 1982. Chemical composition of cometary nuclei. In *Comets* (L. L. Wilkening, Ed.), pp. 85–130. Univ. of Arizona Press, Tucson.

Divine, N., H. Fechtig, T. I. Gombosi, M. S. Hanner, H. U. Keller, S. M. Larson, D. A. Mendis, R. L. Newburn, R. Reinhard, Z. Sekanina, and D. K. Yeomans 1986. The Comet Halley dust and gas environment. *Space Sci. Rev.* **43,** 1–104.

Draganić, I. G., Z. D. Draganić, and S. Vujosecić 1984. Some radiation–chemical aspects of chemistry in cometary nuclei. *Icarus* **60,** 464–475.

Drapatz, S., H. P. Larson, and D. S. Davis 1987. Search for methane in Comet P/Halley. *Astron. Astrophys.* **187,** 497–501.

Dumont, R., and A.-C. Levasseur-Regourd 1988. Properties of interplanetary dust from infrared and optical observations. *Astron. Astrophys.* **191,** 154–160.

Edoh, O. 1983. *Optical Properties of Carbon from the Far Infrared to the Far Ultraviolet.* Ph.D. dissertation, Dept. of Physics, University of Arizona. Cited by M. Hanner 1988. Grain optical properties. In *Infrared Observations of Comets Halley and Wilson and Properties of the Grains,* NASA Conference Publication 3004 (M. S. Hanner, Ed.), pp. 22–49.

Gehrz, R. D., and E. P. Ney 1986. Infrared temporal development of P/Halley. In *20th Eslab Symposium on the Exploration of Halley's Comet,* Vol. 2 (ESA SP-250), pp. 101–106.

Green, D. W. E., and C. S. Morris 1987. The visual brightness behavior of P/Halley during 1981–1987. *Astron. Astrophys.* **187,** 560–568.

Green, S. F., J. A. M. McDonnell, G. S. A. Pankiewicz, and J. C. Zarnecki 1986. The UKIRT Infrared observational program. In *20th Eslab Symposium on the Exploration of Halley's Comet,* Vol. 2 (ESA SP-250), pp. 81–86.

GREENBERG, J. M. 1971. Interstellar grain temperatures: Effects of grain materials and radiation fields. *Astron. Astrophys.* **12,** 240–249.

GREENBERG, J. M. 1982. What are comets made of? A model based on interstellar dust. In *Comets* (L. L. Wilkening, Ed.), pp. 131–163. Univ. Arizona Press, Tucson.

GREENBERG, J. M., AND R. GRIM 1986. The origin and evolution of comet nuclei and Comet Halley results. In *20th Eslab Symposium on the Exploration of Halley's Comet,* Vol. 2 (ESA SP-250), pp. 255–263.

GREENBERG, J. M., AND N. ZHAO 1989. The 3.4 μm and 10 μm emissions from Comet Halley: A blizzard of fluffy aggregates of interstellar dust. *Nature (London),* submitted for publication.

HANNER, M. S. 1983. The nature of cometary dust from remote sensing. In *Cometary Exploration II* (T. I. Gombosi, Ed.), pp. 1–22. Hungarian Acad. Sci., Budapest.

HANNER, M. S. 1986. A preliminary look at the dust in Comet Halley. *Adv. Space Res.* **5,** 325–334.

HANNER, M. S., Ed. 1988. *Infrared Observations of Comets Halley and Wilson and Properties of the Grains,* NASA Conference Publication 3004.

JESSBERGER, E. K., A. CHRISTOFORIDIS, AND J. KISSEL 1988. Aspects of the major element composition of Halley's dust. *Nature (London)* **332,** 691–695.

JOHNSON, R. E., J. F. COOPER, L. J. LANZEROTTI, AND G. STRAZZULLA 1987. Radiation formation of a non-volatile comet crust. *Astron. Astrophys.* **187,** 889–892.

KHARE, B. N., C. SAGAN, E. T. ARAKAWA, F. SUITS, T. A. CALCOTT, AND M. W. WILLIAMS 1984. Optical constants of organic tholins produced in simulated Titanian atmospheres: From soft X-ray to microwave frequencies. *Icarus* **60,** 127–137.

KHARE, B. N., W. R. THOMPSON, B. G. J. P. T. MURRAY, C. F. CHYBA, C. SAGAN, AND E. T. ARAKAWA 1989. Solid organic residues produced by irradiation of hydrocarbon-containing H_2O and H_2O/NH_3 ices: Infrared spectroscopy and astronomical implications. *Icarus,* this volume.

KISSEL, J., AND F. R. KRUEGER 1987. The organic component in dust from Comet Halley as measured by the PUMA mass spectrometer on board Vega 1. *Nature (London)* **326,** 755–760.

KNACKE, R. F., T. Y. BROOKE, AND R. R. JOYCE 1986. Observations of 3.2–3.6 micron emission features in Comet Halley. *Astrophys. J.* **310,** L49–L53.

LAMY, P. L., AND J. M. PERRIN 1988. Optical properties of organic grains: Implications for interplanetary and cometary dust. *Icarus* **76,** 100–109.

LARSON, H. P., H. A. WEAVER, M. J. MUMMA, AND S. DRAPATZ 1989. Airborne infrared spectroscopy of Comet Wilson (1986*l*) and comparisons with Comet Halley. *Astrophys. J.,* submitted for publication.

LYNCH, D. K., R. W. RUSSELL, F. C. WITTEBORN, J. D. BREGMAN, D. M. RANK, M. C. COHEN, AND H. CAMPINS 1988. 5–13 μm airborne observations of Comet Wilson 1986*l*: Preliminary results. In *Infrared Observations of Comets Halley and Wilson and Properties of the Grains,* NASA Conference Publication 3004 (M. S. Hanner, Ed.), p. 165.

MCDONNELL, J. A. M., W. M. ALEXANDER, W. M. BURTON, E. BUSSOLETTI, G. C. EVANS, S. T. EVANS, J. G. FIRTH, R. J. L. GRARD, S. F. GREEN, E. GRUN, M. S. HANNER, D. W. HUGHES, E. IGENBERGS, J. KISSEL, H. KUCZERA, B. A. LINDBLAD, Y. LANGEVIN, J.-C. MANDEVILLE, S. NAPPO, G. S. A. PANKIEWICZ, C. H. PERRY, G. H. SCHWEHM, Z. SEKANINA, T. J. STEVENSON, R. F. TURNER, U. WEISHAUPT, M. K. WALLIS, AND J. C. ZARNECKI 1987. The dust distribution within the inner coma of Comet P/Halley 1982i: Encounter by Giotto's impact detectors. *Astron. Astrophys.* **187,** 719–741.

MCDONNELL, J. A. M., J. KISSEL, E. GRÜN, R. J. L. GRARD, Y. LANGEVIN, R. E. OLEARCZYK, C. H. PERRY, AND J. C. ZARNECKI 1986. Giotto's dust impact detection system DIDSY and particulate impact analyser PIA: Interim assessment of the dust distribution and properties within the coma. In *20th Eslab Symposium on the Exploration of Halley's Comet,* Vol. 2 (ESA SP-250), pp. 25–38.

MEAKIN, P., AND B. DONN 1988. Aerodynamic properties of fractal grains: Implications for the primordial solar nebula. In *Infrared Observations of Comets Halley and Wilson and Properties of the Grains,* NASA Conference Publication 3004 (M. S. Hanner, Ed.), pp. 166–171.

PERRY, C. H., S. F. GREEN, AND J. A. M. MCDONNELL 1988. A possible explanation for the inconsistency between the Giotto grain mass distribution and ground-based observations. In *Infrared Observations of Comets Halley and Wilson and Properties of the Grains,* NASA Conference Publication 3004 (M. S. Hanner, Ed.), pp. 178–179.

SAGAN, C., AND B. N. KHARE 1979. Tholins: Organic chemistry of interstellar grains and gas. *Nature (London)* **277,** 102–107.

SAGAN, C., B. N. KHARE, AND J. S. LEWIS 1984. Organic matter in the Saturn system. In *Saturn* (T. Gehrels and M. S. Matthews, Eds.), pp. 788–807. Univ. Arizona Press, Tucson.

SCHLOSSER, W., R. SCHULZ, AND P. KOCZET 1986. The cyan shells of Comet P/Halley. In *20th Eslab Symposium on the Exploration of Halley's Comet,* Vol. 3 (ESA SP-250), pp. 495–498.

SILVA, A. M., AND I. F. MIRABEL 1988. Gaseous outbursts in Comet P/Halley: A model for the dissociation of the OH radical. *Astron. Astrophys.* **201,** 350–354.

STRAZZULLA, G., L. CALCAGNO, AND G. FOTI 1983. Polymerization induced on interstellar grains by low-energy cosmic rays. *Mon. Not. R. Astron. Soc.* **204,** 59p–62p.

THOMPSON, W. R., B. G. J. P. T. MURRAY, B. N. KHARE, AND C. SAGAN 1987. Coloration and darkening of methane clathrate and other ices by charged particle irradiation: Applications to the outer solar system. *J. Geophys. Res.* **92,** 14,933–14,947.

Tokunaga, A. T., and T. Brooke 1988. Comparison of the 3.36 μm feature to the ISM. In *Infrared Observations of Comets Halley and Wilson and Properties of the Grains,* NASA Conference Publication 3004 (M. S. Hanner, Ed.) 79–82.

Tokunaga, A. T., W. F. Golisch, D. M. Griep, C. D. Kaminski, and M. S. Hanner 1986. The NASA infrared telescope facility Comet Halley monitoring program. I. Preperihelion results. *Astron. J.* **92,** 1183–1189.

Tokunaga, A. T., W. F. Golisch, D. M. Griep, C. D. Kaminski, and M. S. Hanner 1988. The NASA infrared telescope facility Comet Halley monitoring program. II. Postperihelion results. *Astron. J.* **96,** 1971–1976.

Tokunaga, A. T., T. Nagata, and R. G. Smith 1987. Detection of a new emission band at 2.8 μm in Comet P/Halley. *Astron. Astrophys.* **187,** 519–522.

Walker, R. M. 1988. Comparison of laboratory determined properties of interplanetary dust with those of Comet Halley particles: What are comets made of? In *Infrared Observations of Comets Halley and Wilson and Properties of the Grains,* NASA Conference Publications 3004 (M. S. Hanner, Ed.), pp. 53–63.

Wallis, M. K., R. Rabilizirov, and N. C. Wickramasinghe 1987. Evaporating grains in P/Halley's coma. *Astron. Astrophys.* **187,** 801–806.

Weaver, H. A., M. J. Mumma, and H. P. Larson 1987. Infrared investigation of water in Comet P/Halley. *Astron. Astrophys.* **187,** 411–418.

Wickramasinghe, D. T., and D. A. Allen 1986. Discovery of organic grains in Comet Halley. *Nature (London)* **323,** 44–46.

Wickramasinghe, N. C. 1973. *Light Scattering Functions for Small Particles, with Applications in Astronomy.* Halsted, New York.

Yeomans, D. K. 1986. The Comet Halley ephemeris development effort. In *Space Missions to Halley's Comet* (ESA SP-1066), pp. 179–197.

ICARUS 79, 382–395 (1989)

The Relevance of the Background Impact Flux to Cyclic Impact/Mass Extinction Hypotheses

MARTYN J. FOGG[1]

University of London, Department of Extra-mural Studies, 26 Russell Square, London WC1B 5DQ, England

Received January 29, 1988; revised August 22 1988

The belief that mass extinctions of species on Earth have occurred on a ~26- to 33-my cycle is supported by some rather equivocal geological evidence. This has prompted a search for cosmic phenomena that could subject the Earth at regular intervals to bombardment by showers of comets, with resulting damage to the biosphere. A crucial assumption that an impact-driven mass extinction cycle would automatically show up in the geological record is questioned. Might the background flux of random impacts distort the cycle and render it unrecognizable? Computer simulation of the impact bombardment of the Earth over a 250-my period, in which the background impact flux is overlaid by a 26-my comet shower cycle, showed a periodicity in the mass extinction data between 24 and 33 my in ~40–60% of runs, dependent on the magnitude of the background flux chosen, and only ~20–40% indicated the "true" 26-my periodicity. Thus, background impact "noise" can be identified as an additional constraint on cyclic impact/mass extinction hypotheses. © 1989 Academic Press, Inc.

1. INTRODUCTION

The geological record shows that the history of life has been punctuated by a number of discrete events during which a large number of species have become extinct. When of global extent, these biotic crises are known as mass extinctions. The causes most favored by paleontologists to account for mass extinctions are climatic change and alteration in sea level (Stanley 1987), both being mechanisms that might operate over millenia and yet still appear to be near instantaneous events in the geological record.

A challenge to this "gradualist" approach followed the discovery by Alvarez *et al.* (1980) of an anomalous iridium concentration in sediments at the Cretaceous–Palaeogene (K-Pg) boundary that is suggestive of an admixture of extraterrestrial material. The possibility that this excess resulted from the impact of a ~10-km-diameter asteroid which might have caused the K-Pg mass extinction has lead to the revival of the "catastrophist" approach to Earth evolution. Long relegated to the sidelines, catastrophism is once again being discussed seriously (Silver and Schultz 1982).

The debate was given greater impetus by Raup and Sepkoski (1984) who presented evidence that mass extinctions occurred periodically over ~26-my intervals. In another analysis of the extinction data Rampino and Stothers (1984a) identified a mass extinction periodicity of 30 ± 1 my, and a rough periodicity of geological upheavals as a whole of ~33 my (Rampino and Stothers 1984b). Since 1984, there has been much debate concerning the statistical significance of the extinction data, although more recent analyses continue to identify periods of ~26–33 my.

A number of alternative models have been proposed for astronomical mechanisms that might drive an impact/extinction cycle. All rely for lethal effect on the

---

[1] Current address: 44 Hogarth Court, Fountain Drive, London SE19 1UY, United Kingdom.

0019-1035/89 $3.00
Copyright © 1989 by Academic Press, Inc.
All rights of reproduction in any form reserved.

"comet shower," a huge influx of comets into the inner Solar System, precipitated by gravitational disturbance of the Sun's comet cloud. A shower of sufficient magnitude might cause several Earth impacts, initiating a global biotic crisis. Hypotheses fall into two classes dependent on the source of comet showers.

1.1. The Standard Oort Cloud

Clube and Napier have linked mass extinctions to the 60-my epicyclic motion of the Sun relative to the galactic plane. They propose a theory of "terrestrial catastrophism" (Napier and Clube 1979, Clube and Napier 1982, 1984a, 1984b) in which the Oort cloud is disturbed every 30-my half-period by encounters with molecular clouds as the Sun crosses the galactic plane. Comets in showers of ~6 my in duration cause mass extinction, either through direct impact with the Earth or by creating a dusty interplanetary environment. Apollo asteroids are seen as being the decayed remnants of a comet shower and thus the population density of these bodies would also exhibit a periodicity. Clube and Napier also point out that the Oort cloud is not likely to be stable, over the lifetime of the Solar System, from gravitational disruption by molecular cloud encounters. They overcome this problem by proposing that interstellar comets can form in molecular clouds (Clube and Napier 1985) and thus an encounter of the Sun with a molecular cloud results in both loss and replenishment of Oort cloud comets. It is this facet of the Clube/Napier hypothesis that causes many astronomers to reject it as too radical.

1.2. The Inner Comet Cloud

The galactic tidal field is of sufficient strength to perturb a continuous flux of "new" Oort cloud comets from $\sim 2.5 \times 10^4$ to 10^5 AU into the inner system. Hills (1981) believes the inner boundary of the Oort cloud therefore to be an observational artifact and has proposed the existence of a more massive inner comet cloud between $\sim 10^3$ and 2×10^4 AU. When disturbed, comets from this inner cloud would enter the planetary system in an intense shower of ~2 my duration causing a number of Earth impacts. The Oort cloud is replenished by the perturbation of a small fraction of these comets into more loosely bound orbits. The anatomy of comet showers originating from the inner cloud has been studied in more detail by Fernandez and Ip (1987) and Hut *et al.* (1987).

The existence of a massive inner comet cloud is still subject to speculation; however, the majority of cyclic extinction hypotheses assumes it to be present.

Davis *et al.* (1984) and Whitmire and Jackson (1984a) proposed the "death star" or "Nemesis" hypothesis, in which an undiscovered low-mass solar companion star follows a highly eccentric orbit with a period of 26 my. At perihelion Nemesis would come close enough to the inner comet cloud to precipitiate a comet shower.

Rampino and Stothers (1984a) link mass extinctions to disturbances of the inner comet cloud by encounters with molecular clouds. As in the Clube/Napier hypothesis, a cyclicity is imposed every ~30 my as the Sun passes through a concentration of molecular clouds in the galactic plane.

If the postulated inner comet cloud extends to the fringes of the planetary system then comet showers might be precipitated from this region. In the "planet X" hypothesis, proposed by Matese and Whitmire (1986), periodic comet showers are precipitated by the precession of the orbit of a hypothetical tenth planet through a primordial disk of comets they believe to lie beyond Neptune.

All of the above hypotheses have their distinct difficulties, although none have been so far totally disproved. For instance, it is not certain whether the orbit of Nemesis would be stable or that the star could act as a reliable "clock" (Clube and Napier 1984c, Torbett and Smoluchowski 1984, Hut 1984). Galactic regulation of comet showers may not appear if the concentration of molecular clouds close to the galactic plane is not sufficient to produce a strong periodicity (Thaddeus and Chanan 1985). The biological reality of the mass extinctions themselves has also come into question (Patterson and Smith 1987, Smith 1988); periodicity in fish and echinoderm family extinctions appears to be a taxonomic artifact produced by sampling errors. Recent papers detailing the competing arguments are found in Smoluchowski *et al.* (1986).

There is, however, another potential problem common to all cyclic impact/mass extinction hypotheses that has been largely neglected. This is the obscuring role of random impact "noise." Cyclical impact models proceed on the implicit assumption that the background flux of Earth impacts has been low enough for major irregularities in the periodicity of extinctions not to have occurred. This assumption may not be well founded, for if the background flux is significant, and cannot be linked to mass extinctions, then both the impact/mass extinction hypotheses and the validity of apparent periodicities in the geological record must be reexamined.

The following examination of the problem concentrates on those hypotheses which require the presence of an inner comet cloud.

2. THE BACKGROUND OR RANDOM IMPACT FLUX

The terrestrial cratering rate in the Phanerzoic Eon for craters of diameter >10 km has been estimated by Grieve and Dence (1979), from a study of craters on the North American and East European cratons, to be ~1.4×10^{-14} km^{-2} year^{-1}. For craters with $D >$ ~20 km the cumulative abundance follows a power law $N\ (\geq D) \propto D^{-2}$ which is in good agreement with the size frequency distribution of lunar craters.

Converting the formula of Shoemaker *et al.* (1979) from kilotons of TNT equivalent to Joules, and taking into account crater collapse, the diameter in kilometers of an impact crater on the Earth scales with energy approximately as

$$D \simeq 1.96 \times 10^{-5}(E_K)^{1/3.4}, \qquad (1)$$

where E_K is the kinetic energy of impact in Joules. Taking a typical missile density of 2380 kg m^{-3} and impact velocity of 20 km sec^{-1}, then a missile of diameter $d = 1$ km will create a crater of $D = 19.4$ km. The infall rate for bodies of $d \geq 1$ km is therefore $\simeq 1.9$ my^{-1}.

Observations of Earth-crossing (Apollo and Aten) asteroids lead to higher estimates for impact and cratering rates. Shoemaker *et al.* (1979) estimate the impact flux for the current population of Earth-crossing asteroids to be $N(d \geq 1\text{ km}) \simeq 3.5$ my^{-1}, with a cratering rate of $N(D \geq 10\text{ km}) \simeq 2.3 \times 10^{-14}$ km^{-2} year^{-1}. Steel and Baggeley (1985) have obtained an impact rate of $N(d \geq 1\text{ km}) \simeq 6$ my^{-1}, although removing four Apollo asteroids from their sample that they believed might have introduced a bias into their results, reduces the estimate to $N(d \geq 1\text{ km}) \simeq 4$ my^{-1}. These higher impact rates do not necessarily conflict with the production of craters, as estimates for the terrestrial cratering rate from studies of surviving craters vary. There is good agreement between the cratering estimate derived from asteroid observations and the cratering rate of $N(D \geq 10\text{ km}) \simeq 2.2 \times 10^{-14}$ km^{-2} year^{-1} estimated by Shoemaker (1977) from impact structures in North America.

Steel and Baggeley (1985) also derived the mean lifetime for Earth-crossing asteroids against collision, with any of the terrestrial planets, to be ~2.5×10^{7} years for the Aten and ~10^{8} years for the Apollo asteroids. However, since the number of Aten asteroids is thought to be considerably fewer than the number of Apollos, each class contributes about equally to the flux of asteroids impacting the Earth. Since these bodies have a finite lifetime, a continued replenishment mechanism must be invoked to explain their continued existence. The population may be maintained in a quasi-steady state by asteroids perturbed from the main belt and the decay of short period comets (see Shoemaker *et al.* 1979 for discussion), or it may be replenished at intervals by the remnants of a comet shower. The three Apollo asteroids discovered by IRAS all show characteristics that suggest they may be burnt out comet nuclei (Davies 1986).

The Earth is also subjected to bombardment by the steady-state flux of long-period comets perturbed from the Oort cloud by both the galactic tidal field and passing stars (Morris and Muller 1986, Heisler and Tremaine 1986, Heisler *et al.* 1987). However, Weissman (1982) has estimated that the rate of such impacts is only about one-tenth the asteroidal impact frequency. Thus, long-period comets are of little significance and can be disregarded for the purposes of this paper without committing serious error.

An impact rate of one asteroid hitting the Earth every 250,000 years seems high; however, this figure is for asteroids as small as ~1 km in diameter. The impact of a body of 10 km or greater, such as that envisaged by Alvarez *et al.* (1980) should occur much less frequently and would depend critically on the cumulative asteroidal diameter frequency distribution. Since $E_K \propto d^3$ and $D \propto E_K^{1/3.4}$ then $D \propto d^{0.882}$. Since the diameter frequency distribution for craters is $N(\geq D) \propto D^{-2}$ then the diameter frequency distribution for missiles $\simeq N(\geq d) \propto d^{-1.77}$. Thus from the approximate scaling just discussed, we might expect one impact producing a crater of $D = 150$ km every ~20–30 my and one crater of $D = 200$ km every ~34–55 my.

However, on the assumption that the inner comet cloud exists, the random impact flux is not expected to be just a combination of background fluxes of Earth-crossing asteroids and the occasional Oort cloud comet. It is possible for comet showers from the inner comet cloud to be precipitated on a random basis by close encounters with stars and interstellar gas clouds. Hills (1981) has studied the former of these two processes and calculates that a foreign star will pass within 10,000 AU of the Sun every $\sim 4.4 \times 10^7$ years and with 3000 AU every $\sim 4.9 \times 10^8$ years. He estimates that a 3000-AU close encounter will trigger an intense comet shower with a duration $\sim 6.6 \times 10^5$ years, during which from 10 to 200 comets will strike the Earth, an infall rate ~4–76 times the background impact rate of Earth-crossing asteroids. Fernandez and Ip (1987) have also examined random comet showers produced by the perturbations of passing stars. Although their estimates for the efficiency of a number of processes differs, such as the rate of stellar encounters and the filling of the cometary loss cone, their combined model gives results that are not dissimilar to those of Hills.

Morris and Muller (1986) have examined the effectiveness of the tidal field of interstellar gas clouds at precipitating comet showers. On the assumption that an intense shower can be created by the perturbation of comets from orbits with semimajor axes of 10,000 AU, they conclude that clouds of relatively high density $>10^3$ atoms cm^{-3} are necessary. Encounters with these clouds are rare and would occur at intervals of $\sim 4 \times 10^8$ years. Over this time period about 10 stars would be expected to pass within 10,000 AU of the Sun; thus, in comparison with random stellar encounters, random gas cloud encounters would only precipitate about one-tenth the number of comet showers of a given intensity.

3. MODELING AN EARTH IMPACT CHRONOLOGY

To determine the effect of background impacts upon a cometary impact/mass extinction cycle, a simple Monte Carlo simulation of an Earth impact chronology has been written. The data analyzed by Raup and Sepkoski (1984) (hereafter R & S) extends over 250 my and so the model is capable of simulating at least this time span. All the major random impact processes that would occur, given the existence of an inner comet cloud, are included within this model of the background impact flux. These are (i) the impact flux of Earth-crossing asteroids; (ii) stellar-induced comet showers; (iii) molecular cloud-induced comet showers. The simulation has been run both with and without a superimposed comet shower cycle to look for quasi-periodicities in the background impact flux, to study random distortion of mass extinction periodicities and to compare cratering rates. A description of the program algorithm and embodied assumptions follows.

3.1. Impact Rates

3.1.1. Earth-crossing asteroids. Asteroidal background impact rates were discussed in Section 2., since uncertainty in the figures is still very great, two rates were chosen, a high figure of $N(d \geq 1 \text{ km}) = 4 \text{ my}^{-1}$ based on Earth-crossing asteroid data, and a lower figure of $N(d \geq 1 \text{ km}) = 2 \text{ my}^{-1}$ that is more in line with the estimated terrestrial cratering rate. Thus, to allow for an average of one impact per iteration the basic time step is taken as either $S = 0.25$ my or $S = 0.5$ my. During a comet shower when the impact rate is enhanced, the time step is reduced to maintain the same resolution of impact events. Between 0 and 5 impacts were allowed for each time step; probabilities are assumed to follow a binomial distribution. An interval of 20 my after the last comet shower is considered sufficient to deplete the population of Aten asteroids (Steel and Baggeley 1985) and the asteroidal background impact rate is halved. The next comet shower is assumed to replenish this population and the original impact rate is restored to its former value. Thus the asteroidal impact flux, as modeled here, is partially modulated by the occurrence of comet showers. Considering the magnitude of uncertainty, this is a justifiable compromise between the views that Earth-crossing asteroids originate from the main belt and are the remains of extinct comets.

3.1.2. Random comet showers. The Hills (1981) model of the inner comet cloud has been adopted, in which passing stars provide the primary random perturbing agency. The mean time T_s between encounters in which a star passes within a distance a_e of the Sun is given by

$$T_s = (\pi a_e^2 n_s V_s)^{-1}, \tag{2}$$

where n_s is the number of stars per unit volume in the solar neighborhood and V_s is the average velocity of passing stars. Here, $n_s = 0.1 \text{ pc}^{-3}$ and $V_s = 30 \text{ km sec}^{-1}$. Thus, for $a_e = 10{,}000$ AU, $T_s = 44$ my.

During a comet shower caused by a passing star, the fraction of comets with perihelia less than q is

$$N/N_0 \simeq \frac{2q}{a}\left(1 - \frac{q}{2a}\right), \tag{3}$$

where N_0 is the number of comets in the inner cloud and a is the semimajor axis of the innermost comets affected in AU (for stellar passages, encounter times are short so $a \equiv a_e$). The population of comets within the inner cloud is very uncertain since there is no way to "directly" observe this region like there is for the Oort cloud; here we take $N_0 \sim 10^{13}$. For comets intersecting the orbit of the Earth, $q = 1$ AU and Eq. (3) simplifies to $N_\oplus/N_0 \simeq 2q/a$. This equation should not be viewed as precise, since it is dependent on the unknown distribution of comets within the inner cloud. It does, however, probably represent a reasonable estimate to within a factor of order unity.

Hills (1981) estimated the duration of a comet shower to be approximately equal to four cometary orbital periods. Thus the duration of maximum shower intensity T_ι in years is

$$T_\iota = 4a^{1.5}. \tag{4}$$

Hut *et al.* (1987) have estimated that a typical comet would make an average of ~8.6 returns to the planetary region, having an average lifetime of 0.48 my before being destroyed or ejected on a hyperbolic orbit: a further illustration of the uncertainties inherent in an analysis of this type.

The number of comets expected to hit the Earth has been estimated by Davis *et al.* (1984). The probability that a comet will hit the Earth on a single pass is roughly the projected area of the Earth divided by the area of its orbit, or 1.6×10^{-9}. If each comet makes an average of four trips to the inner Solar System, then there are a total of eight opportunities to hit the Earth. The approximate number of impacts resulting from a comet shower is, therefore,

$$N_{\text{hits}} \simeq 1.28 \times 10^{-8}\, N_{\oplus}. \qquad (5)$$

This estimate for the number of Earth impacts lies between previous upper and lower estimates. For instance, where a_e = 3000 AU, Eq. (5) gives 85 impacts, which compares favorably with the range of 10 to 200 impacts obtained by Hills (1981). Since T_ι, for the range of cometary semimajor axes of interest, is always $\ll$6 my, the average age of a stratigraphic stage, the assumption was made that showering comets were distributed evenly over T_ι. This is a reasonable simplification, for although it is possible to simulate the detailed microstructure of a comet shower, it would not be possible to date any extinction caused by the shower with a similar degree of precision.

Numerical data for comet showers are summarized in Table I. Since the impact rate for a shower where a =10,000 AU is estimated as only 60% greater than that of the asteroidal impact rate, it was decided to make this value of a the upper limit for comet showers and Earth-crossing asteroid replenishment.

Comet showers precipitated by randomly encountered interstellar clouds are also included, even though they are likely to be less common than stellar-induced showers. Talbot and Newman (1977) have found that encounters between the Sun and interstellar clouds can be approximated by a broken power law:

$$N_e(\geq D) = 10(D/10^3)^{-\alpha}, \qquad (6)$$

where the function N_e ($\geq D$) is the number of encounters between the Sun and clouds of number density $\geq D$, D is the number density in atoms cm^{-3}, and the exponent α has the value 0.9 for $D < 10^3$ cm^{-3} and the value 2.3 for $D > 10^3$ cm^{-3}.

Morris and Muller (1986) have shown that for perturbations by interstellar clouds, the lowest value of a in AU for showering comets is dependent on cloud density:

$$a \simeq 6 \times 10^5\, R^{-1/2} D^{-1/2}, \qquad (7)$$

where R is the cloud radius, here represented by an average value of 5 pc.

3.2. Missile Parameters

The mass and velocity distribution of impacting missiles are critical parameters as an impact would have to produce adverse ecological effects worldwide to initiate a mass extinction.

A simple way to represent missile diameter frequency distribution is by a power

TABLE I

NUMERICAL DATA

a_e	T_s (10^6 years)	N_{hits}	T_ι (10^6 years)	Step size (10^6 years)	Impact rate (my^{-1})	Ratio of shower rate to asteroid rate
2,000	1100	128	0.36	2.8	358	89
3,000	490	85	0.66	7.7	129	32
4,000	280	64	1.0	16	63	15
5,000	180	51	1.4	28	36	9
6,000	120	43	1.9	43	23	5.8
7,000	90	37	2.3	63	16	3.9
8,000	69	32	2.9	89	11	2.8
9,000	54	28	3.4	122	8	2.0
10,000	44	26	4.0	154	6.5	1.6

law. However, for asteroids and comets this function can only be estimated between wide limits of uncertainty as observational data is scant. Thus, the missile diameter frequency index $N(\geq d) \propto d^{-1.77}$, estimated in Section 2, was chosen.

Following Shoemaker *et al.* (1979), Earth-crossing asteroids are assumed to be 50% S-type, with a material density of 3500 kg m^{-3}, and 50% C-type, with a material density of 2500 kg m^{-3}. Correcting for about 32% combined internal and external void space gives overall densities of 2380 and 1700 kg m^{-3}, respectively. If comet P/Halley is typical, then the density of comets in general probably lies between 100 and 400 kg m^{-3} (Mendis 1986). A value of 300 kg m^{-3} is used here based upon an estimate of Halley's density derived from the comet's rotational angular momentum (Ferrin 1988).

Impact velocities were assumed to be 18 km sec^{-1} for Earth-crossing asteroids and 40 km sec^{-1} for the 50% of comets in direct orbits (Hartmann 1977). Impact velocities can be very high, however, if there is a head-on collision with a comet in a retrograde orbit. Therefore, 50% of comets were assumed to impact at 68 km sec^{-1}.

3.3. *Mass Extinctions*

The kinetic energy of impacts is chosen as the determining parameter of mass extinction events.

Alvarez *et al.* (1980) have estimated that the K-Pg extinction was caused by the impact of a body 10 ± 4 km across. A 10-km-diameter C-type asteroid with a density of 1700 kg m^{-3} and striking at 18 km sec^{-1} liberates an impact energy $E_K = 1.44 \times 10^{23}$ J or $\sim 3 \times 10^7$ Mt. A number of smaller impacts, occurring over a relatively short space of time, and distributed widely over the Earth's surface, might combine in their adverse environmental effects to cause a stepwise global mass extinction which would appear nearly instantaneous in the geological record (Hut *et al.* 1987). However, whether the precipitating event is a single impact or a number of impacts, the minimum necessary total impact energy is unknown. Thus, it was decided to take the energy of the proposed K-Pg impact, released over a maximum of 1 my as the minimum threshold value to cause a global mass extinction. This assumption of an energy threshold for mass extinctions is roughly in line with similar discussions in Berger *et al.* (1985).

The dating of extinction events is fraught with uncertainty. The finest division of the geological column is into stratigraphic stages which, for the Mezozoic through Cenozoic interval, have a mean duration of ~6 my. Although this is a relatively short space of time, R & S have pointed out that is impossible to adequately resolve extinction events less than ~12 my apart. This is because extinctions are dated, by convention, at the end of the stage in which they occur, and at least one stage must lie between events for them to be recognized as separate. A number of arbitrary methods of resolving mass extinctions to within 12 my were tested during the development of the model. None of them, however, was entirely satisfactory, as it was found that the detection of a statistically significant cycle from a simulated extinction sequence was to some degree dependent on the method of resolution. Possibly the best way to simulate the resolution of mass extinctions is to use the geologic time scale itself. This can of course be criticized by pointing out that the mass extinctions came first and the geologic column was "invented" later, rather than vice versa. However, of the 39 stages considered by R & S, only 12 end in mass extinctions and so the structure of the time scale is not strongly influenced by them.

A time scale of 46 stages from Harland *et al.* (1982) is used here. After an extinction sequence has been generated, mass extinctions are dated at the end of the stages in which they occur, in line with geological convention. When two extinction events occur in successive stages, one mass extinction is resolved at the end of the second stage. (This is similar to the situation in the late Permian where a mass extinction is dated at the end of the Tatarian stage, but probably started in the preceding Kazanian stage.) When three extinction events occur in successive stages, mass extinctions are resolved at the terminal dates of the first and third. The minimum separation of extinction events within the simulation is, therefore, two stage lengths, between ~3 and 22 my, averaging at ~12 my.

3.4. *Statistical Testing of the Extinction Series*

Running the simulation produces a series of resolved extinction events. Manual inspection of such data is often not sufficient to reveal the presence of a periodicity, or its statistical significance. The nonparametric testing method of R & S has thus been used to analyze the data. A perfectly periodic impulse function of a given cycle length is superimposed over the extinction series in the best-fit position. The discrepancy between each extinction event and the nearest predicted peak from the impulse function is recorded as an error. The standard deviation of these errors, the SDE, can be used as a gauge of goodness of fit. An SDE of zero thus represents a perfect match of "real" and predicted impulses.

To obtain an SDE value for a given cycle at which their extinction data was considered to exhibit a periodicity, R & S performed 500 Monte Carlo simulations in which 12 extinction impulses were randomly scattered over a 250-my time scale. If the SDE calculated for the geological extinction data was less than 99% of the SDE computed from the random data, a statistically significant periodicity was assumed. The simulation presented here only investigates cycles between 24 and 33 my, but since it produces its own extinction series, with a varying number of impulses, a greater random data base is needed for comparison. For each of 4–18 extinction impulses, 1000 Monte Carlo simulations were run and the <99% SDE threshold values for a given cycle were calculated.

4. RESULTS

4.1. *Simulation of the Background Impact Flux*

Study of the background impact flux as an isolated process is important before investigating its effect on a periodic comet shower cycle. It is essential to determine whether it is likely that this flux may deviate from a purely random process and exhibit a tendency toward periodic behavior. The behavior of the background impact component of the model has, therefore, been investigated by analysis of data from two sets of 1000 runs each for timesteps of 0.5 and 0.25 my.

The results of the simulations are displayed in Table II. Salient characteristics of a sample run where S = 0.5 my are shown in Fig. 1. Ten "lethal events" occurred over 250 my, with seven mass extinction events being resolved. Even though two peaks are missing, calculations of SDE for cycles between 24 and 33 my demonstrate a particularly good fit of a 30-my cycle to the simulated extinction data, with a SDE of 4.31 that is lower than the <99% threshold value. The extinction data for this run can

TABLE II

RANDOM IMPACTS ONLY

Mean numerical value	S	
	0.5 my	0.25 my
Total impacts	581.4	914.9
Comet impacts	247.0	245.8
Asteroid impacts	334.4	669.1
Lethal events	11.0	17.7
Resolved mass extinctions	7.43	10.5
Resolution fraction	0.67	0.59
Total comet showers	5.91	5.92
Lethal showers	2.82	2.96
Shower lethality fraction	0.48	0.50
No. of quasi-periodic runs	102	94
Total No. of quasi-periods	148	148

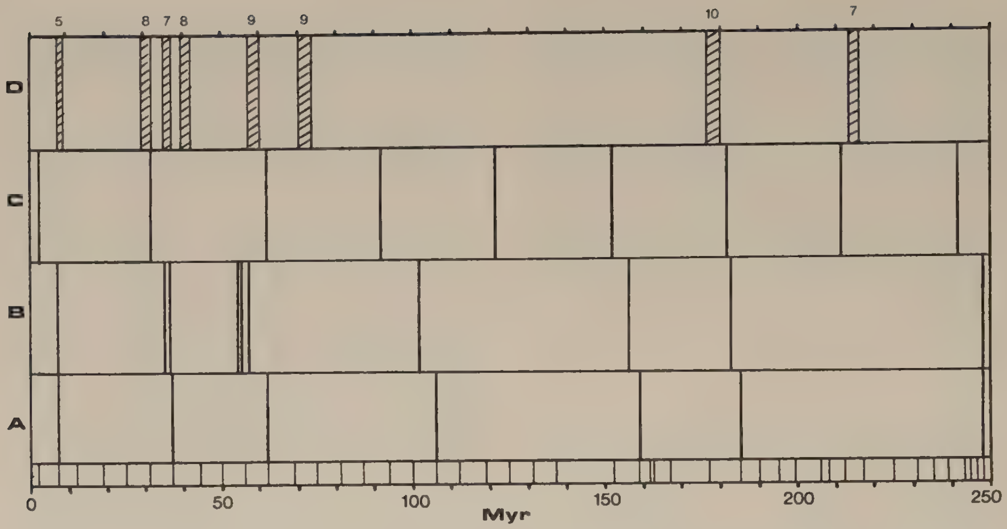

FIG. 1. Salient characteristics of a sample run where $S = 0.5$ my. Elapsed time, in million years from the start of the simulation (250 my B.P.), and the divisions of the geologic time scale are on the horizontal axis. Row A displays the resolved mass extinction events, row B shows the total number of lethal events, and the impulses for a best fit 30-my cycle are shown in row C. The occurrence of comet showers is displayed in row D along with specific values of a in units of 1000 AU.

therefore be stated to possess a quasi-periodicity at 30 my.

Table II shows that ~100 quasi-periodic runs are produced from each run set; this is what would be expected, testing 10 cycles between 24 and 33 my 100 times, if the model background flux is behaving randomly. A slightly higher number of significant quasi-periods were detected as some extinction sequences could be well fitted by a pair or triplet of successive cycles. The total number of quasi-periods per cycle, for both run sets, are displayed in Table III; none of the numbers shown deviate significantly from the approximate expectation of ~10–20 quasi-periods per cycle. No abnormal tendency to produce quasi-periodicities between 24 and 33 my is observed.

It is interesting to compare simulated background flux impact rates with the terrestrial cratering rate. The $S = 0.5$ my run set produces an average impact rate by missiles of $d \geq 1$ km of 4.55×10^{-15} km^{-2} year^{-1}. The $S = 0.25$ my run set gives an average impact rate of 7.16×10^{-15} km^{-2} year^{-1}. Converting these figures to the production rate of craters of $D \geq 10$ km, gives rates of $\sim 1.7 \times 10^{-14}$ and $\sim 2.7 \times 10^{-14}$ km^{-2} year^{-1} which are similar to the cratering rates calculated by Grieve and Dence (1979) and Shoemaker (1977), respectively. Thus, although the production of impact craters can be explained entirely by the cur-

TABLE III

RANDOM IMPACTS ONLY

Cycle	No. of quasi-periods $S = 0.5$ my	$S = 0.25$ my
24	10	8
25	16	16
26	17	19
27	18	16
28	21	15
29	18	18
30	19	21
31	9	18
32	12	9
33	8	8

rent asteroidal impact flux, it can also be accounted for by a model which includes random comet showers. This model of the background impact flux, therefore, appears a reasonable one over which to superimpose a comet shower cycle.

4.2. *Simulation of a Comet Shower Cycle*

A 26-my perfectly periodic comet shower cycle has been chosen for detailed study, for reasons of comparison with the data of R & S and the Nemesis hypothesis of Davis *et al.* (1984). If a mass extinction cycle is to be driven by comet showers, then each shower must have a high probability of being "lethal" and leaving its mark in the geological record. As can be seen from Table II, only about half of the modeled random comet showers cause a mass extinction event. This is because the majority of showers are minor, the loss cone being filled for comets of $a > 7000$ AU. A more substantial disturbance of the inner Oort cloud is required. Since Nemesis would be moving more slowly than a passing star, relative to the comet cloud, it would disturb comets to a distance of less than its pericenter. Hills (1984) has estimated that it is necessary to disturb comets with $a \sim 4000$ AU in order to cause a shower of sufficient intensity to cause mass extinctions. He estimates that the loss cone could be filled to this distance by a Nemesis of $0.05\ M_\odot$, pericenter $<1.04 \times 10^4$ AU, and orbital eccentricity 0.88.

A 26-my cycle of comet showers of $a =$ 4000 AU has, therefore, been simulated. To accord with the best fit postion of the cycle found by R & S to their extinction data, the first shower was initiated 2 my after the start of each simulation. Two run sets were chosen, with differing intensities of background impact flux: 1000 runs at $S = 0.5$ my and $S = 0.25$ my were performed and the relevant data are presented in Tables IV and V.

TABLE IV

26-my Comet Shower Cycle

Mean numerical value	S	
	0.5 my	0.25 my
Total impacts	1286.9	1703.6
Comet impacts	863.9	854.7
Asteroid impacts	422.9	848.9
Lethal events	22.3	30.3
Resolved mass extinctions	13.6	15.6
Resolution fraction	0.61	0.51
Total Comet showers	15.2	15.1
Lethal showers	12.0	12.1
Shower lethality fraction	0.79	0.80
No. of periodic runs	557	375
Total No. of periods	994	568

Characteristics of a sample run where $S = 0.5$ my are shown in Fig. 2. Thirteen extinction peaks were resolved from a total of 17 lethal events. The extinction data were found to exhibit a periodicity, at 26 my with an SDE of 4.88, so the comet shower cycle is showing through as a mass extinction cycle at the 99% significance level. The effects of background impact noise are apparent, however, as the best-fit 26-my cycle has been displaced 7 my from the shower cycle. Row B of Fig. 2 makes it apparent that if the resolution of lethal events was better, the 26-my periodicity would not have been recorded for this run at all.

Another run, with $S = 0.5$, is shown in Fig. 3. Here, 19 lethal events have occurred, 12 of them being resolved as mass extinctions. Row C shows the best fit for a 26-my cycle which has an SDE of 6.15. In this case, therefore, background impact noise, and the fact that the 184- my and 210-my comet showers were not lethal, have combined to obscure the shower cycle entirely.

If the effect of the background flux is to totally obscure the 26-my cycle and to randomize extinction peaks produced, then only about 100 periodic runs would be expected. If no obscuration occurs then extinction data from every run would be expected to show a strong 26-my periodicity.

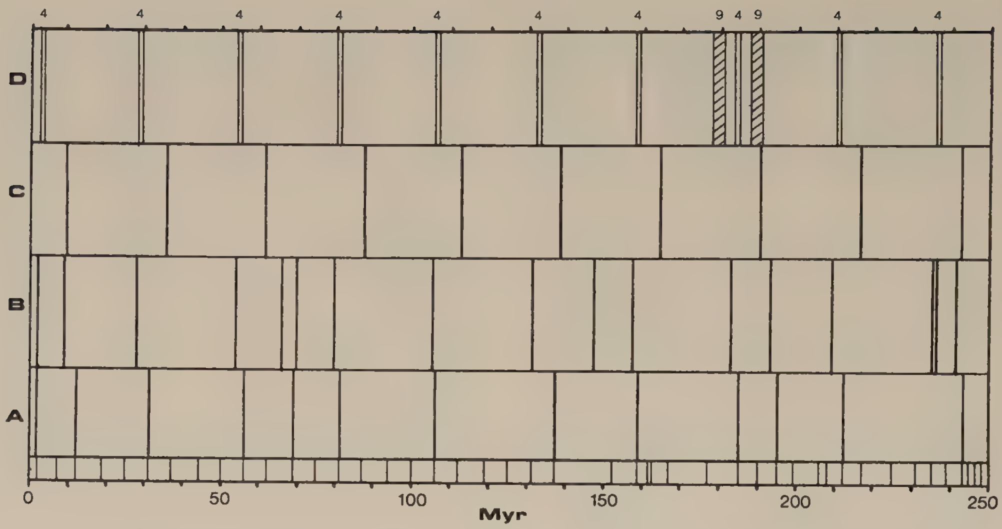

FIG. 2. Salient characteristics of a sample run where S = 0.5 my and a = 4000 AU. A 26-my comet shower cycle, starting at 2 my, is imposed. In row D, comet showers without diagonal hatching represent those belonging to the cycle. The best-fit impulse function in row C is that of a 26-my cycle.

The results in Tables IV and V show that the situation, as modeled, lies somewhere in between. Sufficient periodicities were found to demonstrate that obscuration of the shower cycle is not certain in every case. As expected, the S = 0.5 my runs, where the asteroidal background flux is set at a low value, allowed the detection of the largest number of cycles. Even so, only 56% of runs produced an extinction sequence with a significant periodicity betwen 24 and 33 my; 38% of runs showed the true 26-my cycle. For the higher background impact rate, 38% of runs produced a periodic extinction sequence, the 26-my cycle being detectable in only 19% of runs. It is clear that the background impact flux is not totally randomizing all extinction sequences. However, there is nonetheless a high probability (~60–80%) of random impacts introducing sufficient noise into a cyclic extinction sequence to either obscure it completely or to shift the cycle detected by −1 to +2 my. A similar series of runs, incorporating a 30-my comet shower cycle, gave nearly identical results, demonstrating that background impact noise is also relevant to the Rampino and Stothers (1984a, 1984b) hypothesis where comet showers are regulated by the Sun's motion through the galaxy.

The cycles investigated above were assumed to be perfectly periodic. However, Hut (1984) has shown that, for the past 250 my, the period of revolution of a putative Nemesis would have varied by ~10–20%

TABLE V

26-my COMET SHOWER CYCLE

Cycle	No. of periods	
	S = 0.5 my	S = 0.25 my
24	5	9
25	145	53
26	376	194
27	370	229
28	62	55
29	3	4
30	8	9
31	13	8
32	6	4
33	6	3

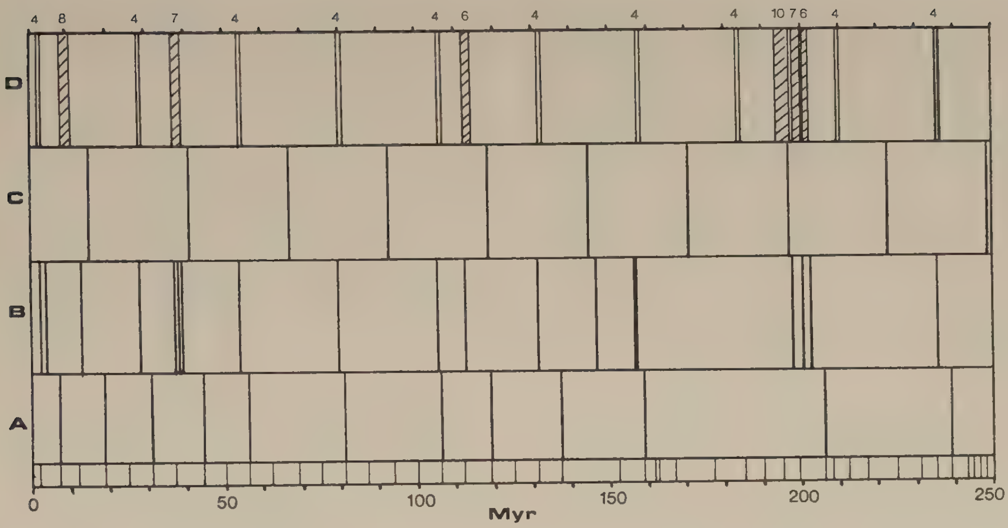

FIG. 3. Salient characteristics of a sample run where $S = 0.5$ my and $a = 4000$ AU. A 26-my comet shower cycle, starting at 2 my, is imposed. No cycle between 24 and 33 my fits the extinction data well; the best fit of a 26-my cycle is shown in row C.

because of perturbations by passing stars and the galactic tidal field. To investigate the consequences of this effect on the number of detected mass extinction cycles, two comet shower cycles were simulated: 26 and 30 my. The date of each impulse was randomized uniformly between ±2 and ±4 my, respectively, superimposed over an $S = 0.5$-my background impact flux. The results of 200 runs of the 26 ± 2 my set were that 45% of runs show a periodic extinction sequence and 28% of runs revealed the average 26-my cycle. Only 41% of the 200 runs of the 30 ± 4 my set showed a periodicity, the 30-my cycle being significant in 25% of runs. These results are possibly more realistic than those obtained from runs in which the imposed cycle was perfectly periodic, although they differ by only a factor of ~1.25.

Mean crater production rates for $D \geq 10$ km are $\sim 3.8 \times 10^{-14}$ km^{-2} year^{-1} for the $S = 0.5$ my run sets and $\sim 5 \times 10^{-14}$ km^{-2} year^{-1} for $S = 0.25$ my. These rates range from ~1.7 to 3.6 times more than the estimates of the terrestrial cratering rate already mentioned. The density of impact craters discovered on the Earth does not seem sufficient to account for the number of cometary impacts expected in this cyclic comet shower scenario.

5. CONCLUSIONS

All the proposed cyclical extinction mechanisms have their difficulties but none has yet been totally rejected (Smoluchowski *et al.* 1986). A model of background impact "noise" has been applied here to the class of cyclic impact/mass extinction hypotheses that require the existence of an inner comet cloud. The computation of simulated Earth impact chronologies identifies significant further constraints on such theories and renders them more improbable, but does not rule them out completely. Distortion of the extinction record by background impacts is a significant factor that has been hitherto largely disregarded (see the replies by Muller *et al.* (1984) and Whitmire and Jackson (1984b) to Weissman (1984)). The probability of a simulated 250-my impact history showing a mass extinction periodicity within a few million years of an imposed perfectly periodic 26-my comet shower cycle is ~40–60%. The occurrence of a periodicity of the same frequency as the shower cycle has a probability of only ~20–40%. Shower cycles of 30 my, as might be produced by the galactic plane triggering mechanism, undergo a similar distortion by the background flux. The number of detected periodicities is reduced by a factor of ~1.25 when irregularity in the periods of comet shower cycles is taken into account. The discrepancy between the estimated terrestrial cratering rate and the estimated production of impact craters by a comet shower cycle is a further problem.

The random impact model presented here is incompatible with the Clube/Napier hypothesis. In their model the inner comet cloud is deemed not to exist and thus intense, random, stellar-induced comet showers would not occur. Moreover, the flux of Earth-crossing asteroids is expected to exhibit a strong periodicity in step with the comet shower cycle. Thus, it would seem that an impact cycle generated by the Clube/Napier mechanism would be less vulnerable to random impact distortion, although by no means completely so.

Study of the Earth impact probabilities of Earth-crossing asteroids shows that it is likely that there have been several encounters of large bodies with the Earth over the last 250 my, with inevitable deleterious consequences to the biosphere. The case for impacts playing a part in the K-Pg mass extinction remains strong. A cyclic impact/extinction scenario, however, requires acceptance of a number of improbable processes and the current state of the debate renders it impossible to draw any definite conclusions. This has not prevented many scientists from expressing opinions. It is the opinion of the present author that, on the basis of the available evidence, mass extinctions are not linked by an externally driven cycle. Mass extinctions are difficult to identify and resolve, and correlation depends on which geological time scale is used. Dating of most of these events is still not precise enough to be confident that a periodicity actually exists. This is perhaps not surprising in view of the improbability of the various proposed cyclic extinction mechanisms.

ACKNOWLEDGMENTS

The author thanks S. V. M. Clube, J. A. Fernandez, J. Heisler, and R. L. S. Taylor for their criticisms, and W. J. and A. C. Fogg for their encouragement and acknowledge the invaluable assistance of the librarians of the Royal Astronomical Society.

REFERENCES

Alvarez, L. W., W. Alvarez, F. Asaro, and H. V. Michel 1980. Extraterrestrial cause for the Cretaceous–Tertiary extinction. *Science* **208,** 1095–1107.

Berger, W. H., J. A. Eddy, and E. M. Shoemaker 1985. In *The Evolution of Complex and Higher Organisms,* p. 111, NASA SP-478.

Clube, S. V. M., and W. M. Napier 1982. *The Cosmic Serpent.* Faber & Faber, London.

Clube, S. V. M., and W. M. Napier 1984a. Comet capture from molecular clouds: A dynamical constraint on star and planet formation. *Mon. Not. R. Astron. Soc.* **208,** 575–588.

Clube, S. V. M., and W. M. Napier 1984b. The microstructure of terrestrial catastrophism. *Mon. Not. R. Astron. Soc.* **211,** 953–968.

Clube, S. V. M., and W. M. Napier 1984c. Terrestrial catastrophism—Nemesis or Galaxy? *Nature* **311,** 635–636.

Clube, S. V. M., and W. M. Napier 1985. Comet formation in molecular clouds. *Icarus* **62,** 384–388.

Davies, J. K. 1986. Are the IRAS-detected Apollo asteroids extinct comets? *Mon. Not. R. Astron. Soc.* **221,** 19p–23p.

Davis, M., P. Hut, and R. A. Muller 1984. Extinction of species by periodic comet showers. *Nature* **308,** 715–717.

Fernandez, J. A., and W.-H. Ip 1987. Time-dependent injection of Oort cloud comets into Earth-crossing orbits. *Icarus* **71,** 46–56.

Ferrin, I. 1988. Has comet Halley retained its primordial angular momentum? *Nature* **333,** 834–835.

Grieve, R. A. F., and M. R. Dence 1979. The terrestrial cratering record. II. The crater production rate. *Icarus* **38,** 230–242.

Harland, W. B., A. V. Cox, P. G. Llewellyn, C. A. G. Pickton, A. G. Smith, and R. Walters 1982. *A Geologic Time Scale.* Cambridge Univ. Press, Cambridge.

Hartmann, W. K. 1977. Relative crater production rates on planets. *Icarus* **31,** 260–276.

Heisler, J., and S. Treamaine 1986. The influence of the Galactic tidal field on the Oort comet cloud. *Icarus* **65,** 13–26.

HEISLER, J., S. TREMAINE, AND C. ALCOCK 1987. The frequency and intensity of comet showers from the Oort cloud. *Icarus* **70,** 269–288.

HILLS, J. G. 1981. Comet showers and the steady-state infall of comets from the Oort cloud. *Astron. J.* **86,** 1730–1740.

HILLS, J. G. 1984. Dynamical constraints on the mass and perihelion distance of Nemesis and the stability of its orbit. *Nature* **311,** 636–638.

HUT, P. 1984. How stable is an astronomical clock that can trigger mass extinctions on Earth? *Nature* **311,** 638–641.

HUT, P., W. ALVAREZ, W. P. ELDER, T. HANSEN, E. G. KAUFFMAN, G. KELLER, E. M. SHOEMAKER, AND P. R. WEISSMAN 1987. Comet showers as a cause of mass extinctions. *Nature* **329,** 118–126.

MATESE, J. J., AND D. P. WHITMIRE 1986. Planet X and the origins of the shower and steady state flux of short-period comets. *Icarus* **65,** 37–50.

MENDIS, D. A. 1986. *Proc. 20th ESLAB Symp. Exploration Halley's Comet.* ESA SP-250.

MORRIS, D. E., AND R. A. MULLER 1986. Tidal gravitational forces: the infall of "new" comets and comet showers. *Icarus* **65,** 1–12.

MULLER, R. A., P. HUT, M. DAVIS, AND W. ALVAREZ 1984. Matters arising in *Science* **312,** 380–381.

NAPIER, W. M., AND S. V. M. CLUBE 1979. A theory of terrestrial catastrophism. *Nature* **282,** 455–459.

PATTERSON, C., AND A. B. SMITH 1987. Is the periodicity of extinctions a taxonomic artefact? *Nature* **330,** 348–351.

RAMPINO, M. R., AND R. B. STOTHERS 1984a. Terrestrial mass extinctions, cometary impacts and the Sun's motion perpendicular to the galactic plane. *Nature* **308,** 709–712.

RAMPINO, M. R., AND R. B. STOTHERS 1984b. Geological rhythms and cometary impacts. *Science* **226,** 1427–1431.

RAUP, D. M., AND J. J. SEPKOSKI 1984. Periodicity of extinctions in the geologic past. *Proc. Natl. Acad. Sci. USA* **81,** 801–805.

SHOEMAKER, E. M. 1977. Astronomically observable crater-forming projectiles. In *Impact and Explosion Cratering* (D. J. Roddy, *et al.*, Eds.), p. 617. Pergamon, Elmsford, NY.

SHOEMAKER, E. M., J. G. WILLIAMS, E. F. HELIN, AND R. F. WOLFE 1979. Earth crossing asteroids: Orbital classes, collision rates with Earth and origin. In *Asteroids* (T. Gehrels, Ed.) pp. 253–282. Univ. of Arizona Press, Tucson.

SILVER, L. T., AND P. H. SCHULTZ, Eds. 1982. Geological implications of impacts of large asteroids and comets on the Earth. *Geo. Soc. Amer. Spec. Pap.* **190.**

SMITH, A. B. 1988. Cyclic events and fossil faunas. Paper presented at University of London Department of Extra-mural Studies meeting. *Mass Extinctions and Cosmic Impacts.*

SMOLUCHOWSKI, R., J. N. BAHCALL, AND M. S. MATTHEWS, EDS. 1986. *The Galaxy and the Solar System.* Univ. of Arizona Press, Tucson.

STANLEY, S. M. 1987. *Extinction.* Sci. Amer. Books, New York.

STEEL, D. I., AND W. J. BAGGELEY 1985. Collisions in the Solar System. I. Impacts of the Apollo–Amor–Aten asteroids upon the terrestrial planets. *Mon. Not. R. Astron. Soc.* **212,** 817–836.

TALBOT, R. J., AND M. J. NEWMAN 1977. Encounters between stars and dense interstellar clouds. *Astrophys. J. Suppl.* **34,** 295–308.

THADDEUS, P., AND G. A. CHANAN 1985. Cometary impacts, molecular clouds, and the motion of the Sun perpendicular to the galactic plane. *Nature* **314,** 73–75.

TORBETT, M. V., AND R. SMOLUCHOWSKI 1984. Orbital stability of the unseen solar companion linked to periodic extinction events. *Nature* **311,** 641–642.

WEISSMAN, P. R. 1982. Terrestrial impact rates for long and short period comets. *Geo. Soc. Amer. Spec. Pap.* **190,** 15–24.

WEISSMAN, P. R. 1984. Cometary showers and unseen solar companions. *Science* **312,** 380.

WHITMIRE, D. P., AND A. A. JACKSON 1984a. Are periodic mass extinctions driven by a distant solar companion? *Nature* **308,** 713–715.

WHITMIRE, D. P., AND A. A. JACKSON 1984b. Matters arising. *Science* **312,** 381.

ICARUS **79**, 396–430 (1989)

Rotation of Halley's Comet

S. J. PEALE AND JACK J. LISSAUER[1],*

Department of Physics, University of California at Santa Barbara, Santa Barbara, California 93106; and
**Astronomy Program, Department of Earth and Space Sciences, State University of New York*
at Stony Brook, Stony Brook, New York 11794

Received July 5, 1988; revised September 12, 1988

The two distinct periodicities of 2.2 days and 7.4 days inferred from the coma structure and lightcurves of Halley's comet together with the irregular shape of its nucleus suggest that the nucleus is not in a state of principal axis rotation. We model this situation using numerical simulations supported by analytic calculations. It is easy to numerically generate lightcurves from modulated jets of material which exhibit both periodicities if we choose initial conditions for a representative nucleus such that the shorter period is the rotation period and the longer period is that of precession of the spin vector in the body frame of reference. The dominant spectral power in such curves most often corresponds to the 7.4 day period unless the amplitude of precession is very small. Although curves similar to those observed over short time intervals are obtained for precession about either of the axes with extreme moments of inertia, the observed marked seasonal changes in the lightcurve are only produced for precession about the axis of maximum moment of inertia. The generation and stability of a wobble-type rotation state is investigated by numerically solving Euler's equations for the reaction torque from a jet of ejected material. A nonprincipal axis rotation is easy to excite from an initial rotation about the axis of maximum moment of inertia (minimum energy) only if the nucleus is nearly axisymmetric. Except for almost perfect axial symmetry, excitation of a precession about the axis of minimum moment of inertia is always frustrated by an initial precession about the axis of maximum moment of inertia. In the more probable case of significant triaxiality, even a precession of the spin about the axis of maximum moment of inertia is difficult to excite from an initial minimum energy state, and it can change only slowly from the jet-induced torques. However, this slow change could suffice to generate a substantial amplitude wobble from the cumulative effects of many apparitions. The damping time for the wobble is $O(10^6$ to $10^8)$ years, which rules out a primordial origin of a wobble but allows a gradual excitation. Significant changes in the spin angular momentum can occur in a single apparition, but the stability of the amplitude of precession about the axis of maximum moment of inertia means that a rotation state which is relatively stable over many apparitions is not unreasonable. The improbability of exciting a spin precession about the axis of minimum moment of inertia, the relative instability of this state to the jet-induced torques, and the smaller probability of observing significant seasonal changes in the lightcurve in this state all favor the model in which Halley's nucleus precesses about the axis of maximum moment of inertia. © 1989 Academic Press, Inc.

I. INTRODUCTION

Comet Halley has been the subject of intensive study for the several years spanning its perihelion passage on February 9.46, 1986. This study was highlighted by the close spacecraft encounters shortly after perihelion passage which revealed the shape and size of the nucleus (Keller *et al.* 1987, Figure 1), allowed estimates of the mass ejection rate (Krankowsky *et al.* 1986, McDonnell *et al.* 1986, Sagdeev *et al.* 1988,

---

[1] Alfred P. Sloan Research Fellow.

0019-1035/89 $3.00
Copyright © 1989 by Academic Press, Inc.
All rights of reproduction in any form reserved.

Hanner *et al.* 1987), constrained the current state of rotation (Keller *et al.* 1987, Smith *et al.* 1987), and showed that mass was ejected primarily in the form of very localized jets (Keller *et al.* 1987). Quasiperiodic variations in the apparent brightness and the difference in the brightness between the pre- and postperihelion periods are probably related to its state of rotation (Weissman 1987). As other physical processes also influence these variations, it is important to understand the rotation state and its evolution in order to isolate for study the many processes affecting comet activity.

A rotation period near 2.2 days has been obtained from the analysis of the expansion velocities and curvatures of jet features in the coma during the active phases of the comet in 1985 and 1986 (Larson *et al.* 1987). A similar analysis of photographs of Halley's coma taken during the 1910 apparition yielded a similar rotation period (Larson and Sekanina 1984, 1985, Sekanina and Larson 1984, 1986). This period of rotation has also been indicated by photometric studies (Liebowitz and Brosch 1986), the breathing of the hydrogen coma (Kaneda *et al.* 1986), the formation of cyanogen shells (Schlosser *et al.* 1986), and by an unpublished lightcurve obtained by M. Belton (private communication, 1987). The images of the nucleus made by the Vega and Giotto spacecraft are consistent with the 2.2-day rotation period (Keller *et al.* 1987).

Yet a period near 7.4 days was observed in the production of the C_2 radical in March and April of 1986 (Millis and Schleicher 1986). Narrowband photometric data taken by Williams *et al.* (1987) were entirely consistent with this period, and observations at zero phase angle in 1985 showed a similar period in the variations of molecular emission bands (Meech and Jewitt 1987). A 7.3-day period in the preperihelion lightcurve was found in a reanalysis of extensive photometric data by Festou *et al.* (1987).

The strong evidence for both periodicities led researchers to suggest that rotation of the nucleus about a nonprincipal axis could lead to the observed variations with two dominant periods—the short period being the average value of the rotation period and the long period being that of the precession of the spin vector in a coordinate system fixed in the nucleus (Lissauer 1986, Kerr 1986). Wilhelm *et al.* (1986) independently suggested that nutation of the nucleus by 5° to 10° about the short axis would improve the fit of rotation models to the images of the Giotto and Vega spacecraft. Several models based on this idea have been proposed. Sekanina (1987) and Festou *et al.* 1987 both consider an axisymmetric body where the spin, having nearly a 2.2-day period, is precessing around the symmetry axis (axis of minimum moment of inertia) but with periods near 7.4 and 14.8 days, respectively. Wilhelm (1987) also assumes a 14.8-day precession period, but his model nucleus is triaxial and precession is about the axis of maximum moment of inertia. For both the models with 14.8-day precession periods, the instantaneous axis of rotation is always nearly perpendicular to the long axis of the potato-shaped body, so the periodic illumination of a localized source with a 2.2-day period is modulated with a period of half the precession period. Julian (1987) considers a triaxial body with precession about either of the principal axes corresponding to extreme values of the moments of inertia. The spin period in Julian's model is 2.08 days whereas the precession period is 7.4 days in the body frame of reference. Julian favors the model where the precession is about the axis of maximum moment of inertia as being more compatible with the rejection of the 7.4-day rotation period by Smith *et al.* (1987). However, the correctness of the constraint on the rotation imposed by Smith *et al.* has been questioned (Sekanina 1989), so neither mode of precession has been necessarily ruled out by observation.

The fact that the material emitted from the comet comes from localized jets means that time-varying torques are applied to the nucleus during the active periods. These

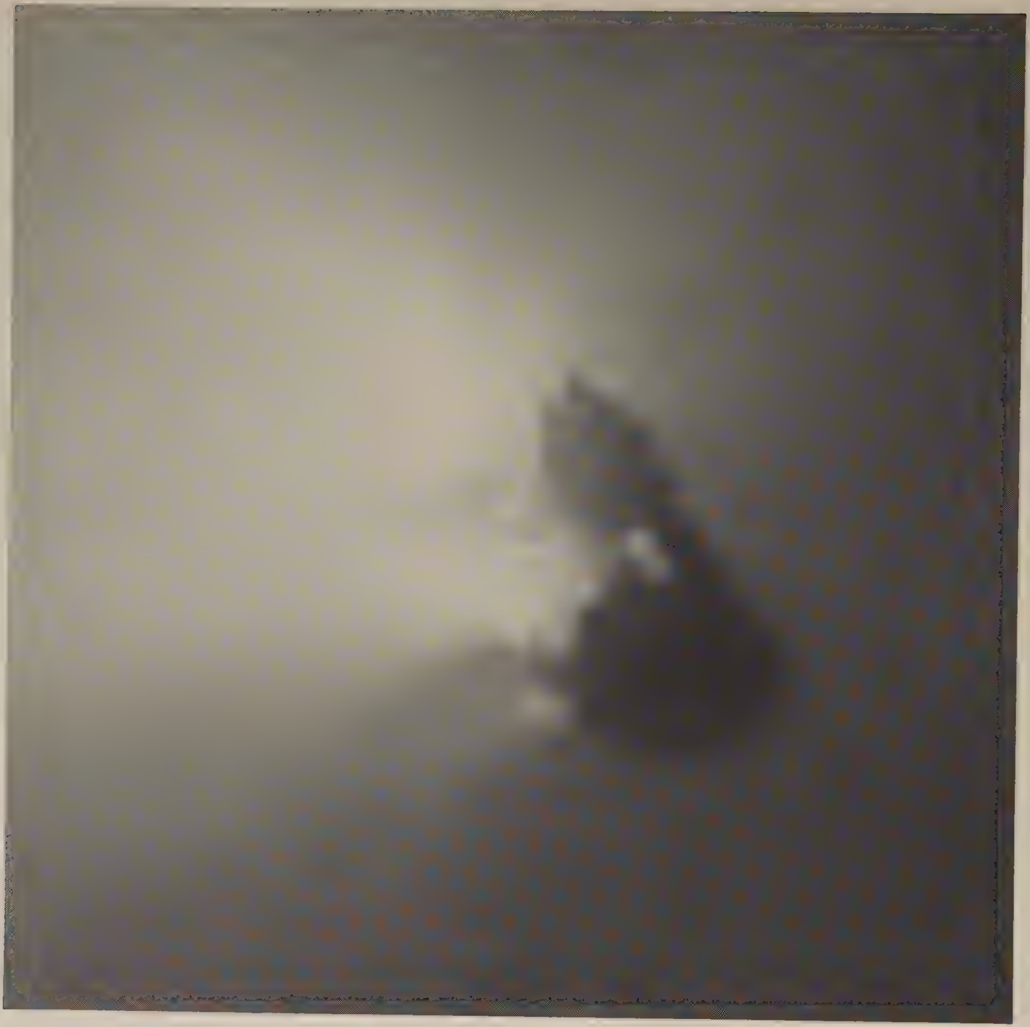

FIG. 1. The nucleus of Comet Halley seen in a composite of images (3416, 3457, 3475, 3480, 3491, 3496, 3500) obtained by the Halley Multicolor Camera aboard the Giotto spacecraft. Note the nature of the jet-like sources of ejected material. (This image has been kindly provided by H. U. Keller, 1986, Max Planck Institut für Aeronomie, Lindau/Harz, FRG.)

torques can induce the inferred nonprincipal axis rotation and alter the angular momentum of the nucleus. Wilhelm (1987) has considered the effect of these torques in changing an initial state of rotation about the axis of maximum moment of inertia. However, the emission jets are not fixed in position on the nucleus in Wilhelm's model but remain nearly subsolar as the nucleus rotates. The observations of the nucleus favor a model where the jets are fixed in position with their activity modulated nearly in phase with the local solar illumination. We investigate here the consequences of this type of jet on the evolution of the rotation state of Halley's nucleus (see Fig. 1).

The rather pronounced topography of the nucleus implies considerable rigidity (Keller *et al.* 1987), so the equations governing the motion are the inhomogeneous Euler equations for rigid body motion,

$$\begin{aligned} A\dot{\omega}_x - (B - C)\omega_y\omega_z &= N_x, \\ B\dot{\omega}_y - (C - A)\omega_z\omega_x &= N_y, \qquad (1) \\ C\dot{\omega}_z - (A - B)\omega_x\omega_y &= N_z, \end{aligned}$$

where $A \leq B \leq C$ are the moments of inertia about the principal x, y, z axes of the nucleus, respectively, ω_x, ω_y, ω_z are the components of the angular velocity along the principal axes, and N_x, N_y, N_z are the components of the torque about these axes. It is possible to obtain a formal solution of Eqs. (1) if the components of the torque are known as a function of time only. However, a localized jet whose activity is controlled by the amount of illumination by the Sun is also coordinate dependent, so the only viable means of solving these equations is numerical. The formal solution of Eqs. (1) for time-dependent torques in the case of axial symmetry ($B = C$) is given in Appendix A, along with a particular solution used to test the numerical code.

The model for the numerical integrations (developed in Section II) is accurate up to 10 significant figures for integrations over a single apparition. A jet can be located arbitrarily on the ellipsoid representing the nucleus, and it can be inclined at an arbitrary angle with respect to the local normal to the ellipsoid surface. This inclination of the jet to the ellipsoid surface is necessary, since local areas on the real nucleus are inclined by as much as several tens of degrees relative to the surface of a representative smooth ellipsoid. The jet activity is determined by the zenith angle of the Sun (relative to the local inclined surface) and the heliocentric distance of the comet nucleus. The magnitude of the reaction force and consequent torque is constrained by the observed change in the comet orbital period from nongravitational forces. In Section III the observational consequences of torque-free, wobbling motion of Halley's nucleus are determined. Lightcurves both for the active period when the comet is close to the Sun and for the distant bare nucleus are generated. Here we follow Julian (1987) except we use an initial 2.2-day rotation period and initial conditions giving a 7.4-day period of precession about either of the axes corresponding to maximum and minimum moments of inertia. Two jets of unequal magnitudes on opposite sides of the nucleus are used to generate the lightcurves near perihelion. It is easy to generate curves with a 7.4-day modulation which almost masks the 2.2-day variations in all of the models. The high frequency modulations are smoothed by the accumulation of visible material except in the case where observations are assumed to be made from a narrow aperature telescope. However, the addition of more than two sources distributed around the nucleus would smooth the 2.2-day variations even for narrow aperture observations. It is shown that the lightcurves can vary significantly with comet season. In Section IV we demonstrate that the torque resulting from a realistic jet can cause significant changes in the rotation state during a single apparition. Both axisymmetric and triaxial models are investigated, where wobble motion is easy to excite for the former but much more difficult for the latter. However, the long damping time of any wobble motion means that the perturbations of many apparitions are cumulative, and there should be no difficulty in generating the wobble motion inferred by the observed lightcurves, even for a triaxial body. In addition, we show that even a minor deviation from axial symmetry makes excitation of a precession about the axis of minimum moment of inertia unlikely and that precession about the axis of maximum moment of inertia is much more stable against the perturbations than precession about the axis of minimum moment. A discussion of these results follows in Section V.

II. MODEL FOR NUMERICAL CALCULATIONS

The numerical solution of the inhomogeneous Euler's equations is computed by using an integrator based on the extrapolation method of Burlisch and Stoer (1966). The algorithm is that used in Wisdom *et al.* (1984) to follow the rotation of Saturn's satellite Hyperion with torques due to the asymmetry of the body in Saturn's gravitational field. For the comet nucleus, torques due to the gravitational field of the Sun are negligibly small, and they are replaced by torques due to the reaction forces of localized jets of volatiles and dust. Euler's equations are written in terms of angle variables (ϕ, θ, ψ) orienting the principal body axes of the nucleus with respect to an inertial frame whose X axis is parallel to the line of apsides with X increasing toward the perihelion of the orbit and whose Z axis is parallel to the orbital angular momentum. Two sets of angle variables are required to avoid the coordinate singularity in the equations of variation of these angles deduced from Euler's equations. The set of ordinary Euler angles (e.g., Goldstein 1980, p. 146) is supplemented with a second set in which the first two rotations of the body axes relative to the inertial axes are the same as those for the Euler angles, but the third rotation is about the last position of the y axis instead of about the z axis. Calculations are conducted in the second set of variables until the trajectory approaches the singularity ($\cos\theta = 0$) in that set. The code then transforms the calculations to the first set of variables (the ordinary Euler angles) and continues until the end of the time step is reached, whereupon the code transforms back to the second set to continue. Nearness to a singularity is tested at every step of the calculation ($\cos\theta$ or $\sin\theta < 0.2$, respectively, in each set), and the scheme successfully maintains high accuracy as evidenced by the tests described below. The equations which were integrated are given in Appendix B.

The torque on the nucleus due to a localized jet is of the form

$$\mathbf{N} = -\mathbf{R} \times \mathbf{v}\frac{dm}{dt}, \tag{2}$$

where $\mathbf{R}$ is the radius vector from the center of mass of the nucleus to the surface location of the jet, $\mathbf{v}$ is the velocity vector of the jet material assumed to be coming from a point, and dm/dt is the mass flow rate. The jet velocity $\mathbf{v}$ can be oriented at any angle relative to the local surface of the ellipsoid representing the nucleus to account for the actual rough topography of the real nucleus.

Estimates of the total mass production rate of 2×10^7 g/sec (Sagdeev *et al.* 1988, Krankowski *et al.* 1986, McDonnell *et al.* 1986) and a velocity of the expanding material of 0.9 km/sec (Krankowski *et al.* 1986) were made at the time of the spacecraft flybys of the nucleus. Sagdeev *et al.* (1988) estimate v from the evaporation of ice into a vacuum, where the temperature of the surface is determined by matching the evaporation rate, assumed uniform over the sunlit cross section, to the observed production rate of water molecules. Velocities of 0.3 to 0.4 km/sec are obtained. Dust velocities of about 0.4 km/sec were determined by Keller and Thomas (1988). As we are concerned with the back reaction of the nucleus to the emitted jet, the relevant velocity is that with which the gas and dust leave the nucleus *plus* that gained close enough to the jet source that the nucleus is subjected to a reaction torque via gas pressure. We therefore choose a value of v = 0.5 km/sec. But the value of v is not critical for our purposes here as only the product $v(dm/dt)$ appears in our calculations.

The actual value of $\mathbf{v}dm/dt$ appropriate to a single jet is highly uncertain. We choose to relate the reaction force of a single jet to the nongravitational forces leading to the observed increase in Halley's orbital period of 4 days per apparition (Marsden *et al.* 1973). For the instantaneous value of dm/dt, we write

$$\begin{aligned}\frac{dm}{dt} &= \left(\frac{dm}{dt}\right)_{\max} g_p(r)\cos\theta_\odot, & \theta_\odot \leq 90^\circ, \\ &= 0, & \theta_\odot > 90^\circ,\end{aligned} \tag{3}$$

where $\theta_\odot$ is the solar zenith angle relative to the local surface element perpendicular to $\mathbf{v}$, and $(dm/dt)_{\max}$ is the value dm/dt a given jet source would have if and when that source were to rotate directly under the Sun at perihelion. A measure of the depen-

TABLE I

PARAMETERS FOR HALLEY'S COMET

Perihelion passage:	T = Feb. 9.45894, 1986
Perihelion distance:	$r_p = 0.5871029$ AU
Eccentricity:	$e = 0.9672755$
Period:	$P = 75.99094$ years
Semimajor axis:	$a = 17.94077$ AU
	$A_1 = 0.0717$ (AU)/(10^4 days)^2
	$A_2 = 0.0155$ (AU)/(10^4 days)^2

dence of the evaporation rate of water ice on heliocentric distance r is given by (Delsemme 1982, Marsden *et al.* 1973)

$$g(r) = \alpha \left(\frac{r}{r_0}\right)^{-\beta} \left[1 + \left(\frac{r}{r_0}\right)^{\gamma}\right]^{-\delta}, \qquad (4)$$

where $r_0 = 2.808$ AU, $\beta = 2.15$, $\gamma = 5.093$, and $\delta = 4.6142$. We use two normalizations of $g(r)$; $g_p(r_p) = 1$, where r_p is the perihelion distance of Halley's orbit ($\alpha = 0.0347$) and $g_1(1 \text{ AU}) = 1$ ($\alpha = 0.1113$).

The nongravitational acceleration of the nucleus (averaged over a nucleus rotation period) is separated into a radial component $\mathbf{F}_1$ and a component $\mathbf{F}_2$ in the direction of $\mathbf{r} \times \mathbf{h}$, where $\mathbf{h}$ is the orbital angular momentum. In determining the effect of the outgassing on the orbit, it is assumed that $F_i = A_i g_1(r)$, where A_i are constants (Marsden *et al.* 1973). The values of A_i for Halley's comet are given in Table I, along with the most recent determination of the orbital parameters (D. K. Yeomans, private communication, 1987), which are slight updates to those given in Yoemans (1986).

The values of A_1 and A_2 given in Table I are deduced for the "standard model" where it is assumed that the mass production rate from the nucleus is symmetric about the perihelion. For this model, A_1 does not contribute to the change in orbital period. The actual lightcurve for Halley's comet is very asymmetric, being brighter after the perihelion passage than before (Green and Morris 1987). If, for example, the nongravitational force is assumed to peak 20° past perihelion, $A_1 = 0.0452$ and $A_2 = 0.003$ (in the units of Table I) become the values leading to the least residuals (D. K. Yeomans, private communication, 1988). We shall use the values of A_1 and A_2 from Table I in constraining the magnitude of dm/dt, but it must be kept in mind that the error in the constraint may exceed a factor of 2. We shall compensate for this uncertainty by restricting the value of dm/dt for a single jet to be considerably less than that value which would yield the 4-day increment in the orbital period per apparition.

The tangential acceleration due to the outgassing of the nucleus is presumed to result from a phase lag in the response of the surface to the solar heating as a prograde rotation carries a jet, which is declining in activity, across the terminator opposite the direction of orbital motion. The resultant acceleration (essentially A_1 from Table I) can then be thought of as a measure of the strength of the reaction normal to the comet surface. The acceleration is given by $F_{1p} = A_1 g_1(r_p) = 4.62 \times 10^{-6}$ cm/sec^2. The average value of $v(dm/dt) \cos \theta_\odot$ over a rotation period of the nucleus is the maximum value divided by π if the spin axis is normal to the orbit plane and the jet is normal to the surface at a point on the equator. Then at perihelion

$$\frac{1}{\pi m}\left[v \frac{dm}{dt}\right]_{\max} = F_{1p} = 4.62 \times 10^{-6} \text{ cm/sec}^2, \qquad (5)$$

where the subscript max has the same meaning as in Eq. (3).

If the nucleus is modeled as an axisymmetric ellipsoid with semiaxes of 8, 4, and 4 km, $m = 5.4 \times 10^{17}\rho$ g, where ρ is the density in g/cm^3. With $v = 0.5$ km/sec, $(dm/dt)_{\max} = 1.57 \times 10^8\rho$ g/sec is an estimate of the coefficient on the right-hand side of Eq. (3) if a single equatorial jet (or the sum of the coefficients for several equatorial jets) were to produce the observed nongravitational perturbations of Halley's orbit. (A smaller value of v would require a correspondingly larger value of $(dm/dt)_{\max}$ to yield the given acceleration.) This compares with the value of 2×10^7 g/sec estimated at the time of encounter (Wilhelm 1987). Constraining the jet reaction force by the nongravitational acceleration causing the change in the orbital period means that the actual value of the mass used in Eq. (5) does not affect our conclusions concerning the jet-induced changes in the rotation state. The acceleration of the nucleus is inversely proportional to the mass and the angular acceleration about the center of mass is inversely proportional to the mass through the moment of inertia. Estimates of the density of the nucleus less than 1 (Rickman 1986) would lead to a reduced mass flux for a given acceleration and also a reduced mass flux for a given change in the rotation state. As the total mass lost from Halley during a single apparition is less than $10^{-3}\rho^{-1}$ times its nominal mass, the high ejection velocity means that the reaction torques are much more important in changing the rotation state than is the change in the inertia tensor from the mass loss. Changes in the principal moments are therefore neglected.

For the integrations, all lengths are normalized by the 8 km length of the long semiaxis of the equivalent ellipsoid, a dimensionless time parameter increases by 2π per day, which means that the magnitude of a dimensionless angular frequency is the inverse of the period in days. Mass increments are normalized by the mass of the nucleus. A velocity of 0.5 km/sec becomes 860 in these units and $[(dm/dt)/m]_{\max} = 2.9 \times 10^{-10}$ sec^{-1} from Eq. (5) becomes 4.0×10^{-6}. The orbital motion is that of an unperturbed ellipse with parameters of Table I, and an apparition is followed for 344 days centered at perihelion ($-128° \leq f \leq 128°$, where f is the true anomaly).

A number of checks were carried out to verify the accuracy of the code. The numerical calculation for force-free motion used in the determination of the lightcurves over a complete apparition conserved angular momentum and energy of rotation to at least 10 significant figures for all sets of initial conditions. The numerical solution to Euler's equations for a symmetric rotator with $A < B = C$ subjected to the integrable time-dependent torque given in Appendix A agrees with the analytic solution to nine significant figures after 344 days. Finally the algorithm for calculating the reaction torque from the jet was checked by starting the nucleus rotating about its axis of maximum moment with zero obliquity and locating a jet at the end of the long axis with orientation perpendicular to the spin angular momentum so as to yield a maximum retarding torque. The total change in angular momentum calculated numerically over the 344-day time span was compared with an analytic approximation to this change in which the torque was averaged over a rotation period with r fixed and integrated over the apparition modulated by $g(r)$. The analytic approximation differed from the numerical value only in the third significant figure. We are therefore confident that the code is integrating the inhomogeneous Euler equations correctly, and that no numerical artifacts are being introduced.

III. NUMERICAL LIGHTCURVES FOR TORQUE-FREE MOTION

In this section, lightcurves are constructed for a wobbling nucleus undergoing force-free rotation for two situations. Either the light is entirely due to scattering from the dispersed material ejected from the nucleus, or the light is scattered only by the nucleus. In all of our examples we choose an initial rotational angular velocity corresponding to a 2.2-day period and initial conditions yielding a 7.4-day precession period of the angular velocity in the body frame of reference. Beyond these periodicities, we make no attempt to match in detail any lightcurves constructed from observation. We shall use the term "precession" to refer to the precession of the spin vector in the body frame of reference, whereas "rotation" will refer to the instantaneous angular velocity. These definitions are essentially reversed in the discussion by Sekanina (1987) and Festou *et al.* (1987).

For a rotating, torque-free rigid body with three distinct principal moments of inertia, the angular velocity vector will precess in the body frame of reference about either the axis of maximum moment of inertia or the axis of minimum moment of inertia (z and x axes) unless it coincides with one of these axes. (No closed trajectories of the spin around the axis of intermediate moment of inertia (y axis) are possible.) The angular velocity and the orientation of the body can thereby go through large changes relative to the fixed angular momentum. The seemingly erratic motion of the body when viewed from inertial space is often called wobble or nutation. The period of precession of the spin vector ω about the x or z axis is given by (e.g., Julian 1987)

$$T_1 = \frac{4K(\varepsilon^{-1})}{\sqrt{\gamma\kappa_1}}, \qquad (6)$$

$$T_3 = \frac{4K(\varepsilon)}{\sqrt{\alpha\kappa_3}},$$

where $K(\varepsilon)$ is a complete elliptic integral of the first kind, $\varepsilon \equiv \gamma\kappa_1/\alpha\kappa_2$, $\kappa_1 \equiv \beta\omega_x^2 + \alpha\omega_y^2$, and $\kappa_3 \equiv \gamma\omega_y^2 + \beta\omega_z^2$ are constants of force-free motion, with $\alpha \equiv (C - B)/A$, $\beta \equiv (C - A)/B$, and $\gamma \equiv (B - A)/C$ where $A < B < C$ are the principal moments of inertia. Note that one of the periods becomes infinite if the nucleus is axisymmetric ($A = B$ or $B = C$), and that there can be no precession for a spherically symmetric body. Although we shall choose initial conditions such that $T_{1,3} = 7.4$ days, the actual periods observed in the lightcurve will be slightly different from these values because the precession is not uniform, different projections of ω are seen in inertial space, and the orbital motion introduces synodic modulations of the illumination of a point on the nucleus. The choice of initial conditions is thus reduced to finding the position of the spin vector in the yz plane which leads to the correct precession period from Eqs. (6). Following Julian (1987), we define $\theta_1 = \tan^{-1}(\omega_z/\omega_x)$ when $\omega_y = 0$ for precession about the x axis, and $\theta_3 = \tan^{-1}(\omega_x/\omega_z)$ when $\omega_y = 0$ for precession about the z axis. Then, for example,

$$T_3 = \frac{4K((\gamma/\alpha)\tan^2\theta_3)}{\sqrt{\alpha\beta}\,\omega\cos\theta_3} \qquad (7)$$

and a similar expression for T_1 can be solved for θ_i to yield $T_i = 7.4$ days for given α, β, γ, ω.

Spacecraft images revealed a potato-shaped nucleus with semiaxes of approximately 8 × 4 × 3.75 km (Smith *et al.* 1987) or 8 × 4.2 × 4.1 km (Keller *et al.* 1987). Here we shall choose dimensions of $8 \times 4 \times 3.4 = a \times b \times c$ km as the semiaxes of the equivalent triaxial ellipsoid, where the value of c was reduced from the published estimate to allow the 7.4-day period of precession of the spin about the axis of maximum moment of inertia. If the rotation period is slightly greater than 2.2 days or the short axis is increased by as little as 0.1 km, the period of precession about the axis of maximum moment of inertia must exceed 7.4 days. (We give arguments below showing why a 14.8-day precession period is not likely.) Some researchers may object to our shortening the value of c so much below what was estimated from observations. But one must remember that a, b, c are axes for a *dynamically* equivalent ellipsoid. The nucleus is not an ellipsoid, nor is it necessarily homogeneous in density, so estimates of dynamic axes from geometric shape can easily accommodate our values for a, b, c within the uncertainties. In any case, we regard the determination of the 2.2- and 7.4-day periods as being much more secure than any assignment of equivalent ellipsoid axis lengths which precludes a 7.4-day precession. With the normalizations discussed in the last section, a, b, c are respectively 1, 0.5, 0.425 and the principal moments of inertia for the ellipsoid are $A = (b^2 + c^2)/5 = 0.086125$, $B = (c^2 + a^2)/5 = 0.236125$, $C = (a^2 + b^2)/5 = 0.25$, and α, β, γ = 0.16110, 0.69402, 0.60000. With the nondimensional initial value of $\omega = 1/2.2 = 0.4545$, we find

$$\begin{aligned} \theta_1 &= 55.8^\circ, \\ \theta_3 &= 15.4^\circ. \end{aligned} \tag{8}$$

Wilhelm (1987) gives a direction of the spin axis near right ascension 50° and declination -45°, which corresponds to an obliquity of about 25° (Euler angle $\theta = 25^\circ$) and a projection of the axis on the orbit plane separated from the Sun–perihelion direction by -112.5°. We choose initial values of the angles orienting the nucleus in the inertial frame as $\phi = -22.5^\circ$, $\theta = 20^\circ$, and $\psi = 0^\circ$, where an initial obliquity of 20° more closely aligns the spin angular momentum $\mathbf{L}$ with Wilhelm's pole position ($\mathbf{L}$ is initially separated from $\boldsymbol{\omega}$ by 5.42°). (See Appendix B for a precise definition of ϕ, θ, ψ.) These initial conditions cause the vernal equinox to occur when Halley is near the perihelion of its orbit.

With these initial conditions we consider first the light scattered from ejected gas and dust when Halley is near the Sun. For the purpose of generating a lightcurve, we rather arbitrarily locate two jets on opposite sides of the ellipsoid with normalized body coordinates $x, y, z = 0, -0.4248, 0.2242$, and $0, 0.4248, -0.2242$, respectively. The instantaneous mass production rate from each jet is given by Eq. (3) with the jet at the first location having twice the intrinsic strength of the other. Normalization of the jet strengths is immaterial for simulations presented in this section as we neglect reaction torques and are only concerned with the relative brightness of the comet. The motion is made force free by setting $\mathbf{v} = 0$ in Eq. (2). The jets quasiperiodically produce material as they rotate in and out of sunlight, but at any instant light is being scattered to the observer from gas and dust emitted over some period into the past. The length of time a given molecule or dust particle is contributing scattered light to a detector depends on the rate of dispersion away from the nucleus, the lifetime of the molecule against photodissociation, and the field of the telescope being used. A data file of the instantaneous mass production rate is produced by integrating the equations of motion given in Appendix B for the 344-day period spanning the perihelion passage. A given point on a lightcurve is generated by integrating the mass production rate over a given time interval T, with dm/dt being multiplied by a linear weighting function which is 0 at the beginning of the interval and 1 at the end. This window is then marched down the emission data file one point at a time and the integral recorded as the amount of material seen. Thus the scattered light seen at any time is proportional to the amount of material emitted over the preceding interval T as weighted by the linear function. This procedure simulates the $V(1, 0)$ magnitude rather than the apparent magnitude. The weighting function ensures that all of the material just emitted is seen, but no material is seen which was emitted more than interval T ago. The value of dm/dt was recorded every 0.1 days, and $T = 5$ days was chosen for most of the curves generated here.

This rather large value of T may be appropriate for light from the entire coma region. This would include dust scattering as well as resonance fluorescence scattering by the molecules. The linear weighting function is not appropriate for a lightcurve generated from a single molecular band of, say, the molecule C_2. This is the molecule observed by Millis and Schleicher (1986) from which a 7.4-day periodicity was deduced, so it is appropriate that we consider its characteristics. The molecule C_2 is apparently derived from an unknown parent by chemical reactions within the coma (A'Hearn 1982), although its distribution is commonly represented by assigning empirically determined lifetimes (time constants for exponential decay of the species abundance) used in the standard Haser (1957) model for photodissociation of parent and daughter. The lifetimes are generally expressed in terms of scale lengths by assuming a uniform expansion of the gas cloud at

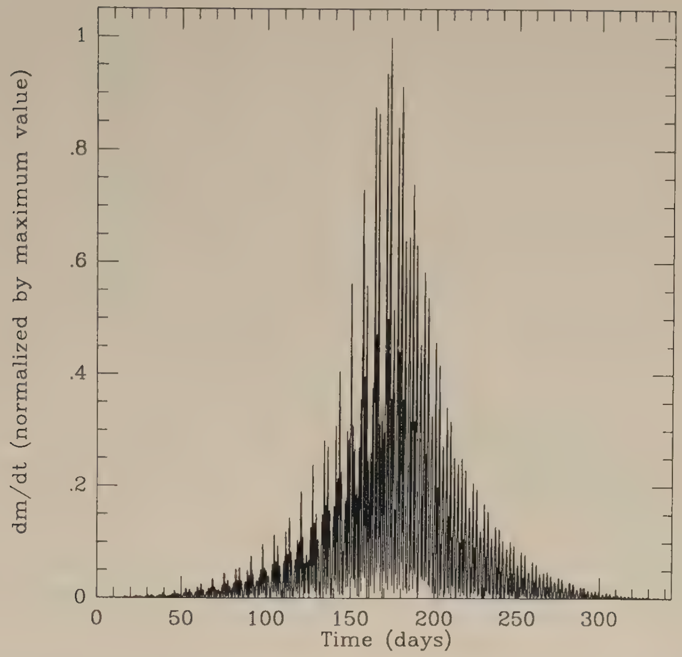

FIG. 2. Mass ejection rate dm/dt for the portion of Halley's orbit within 2.8 AU. The nucleus rotates with a period near 2.2 days while the spin axis precesses about the axis of maximum moment of inertia with a period of 7.4 days. The spin angular momentum has an obliquity to the orbital angular momentum near 20° and the vernal equinox is near the perihelion; initial values of Euler angles are ϕ, θ, ψ = −22.5°, 20°, 0°. The axis ratios for the nucleus are $a:b:c = 1.0:0.5:0.425$, and the motion is force free. The jet sources are located at $x, y, z = 0, -0.4248, 0.2242$, and $0, 0.4248, -0.2242$, where the jet located at positive z is twice the strength of the other jet.

1 km/sec. When photodissociation dominates the creation and loss of a particular molecule, the scale lengths vary as r^2. However, the empirically derived scale length of the "parent" of C_2 varies as r. The scale lengths commonly assigned to C_2 at r = 1 AU are 1.7×10^4 km for the parent and 1.1×10^5 km for C_2 (A'Hearn 1982). These lengths correspond to lifetimes of 0.20 and 1.27 days, respectively. The Millis and Schleicher (1986) lightcurves were obtained when Halley was approximately 1 AU from the Sun, so these two lifetimes are appropriate for the appropriate weighting functions. We show one example of a lightcurve generated with a weighting function involving the exponential decay of parent and daughter and a second example containing an additional factor accounting for the narrow aperture of 39 arcsec radius. The first example would correspond to a field of view including the entire coma, whereas the second corresponds to the actual field used by Millis and Schleicher (1986). These lightcurves are compared with that for the linear weighting function generated from the same data set for dm/dt.

The first case we consider is precession of the spin about the axis of maximum moment of inertia (z axis). While ω_x, ω_y, and ω_z exhibit smoothly periodic variations with the 7.4-day period and the angular momentum **L** remains fixed in the inertial space, material is ejected by the two jets as shown in Fig. 2 for 344 days centered on perihelion passage. The production is normalized by the maximum value near perihelion (passed on day 172). The high frequency modulation of dm/dt due to the rotation is further modulated by the precession. Precessional modulation occurs as the body's orientation relative to inertial space changes with respect to the fixed angular momentum. For precession of the spin about the z axis considered here, $\boldsymbol{\omega}$ is initially displaced from the unit vector $\hat{\mathbf{e}}_z$ (parallel to the body z axis) by 15.4° and from $\mathbf{L}$ by 5.4°, and the three vectors are instantaneously coplanar. A quarter of a precession period later, when $\omega_x = 0$ and ω_y has its maximum value, $\boldsymbol{\omega}$ is separated from $\hat{\mathbf{e}}_z$ by almost 32°, but only a little over 0.5° from $\mathbf{L}$. As similar separations will occur a half precession period later when $\boldsymbol{\omega}$ is on the opposite side of $\hat{\mathbf{e}}_z$, the nucleus will have changed its orientation relative to the fixed $\mathbf{L}$ in inertial space by about 60°. A jet source can have this much variation in the maximum elevation angle of the Sun with the consequent variation in dm/dt.

Figure 3 shows the lightcurve constructed from the data in Fig. 2 for the linear weighting function with the interval $T = 5$ days, where the values are normalized by the maximum near perihelion. The preperihelion curve is clearly dominated by the long period variation, but note the change in the lightcurve with season. After perihelion, the short period variations dominate. The Fourier transform of the entire lightcurve is shown in Fig. 4, where the dominant peak corresponds to a period of 7.45 days and the next peak corresponds to a period of 2.27 days. The 2.27-day peak dominates the first harmonic because the jets on opposite sides of the ellipsoid are of unequal magnitude. The preperihelion curve is expanded in Fig. 5a to show how the detailed shape varies from period to period. This variation is not surprising, since a return of the spin vector to the same point relative to the body axes does not generally correspond to its having the same orientation in inertial space nor to the body having the same phase of rotation. A given source does not generally receive its maximum illumination at the same phase of each precession period. Still, near commensurabili-

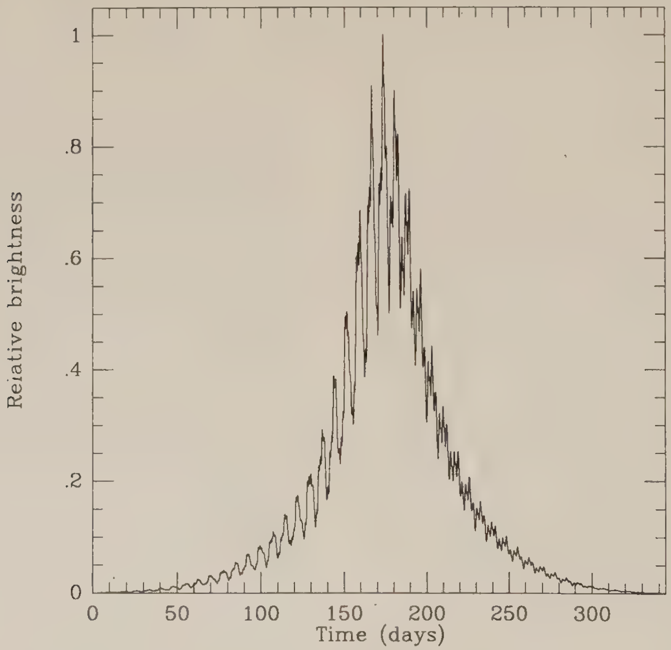

FIG. 3. The lightcurve generated from the mass production rate shown in Fig. 2. The gas and dust in the coma were assumed to dissipate at a constant rate over a 5-day decay period (i.e., the linear weighting function was used).

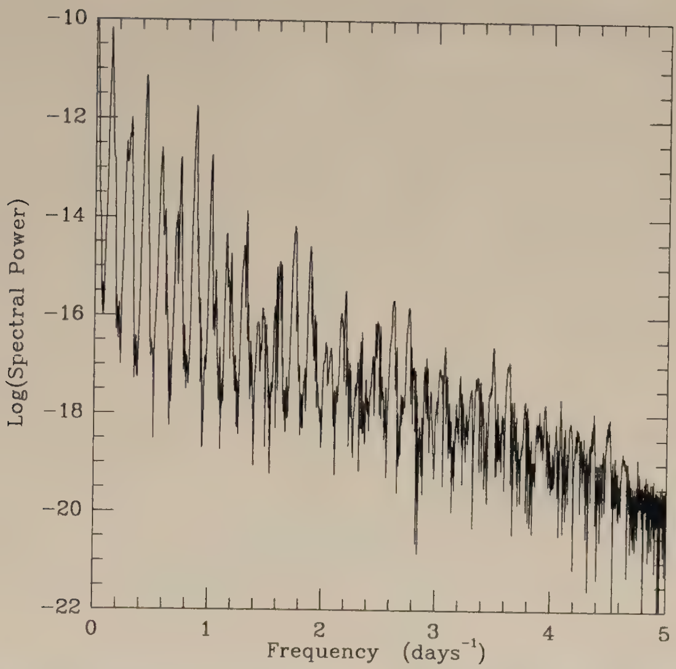

FIG. 4. The Fourier transform of the lightcurve in Fig. 3. The highest peak corresponds to a period of 7.45 days and the next highest peak to a period of 2.27 days.

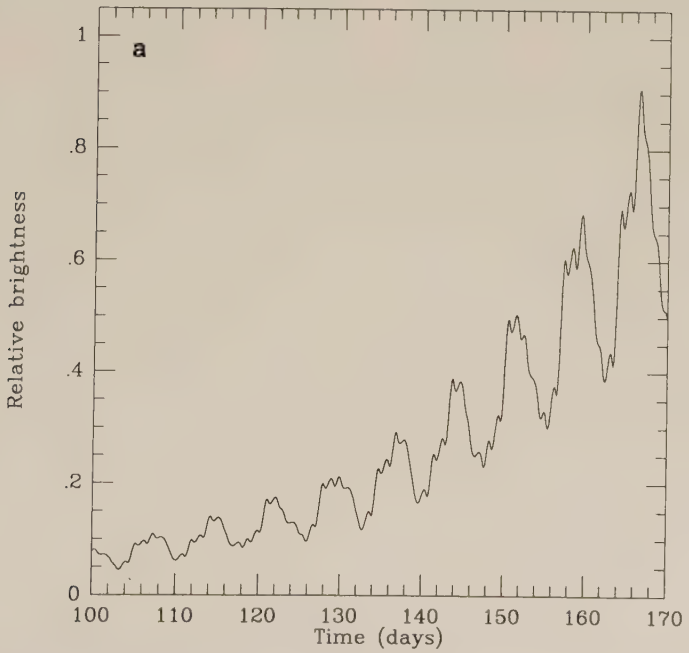

FIG. 5a. A preperihelion segment of the lightcurve of Fig. 3 expanded to show the detailed shape of the variation (linear weighting function).

ties of the periods often lead to similar shapes for adjacent peaks.

Figure 5b shows the expanded lightcurve for the same mass production data as that used in Fig. 5a (Fig. 2) with the weighting function $e^{-\Delta t/t_d} - e^{\Delta t/t_p}$ (instead of the linear weighting function), where $t_d = 1.27$ days and $t_p = 0.20$ days are the lifetimes of the daughter and parent molecules, respectively, and Δt is the time since the parent was emitted from the nucleus. This is how the lightcurve would appear if the entire coma were viewed in light of the C_2 bands for the two diametric sources. Although there is a change in overall shape of the peaks, this lightcurve resembles that for the linear weighting function with 5-day interval. The time constant for loss of C_2 is sufficiently long to mask most of the short period (2.2 day) fluctuations in the gas production rate, and the 7.4-day period still contains the dominant spectral power. In fact, the Fourier transform of the lightcurve for the complete apparition with exponential weighting is essentially identical to that shown in Fig. 4 for linear weighting.

A far different lightcurve is shown in Fig. 5c, where in addition to the exponential weighting characterizing the photodissociation of C_2, an additional factor is included in the weighting to account for the narrow field of view of 39 arcsec radius. At the time of the Millis and Schleicher (1986) observations, this field corresponded to a cylinder with a radius near 2×10^4 km at the position of the comet. A spherical shell of C_2 molecules reaches the edge of this field of view in only 0.23 days after leaving the nucleus with the assumed 1 km/sec expansion velocity. After this time, only the molecules in that particular shell which are contained in the two spherical caps within the cylinder of the field contribute to light received by the telescope. If we convert distances to time by the assumption of a constant expansion velocity for both daughter and parent, the "aperture" factor in the weighting function is 1 for $\Delta t \leq 0.23$ days and 1 −

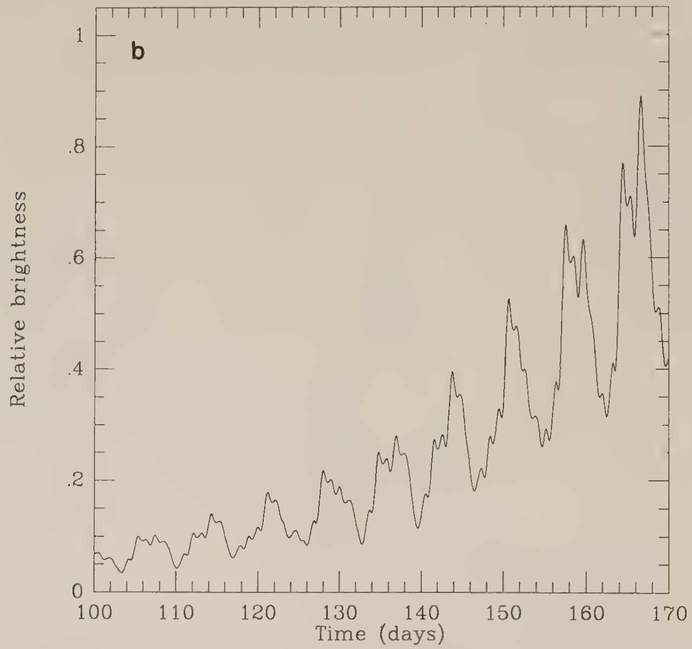

FIG. 5b. Same as Fig. 5a except an exponential weighting function appropriate to the scale lengths at 1 AU for the C_2 molecule and its parent has been applied to the *dm*/*dt* data set of Fig. 2 instead of the linear weighting function. Note that although the shapes of the peaks are different from those in Fig. 5a, the basic periodicities remain unaltered.

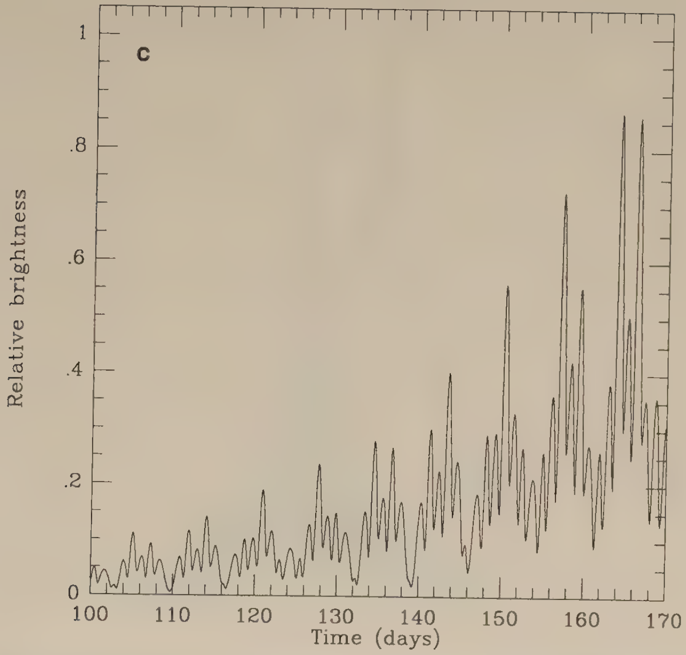

FIG. 5c. Same as Fig. 5b except an additional factor in the weighting function accounts for a narrow telescope aperture equivalent to a 2×10^4 km radius at the comet. Here the 2.2-day periodicity is much more apparent than in Figs. 5a and 5b.

$\sqrt{(\Delta t)^2 - .23^2}/\Delta t$ for $\Delta t > 0.23$ days, where Δt is the time in days after emission of the parent molecules. The cutoff is rather abrupt as most of the area of the spherical shell is quickly outside the cylinder as the shell expands. The smoothing of the instantaneous mass production rate from the two sources as seen in the lightcurve is rather modest in Fig. 5c, and the Fourier transform now has the 7.4-day peak in the spectral power slightly dominated by the 2.2-day peak. However, it is clear that this lightcurve can be made to resemble those of Figs. 5a and 5b by the addition of more sources spaced between the two diametrically opposite sources used to generate this figure. That is, the smoothing of the 2.2-day fluctuations can just as well be effected by the addition of more sources as by a persistence of emitted material in the field of view, and the 7.4-day period would regain its dominance in the power spectrum of molecular lightcurves for narrow angle as well as wide angle viewing apertures. The somewhat long interval of 5 days in our linear weighting function compensates for our including only two sources in the generation of the lightcurves. Some molecular species may be made more persistent by delayed emission from the dust grains (A'Hearn *et al.* 1986). This delayed emission would further smooth the short period fluctuations in a molecular lightcurve.

The first harmonic of the 7.4-day precession period would dominate the fundamental if the spin angular momentum of the nucleus were perpendicular to the orbit plane and the jet sources were symmetrically placed in the *xy* plane. The changing orientation of the nucleus relative to the spin angular momentum would then result in symmetrical periodic illumination of the sources at extremes of the precession cycle. This possibility led Wilhelm (1987) and Festou *et al.* (1987) to hypothesize a 14.8-day precession period to produce the 7.4-day variations. However, we see here that the nonzero obliquity of the angular mo-

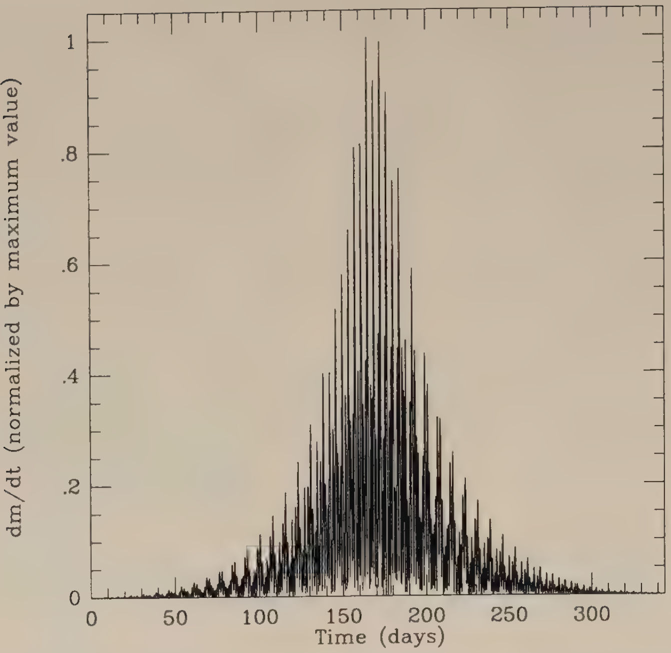

FIG. 6. The mass ejection rate *dm*/*dt* during a complete apparition for a parameter set identical to that of Fig. 2 except the precession is now around the axis of minimum moment of inertia.

mentum and the location of the sources out of the *xy* plane lead to a dominant period in the lightcurve nearly equal to the precession period. We shall see in the next case of precession about the axis of minimum moment of inertia that the fundamental precession period again dominates the lightcurve *except* for a brief time near perihelion where the angular momentum becomes perpendicular to the comet-Sun line. Only at this time does the first harmonic of the precession frequency dominate the lightcurve spectrum.

Our second simulation involves precession of the spin axis about the axis of minimum moment of inertia (*x* axis). We use the same initial orientation of the nucleus as in case 1 which leads to an obliquity of **L** of 23.8°—almost the same as that for the *z* axis precession above. The mass production rate for precession of the spin about the *x* axis is shown in Fig. 6. The modulation by the precession is uniformly strong throughout the apparition in this case, in contrast to Fig. 2. This situation does not differ significantly from Sekanina's (1987) model, since the two shorter axes of the ellipsoid are of comparable length. Viewed from inertial space, the *x* axis and $\boldsymbol{\omega}$ remain nearly coplanar with **L** as they rotate around the fixed **L** vector with an angular velocity which varies between L/B and L/C (e.g., Landau and Lifshitz 1976, p. 106). The corresponding instantaneous period is between 2.45 and 2.59 days—somewhat longer than the starting period for the rotation of 2.2 days. At the same time the ellipsoid appears to rotate about the *x* axis with the period of the body frame precession, thereby alternating high maximum elevation angles with very low maximum elevation angles of the Sun over the jet sources during the rotation.

Figure 7 shows the lightcurve generated from the data in Fig. 6 with the linear weighting function. Pre- and postperihelion parts of the curve are now very similar with the precessional modulation dominating the

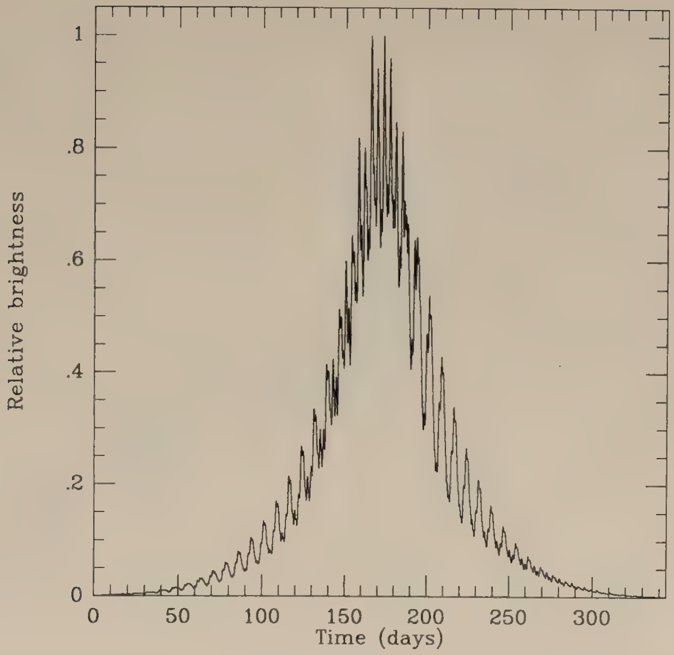

FIG. 7. The lightcurve generated from the mass production rate shown in Fig. 6 (linear weighting function).

variations. Around perihelion, which is not far from the point where **L** is perpendicular to the Sun–comet line, variations with approximately half the precession period dominate. This is evident in the Fourier transform of the lightcurve shown in Fig. 8, where the spectral power in the peak corresponding to a period of 3.8 days is comparable to that corresponding to 7.7 days. Other harmonics of the 7.7-day term (the precession as modified by the orbital motion) are prominent. The 2.5-day rotation of the x axis about **L** is also evident although much suppressed relative to the dominant 7.7-day and 3.8-day terms. This latter peak in spectral power almost coincides with the third harmonic of the dominant 7.7-day term, although the two frequencies are resolved as a double peak in Fig. 8. As is evident in Fig. 7, the expanded curve in Fig. 9 shows that here the peaks are very similar in shape. A pair of adjacent peaks is reasonably similar to the lightcurve obtained by Millis and Schleicher (1986). However, the better repeatability of the shapes of the lightcurve here should not be construed to indicate a precession about the axis of minimum moment, since similar adjacent peaks have also been obtained for precession about the axis of maximum moment of inertia for a different set of parameters.

The contrast in the seasonal effects between the two modes of precession is easy to understand. In the example of precession of the spin about the axis of maximum moment of inertia, the maximum change in the orientation of the nucleus relative to the fixed angular momentum as the spin precesses is about 60°, where the spin vector remains reasonably close to the angular momentum as the body nutates. The nutation is symmetric about the angular momentum, so a source in the Northern Hemisphere would have a low illumination a larger fraction of time during a precession period when **L** is tilted away from the Sun (northern winter) than when **L** is tilted toward the Sun (northern summer). An ex-

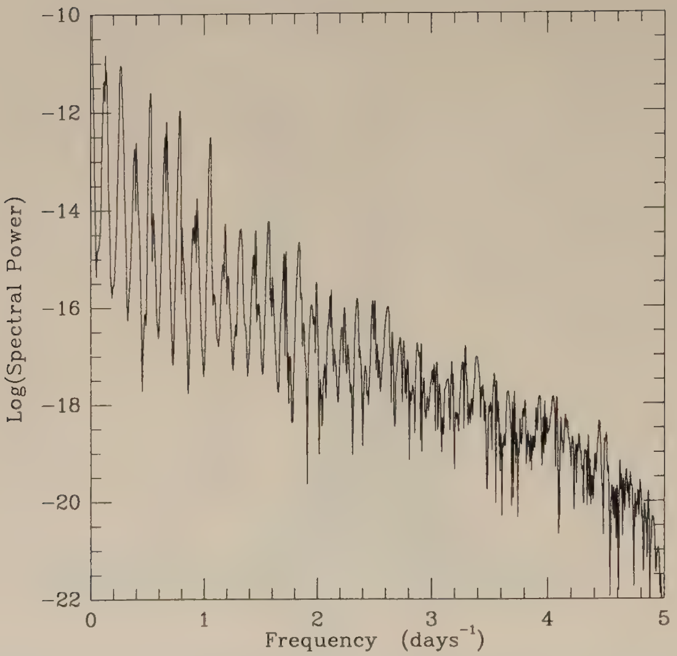

FIG. 8. The Fourier transform of the lightcurve shown in Fig. 7. The highest peak corresponds to a period of 7.7 days and the next highest peak to a period of 3.69 days.

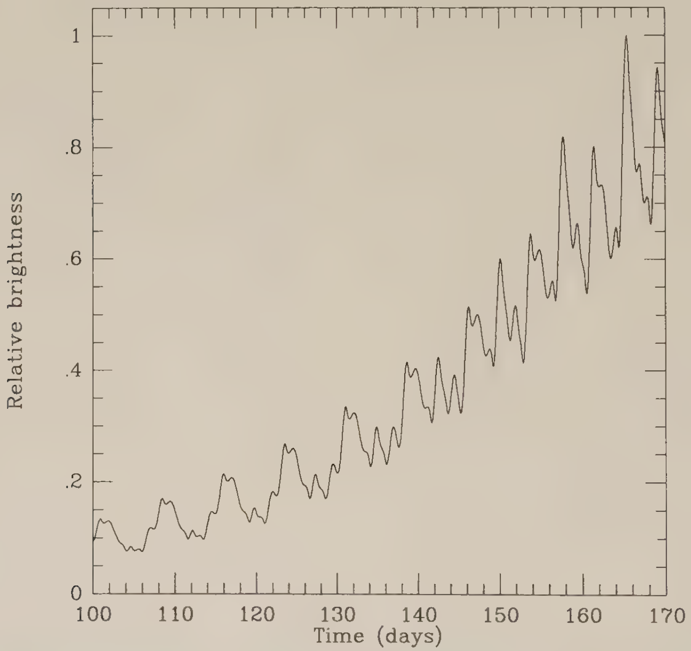

FIG. 9. A preperihelion segment of the lightcurve of Fig. 7 expanded to show the detailed shape of the variation (linear weighting function).

treme case would be a source near the axis of maximum moment of inertia in the Northern Hemisphere. Such a source could be almost continuously in shadow during the northern winter and continuously illuminated during the northern summer. With several sources, the average mass ejection rate may be comparable in winter and summer, but the detailed variations will generally be different as demonstrated in Fig. 3. The seasonal change is due to the limited variation in the orientation of the body for precession about the axis of maximum moment of inertia.

For precession about the axis of minimum moment of inertia, the body rotates about the x axis repeatedly through a full 360° relative to the angular momentum. This means that a source will be carried directly under the Sun as the body rotates during one part of the precession period but remain near a direction close to that of the orbit pole during another part. Nearly the full amplitude of variation for each source will be maintained regardless of the season.

Weissman (1987) attributes the large increase in brightness of the comet after perihelion over that at similar heliocentric distances before perihelion to seasonal effects, and Schleicher *et al.* (1987) find the amplitude of the variations in Halley's light output to be almost 50% greater after perihelion than before. This latter observation is the reverse of the change in variations in Fig. 3, but we can change our simulations to more closely conform to the observations simply by reversing the hemispheres of the source locations. The observed large seasonal changes suggest that Halley's precession is most likely about its axis of maximum moment of inertia.

These examples show explicitly that a wobbling motion of the nucleus of Halley's comet can produce a lightcurve similar to that recorded by Millis and Schleicher (1986), while allowing the much shorter rotation period of 2.2 days. As one method of determining the latter period was from light scattered from the presumably bare nucleus (e.g., Belton, private communication, 1987), a question which naturally arises is whether the wobbling motion could have been detected before the obscuration of the nucleus by the gas and dust. To investigate this possibility, we assume that since the nucleus is far from the Sun when it is unobscured, it remains relatively fixed in the sky during many rotation periods, that it shines by back scattered light, and that therefore the apparent brightness is proportional to the projected area on the sky. We view the nucleus from the perihelion direction, assume an obliquity of **L** near 25°, and consider the cases where **L** is tilted in a direction perpendicular to the line of sight and where **L** is tilted toward the observer. The results for initial conditions leading to the 7.4-day precession of the spin about the body z axis with an initial value of the spin period of 2.2 days are compared with those for rotation about the principal z axis. Figure 10 shows the lightcurves for the case where the nucleus is rotating about the axis of maximum moment of inertia with **L** tilted in the direction perpendicular to the line of sight and for a wobbling nucleus for the two orientations of **L**. Figure 11 shows the Fourier transforms of the respective curves in Fig. 10, where a Hanning window has been used to suppress the continuum from step function termination of the lightcurve data.

As would be expected, the principal axis case produced a lightcurve which was strictly periodic, with a Fourier transform showing only the fundamental corresponding to a period of 1.1 days (half the rotation period) and several harmonics. The actual nucleus may exhibit a 2.2-day periodicity as well due to albedo patterns and local slopes on the nucleus which were not included in our model. For the wobbling case the periodic lightcurve is modulated by the precession, where the amplitude of the modulation is greater for the case where **L** is tilted toward the observer. The Fourier transform now shows a rich spectrum consisting

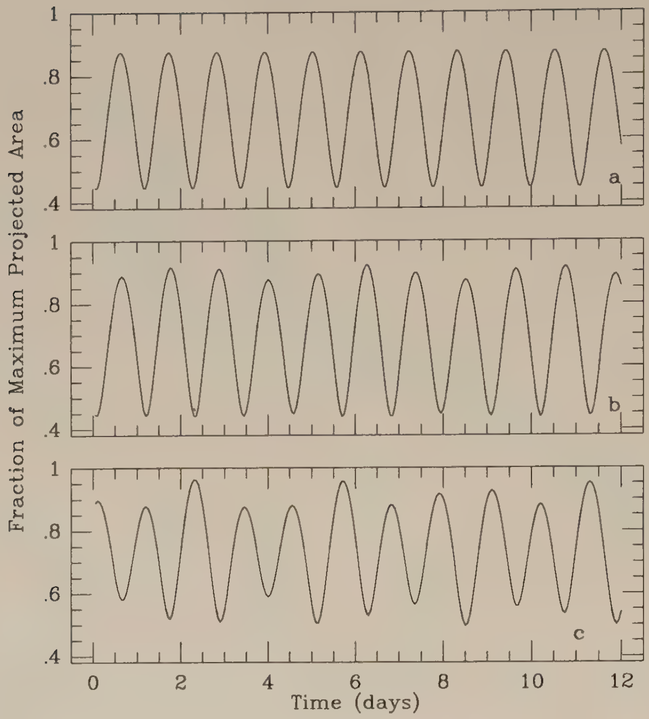

FIG. 10. Simulated lightcurves for a distant, bare nucleus as time histories of the projected cross section. (a) Pure rotation about the axis of maximum moment of inertia. (b) Precession of the spin about the axis of maximum moment of inertia with a 7.4-day period and the angular momentum in the plane perpendicular to the line of sight with obliquity near 25°. (c) Same as (b) except the angular momentum is tilted toward the observer in the plane containing the line of sight.

of multiples and sums and differences of the two frequencies. The frequencies with significant spectral power are identical in the two wobble trials, but the distribution of power among them differs. Here, one might claim, is a signature of the wobble that is uncomplicated by the gas and dust. However, we sampled our lightcurves every 0.1 days over more than 100 rotation periods. It is probably true that existing lightcurves of the faint nucleus have insufficient precision and frequency of sampling to resolve the variations induced by the wobble and to construct a meaningful Fourier transform. The 7.4-day periodic variations in the gas and dust output from the nucleus when Halley was near perihelion, contrasted with the 2.2-day period implied by the coma structure (also near perihelion) and the lightcurves obtained when Halley was on approach at a great distance, remain the best evidence that Halley's nucleus is in fact not rotating about a principal body axis.

If observations support the hypothesis that Halley's nucleus is wobbling, is such a rotation state to be expected? How stable is any state of rotation in the presence of localized jets of material from the surface? We turn to these questions in the next section where the torque of a single jet is restored to the equations of motion as described in Section II.

IV. JET-INDUCED CHANGES IN THE ROTATION STATE

Before proceeding with these numerical experiments, it is appropriate to establish the time scale for the damping of the wobble motion. A rotating, force-free solid body secularly evolves toward a rotation

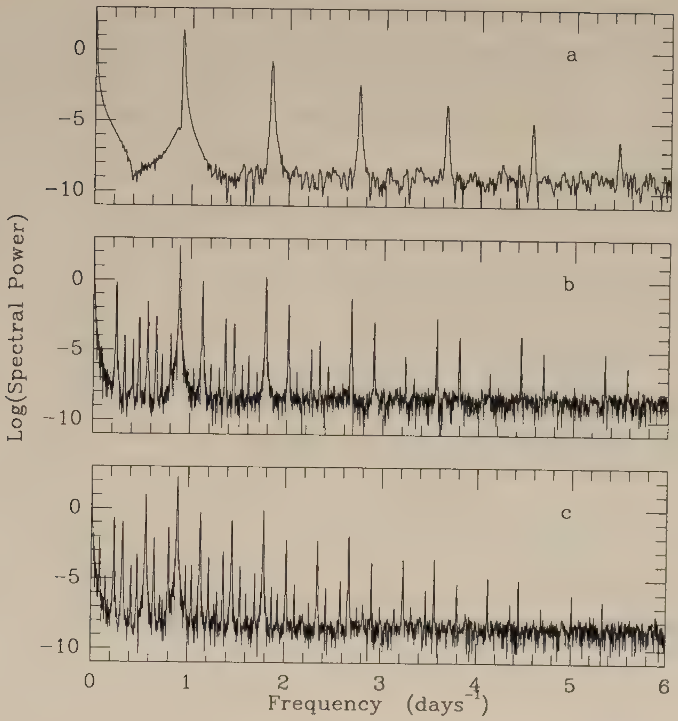

FIG. 11. Fourier transforms of the curves in Fig. 10. Most of the spectral power corresponds to a period at or near 1.1 days which is half the rotation period. This is like asteroidal lightcurves.

about the axis of maximum moment of inertia regardless of initial conditions. This is the configuration of minimum energy for a given angular momentum. During a wobble motion, the instantaneous equator is constantly changing as the spin vector precesses in the body frame of reference. The body is thereby constantly adjusting its elastic distortion due to the rotation, and it dissipates rotational energy in the process. The time constant for the relaxation of a wobble motion is given by (Peale 1973, Burns and Safronov 1973, McAdoo and Burns 1974)

$$\tau = K \frac{\mu Q}{\rho R^2 \omega^3} \approx 10^6 Q \text{ years}, \tag{9}$$

where $\mu = 4 \times 10^{10}$ dyn/cm^2 is the coefficient of rigidity for ice, $\rho = 1$ g/cm^3 is the density, $R = 5.3$ km is a characteristic radius, ω corresponds to the 2.2-day rotation period, and $K = \frac{38}{5}$ for a nearly spherical, homogeneous body (Peale 1973), or $K = O(10)$ if R is the shortest axis of the ellipsoidal shape (Burns and Safronov 1973, Mc Adoo and Burns 1974). The specific dissipation function Q has a typical value near 100 for rocky materials, although Q for ice may be less (e.g., Munk and MacDonald 1960). Even with $Q = 1$ or with a rigidity considerably smaller than that of ice, the decay time for a wobble of Halley's nucleus is long compared with the recorded history of the comet, but short compared with the age of the Solar System. We thus expect the nucleus to have been rotating about the axis of maximum moment of inertia when Halley was first scattered into the inner Solar System, and any current wobble would have been excited by the effects of the close approaches to the Sun. Since the damping time is very long compared to the orbital period, the consequences of many apparitions are cumulative. We can almost certainly neglect the dissipative damping of the wobble over the recorded history of the comet and omit its consideration completely for the single apparitions discussed below.

Two models describing the nucleus as a prolate, axisymmetric ellipsoid have been proposed to account for the two periods of 2.2 and 7.4 days observed in Halley's lightcurve (Sekanina 1987, Festou *et al.* 1987). We have seen in the last section that precession around the long axis of a triaxial ellipsoid did not differ significantly from these models, and that lightcurves resembling those observed were easily generated by the wobbling nucleus. We show below that a nonprincipal axis rotation leading to the observed periodicities is easily generated for a dynamically axisymmetric nucleus. On the other hand, the rotation state is also easily changed, and one might expect an observable change in the rotation during a single apparition. Also, a rather minor deviation from axial symmetry can severely reduce the rate of wobble excitation, since free precession of the spin vector about the now unique axis of maximum moment of inertia dominates the reaction to the torque.

For all of our simulations with axial or near axial symmetry, we start the ellipsoid rotating around the axis of maximum moment of inertia with a period of 2.2 days ($\omega_0 = 0.4545$ in our dimensionless units) when the comet is 2.8 AU from the Sun. The value of $(dm/dt)_{\max}$ used in Eq. (5) is $1.26 \times 10^{-6}\rho$ in the dimensionless units defined in Section III. This value of $(dm/dt)_{\max}$ is approximately one-third the value of $(dm/dt)_{\max}$ which would lead to the 4-day increase in the orbital period for each apparition for a single, optimally located jet with the values of A_1 and A_2 from Table I being assumed. (The reader is again cautioned to be aware of the uncertainty in this constraint on $(dm/dt)_{\max}$ because of the uncertainty in the accelerations A_1 and A_2.) Our chosen value of $(dm/dt)_{\max}$ approximately satisfies $(dm/dt)_{\max} = (dm/dt)_{\mathrm{enc}}\, g(r_p)/g(r_{\mathrm{enc}})$, where $r_{\mathrm{enc}} \approx 0.89$ AU is the heliocentric distance at the time of spacecraft encounter and $(dm/dt)_{\mathrm{enc}} = 2 \times 10^7$ g/sec is the estimate of the mass production rate at that time. Of course the observed dm/dt may be more representative of an average over a rotation period than it is of a maximum value for a single jet, and we would multiply the observed value by π to obtain $(dm/dt)_{\max}$ at encounter. But several active areas contributed to the observed mass production rate (Keller *et al.* 1987), so the smaller value we have chosen is more appropriate for a single large jet. The jet is arbitrarily placed at a point on the surface whose body coordinates are (0.0, 0.4, 0.3), and rotated by an angle of 30° about the body x axis away from the local normal to the surface *of the ellipsoid*. The latter tilt of the jet leads to a torque about the x axis, which is instrumental in exciting the precession of the spin about the x axis. A jet on the real nucleus is likely to be more or less perpendicular to the local surface, but that local surface will typically be inclined to the representative ellipsoidal surface by as much as several tens of degrees given the rather rugged observed topography. The spin angular momentum **L** is aligned approximately with the pole given by Wilhelm (1987) which is described in Section III.

The consequences of a jet torque for the rotational evolution of the nucleus of course depends critically on the strength, placement on the surface, and the orientation of the jet relative to the principal axis system of coordinates. Rather than compile an extensive set of consequences for various choices of jet parameters, we have chosen a single jet location and orientation on the ellipsoid which we believe may be typical of a strong jet. It is then not too difficult to infer the effects on the dynamical evolutions we shall derive of the addition of other jets at other locations. Both enhancements and suppressions of the rotational changes we find are then possible.

Figure 12 shows the evolution of the components of the angular velocity in the

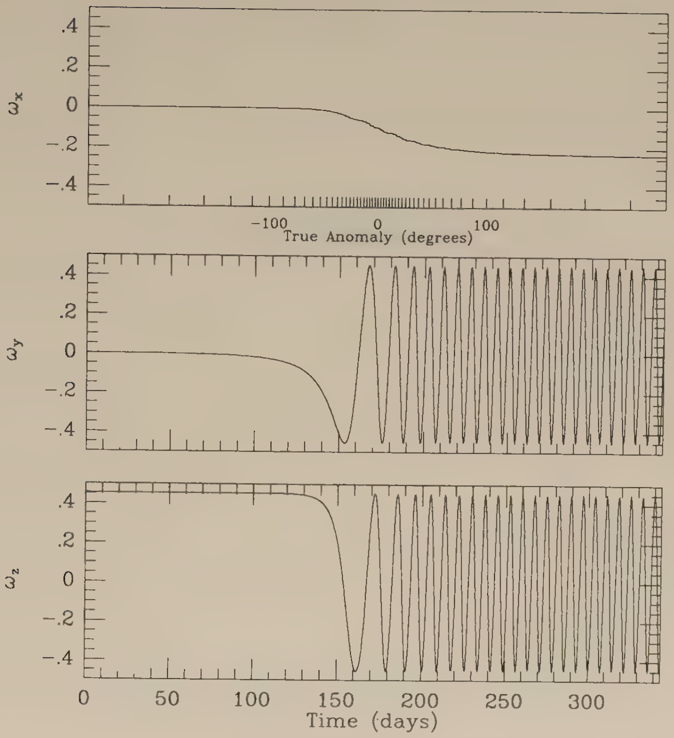

FIG. 12. Evolution of the components of angular velocity relative to the principal body axes during a single apparition for an axisymmetric nucleus initially rotating around an axis of maximum moment of inertia. The initial conditions are the same as those of Fig. 2. Axis ratios are $a : b : c = 1.0 : 0.5 : 0.5$, and a single jet is located at $x, y, z = 0.0, 0.4, 0.3$ and rotated 30° about the x axis away from the local surface normal; $(dm/dt)_{\max} = 1.26 \times 10^{-6}\rho$.

body frame for a symmetric rotator with ellipsoidal axes a, b, c = 1.0, 0.5, 0.5, and Fig. 13 shows the changes in the components of **L** relative to the inertial coordinate system. As no *unique* axis of maximum moment of inertia exists for the axial symmetry considered here ($\alpha = 0$ in Eq. (6)), precession about the axis of minimum moment of inertia is the only possible mode. The persistent torque about the x axis induces a component of $\boldsymbol{\omega}$ along the x symmetry axis, which in turn causes the large amplitude variation in ω_y and ω_z. The spin vector ends up precessing around the x axis with a period of about 7.25 days after the single apparition. The nearness of this period to the observed 7.4-day period is entirely fortuitous. From the inertial space viewpoint adopted by Sekanina (1987), the nucleus appears to rotate around the long axis with the 7.25-day period as it spins about **L**, which is nearly perpendicular to the long axis, with a period near 2.2 days. Figure 14 shows the development of the long period modulation of the jet activity, which would lead to a rather striking change in the lightcurve during the apparition. Of course, a change in the lightcurve due to a major change in the rotational state might be hard to distinguish from a change due to a seasonal effect with a stable rotation state, which was discussed in Section III. Given that the maximum value of dm/dt used here was only one-third that necessary to induce the observed 4-day increase in the orbital period per apparition, one must conclude that a wobble for a dynamically axially symmetric nucleus is quite easy to excite.

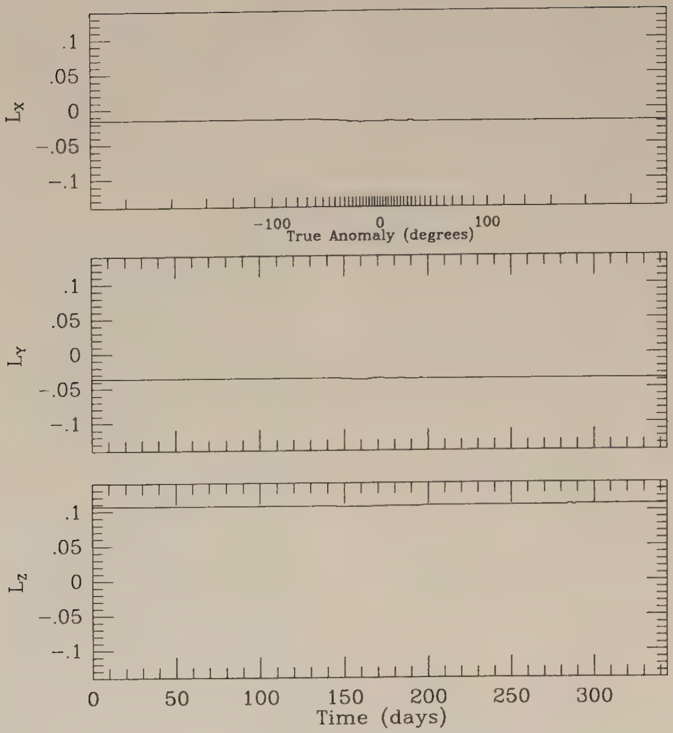

FIG. 13. Evolution of the components of angular momentum of the nucleus relative to the inertial coordinate system for the parameters of Fig. 12.

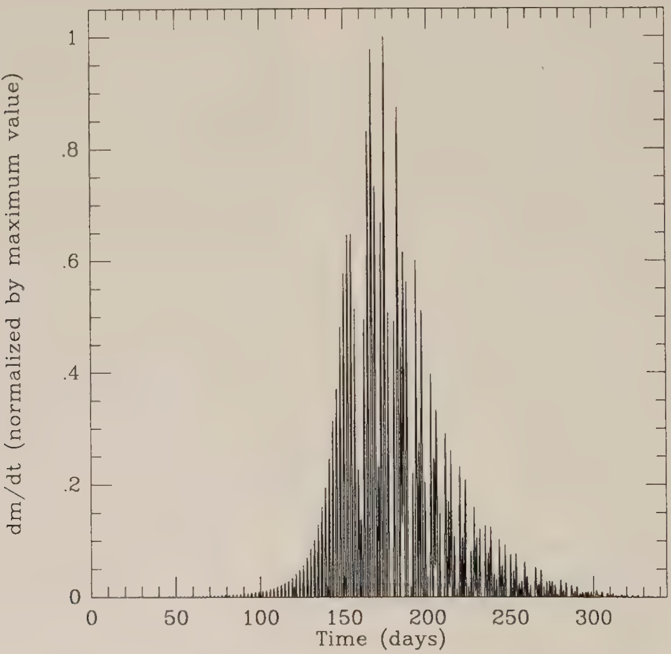

FIG. 14. Instantaneous mass ejection rate during a complete apparition for the parameters of Fig. 12.

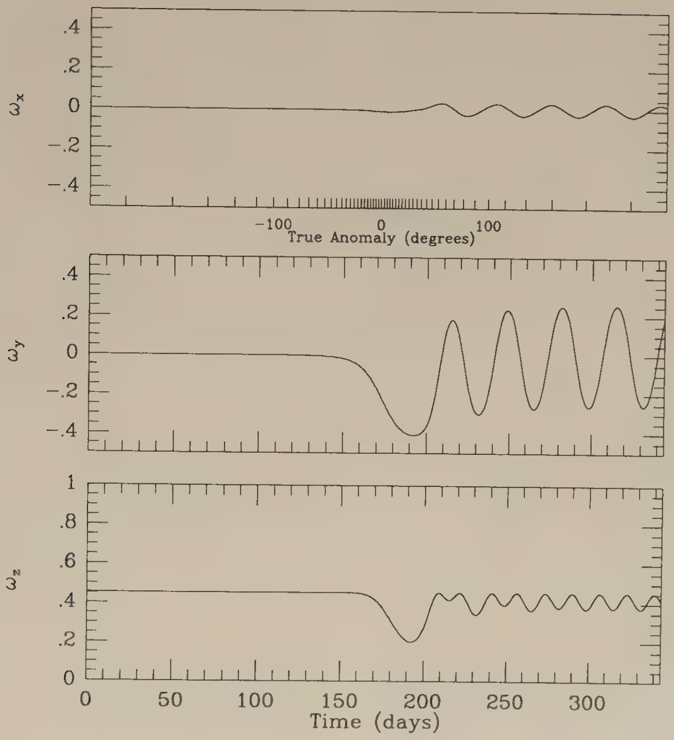

FIG. 15. Same as Fig. 12 except the nucleus has been given a slight asymmetry: $a:b:c$ = 1.0 : 0.5022 : 0.4978.

One would also expect a significant change in the precession period from pre- to post-perihelion and from one apparition to the next if the distribution of jets led to a persistent torque about the symmetry axis. The apparent constancy of the nongravitational acceleration of Halley's orbital motion over several apparitions implies little variation in Halley's rotation state over that period (Yeomans 1986).

A dynamically axially symmetric nucleus is a singular state and therefore has zero probability of being realized. We thus need to investigate the question of how much the nucleus can deviate from axial symmetry for the above evolution to persist. The answer appears to be very little. Figure 15 shows the evolution of the components of $\boldsymbol{\omega}$ for a slightly triaxial body with a, b, c = 1.0, 0.5022, 0.4978 subject to the identical set of initial conditions as the axisymmetric body in the previous example. Here the precession about the axis of maximum moment of inertia wins out in spite of the persistent torque about the x axis. As the torque grows near perihelion, a relatively large negative value of ω_y is induced, as in the axially symmetric case. But now there is an additional, free body term in the first of the Euler equations (1), since $C - B \neq 0$. As $\omega_y < 0$, this free body torque tends to increase ω_x in opposition to the negative torque N_x from the jet. If the free body term dominates N_x sufficiently, ω_x becomes positive, and the free body term in the second Euler equation reverses the initial increase in ω_y, thereby initiating the precession of the spin vector about the z axis. As N_x is small, it takes only the small deviation from axial symmetry to frustrate the attempt to precess about the axis of minimum moment. The z axis precession period ends up near 32.5 days after the apparition. From an alternative point of view, the initial condition of rotation about the z axis is one of minimum energy for the given angular momentum. The weak torques have increased the energy, but not sufficiently for the spin to cross the separatrix between z axis and x axis precession. However, for the small deviation from axial symmetry considered here, the slow change in the amplitude of the wobble over several apparitions discussed below for large triaxiality could lead to precession about the axis of minimum moment of inertia without any catastrophic events. Figure 16 shows that the large amplitude z axis wobble can lead to a rather striking modulation of the high frequency variation of dm/dt postperihelion.

The high probability that Halley's nucleus deviates from axial symmetry considerably more than does this example suggests that excitation of a precession of the spin axis about the axis of minimum moment by torques from one or more jets is unlikely. However, if a piece of the nucleus were to have broken off during an apparition in the prehistoric past, Halley's nucleus could have been left with such a precession. Otherwise, a precession around the axis of maximum moment seems more likely to be excited. One would not expect a wobble amplitude to change from the slow change in the moments of inertia due to the ordinary mass loss when the comet is near perihelion because of the adiabatic invariance of the solid angle defined by the motion of $\boldsymbol{\omega}$ in the body frame of reference (Goldreich and Toomre 1969).

Even for precession around the axis of maximum moment of inertia, a substantial deviation from axial symmetry severely restricts the evolution of the wobble amplitude from a jet-induced torque as shown by the following examples. The initial orientation of the nucleus is again chosen with **L** nearly aligned with Wilhelm's (1987) pole position for all of the following examples. A significant deviation from axial symmetry is assumed with a, b, c = 1.0, 0.5, 0.425, which are the axes used in the generation of the lightcurves in Section III. The nucleus model shown in Fig. 17 illustrates three initial positions of the spin vector, where $\boldsymbol{\omega}_1$ corresponds to rotation about the principal

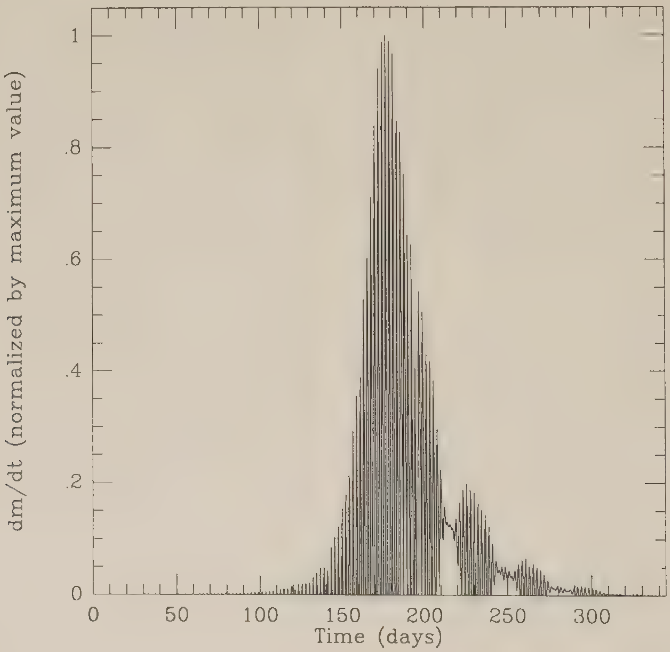

FIG. 16. Instantaneous mass ejection rate during a complete apparition for the parameters of Fig. 15.

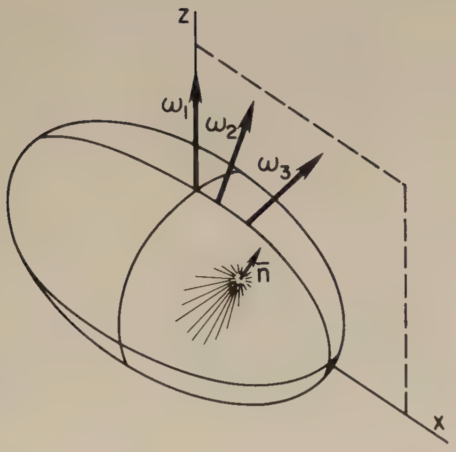

FIG. 17. Location of three initial positions of the spin angular velocity and the position of the jet for determining the effect of the reaction torque on a triaxial nucleus with $a:b:c = 1.0:0.5:0.425$.

z axis (maximum moment of inertia). The vectors $\boldsymbol{\omega}_2$ and $\boldsymbol{\omega}_3$ are inclined relative to the z axis by 15.4° and 34.2°, respectively, to give a 7.4-day precession of the spin about the z and x axes, respectively. As for the lightcurves, the dimensionless $\omega = 0.4545$ corresponds to a 2.2-day period. However, there is significant change in ω over the apparition, so the initial value is less bound by the observations. Also shown in Fig. 17 is the position of the jet at $x, y, z = 0.5000, -0.2000, 0.3361$, where the jet is rotated by 30° about the x axis direction away from the local normal to the ellipsoid. This is again presumed to ge a typical location and orientation of a jet relative to the principal axes of the real nucleus with its rugged topography, and like the previous examples, other evolutions for other jet parameters can be inferred from our results here. Again we use $(dm/dt)_{\max} = 1.26 \times 10^{-6}\rho$ and $v = 860$. Figure 18 shows the evolution of the components of the spin vector in the body frame of reference for the initial principal axis rotation. There is essentially no wobble excitation as ω_z and

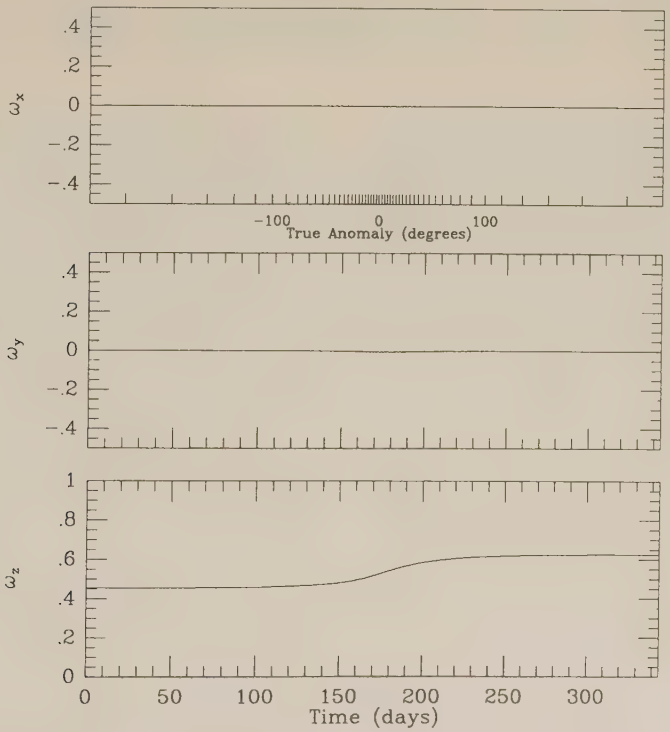

FIG. 18. Evolution of the components of angular velocity of the nucleus relative to the body principal axes for an initial rotation about the axis of maximum moment of inertia ($\boldsymbol{\omega}_1$ in Fig. 17).

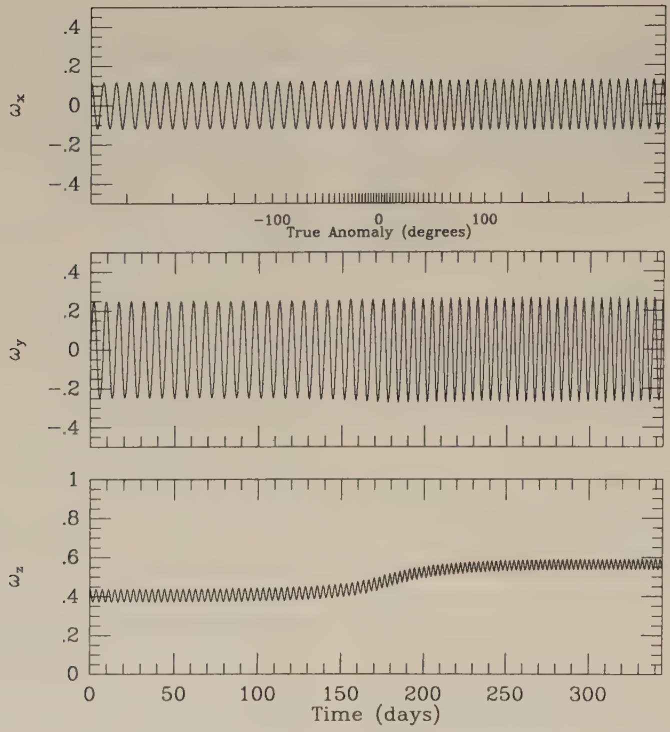

FIG. 19. Same as Fig. 18 except the initial rotation leads to an initial precession about the axis of maximum moment of inertia with a 7.4-day period (ω_2 in Fig. 17).

the angular momentum both increase, except for some high frequency fluctuations of less than 1° away from spin alignment with the z axis when the comet is near perihelion. Figure 19 shows the spin vector evolution for the initial 7.4-day precession about the z axis. The most striking change is again the relatively large increase in ω_z. There is also about an 8% increase in the maximum values of ω_x and ω_y. But if we represent the wobble amplitude by the angle θ_3 between the spin and the z axis as the spin crosses the xz plane, the amplitude has actually been reduced by the jet torque from an initial 15.4° to 12.4°. This results from the approximately 40% increase in ω_z compared with the more modest increases in the maximum values of ω_x and ω_y. The magnitude of the angular momentum has increased from 0.1104 to 0.1415 for initial precession about the z axis with a 7.4-day period and from 0.1145 to 0.1560 for the principal axis rotation.

The lack of any *large* change in the wobble amplitude both for the principal z axis rotation and for precession about the z axis in spite of the large changes in the spin angular momentum is easily understood. Although the torque component N_x here always tends to decrease ω_x, the free precession about the z axis periodically changes the sign of ω_x. When $\omega_x < 0$, N_x tends to increase the amplitude of the precession, but when $\omega_x > 0$, N_x tends to reduce the amplitude leading to a nearly zero net change over the precession period. A similar argument follows for ω_y and N_y. On the other hand, the wobble amplitude was changed somewhat for the precession case, and one could imagine situations where there was a systematic variation in the average jet magnitude over a precession pe-

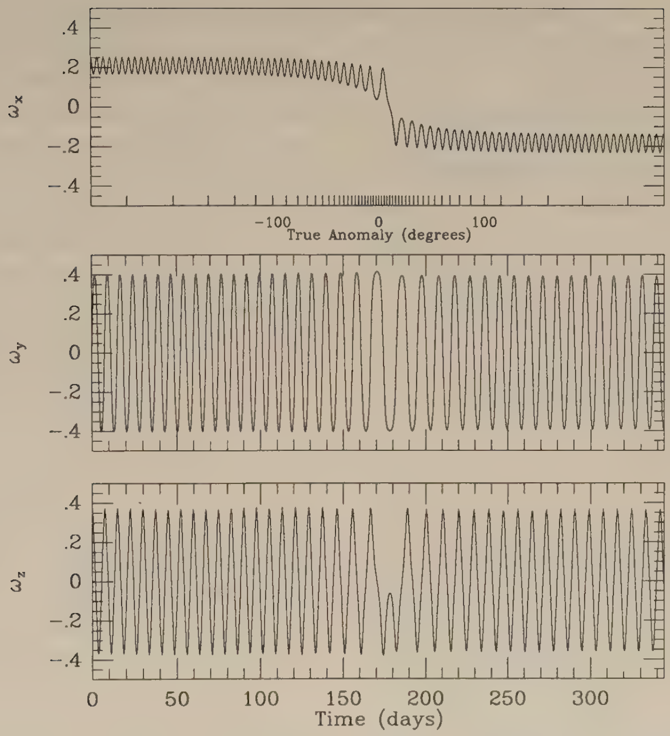

FIG. 20. Same as Fig. 18 except the initial rotation leads to an initial precession about the axis of minimum moment of inertia with a 7.4-day period ($\boldsymbol{\omega}_3$ in Fig. 17).

riod which could unbalance the periodic variations in the wobble amplitude for a more substantial change. The average value of ω_z (and ω) and also of L_z (and L) each secularly increase in both cases because the reaction torque from the jet always has a persistent component parallel to the z axis and a component parallel to $\mathbf{L}$. The precession in the second case causes a fluctuation in the magnitudes of these torque components, but does not change their signs.

Figure 20 shows the evolution of spin components for the third case, where precession of the spin vector is about the x axis. Now the amplitudes of the fluctuations in ω_y and ω_z are approximately constant as ω_x is secularly decreased. Again the amplitude of the wobble is reasonably stable in spite of the constant sign of the components of the torque about the y and z axes because the precession periodically reverses the sign of ω_y and ω_z, and the constant signs of the torque components about the axes cause alternate decreases and increases in the wobble amplitude over a precession period. For the precession around the x axis, the initial positive sign of ω_x is maintained for many precession periods, but the magnitude is slowly decreased by the persistent negative sign of this component of the torque. As ω_x is reduced by the jet torque, the trajectory of the spin in the body frame of the reference approaches the separatrix between the region where precession is about the z axis and that where precession is about the x axis. In this example the spin eventually makes one pass around the z axis on a trajectory near the separatrix and emerges on the other side where ω_x is now negative and where its average value continues to decrease. It is possible for the spin to be trapped into a precession about the z axis during this transition with a subsequent evolution similar to that of case 2 above.

Unlike the case where the precession of the spin is about the z axis, there is almost no change in **L** here. This follows from the fact that the instantaneous spin axis is initially inclined by about 14.4° from **L** and it remains reasonably close. As the nucleus rolls around the x axis as viewed from inertial space, the jet is alternately activated by the Sun when it is on a leading side, thereby exerting a reaction torque which decreases **L**, and then activated when it is on a trailing side, thereby increasing **L**. The net change in **L** over the apparition averages nearly to zero.

Excitation of a precession of the spin vector about the axis of minimum moment of inertia from torques caused by a jet of gas and dust is relatively easy if the nucleus is axisymmetric. But it is apparently difficult to excite a precession about the axis of minimum moment of inertia from an initial rotation about the axis of maximum moment if the nucleus is of its current general shape even with only a small axial asymmetry. Such a nearly axially symmetric body would then be more likely to be precessing about the axis of maximum moment as a significant amplitude of such a wobble can be generated. A substantially triaxial body, which is more likely the real case, has a very stable rotation about the principal axis of maximum moment of inertia in spite of torques which may be able to change the angular momentum considerably in a single apparition. A small amplitude precession about the axis of maximum moment of inertia is also very stable, although small changes in the wobble amplitude can occur during an apparition. More than one jet was observed to be active during the spacecraft encounter (Smith *et al.* 1987, Keller *et al.* 1987; Fig. 1). The distribution of several jets together with varying times of activation from seasonal effects could lead to less or more spectacular changes in the angular momentum during an apparition, but the change in a precession about the axis of maximum moment of inertia should always be small. Still, a substantial wobble could be excited by a random walk process of change, where a step occurs each apparition. This follows because of the very long damping time of the free wobble. The ease with which the angular momentum is changed by the jet torques may preclude the establishment of a reliable ephemerides describing the rotation.

V. DISCUSSION

We have explicitly demonstrated that the 2.2-day rotation period of Halley's comet nucleus indicated by the coma structure and dynamics and by distant lightcurves is compatible with the 7.4-day period observed in the lightcurve and molecule production rates when Halley is near the Sun. Lightcurves similar to those observed with a dominant period near 7.4 days are easily realized if Halley is in a wobbling rotation state with a rotation period near 2.2 days and a period of precession of the spin in the body frame of reference near 7.4 days. The precession could be either about the axis of maximum moment of inertia or about the axis of minimum moment of inertia, where the former is likely to produce a more pronounced seasonal change similar to that observed. The dominance of spectral power at frequencies corresponding to the rotation and precession periods rather than their first harmonic results if the mass ejection rate from one or more jets is not symmetric around the nucleus, and, for the precession period, if the obliquity of the cometary spin vector is significant. The rather pronounced seasonal changes in the lightcurve for precession about the axis of maximum moment of inertia can include a change in the dominant spectral frequency. The detailed shape of the lightcurve may or may not be similar from period to period, depending on the instantaneous geometry and whether or not the local synodic periods are nearly commensurate with the precession period. The ease with which these lightcurves are constructed indicates that the locations of a few jets over the nucleus are not very constrained by observed lightcurves, although some jet configurations can be ruled out (e.g., a single jet on the pole) because of the unusual lightcurve that would be produced over a complete apparition. The compatibility of these results with observations supports the notion that Halley was indeed wobbling during the 1986 apparition—most probably with the spin precessing about the axis of maximum moment of inertia.

Excitation of a significant precession about the axis of minimum moment of inertia from an initial (minimum energy) state of rotation about the axis of maximum moment of inertia can be accomplished during a single apparition only if the nucleus is axially symmetric. A slight difference in the two larger moments of inertia introduces a new degree of freedom in which the spin can precess about the axis of maximum moment of inertia. This new mode is preferably and easily excited by the jet-induced torque if the deviation from axial symmetry exceeds about 0.5%, but the amplitude generated during a single apparition rapidly decreases as the body is made more asymmetric. For axis ratios, 1.0 : 0.5 : 0.425, which are probably closer to reality than is the axisymmetric case, there is virtually no excitation of wobble during a single apparition from an initial rotation about the axis of maximum moment of inertia even though there can be large changes in the angular momentum. Still, the amplitude of an initial 7.4-day precession about the axis of maximum moment of inertia can change by a small amount during an apparition. In contrast, the geometry of an initial 7.4-day precession about the axis of minimum moment of inertia can change drastically during a single apparition. The difficulty in exciting this latter precession together with its relative instability indicates that it is unlikely to be seen at any random apparition. However, a sudden change in the shape of the nucleus, as would occur if a piece were to break off, could leave the larger remnant in a state of spin precession about the axis of minimum moment of inertia.

Although only small changes in the wobble amplitude seem to be possible during a single apparition for precession about the axis of maximum moment of inertia, the long damping time of the wobble due to internal dissipation means that these small changes can accumulate over many apparitions. The current, apparently large, amplitude wobble could have been excited as a random walk over a series of apparitions, or perhaps as a not so random walk if the jet configuration does not change much over the series. Slow change in the nucleus shape due to the ordinary evaporation of volatiles and loss of dust would leave the wobble amplitude of the remnant nucleus unchanged because of the adiabatic invariance of this amplitude. A sudden change in nucleus shape would generally produce a large wobble amplitude, which would persist for a long time in view of the slow damping. Because the jet-induced change in the wobble amplitude is slow for precession about the axis of maximum moment, it would not be unreasonable for the general rotation state of the nucleus to remain relatively unchanged over many apparitions. This is suggested by the apparently constant nongravitational acceleration of the orbital motion over the past several apparitions (Yeomans 1986). On the other hand, unbalanced torques from the jet reaction forces could lead to relatively rapid changes in the angular momentum.

In conclusion, there is very strong evidence that Halley rotates with a period near 2.2 days while its spin axis precesses in the body frame of reference with a period near 7.4 days. There are several indications that this precession is most likely to be about the axis of maximum moment of inertia. First, some interpretations of the spacecraft observations favor this mode of precession (Wilhelm *et al.* 1986, Julian 1987 (from Smith *et al.* 1987), Szegö *et al.* 1988; but see Sekanina 1988). Second, the observed large seasonal change in the amplitude of variation of the lightcurve and the possible seasonal cause of the brightness asymmetry from pre- to postperihelion seem to require the limited nutation characteristic of precession about the axis of maximum moment of inertia (Section II). Third, for a triaxial nucleus, a precession about the axis of minimum moment of inertia is more difficult to excite, and it is less stable once excited than a precession about the axis of maximum moment of inertia. Changing the wobble amplitude in this more probable state is very slow, but a large amplitude could accumulate over the history of close approaches to the Sun. Significant changes in the specific angular momentum of the nucleus over its active history have almost certainly occurred, and an unbalanced distribution of jets could result in major change during a single apparition, if the effect of the nongravitational forces on the orbit gives a reliable estimate of the magnitude of the reaction forces. A rotational ephemeris would be useful as a basis for determining the magnitude of the changes in the rotation state, but such an ephemeris should probably be used with caution in predicting orientation and phase of the nucleus from the beginning to the end of an apparition. (See note added in proof.)

APPENDIX A: ANALYTIC SOLUTION OF EULER'S EQUATIONS

The complication of elliptic integrals is avoided by finding a solution of Euler's equations for an axially symmetric, prolate ellipsoid with torques depending only on the time. We designate the principal moments of inertia by $A < B = C$, and the Euler equations become

$$\begin{aligned} \dot{\omega}_x &= \frac{N_x}{A}, \\ \dot{\omega}_y - \frac{C - A}{C}\,\omega_x\omega_z &= \frac{N_y}{C}, \\ \dot{\omega}_z + \frac{C - A}{C}\,\omega_x\omega_y &= \frac{N_z}{C}, \end{aligned} \tag{A1}$$

where, as before, ω_x, ω_y, and ω_z are the components of the angular velocity about the xyz body axes and $N_x(t)$, $N_y(t)$, and $N_z(t)$ are the components of the torque about these axes. The solution is

$$\begin{aligned} \omega_x(t) &= \omega_{x0} + \int_0^t \frac{N_x(t')}{A}\,dt', \\ \omega_y(t) &= \cos\left(\int_0^t \Omega(t')dt'\right)\left[\omega_{y0} - \int_0^t \sin\left(\int^{t'} \Omega(t'')dt''\right)\tilde{N}_y(t')dt'\right] \\ &\quad + \sin\left(\int_0^t \Omega(t')dt'\right)\left[\omega_{z0} + \frac{N_y(0)}{C\Omega(0)} + \int_0^t \cos\left(\int^{t'} \Omega(t'')dt''\right)\tilde{N}_y(t')dt'\right], \\ \omega_z(t) &= \cos\left(\int_0^t \Omega(t')dt'\right)\left[\omega_{z0} + \int_0^t \sin\left(\int^{t'} \Omega(t'')dt''\right)\tilde{N}_z(t')dt'\right] \\ &\quad - \sin\left(\int_0^t \Omega(t')dt'\right)\left[\omega_{y0} + \frac{N_z(0)}{C\Omega(0)} + \int_0^t \cos\left(\int^{t'} \Omega(t'')dt''\right)\tilde{N}_z(t')dt'\right], \end{aligned} \tag{A2}$$

where

$$\omega_{i0} = \omega_i(0),$$

$$\Omega(t) = \frac{C - A}{C}\,\omega_x(t),$$

$$\tilde{N}_y(t) = \frac{\dot{N}_y(t)}{C\Omega(t)} + \frac{N_z(t)}{C} - \frac{\dot{\Omega}(t)}{\Omega^2(t)}\,\frac{N_y(t)}{C},$$

$$\tilde{N}_z(t) = -\frac{\dot{N}_z(t)}{C\Omega(t)} + \frac{N_y(t)}{C} - \frac{\dot{\Omega}(t)}{\Omega^2(t)}\,\frac{N_z(t)}{C}.$$

The particular solution used to test the numerical integration described in Section II was obtained by assuming

$$N_x = 0, \quad N_y = \alpha + \beta t + \gamma \sin \Omega t, \quad N_z = 0, \qquad \text{(A3)}$$

where α, β, and γ are constants and

$$\Omega(t) = \frac{C - A}{C}\, \omega_{x0} \equiv \Omega,$$

$$\tilde{N}_y(t) = \frac{\beta}{C\Omega} + \frac{\gamma}{C} \cos \Omega t,$$

$$\tilde{N}_z(t) = \frac{\alpha}{C} + \frac{\beta}{C} t + \frac{\gamma}{C} \sin \Omega t.$$

The solution is then

$$\omega_x(t) = \omega_{x0},$$

$$\omega_y(t) = \frac{\beta}{C\Omega^2} + \left(\omega_{y0} - \frac{\beta}{C\Omega^2}\right) \cos \Omega t + \left(\omega_{z0} + \frac{\alpha}{C\Omega} + \frac{\gamma}{2C} t\right) \sin \Omega t,$$

$$\omega_z(t) = -\frac{\alpha}{C\Omega} - \frac{\beta}{C\Omega} t + \left(\omega_{z0} + \frac{\alpha}{C\Omega} + \frac{\gamma}{2C} t\right) \cos \Omega t + \left(-\omega_{y0} - \frac{\gamma}{2C\Omega} + \frac{\beta}{C\Omega^2}\right) \sin \Omega t. \qquad \text{(A4)}$$

We wish to compare this solution for t = 344 days to the solution found by numerically integrating Eqs. (A1) from $t = 0$ to t = 344 days. We choose the semiaxes of the ellipsoid, $a, b, c = 1, 0.5, 0.5$ in the normalized units of Section II and the initial normalized angular velocities $\omega_{x0}, \omega_{y0}, \omega_{z0} = 0.3, -1.311, -3.365$. The normalized time parameter increases by 2π per day as in Section II, and N_y in Eqs. (A3) is normalized by $ma^2n_0^2$, where $n_0 = 2\pi$ rad per day. In these normalized units we choose $\alpha, \beta, \gamma = 10^{-3}, 10^{-6}, 10^{-3}$, and $(C - A)/C = 0.6$ such that $\Omega = 0.18$. For $t = 344 \times 2\pi$, the results listed in Table A1 are obtained.

APPENDIX B: EQUATIONS USED IN NUMERICAL INTEGRATION

1. *In Terms of Euler Angles*

The Euler angles orient the nucleus with respect to an inertial coordinate system by the following sequence of rotations. With the body principal axes (xyz) initially coincident with the inertial axes (XYZ), a rotation of the body axes about the z axis by angle ϕ is followed by a second rotation of the body system by an angle θ about the x axis in its new position and finally by a third rotation about the z axis in its new position by an angle ψ. All rotations are in the right-hand sense when the axes are viewed from the origin (e.g., see Goldstein 1980, p. 146). The equations of variation of these angles are obtained from Eqs. (1) by substituting the following expressions for the components of the angular velocity in the body frame of reference:

$$\begin{aligned} \omega_x &= \dot{\phi} \sin \theta \sin \psi + \dot{\theta} \cos \psi, \\ \omega_y &= \dot{\phi} \sin \theta \cos \psi - \dot{\theta} \sin \psi, \qquad \text{(B1)} \\ \omega_z &= \dot{\phi} \cos \theta + \dot{\psi}. \end{aligned}$$

TABLE A1

ω_y	ω_z	Calculation type
−2.33410715694974	4.18079259396651	Analytic [Eqs. (A4)]
−2.33410679950485	4.18079278971580	Numerical [$\varepsilon = 10^{-10}$]
−2.33410715651603	4.18079259420361	Numerical [$\varepsilon = 10^{-13}$]

Note. Here ε is the limiting precision demanded at each step of the numerical calculation and the ω_i are normalized as in Section II. The accuracy of the numerical calculations were judged adequate for $\varepsilon = 10^{-10}$.

There results

$$\ddot{\phi} = \frac{1}{\sin\theta}(f_1 \sin\psi + f_2 \cos\psi),$$

$$\ddot{\theta} = -f_2 \sin\psi + f_1 \cos\psi, \tag{B2}$$

$$\ddot{\psi} = f_3 - \frac{1}{\sin\theta}(f_1 \sin\psi \cos\theta + f_2 \cos\psi \cos\theta),$$

where

$$f_1 = h_1 + \frac{B-C}{A}\omega_y\omega_z + \frac{N_x}{A},$$

$$f_2 = h_2 + \frac{C-A}{B}\omega_z\omega_x + \frac{N_y}{B}, \tag{B3}$$

$$f_3 = h_3 + \frac{A-B}{C}\omega_x\omega_y + \frac{N_z}{C},$$

where $A \leq B \leq C$ are the principal moments of inertia as before with

$$h_1 = -\dot{\phi}\dot{\theta}\cos\theta\sin\psi - \dot{\phi}\dot{\psi}\sin\theta\cos\psi + \dot{\theta}\dot{\psi}\sin\psi,$$

$$h_2 = -\dot{\phi}\dot{\theta}\cos\theta\cos\psi + \dot{\phi}\dot{\psi}\sin\theta\sin\psi + \dot{\theta}\dot{\psi}\cos\psi, \tag{B4}$$

$$h_3 = \dot{\phi}\dot{\theta}\sin\theta.$$

2. *In Terms of the Alternate Set of Angles*

Again the rotations are defined from an initial coincidence of the body principal axes and the inertial axes. The first two rotations in this set are identical to the first two Euler angles, but the last right-hand rotation is about the y axis instead of the z axis. In this set

$$\omega_x = -\dot{\phi}\sin\psi\cos\theta + \dot{\theta}\cos\psi,$$

$$\omega_y = \dot{\phi}\sin\theta + \dot{\psi}, \tag{B5}$$

$$\omega_z = \dot{\phi}\cos\psi\cos\theta + \dot{\theta}\sin\psi.$$

There results

$$\ddot{\phi} = \frac{1}{\cos\theta}(f_3\cos\psi + f_1\sin\psi),$$

$$\ddot{\theta} = f_1\cos\psi + f_3\sin\psi, \tag{B6}$$

$$\ddot{\psi} = f_2 + \frac{1}{\cos\theta}(f_1\sin\theta\sin\psi - f_3\sin\theta\cos\psi),$$

where f_i are given in Eqs. (B3), but now

$$h_1 = -\dot{\phi}\dot{\psi}\cos\psi\cos\theta - \dot{\phi}\dot{\theta}\sin\psi\sin\theta + \dot{\theta}\dot{\psi}\sin\psi,$$

$$h_2 = -\dot{\phi}\dot{\theta}\cos\theta, \tag{B7}$$

$$h_3 = -\dot{\phi}\dot{\psi}\sin\psi\cos\theta + \dot{\phi}\dot{\theta}\cos\psi\sin\theta - \dot{\theta}\dot{\psi}\cos\psi.$$

ACKNOWLEDGMENTS

We thank M. Belton for numerous information discussions and for providing us with the results of his photometric observations. We also thank D. Yeomans for kindly providing us with the revised parameters for Halley's orbit, including the new values for the components of the nongravitational acceleration for two different models. This work was supported in part by the Planetary Geology and Geophysics Program of the National Aeronautics and Space Administration under Grants NGR 05-010-062 (UCSB) and NAGW1107 (SUNYSB).

Note added in proof. In a recent publication, (The Rotation of P/Halley, *Astron. J.* **97,** 546–551, 1989), Sagdeev *et al.* present observations that appear to verify the 7.4-day precession of Halley's spin axis about the axis of maximum moment of inertia.

REFERENCES

A'Hearn, M. F. 1982. Spectrophotometry of comets at optical wavelengths. In *Comets* (L. L. Wilkening, Ed.), pp. 433–460. Univ. of Arizona Press, Tucson.

A'Hearn, M. F., S. Hoban, P. V. Birch, C. Bowers, R. Martin, and D. A. Klinglesmith 1986. Cyanogen jets in Comet Halley. *Nature (London)* **324,** 649–651.

Burlisch, R., and J. Stoer 1966. Numerical treatment of ordinary differential equations by extrapolation methods. *Numer. Math.* **8,** 1–13.

Burns, J. A., and V. Safronov 1973. Asteroid nutation angles. *Mon. Not. R. Astron. Soc.* **165,** 403–411.

Delsemme, A. H. 1982. Chemical composition of cometary nuclei. In *Comets* (L. L. Wilkening, Ed.), pp. 85–130. Univ. of Arizona Press, Tucson.

Festou, M. C., P. Drossart, J. Lecacheux, T. Encrenaz, F. Puel, and J. L. Kohl-Moreiera 1987. Periodicities in the light curve of P/Halley and the rotation of its nucleus. *Astron. Astrophys.* **187,** 575–580.

Goldreich, P., and A. Toomre 1969. Some remarks on polar wandering. *J. Geophys. Res.* **74,** 2555–2567.

Goldstein, H. 1980. *Classical Mechanics*. Addison–Wesley, Reading, MA.

Green, D. W. E., and C. S. Morris 1987. The visual brightness behavior of P/Halley during 1981–1987. *Astron. Astrophys.* **187,** 560–568.

Hanner, M. S., A. T. Tokunaga, W. F. Golisch, D. M. Griep, and C. D. Kaminski 1987. Infrared emission from P/Halley's dust coma during March 1986. *Astron. Astrophys.* **187,** 653–660.

Haser, L. 1957. Distribution d'intensité dans la tête d'une comete. *Bull. Cl. Sci. Acad. R. Belg. Ser. 5* **18,** 740–750.

Julian, W. H. 1987. Free precession of the Comet Halley nucleus. *Nature* (*London*) **326,** 57–58.

Kaneda, E., O. Ashihara, M. Shimizu, M. Takagi, and K. Hirao 1986. Observation of Comet Halley by the ultraviolet imager of Suisei. *Nature* (*London*) **321,** 299–303.

Keller, H. U., W. A. Delamere, W. F. Huebner, H. J. Reitsema, H. U. Schmidt, F. L. Whipple, K. Wilhelm, W. Curdt, R. Kramm, N. Thomas, C. Arpigny, C. Barbieri, R. M. Bonnet, S. Cazes, M. Coradini, C. B. Cosmovici, D. W. Hughes, C. Jamar, D. Malaise, K. Schmidt, W. K. H. Schmidt, and P. Seige 1987. Comet P/Halley's nucleus and its activity. *Astron. Astrophys.* **187,** 807–823.

Keller, H. U., and N. Thomas 1988. On the rotation axis of Comet Halley. *Nature* (*London*) **333,** 146–148.

Kerr, R. A. 1986. Halley's confounding fireworks. *Science* **234,** 1196–1198.

Krankowsky, D., P. Lämmerzahl, I., Herrwerth, J. Woweries, P. Eberhardt, U. Dolder, U. Herrmann, W. Schulte, J. J. Berthelier, J. M. Illiano, R. R. Hodges, and J. H. Hoffman 1986. *In situ* gas and ion measurements at Comet Halley. *Nature* (*London*) **321,** 320–326.

Landau, L. D., and E. M. Lifschitz 1976. *Mechanics*. Pergamon, Oxford.

Larson, S. M., and Z. Sekanina 1984. Coma morphology and dust emission pattern of periodic Comet Halley. I. High resolution images taken at Mount Wilson in 1910. *Astron. J.* **89,** 571–578, 600–606.

Larson, S. M., and Z. Sekanina 1985. Coma morphology and dust emission pattern of periodic Comet Halley. III. Additional high resolution images taken in 1910. *Astron. J.* **90,** 823–826, 917–923.

Larson, S., Z. Sekanina, D. Levy, S. Tapia, and M. Senay 1987. Comet P/Halley near-nucleus phenomena in 1986. *Astron. Astrophys.* **187,** 639–644.

Liebowitz, E. M., and N. Brosh 1986. Photoelectric discovery of a 52-hr periodicity in the nuclear activity of P/Halley. *Icarus* **68,** 418–429.

Lissauer, J. 1986. How can Halley rotate? Presentation at the *20th ESLAB Symposium on the Exploration of Halley's Comet, Heidelberg, FRG, October, 1986.*

Marsden, B. G., Z. Sekanina, and D. K. Yeomans 1973. Comets and nongravitational forces, *Astron. J.* **78,** 211–225.

McAdoo, D. C., and J. A. Burns 1974. Approximate axial alignment times for spinning bodies. *Icarus* **21,** 86–93.

McDonnell, J. A. M., W. M. Alexander, W. M. Burton, E. Bussoletti, D. H. Clark, R. J. L. Grard, E. Grün, M. S. Hanner, D. W. Hughes, E. Igenbergs, H. Kuczera, B. A. Lindblad, J. C. Mandeville, A. Minafra, G. H. Schwehm, Z. Sekanina, M. K. Wallis, J. C. Zarnecki, S. C. Chakaveh, G. C. Evans, S. T. Evans, J. G. Firth, A. N. Littler, L. Massonne, R. E. Olearczyk, G. S. Pankiewicz, T. J. Stevenson, and R. F. Turner 1986. Dust density and mass distribution near Comet Halley from Giotto observations. *Nature* (*London*) **321,** 338–341.

Meech, K. J., and D. C. Jewitt 1987. Observations of Comet P/Halley at minimum phase angle. *Astron. Astrophys.* **187,** 585–593.

Millis, R. L., and D. G. Schleicher 1986. Rotation period of Comet Halley. *Nature* (*London*) **324,** 646–649.

Munk, W. H., and G. J. F. MacDonald 1960. *The Rotation of the Earth*. Cambridge Univ. Press, Cambridge/New York.

Peale, S. J. 1973. Rotation of solid bodies in the Solar System. *Rev. Geophys. Space Phys.* **11,** 767–793.

Rickman, H. 1986. Masses and densities of Comets Halley and Kopff. In *Proc. ESA Workshop Comet Nucleus Sample Return,* ESA SP-249, Paris, pp. 195–206.

Sagdeev, R. Z., P. E. Elyasberg, and V. I. Moroz 1988. Is the nucleus of Comet Halley a low density body? *Nature* (*London*) **331,** 240–242.

Schleicher, D. G., R. L. Millis, D. J. Tholan, H. B. Hammel, J. R. Piscitelli, N. Lark, P. V. Birch, and R. Martin 1987. The variability of Comet Halley during the 1985/1986 apparition. *Bull. Amer. Astron. Soc.* **19,** 879.

Schlosser, W., R. Schultz, and P. Koczet 1986. The Cyan shells of Comet P/Halley. In *20th ESLAB Symp.,* ESA SP-250, Vol. III, pp. 495–501.

Sekanina, Z. 1987. Nucleus of Comet Halley as a torque-free rigid rotator. *Nature* (*London*) **325,** 326–328.

Sekanina, Z. 1989. Rotation vector of Halley's comet. In *Comet Halley 1986: Worldwide Investigations, Results and Interpretations*. Ellis Howard Library of Science, Series in Astronomy, in press.

Sekanina, Z., and S. M. Larson 1984. Coma morphology and dust emission pattern of periodic Comet Halley. II. Nucleus spin vector and modeling of major dust features in 1910. *Astron. J.* **89,** 1408–1425, 1446–1447.

Sekanina, Z., and S. M. Larson 1986. Coma morphology and dust emission pattern of periodic Comet Halley. IV. Spin vector refinement and map of discrete dust sources for 1910. *Astron. J.* **92,** 462–482.

Smith, B. A., S. M. Larson, K. Szegö, and R. Z. Sagdeev 1987. Rejection of a proposed 7.4-day rotation period of the comet Halley nucleus. *Nature (London)* **326,** 573–574.

Szegö, K., A. Kondor, S. Larson, E. Merenyi, R. Z. Sagdeev, B. A. Smith, and I. Tóth 1988. Analysis of the rotation of Comet Halley. In *Proc. COSPAR, Helsinki, Finland, July 1988,* in press.

Weissman, P. 1987. Post-perihelion brightening of Comet P/Halley: Springtime for Halley. *Astron. Astrophys.* **187,** 873–878.

Wilhelm, K. 1987. Rotation and precession of Comet Halley. *Nature (London)* **327,** 27–30.

Wilhelm, K., C. B. Cosmovici, W. A. Delamere, W. F. Huebner, H. U. Keller, H. Reitsema, Hu. Schmidt, and F. L. Whipple 1986. A three-dimensional model of the nucleus of Comet Halley. In *20th ESLAB Symp.,* ESA SP-250, pp. 367–369.

Williams, I. P., P. J. Andrews, A. Fitzsimmons, and G. P. Williams 1987. The variation in the brightness of Halley's comet from ground-based narrow band photometry. *Mon. Not. R. Astron. Soc.* **226,** 1P–4P.

Wisdom, J., S. J. Peale, and F. Mignard 1984. The chaotic rotation of Hyperion. *Icarus* **58,** 137–152.

Yeomans, D. K. 1986. Physical interpretations from the motions of Comets Halley and Giacobini-Zinner. In *20th ESLAB Symp.,* ESA SP-250, pp. 419–425.

ICARUS **79,** 431 (1989)

Author Index for Volume 79

A

A'Hearn, Michael F., 145
Arakawa, E. T., 350

B

Barker, Edwin S., 125
Bar-Nun, Akiva, 116
Beletic, J. W., 38
Birch, Peter V., 145
Broucke, R., 208
Buie, Marc W., 23

C

Carr, Michael H., 311
Chini, Rolf, 190
Chyba, Christopher F., 350, 362
Cochran, Anita L., 125
Colburn, D. S., 159
Coustenis, A., 328
Cruikshank, Dale P., 15

D

De Pater, Imke, 190
Downs, G. S., 289
Dubouloz, N., 328

F

Fogg, Martyn J., 382
Franklin, Fred, 223
Frère, C., 328

G

Gautier, D., 328
Goody, R. M., 38
Graham, Francis, 47
Green, Jacklyn R., 125

H

Haberle, R. M., 159
Hammel, H. B., 1, 15
Hapke, Bruce, 47, 56
Heifetz, Eyal, 116
Hoban, Susan, 145

K

Khare, B. N., 350
Kreidl, T. J., 1
Kreysa, Ernst, 190

L

Lark, Neil L., 1, 15
Lecar, Myron, 223
Lellouch, E., 328
Lissauer, Jack J., 396

M

Manabe, S., 208
Martin, Ralph, 145
McKinnon, William B., 75
Mendis, D. A., 101
Mumma, Michael J., 362
Murray, B. G. J. P. T., 350

N

Northrop, T. G., 101

P

Peale, S. J., 396
Pirraglia, Joseph A., 196
Pollack, J. B., 159
Prialnik, Dina, 116

R

Raulin, F., 328
Rigler, Michael A., 1, 15
Roth, L. E., 289

S

Sagan, Carl, 350, 362
Saunders, R. S., 289
Schaffer, Les, 101
Schenk, Paul M., 75
Schubert, G., 289
Soper, Paul, 223
Squyres, Steven W., 229

T

Tanikawa, K., 208
Tholen, David J., 15, 23, 38
Thompson, W. R., 350

U

Ulich, Bobby L., 190

NOTICE

The Subject Index for Volume 79 will appear in the December 1989 issue as part of a cumulative index for the year 1989.

Copyright © 1989 by Academic Press, Inc.
All rights of reproduction in any form reserved.

Icarus

INTERNATIONAL JOURNAL OF SOLAR SYSTEM STUDIES

Volume 79 • 1989

EDITOR: *Joseph A. Burns*

Space Sciences Building
Cornell University
Ithaca, New York 14853

ACADEMIC PRESS, INC.
Harcourt Brace Jovanovich, Publishers
San Diego New York Boston
London Sydney Tokyo Toronto

Copyright © 1989 by Academic Press, Inc.

ALL RIGHTS RESERVED

No part of this publication may be reproduced or transmitted in any form or by any means, electronic or mechanical, including photocopy, recording, or any information storage and retrieval system, without permission in writing from the copyright owner.

The appearance of the code at the bottom of the first page of an article in this journal indicates the copyright owner's consent that copies of the article may be made for personal or internal use, or for the personal or internal use of specific clients. This consent is given on the condition, however, that the copier pay the stated per copy fee through the Copyright Clearance Center, Inc. (27 Congress Street, Salem, Massachusetts 01970), for copying beyond that permitted by Sections 107 or 108 of the U.S. Copyright Law. This consent does not extend to other kinds of copying, such as copying for general distribution, for advertising or promotional purposes, for creating new collective works, or for resale. Copy fees for pre-1989 articles are as shown on the article title pages; if no fee code appears on the title page, the copy fee is the same as for current articles.

0019-1035/89 $3.00

MADE IN THE UNITED STATES OF AMERICA

CONTENTS OF VOLUME 79

NUMBER 1, MAY 1989

H. B. HAMMEL, N. L. LARK, M. RIGLER, AND T. J. KREIDL. Disk-Integrated Photometry of Neptune at Methane-Band and Continuum Wavelengths 1
NEIL L. LARK, H. B. HAMMEL, DALE P. CRUIKSHANK, DAVID J. THOLEN, AND MICHAEL A. RIGLER. The Brightness and Lightcurve of Triton in 1987 15
MARC W. BUIE AND DAVID J. THOLEN. The Surface Albedo Distribution of Pluto 23
J. W. BELETIC, R. M. GOODY, AND D. J. THOLEN. Orbital Elements of Charon from Speckle Interferometry 38
BRUCE HAPKE AND FRANCIS GRAHAM. Spectral Properties of Condensed Phases of Disulfur Monoxide, Polysulfur Oxide, and Irradiated Sulfur................. 47
BRUCE HAPKE. The Surface of Io: A New Model............................ 56
PAUL M. SCHENK AND WILLIAM B. MCKINNON. Fault Offsets and Lateral Crustal Movement on Europa: Evidence for a Mobile Ice Shell 75
T. G. NORTHROP, D. A. MENDIS, AND LES SCHAFFER. Gyrophase Drifts and the Orbital Evolution of Dust at Jupiter's Gossamer Ring 101
AKIVA BAR-NUN, EYAL HEIFETZ, AND DINA PRIALNIK. Thermal Evolution of Comet P/Tempel 1—Representing the Group of Targets for the *CRAF* and *CNSR* Missions.. 116
ANITA L. COCHRAN, JACKLYN R. GREEN, AND EDWIN S. BARKER. Are Low-Activity Comets Intrinsically Different from More Active Comets?............... 125
SUSAN HOBAN, MICHAEL F. A'HEARN, PETER V. BIRCH, AND RALPH MARTIN. Spatial Structure in the Color of the Dust Coma of Comet P/Halley 145
D. S. COLBURN, J. B. POLLACK, AND R. M. HABERLE. Diurnal Variations in Optical Depth at Mars 159
IMKE DE PATER, BOBBY L. ULICH, ERNST KREYSA, AND ROLF CHINI. Planetary Observations at a Wavelength of 355 μm 190
JOSEPH A. PIRRAGLIA. Dissipationless Decay of Jovian Jets 196
K. TANIKAWA, S. MANABE, AND R. BROUCKE. On the Origin of the Planetary Spin Angular Momentum by Accretion of Planetesimals: Property of Collision Orbits 208

NOTE

FRED FRANKLIN, MYRON LECAR, AND PAUL SOPER. On the Original Distribution of the Asteroids. II. Do Stable Orbits Exist between Jupiter and Saturn? 223

NUMBER 2, JUNE 1989

STEVEN W. SQUYRES. Urey Prize Lecture: Water on Mars 229
L. E. ROTH, R. S. SAUNDERS, G. S. DOWNS, AND G. SCHUBERT. Radar Altimetry of Large Martian Craters 289
MICHAEL H. CARR. Recharge of the Early Atmosphere of Mars by Impact-Induced Release of CO_2 311
E. LELLOUCH, A. COUSTENIS, D. GAUTIER, F. RAULIN, N. DUBOULOZ, AND C. FRÈRE. Titan's Atmosphere and Hypothesized Ocean: A Reanalysis of the *Voyager 1* Radio-Occultation and IRIS 7.7-μm Data.......................... 328

B. N. Khare, W. R. Thompson, B. G. J. P. T. Murray, C. F. Chyba, C. Sagan, and E. T. Arakawa. Solid Organic Residues Produced by Irradiation of Hydrocarbon-Containing H_2O and H_2O/NH_3 Ices: Infrared Spectroscopy and Astronomical Implications 3

Christopher F. Chyba, Carl Sagan, and Michael J. Mumma. The Heliocentric Evolution of Cometary Infrared Spectra: Results from an Organic Grain Model 3

Martyn J. Fogg. The Relevance of the Background Impact Flux to Cyclic Impact/Mass Extinction Hypotheses 38

S. J. Peale and Jack J. Lissauer. Rotation of Halley's Comet 39

Author Index for Volume 79.. 43

NOTICE

The Subject Index for Volume 79 will appear in the December 1989 issue as part of a cumulative index for the year 1989.

INFORMATION FOR AUTHORS

ICARUS is devoted to the publication of original contributions in the field of solar system studies. Manuscripts reporting the results of new research—observational, experimental, or theoretical—concerning the astronomy, geology, meteorology, physics, chemistry, biology, and other scientific aspects of our solar system or extrasolar systems are welcome. The journal generally does not publish papers devoted **exclusively** to the Sun, the Earth, celestial mechanics, meteorite studies or astrophysics. The preferred language of publication is English, but in special cases manuscripts are considered in French, German, or Russian. All papers are reviewed, generally by two independent referees. Authors are invited to submit a list of no more than five potential referees; the Editor may use this to guide his selection of referees. If authors so request in their cover letters, manuscripts will be handled anonymously during the refereeing process. Authors will usually be asked to respond to criticisms and suggestions by the referees prior to publication.

Manuscripts are accepted for review with the understanding that the same work has not been and will not be nor is presently submitted elsewhere, and that its submission for publication has been approved by all of the authors and by the institution where the work was carried out; further, that any person cited as a source of personal communications has approved such citation. Written authorization may be required at the Editor's discretion. For the benefit of the reviewers, three (3) copies of all crucial references cited in the manuscript as *submitted* or *in press* must accompany the paper. Articles and any other material published in ICARUS represent the opinions of the authors and should not be construed to reflect the opinions of the Editors or the Publisher.

Authors submitting a manuscript do so on the understanding that if it is accepted for publication, copyright in the article, including the right to reproduce the article in all forms and media, shall be assigned exclusively to the Publisher. The Publisher will not refuse any reasonable request by the author for permission to reproduce any of his or her contributions to the journal.

There are no page charges. However, authors will be charged for color reproduction or foldout pages; the publisher will provide an estimate of cost on request. Fifty **reprints** of each paper will be furnished gratis to the author and additional reprints may be purchased.

Manuscripts. *Four copies* of the manuscript, including figures, tables, etc., should be submitted to *Joseph A. Burns, Space Sciences Building, Cornell University, Ithaca, New York 14853-6801, telephone: 607-255-4875*. Authors should retain the original typescript. At least one set of figures should be suitable for camera-ready reproduction. All manuscripts must be typewritten with wide margins and *double-spaced throughout,* including references and footnotes. Number each page of the manuscript. Include on the first page the title of the paper and the name(s) and affiliation(s) of the author(s), including mailing address(es) and telephone number(s) [or telex number(s) or electronic mail address(es)]. At the bottom of the first page note the number of manuscript pages, figures, and tables. On the second page indicate a proposed running head of not more than 35 characters, and the name and address to which editorial correspondence and proofs should be directed. The third page should contain a brief abstract, and the text should begin on the following page. Following the main text, give Appendices, Acknowledgments, references, tables, figure captions, and figures, in that order. Places where figures and tables are to appear in the published paper should be marked in the margins of the manuscript.

Please write with attention to organization, style, and especially brevity. Present results logically, with order dictated by the needs of the reader. Take special care in composing the title and abstract, since these will be the most frequently read sections of the paper. In the title, specific words are preferable to general ones. The abstract should summarize the conclusions of the research, including quantitative results where appropriate, rather than merely stating the problem.

Whenever possible, quotients in mathematical expressions should employ the solidus (/) rather than being displayed in built-up form. However, for units, exponential notation is preferred (e.g., erg cm^{-2} sec^{-1}, not erg/cm^2 sec). Most authors will recall the difference between ''i.e.,'' and ''e.g.,'' will note that such nouns as ''data'' are plural and ''mare'' singular, and will take care to insert a zero before decimal fractions lying between $+1$ and -1.

Guidelines for Submission of "Notes": Papers on especially topical subjects will be given unusually rapid handling if they satisfy the following limitations on length:

(i) Manuscripts should be typed double-spaced and should be no longer than nine pages, including a very brief abstract of one or two sentences.

(ii) The sum of figures and tables should be less than, or equal to, two.

We expect that ICARUS will publish ''Notes'' within four months of submission, if no revision is required. We will try to complete refereeing and editorial handling in less than one month. In order to speed publication, proofs of ''Notes'' will be proofread only at Academic Press.

Tables are to be numbered consecutively with Roman numerals in order of their citation in the text. Each table should be typed, *double-spaced,* on a separate sheet with due regard to the proportions of the printed page. All tables should bear appropriate headings. Unusually elaborate tables should be prepared to allow them to be reproduced in the journal directly without typesetting.

Figures. At the time of submission of the manuscript, one original of each figure is to be submitted in such form as to permit photographic reproduction without redrawing: Line glossies should be carefully drafted, no larger than 22 × 30 cm. Original drawings, laser prints, or standard glossy photographic reproductions are acceptable. Authors should design figures so that they will fit one or two columns of print; in particular, the lettering should be large enough to allow a reduction to ⅓ the original size. *Each figure should be identified with the author's name and figure number.* All figures, whether line drawings or halftones, should be numbered consecutively in Arabic numerals, in order of their citation in the text. Figure captions should be typewritten on a separate sheet, following the text. Color plates and foldouts are published at the author's expense.

Literature citations in the text should be in one of the following forms: Encrenaz and Combes 1983 (for two authors); Safronov *et al.* 1986 (for three or more authors); Walker 1984, p. 198 (for reference to a specific page). To distinguish two or more works by the same author(s) in the same year, use suffixes a, b, etc., following the year (e.g., Öpik 1983a, 1983b).

Literature citations in the bibliography should be *listed alphabetically* according to the surname of the (first) author. Journal references should contain the *names and initials of all authors, the year, the title of the article, and standard abbreviation of the journal, the volume number, and the first and last page numbers.* Titles of journals and books should be in italics, volume numbers in boldface. (In a typed manuscript, indicate italics by single underlining and boldface by wavy underlining.) Below are shown examples of the proper reference forms for a journal article, a book chapter, and a book, respectively.

Borderies, N., P. Goldreich, and S. Tremaine 1984. Unsolved problems in planetary ring dynamics. In *Planetary Rings* (R. J. Greenberg and A. Brahic, Eds.), pp. 713–734. Univ. of Arizona Press, Tucson.

Jakosky, B. M., and P. R. Christensen 1986. Are the Viking Lander sites representative of the surface of Mars? *Icarus* **66,** 125–133.

Whipple, F. L. 1985. *The Mystery of Comets.* Random House, New York.

Careful compliance with these instructions for the preparation of the list of references is required; manuscripts with incomplete references (or missing abstracts) may be returned to the author for correction before being considered for publication.

Proofs will be sent to authors. When submitting a manuscript, the author should include a list of the symbols employed, identified typographically, not mathematically. This list will not be printed, but will help to avoid costly author's corrections in proof. Authors will be charged for excessive alterations in proof.

"...An awesome work of scholarship."

—CHICAGO TRIBUNE

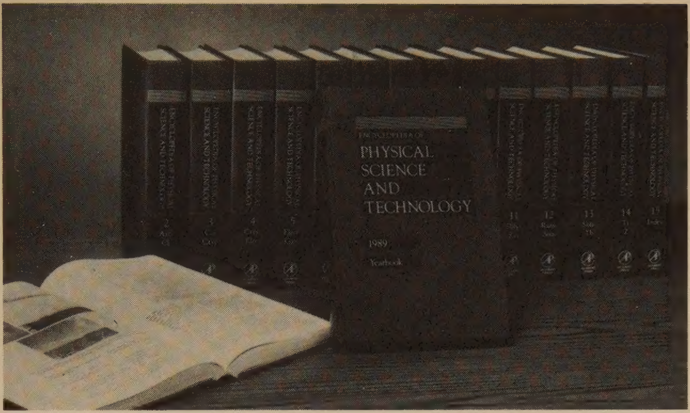

Encyclopedia of Physical Science and Technology

editor-in-chief Robert A. Meyers
TRW, Inc., Redondo Beach, California

> **"... a landmark of specialized publishing, a massive magnum opus from one of the world's most distinguished spreaders of the scientific word... Its very presence is newsworthy and awesome, as is the list of its advisers and contributors, including Nobel laureates Linus Pauling, S. Chandrasekhar, Vladimir Prelog, Abdus Salam, Glenn Seaborg, Kai Siegbahn and Edward Teller."**
>
> **—CHICAGO TRIBUNE**

In the short time since its publication, the **Encyclopedia of Physical Science and Technology** has become *the* contemporary scientific reference for today's technology. From MIT to the Kennedy Space Center to IBM, thousands of academic, industrial, and public libraries are finding that they can't be without this detailed, authoritative, and comprehensive reference work.
1987, 15-volume set including index, $2,500.00

Announcing the 1989 Encyclopedia Yearbook

To keep your set of the **Encyclopedia of Physical Science and Technology** the most up-to-date reference for years to come, Academic Press will begin publishing yearbook volumes in December 1988. Each Yearbook will feature several articles examining new, fast-emerging areas of study or offering the latest information on topics already in the **Encyclopedia**.

1988, 673 pages, $165.00/ ISBN: 0-12-226916-0

Encyclopedia of Astronomy and Astrophysics

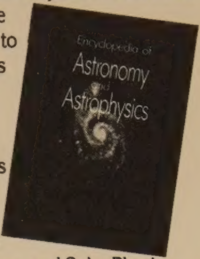

Accurate, up-to-date, and highly informative, the **Encyclopedia of Astronomy and Astrophysics** covers a dynamic area of science in one 770-page volume. Responding to the dramatic changes occurring in these fields, an array of expert practitioners present concise views of topics ranging from Cosmology and Cosmic Inflation to Pulsars, Star Clusters, and Solar Physics.

1988, 770 pages, $49.95/ISBN: 0-12-226690-0

Encyclopedia of Telecommunications

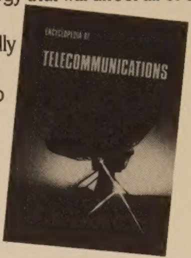

This authoritative, 550-page reference contains the latest advances in telecommunications technology—technology that will affect all of us during the next few decades. Internationally recognized experts have written articles to give you information on leading-edge research and engineering applications, on topics ranging from Fiber Optics to Intelligent and Computer Networks to Speech and Signal Processing.

1988, 550 pages, $49.95/ISBN: 0-12-226691-9

Call now for more information!
National Sales Department, (619) 699-6345.

ACADEMIC PRESS *Harcourt Brace Jovanovich, Publishers*
Book Marketing Department 08058, 1250 Sixth Ave., San Diego, California 92101

© 1988 by Academic Press, Inc. All Right Reserved.

Prices subject to change without notice. DK/SJ—08058

ICARUS

International Journal of Solar System Studies

Volume 79, Number 2, June 1989

CONTENTS

STEVEN W. SQUYRES. Urey Prize Lecture: Water on Mars 229

L. E. ROTH, R. S. SAUNDERS, G. S. DOWNS, AND G. SCHUBERT. Radar Altimetry of Large Martian Craters 289

MICHAEL H. CARR. Recharge of the Early Atmosphere of Mars by Impact-Induced Release of CO_2 311

E. LELLOUCH, A. COUSTENIS, D. GAUTIER, F. RAULIN, N. DUBOULOZ, AND C. FRÈRE. Titan's Atmosphere and Hypothesized Ocean: A Reanalysis of the *Voyager 1* Radio-Occultation and IRIS 7.7-μm Data 328

B. N. KHARE, W. R. THOMPSON, B. G. J. P. T. MURRAY, C. F. CHYBA, C. SAGAN, AND E. T. ARAKAWA. Solid Organic Residues Produced by Irradiation of Hydrocarbon-Containing H_2O and H_2O/NH_3 Ices: Infrared Spectroscopy and Astronomical Implications 350

CHRISTOPHER F. CHYBA, CARL SAGAN, AND MICHAEL J. MUMMA. The Heliocentric Evolution of Cometary Infrared Spectra: Results from an Organic Grain Model 362

MARTYN J. FOGG. The Relevance of the Background Impact Flux to Cyclic Impact/Mass Extinction Hypotheses 382

S. J. PEALE AND JACK J. LISSAUER. Rotation of Halley's Comet 396

AUTHOR INDEX FOR VOLUME 79.. 431

NOTICE

The Subject Index for Volume 79 will appear in the December 1989 issue as part of a cumulative index for the year 1989.